

*Characterization and Exploitation of Protein Ligand
Interactions for Structure Based Drug Design*

Sanjay Nilapwar



Department of Biochemistry and Molecular Biology
University College London

This thesis is submitted in fulfilment of the requirements
of the University College London for the degree of Doctor
of Philosophy

November-2009

Statement

The work described in the thesis was carried out in the laboratories of the Department of Biochemistry and Molecular Biology, University College London between October-2002 and May-2006. The results described are entirely the work of the author except for the parts described below. Acquiring NMR data was carried out by Dr. Mark Williams and ^1H - ^{15}N HSQC assignment of apo Hsp90 N-terminal domain shown in Figure 3.3.9 was carried out by Dr. Reza Salek.

To my Mother, Father, Sarika and Atharva

Acknowledgements

I would like to thank all the people from the UCL biochemistry department who have helped me during the last four years of my PhD. In particular Prof. John Ladbury, my supervisor for his help and continued unending support for the project. Also many thanks to the other molecular biophysics group students/postdocs including Dr. Mark Williams, Dr. Roger George, Dr. Paul Leonard, Dr. Zamal Ahmed, Radwan Fawaz, Dr. Sunita Sardiwal and Tjelvar Olsson. Also thanks to people in Astra-Zeneca including Geoff Holdgate, Dr. Andy Davies, Dr. Walter Ward, Jane Sullivan and Dr. Wendy VanScyoc.

Finally, I would like to thank my wife and my kind father for going along with the idea of doing a PhD at this stage of our lives and for putting up with all of the other twists and turns in my career to date.

Sanjay M. Nilapwar

November 2009

Table of Contents

STATEMENT	II
LIST OF FIGURES	XI
LIST OF TABLES	XVI
ABSTRACT	XX
1. CHAPTER	1
1.1 Role of Thermodynamics in Protein-Ligand Interactions	3
1.2 Forces Involved in Protein-Ligand Interactions	5
1.2.1 The Hydrophobic Effect (Interaction)	5
1.2.1.1 Structure of Water	5
1.2.1.2 Hydrophobic Interactions and Role of Water as a Solvent	7
1.2.1.3 Thermodynamics of Hydrophobic Interaction	8
1.2.2 Hydrogen Bonding	8
1.2.3 Charge-Charge (Electrostatic) Interactions	10
1.2.4 van der Waals Forces (Induced Dipole-Induced Dipole Interactions)	11
1.2.5 π - π Ring Stacking Interactions	12
1.2.6 Cation- π Interaction	13
1.3 Importance of Change in Heat Capacity (ΔC_p) in Protein-Ligand Interactions	14
1.3.1 Correlations Between Changes in Surface Area (SASA) Exposed to Water and ΔC_p	15
1.3.2 Factors Affecting ΔC_p in Protein-Ligand Interactions	16
1.3.2.1 The Hydrophobic Effect	16
1.3.2.2 Electrostatic Interactions	17
1.3.2.3 Hydrogen Bonds	18

1.3.2.4	Intramolecular Vibrations	18
1.3.2.4.1	Defining Intramolecular Vibrations	18
1.3.2.4.2	Intramolecular Vibrations in Protein-Ligand Interactions	18
1.3.2.5	Conformational Entropy	19
1.4	Structure and Function of Hsp90	21
1.4.1	Function of Hsp90	21
1.4.2	Structure of Hsp90	23
1.4.2.1	Structure of the ATP-binding N-terminal domain of Hsp90	23
1.4.2.1.1	The ADP/ATP Binding Site Location in The N-Hsp90	25
1.4.2.1.2	The Geldanamycin Binding Site Location in N- Hsp90	27
1.5	Structure of CDK2 and Function of Cyclin-Dependent Kinases (CDKs)	29
1.5.1	Function of CDKs	29
1.5.2	Structure of CDK2	31
1.5.3	Using Inactive or Active CDK2 as a Design Template	33
1.6	Isothermal Titration Calorimetry (ITC)	35
1.7	Linear Interaction Energy (LIE) Free Energy Change Calculation	38
1.8	Aims of The Project	40
2.	CHAPTER	41
2.1	Expression, Purification and Characterization of N-Hsp90	41
2.1.1	Expression System	41
2.1.2	Preparing Competent Cells	42
2.1.3	Transformation	42
2.1.4	Expression of Protein in LB	42
2.1.5	Expression of Protein in Minimal Media	43
2.1.6	Purification of N-Hsp90	43
2.1.7	Protein Concentration Measurements	44
2.2	Purification and Characterization of CDK2	46
2.3	Isothermal Titration Calorimetry (ITC)	49

2.3.1	ITC of ADP/ATP and its Analogues Binding with N-Hsp90	49
2.3.2	ITC of Geldanamycin and its Analogues Binding with N-Hsp90	49
2.3.3	ITC of 2,4 and 4.6-bis anillino Pyrimidine and its Analogues with CDK2	49
2.4	The GRID Force Field and GRID MIFs	50
2.5	Nuclear Magnetic Resonance (NMR) spectroscopy	51
2.6	Generation of N-Hsp90 Mutants	51
2.7	Circular Dichroism (CD) Spectroscopy of N-Hsp90	52
2.8	Determination of Melting Temperatures (T_m) by CD Spectroscopy	53
2.9	Solvent Accessible Surface Area (SASA) Calculations	53
2.10	Molecular Dynamics (MD) simulations	54
2.10.1	Preparation of N-Hsp90-ADP Structure for MD simulation	54
2.10.2	Preparation of N-Hsp90-geldanamycin Structure for MD simulation	54
2.10.3	Minimization/Equilibration and MD simulation	55
2.10.4	Determination of RMSD and RMSF	56
2.10.5	Determination of Water Residence Times	56
2.11	Linear Interaction Analysis (LIE) Calculation	57
2.11.1	Protein Preparation and Identification of Binding Site	57
2.11.2	Molecular Docking By GOLD	58
2.11.3	LIE Free Energy Change Calculation	58
3.	CHAPTER	59
3.1	Thermodynamics and Structural Properties for Binding of ADP/ATP and Geldanamycin to N-Hsp90	59
3.1.1	Thermodynamics of ADP/ATP Binding to N-Hsp90	60
3.1.2	Comparative Analysis of the Nucleotide Specificity of N-Hsp90 Nucleotide Binding Sites	65
3.1.3	Thermodynamics of Geldanamycin and its Analogues Binding to N-Hsp90	72
3.1.4	Conclusion: Understanding/Interpretation of Positive ΔC_p	80

3.2	Effect of Various Contributions To The ΔC_p	82
3.2.1	Mapping Interfacial Waters Molecules in the Protein-Ligand Binding Sites	83
3.2.2	Investigating The Effect of Mutations in Hsp90-ADP/ATP Binding Site on AMPPNP and 17-DMAG Binding	86
3.2.3	Effect of the Protonation/Deprotonation on the ΔH of AMPPNP Binding to N-Hsp90 and its Effect on Positive ΔC_p	89
3.2.4	Dissection of the pH Dependence of AMPPNP Binding Energetics to N-Hsp90	94
3.2.4.1	AMPPNP Binding to N-Hsp90: pH Dependency of ΔH_{obs} and $\Delta G_{obs}/K_b$	96
3.2.4.2	AMPPNP Binding to N-Hsp90: pH Dependency of $\Delta C_{p_{obs}}$	103
3.2.5	Effect of Salt Concentration on AMPPNP Binding to N-Hsp90	106
3.2.6	Investigating The Effect of D ₂ O on ΔH and ΔC_p of 17-DMAG and AMPPNP Binding to N-Hsp90.	109
3.2.6.1	Isothermal Titration Calorimetry for Association of AMPPNP and Geldanamycin to N-Hsp90 in D ₂ O	110
3.2.6.2	Thermodynamic Difference for Titrations of N-Hsp90-ADP/ATP and N-Hsp90-17-DMAG Interactions Conducted in H ₂ O and D ₂ O	113
3.2.6.3	Differences in Structure of H ₂ O and D ₂ O Can Give Different values for ΔC_p	118
3.2.6.4	Correlating thermodynamics to the data Obtained From Transfer of Model Compounds from H ₂ O to D ₂ O	119
3.2.7	Comparison of Experimental and Empirically Calculated ΔC_p	121
3.2.8	Molecular Dynamics (MD) Simulations Study of Ligand Binding to N-Hsp90	130
3.2.8.1	Identification of Hydration sites in N-Hsp90-ATP/ADP and N-Hsp90-Geldanamycin Binding site	131
3.2.8.2	General Structural Analysis	132
3.2.8.3	Assessment of Water Residence Times In N-Hsp90-ATP/ADP and N-Hsp90-Geldanamycin Binding Site	135
3.2.8.4	Assumption and limitations	139
3.2.9	Conclusion	140
3.3	Role of Metal Ions in the N-Hsp90-AMPPNP Interaction	141

3.3.1	Prediction of Various Divalent Metal Binding and Divalent Metal Binding Site with GRID	144
3.3.2	Thermodynamics of Binding for Various Divalent Metal Cations	147
3.3.3	Two Dimensional ^1H - ^{15}N Heteronuclear Single Quantum Coherence (HSQC) Experiment to Analyze the Effect of Structural Change in Presence of Different Metals	154
3.3.4	Circular Dichroism (CD) Spectroscopy of Divalent Metal-AMPPNP Binding to N-Hsp90	160
3.3.5	Is Tight Ordering of Water Around Mg^{2+} Responsible for Positive ΔC_p in N-Hsp90-ADP/ATP Interactions?	162
3.3.6	Conclusion: Ca^{2+} and Mn^{2+} Substitution in Place of Mg^{2+} : Implications for the Binding Energetics and ΔC_p of binding for ADP/AMPPNP to N-Hsp90	169
3.4	Conclusion	172
4.	CHAPTER	175
4.1	Introduction	175
4.2	Thermodynamics of Binding of Bis anilino pyrimidine to CDK2	177
4.2.1	Thermodynamics of Various 2,4-Bis Anilino Pyrimidine Ligands with CDK2	179
4.2.2	Thermodynamics of Various 4,6-Bis Anilino Pyrimidine Ligands with CDK2	186
4.3	ΔG Calculation by Linear Interaction Energy (LIE) Method	194
4.3.1	Preparation of X-ray Crystal Structure of CDK2 for Docking and Inhibitor Binding Modes	195
4.3.2	Docking Bis anilino Pyrimidine Inhibitors with GOLD	195
4.3.3	Structural Alignment with IAF	196
4.3.4	LIE calculation	197
4.4	Conclusion	204
5.	CHAPTER	205

5.1	Summary of Thesis	205
5.2	Further Work	207
6.	REFERENCES	208

List of Figures

Figure 1.1.1 Hypothetical model describing binding of ligand to the binding site of the target macromolecule protein.	4
Figure 1.2.1 A: Water structure depicting four electron pairs, which arranges themselves symmetrically at the vertices of a tetrahedron around the oxygen nucleus.	6
Figure 1.2.2 A: Water forms hydrogen bonds with other water molecule. B: Insertion of a nonpolar solute results in formation of a cage like structure around the nonpolar solute.	7
Figure 1.2.3 A: A water molecule (centre) can arrange itself in six different ways to form hydrogen bonds with two of its nearest neighbours.	8
Figure 1.2.4 Impact of the protein environment on the pK_b values of a basic ligand group (upper row) and pK_a values of an acidic ligand group (lower row) compared to aqueous solution.	10
Figure 1.2.5 A: Sandwich and B: parallel-displaced, π - π interaction shown by an aromatic ring.	12
Figure 1.2.6 Figure depicts cation- π interactions involving arginine.	13
Figure 1.4.1 Molecular chaperones participate in regulating many aspects of posttranslational protein homeostasis. A: Association of client proteins with HSPs complexes can result in preventing their aggregation B: assist in its intracellular trafficking, especially its translocation across membranous structures such as the endoplasmic reticulum (ER) C: association with the HSPs maintains the proteins in a meta-stable state and allows them to be activated by specific stimuli such as ligand binding, phosphorylation or assembly into multisubunit signalling complexes D: Without appropriate stimuli, HSPs can target the client proteins for their degradation through the ubiquitin-proteasome pathway and in the process regulates its steady-state cellular level.	22
Figure 1.4.2 Cartoon representing structure of N-Hsp90.	24
Figure 1.4.3 Two views of the structure of N-Hsp90 (helices in red, β -sheets in green) bound to ADP (blue) and Geldanamycin (yellow).	24
Figure 1.4.4 Schematic diagram of ADP interacting with the N-Hsp90.	25
Figure 1.4.5 Schematic diagram of geldanamycin interacting with the N-Hsp90.	28
Figure 1.5.1 Roles played by different CDK-Cyclin complexes in mammalian cell cycle.	30
Figure 1.5.2 Cartoon representing structure of full length CDK2.	32
Figure 1.6.1 Diagram of ITC cells and syringe.	36
Figure 1.6.2 Raw data for the titration of AMPPNP into N-Hsp90 solution at 8 °C in Tris-base at pH 8.00.	36
Figure 2.1.1 Primary amino acid sequence, using the single letter abbreviations, for the 207 amino acid yeast N-Hsp90 protein.	41
Figure 2.1.2 SDS PAGE gel shows aliquots collected during purification of the N-Hsp90.	44

Figure 2.1.3 UV/Vis spectrum of purified N-Hsp90 (Residues 1-207).	45
Figure 2.2.1 SDS PAGE gel electrophoresis of human CDK2.	46
Figure 2.2.2 UV/Vis spectrum of purified Human CDK2 recorded at 25 °C.	47
Figure 2.10.1 Front view of the N-Hsp90-ADP placed in a cubic box of pre-equilibrated SPC water molecules. α -helices and β -sheets of the N-Hsp90 are emphasized.	55
Figure 3.1.1 A: Raw data for the titration of ADP into N-Hsp90 solution at 20 °C in 20 mM Tris-base at pH 8.00.	61
Figure 3.1.2 Structure of ADP/ATP.	61
Figure 3.1.3 Thermodynamic parameters of the binding of ADP to N-Hsp90 at pH 8.00 as a function of temperature: ΔH (blue circles); $T\Delta S$ (pink square); ΔG (green triangles).	63
Figure 3.1.4 Structure of Adenine and Adenosine.	65
Figure 3.1.5 Thermodynamic parameters for the binding of the adenosine series of small molecules to N-Hsp90 at 25 °C.	67
Figure 3.1.6 Structure of various ATP/ADP analogues used in the study.	68
Figure 3.1.7 Plot of ΔH versus $T\Delta S$ for the binding of adenosine series of ligands to the N-Hsp90 at 25 °C.	70
Figure 3.1.8 Chemical structures of geldanamycin, 17-AAG and 17-DMAG, used in the present study.	72
Figure 3.1.9 Overlay of geldanamycin over 17-DMAG bound to N-Hsp90. (pink-geldanamycin bound Hsp90 and green 17-DMAG bound). 17-DMAG and geldanamycin bound structures show an all-atom RMS deviation of 1.29 Å.	74
Figure 3.1.10 Thermodynamic parameters of the binding of geldanamycin to N-Hsp90 at pH 8.00 as a function of temperature: ΔH (blue circles); $T\Delta S$ (pink square); ΔG (green triangles).	74
Figure 3.1.11 ^1H - ^{15}N HSQC experiment showing effect of addition of DMSO on N-Hsp90 (Green-Apo, Black-Apo+DMSO).	77
Figure 3.1.12 Two different views of geldanamycin (yellow) over ADP (red) in bound conformation to N-Hsp90, showing similar conformation for the bound form.	78
Figure 3.1.13 Two views of the structure of yeast N-Hsp90 (helices in red, β -sheets in green) bound to ADP (left) and geldanamycin (right).	78
Figure 3.1.14 Temperature dependence of the enthalpy change upon binding of ADP, ATP, AMPPNP and cAMP binding to N-Hsp90 at pH 8.00. The data are summarized in Table 3.1.1, 3.1.2, 3.1.3 and 3.1.4.	79
Figure 3.1.15 Temperature dependence of the enthalpy change upon binding of Geldanamycin, 17-AAG and 17-DMAG binding to N-Hsp90 at pH 8.00. The data are summarized in Table 3.1.6.	79
Figure 3.1.16 Figure showing reduction in solvent accessible surface area of protein-ligand complex upon ligand binding to protein.	80
Figure 3.2.1 Schematic diagram of ADP (Left) and geldanamycin (Right) interacting with the N-Hsp90.	83

Figure 3.2.2 Left: Position of ADP in N-Hsp90-ADP binding site. Right Position of ADP in N-Hsp90-ADP binding site along with surrounding area depicted with the hydrophobic and hydrophilic energy surface derived from the program GRID.	84
Figure 3.2.3 Left: Position of geldanamycin in N-Hsp90-Geldanamycin binding site. Right: Position of geldanamycin in N-Hsp90-Geldanamycin binding site along with surrounding area depicted with the hydrophobic and hydrophilic energy surface derived from the program GRID.	84
Figure 3.2.4 Crystal structure of N-Hsp90-ADP complex with residues selected for mutations labeled.	86
Figure 3.2.5 Binding isotherm for calorimetric titration of AMPPNP binding to N-Hsp90 in 20 mM Tris-base at pH 8.00 (Left) and similar experiment conducted in 20 mM Taps buffer at pH 8.00 (Right).	90
Figure 3.2.6 Proton linkage for AMPPNP binding to N-Hsp90 at pH 8.00 and 25 °C. The observed enthalpy of binding is plotted versus the enthalpy of ionization of the buffer.	92
Figure 3.2.7 Uncorrected ITC data of AMPPNP binding with N-Hsp90 performed at six different pH values at 8 °C in Triple buffer.	95
Figure 3.2.8 pH Dependence of ΔH_{obs} for the binding of AMPPNP to N-Hsp90 at 25 °C and in 100 mM ACES, 50 mM Ethanolamine and 50 mM Tris buffer.	96
Figure 3.2.9 The pH dependence of the logarithm of the association constant of AMPPNP to N-Hsp90 at 8 °C and in 100 mM ACES, 50 mM Tris, 50 mM Ethanolamine (Triple buffer).	102
Figure 3.2.10 $\Delta C_{p_{\text{obs}}}$ as a function of pH using the values in Table 3.2.4.1. The $\Delta C_{p_{\text{obs}}}$ is maximal at pH 8.70. At this pH values, the $\Delta C_{p_{\text{obs}}}$ value is $0.57 \pm 0.21 \text{ kJ}\cdot\text{mol}^{-1}\cdot\text{K}^{-1}$.	104
Figure 3.2.11 Salt dependence of the thermodynamic quantities of the N-Hsp90-AMPPNP interaction (0.0 to 0.2 M NaCl).	107
Figure 3.2.12 Typical calorimetric titration of N-Hsp90 with 17-DMAG in 20 mM Tris buffer (pH = 8.00 and pD = 8.00) in A. D ₂ O and B. H ₂ O.	111
Figure 3.2.13 Temperature dependence of the enthalpy change upon binding (ΔH) of geldanamycin to N-Hsp90 at pH 8.00 in D ₂ O.	112
Figure 3.2.14 Temperature dependence of the enthalpy change upon binding (ΔH) of AMPPNP to N-Hsp90 at pH 8.00 in D ₂ O.	112
Figure 3.2.15 Change in enthalpies of binding AMPPNP (top) and 17-DMAG (bottom) in H ₂ O (square) and D ₂ O (♦) as a function of temperature.	116
Figure 3.2.16 ΔSASA upon complex formation for each residue, positive values on y-axis indicates increase in surface area for respective residue after binding.	125
Figure 3.2.17 CD spectrum for N-Hsp90 bound to AMPPNP and on its own, measured at 25 °C in 20 mM Tris buffer pH 8.00.	128
Figure 3.2.18 Root mean square deviation (RMSD) of the backbone atom positions from their starting positions as a function of time, for simulations of the N-Hsp90 (blue line), N-Hsp90-ADP (green line) and N-Hsp90-geldanamycin models (red line).	133

Figure 3.2.19 Residue-by-residue RMSF fluctuations around their average positions for N-Hsp90 (blue), N-Hsp90-ADP (Green) and N-Hsp90-Geldanamycin (Red).	134
Figure 3.2.20 Structure of N-Hsp90 with ADP along with number of water molecule investigated.	136
Figure 3.2.21 Structure of N-Hsp90 with geldanamycin along with number of water molecule investigated.	137
Figure 3.3.1 Schematic diagram showing protein-ligand binding. In the top diagram protein is shown reacting with ligand. The fuzzy outline surrounding protein, ligand and protein-ligand complex denotes water that is more ordered than the bulk solvent.	141
Figure 3.3.2 Isothermal titration calorimetric plot conducted at 12 °C for Ca ²⁺ -AMPPNP binding to N-Hsp90 (left) and Mn ²⁺ -AMPPNP binding to N-Hsp90 (Right).	147
Figure 3.3.3 ΔH versus temperature plot for binding of Mg ²⁺ -AMPPNP (pink square) and Ca ²⁺ -AMPPNP (blue diamonds) binding to N-Hsp90 in 20 mM Tris-base at pH 8.00.	151
Figure 3.3.4 ΔH versus temperature plot for binding of Mg ²⁺ -AMPPNP (pink Square) and Mn ²⁺ -AMPPNP (blue diamonds) binding to Hsp90. Carried out at pH 6.00, in 100 mM ACES, 50 mM Tris, 50 mM Ethanolamine, 5 mM MgCl ₂ or 5 mM MnCl ₂ .	152
Figure 3.3.5 ¹ H- ¹⁵ N HSQC spectrum of N-Hsp90-MgAMPPNP obtained at 600 MHz and 25 °C.	155
Figure 3.3.6 ¹ H- ¹⁵ N HSQC spectrum of N-Hsp90-MnAMPPNP obtained at 600 MHz and 25 °C.	155
Figure 3.3.7 ¹ H- ¹⁵ N HSQC spectrum of N-Hsp90-CaAMPPNP obtained at 600 MHz and 25 °C.	156
Figure 3.3.8 ¹ H- ¹⁵ N HSQC spectrum of N-Hsp90-CdAMPPNP obtained at 600 MHz and 25 °C.	156
Figure 3.3.9 Corrected ¹ H- ¹⁵ N HSQC spectrum of the N-terminal domain of N-Hsp90.	157
Figure 3.3.10 Circular dichroism spectroscopic analysis (mean residue ellipticity, $[\theta]_{\text{mrw}}$ Vs. wavelength) of the substitution of various divalent metal cations like Mn ²⁺ , Cd ²⁺ , Ca ²⁺ in place of Mg ²⁺ for AMPPNP-binding to N-Hsp90.	160
Figure 3.3.11 Chelate formation of EDTA upon binding to divalent metal cations chelate formation results in complete desolvation of waters from the surface of divalent metal cations.	162
Figure 3.3.12 Isothermal titration calorimetric analysis of Mg ²⁺ -AMPPNP binding (A), Mn ²⁺ -AMPPNP binding (B) and Ca ²⁺ -AMPPNP binding to N-Hsp90 (C).	163
Figure 3.3.13 Temperature dependence of the ΔH on binding of Mg ²⁺ (blue), Mn ²⁺ (pink) and Ca ²⁺ (yellow) to EDTA in 20 mM Tris buffer at pH 8.00, while aqua coloured line denotes Mn ²⁺ binding to EDTA at pH 6.00 (Triple Buffer).	164
Figure 3.3.14 Two different poses of Mg ²⁺ -ADP with bound water molecules and protein residues. Structure coloured according to element, indicates human N-Hsp90; whereas green coloured structure indicates yeast N-Hsp90.	170
Figure 4.1.1 Chemical Structure of 2,4-bis anillino pyrimidine (left) and 4,6-bis anillino pyrimidine (right) with changed position of nitrogen in the pyrimidine ring denoted by red colour.	176

Figure 4.2.1 Raw data for titration of M407492 with a CDK2 at 25 °C in 20 mM. HEPES. pH 7.4.	179
Figure 4.2.2 Superposition of the binding modes of M387441 and M407492, displaying interactions made by bromine with Phe80 of CDK2.	180
Figure 4.2.3 Comparison of relative experimental ΔG vs relative AlogP (with respect to M387441) of binding to CDK2 with various 2,4-bis anilino pyrimidines at 25 °C.	184
Figure 4.2.4 Costructure of M365370 bound to CDK2 showing the Connelly surface of the binding site colour coded according to electrostatic potential. Red indicates negatively charged surface area, and blue indicates positively charged surface area. M365370 indicates two similar binding modes with CDK2 with equal occupancies.	188
Figure 4.2.5 Figure 4.2.5 Overlay of binding modes of M389750 and M365370.	191
Figure 4.2.6 Comparison of relative experimental ΔG vs relative AlogP (with respect to M365377) of binding to CDK2 with various 4,6-bis anilino pyrimidines at 25 °C.	193
Figure 4.3.1 Figure of 8 best conform ations matched with X-crystal structure of M407492.	196
Figure 4.3.2 ΔG values estimated by the SGB-LIE method for 16-bis anillino pyrimidine analogues consisting the experimental ΔG vs. the SGB-LIE ΔG .	199
Figure 4.3.3 Plot of A: van der Waals, B: electrostatic, C: reaction field, and D: cavity energies vs. experimental binding affinity for binding of 2,4-bisanillinopyrimidine and 4,6-bis anilino pyrimidine to CDK2.	201

List of Tables

Table 1.3.1 Thermodynamic properties for the transfer of small hydrocarbons from their pure liquid state to water, based on solubilities at T=25 °C.	17
Table 1.3.2 Expected signs of ΔS and ΔC_p in Protein-ligand reactions.	19
Table 1.4.1 Amino acid residues involved in the binding of ADP/ATP compared with those involved in binding geldanamycin to N-Hsp90.	27
Table 2.2.1 Dynamic Light Scattering (DLS) analysis of full length CDK2. Protein samples were analyzed by use of Protein Solutions DynaPro Molecular Sizing Instrument and Dynamics 6 software.	48
Table 2.6.1 Sequence of various primers used in N-Hsp90 mutations.	52
Table 2.10.1 GROMACS parameters for the normal simulation setup.	55
Table 3.1.1 Summary of the thermodynamic parameters for the binding interaction of N-Hsp90 with ADP as a function of temperature in 20 mM Tris buffer (pH 8.00).	62
Table 3.1.2 Summary of the thermodynamic parameters for the binding interaction of N-Hsp90 with ATP as a function of temperature in 20 mM Tris buffer (pH 8.00).	62
Table 3.1.3 Summary of the thermodynamic parameters for the binding interaction of N-Hsp90 with AMPPNP as a function of temperature (pH 8.00).	69
Table 3.1.4 Summary of the thermodynamic parameters for the binding interaction of N-Hsp90 with cAMP as a function of temperature (pH 8.00).	69
Table 3.1.5 Thermodynamic parameters for binding of various Purine analogues arranged in increasing number of phosphate groups at 25 °C.	70
Table 3.1.6 Summary of the thermodynamic parameters for the binding interaction of N-Hsp90 with different geldanamycin analogues as a function of temperature in 20 mM Tris buffer (pH 8.00).	75
Table 3.2.1 Secondary structure prediction of wild type and mutant N-Hsp90 as determined from CONTIN-CD. While values in bracket shows amount calculated from the X-ray crystal structure.	87
Table 3.2.2 Thermodynamic Parameters for the binding of AMPPNP with different mutants of N-Hsp90.	88
Table 3.2.3 Thermodynamic Parameters for the binding of 17-DMAG with various mutants of N-Hsp90.	88
Table 3.2.4 Thermodynamic data obtained from the titration of AMPPNP with N-Hsp90 at pH 8.00, 0.02 M ionic strength TRIS and TAPS buffer at 25 °C.	90
Table 3.2.5 Summary of the thermodynamic parameters for the binding interaction of N-Hsp90 with AMPPNP in 20 mM Taps buffer function of temperature (pH 8.00).	91
Table 3.2.6 Summary of comparative thermodynamic parameters for the binding interaction of AMPPNP to N-Hsp90 between pH 5.00-10.00 and at 8 °C in 100 mM ACES, 50 mM Tris, 50 mM Ethanolamine buffer.	97

Table 3.2.7 Summary of the thermodynamic parameters for the binding interaction of N-Hsp90-AMPPNP in 100 mM ACES, 50 mM Tris, 50 mM Ethanolamine (Triple buffer) and 5 mM MgCl ₂ as a function of temperature (pH 5.00).	98
Table 3.2.8 Summary of the thermodynamic parameters for the binding interaction of N-Hsp90-AMPPNP in 100 mM ACES, 50 mM Tris, 50 mM Ethanolamine (Triple buffer) and 5 mM MgCl ₂ as a function of temperature (pH 6.00).	98
Table 3.2.9 Summary of the thermodynamic parameters for the binding interaction of N-Hsp90-AMPPNP in 100 mM ACES, 50 mM Tris, 50 mM Ethanolamine (Triple buffer) and 5 mM MgCl ₂ as a function of temperature (pH 7.00).	99
Table 3.2.10 Summary of the thermodynamic parameters for the binding interaction of N-Hsp90-AMPPNP in 100 mM ACES, 50 mM Tris, 50 mM Ethanolamine (Triple buffer) and 5 mM MgCl ₂ as a function of temperature (pH 8.00).	99
Table 3.2.11 Summary of the thermodynamic parameters for the binding interaction of N-Hsp90-AMPPNP in 100 mM ACES, 50 mM Tris, 50 mM Ethanolamine (Triple buffer) and 5 mM MgCl ₂ as a function of temperature (pH 8.70).	100
Table 3.2.12 Summary of the thermodynamic parameters for the binding interaction of N-Hsp90-AMPPNP in 100 mM ACES, 50 mM Tris, 50 mM Ethanolamine (Triple buffer) and 5 mM MgCl ₂ as a function of temperature (pH 9.50).	100
Table 3.2.13 Summary of the thermodynamic parameters for the binding interaction of N-Hsp90-AMPPNP in 100 mM ACES, 50 mM Tris, 50 mM Ethanolamine (Triple buffer) and 5 mM MgCl ₂ as a function of temperature (pH 10.00).	101
Table 3.2.14 Comparison of thermodynamic parameters at different salt concentrations at 15 °C.	106
Table 3.2.15 Summary of the thermodynamic parameters for the binding interaction of N-Hsp90-AMPPNP with 20 mM Tris, 5 mM MgCl ₂ and 100 mM Salt as a function of temperature (pH 8.00).	108
Table 3.2.16 Summary of the thermodynamic parameters for the binding interaction of N-Hsp90 with AMPPNP in 20 mM Tris, 5 mM MgCl ₂ and 200 mM Salt as a function of temperature (pH 8.00).	108
Table 3.2.17 Some physical properties of H ₂ O and D ₂ O. Please note, H-bond length denoted here is used purely for comparison purpose with H-bond length in D ₂ O.	109
Table 3.2.18 TΔS, ΔH, ΔG and ΔC _p for 17-DMAG and AMPPNP binding to N-Hsp90 at 25 °C.	114
Table 3.2.19 Summary of the thermodynamic parameters for the binding interaction of N-Hsp90 AMPPNP with 20 mM Tris in Deuterium Oxide (D ₂ O) as a function of temperature (pD 8.0).	117
Table 3.2.20 Summary of the thermodynamic parameters for the binding interaction of N-Hsp90-17-DMAG in 20 mM Tris buffer in Deuterium Oxide (D ₂ O) as a function of temperature (pD 8.0).	117
Table 3.2.21 ΔSASA calculations for N-Hsp90-ADP complex.	123
Table 3.2.22 ΔSASA calculations for N-Hsp90-Geldanamycin complex.	123
Table 3.2.23 ΔSASA calculations for N-Hsp90-ADP complex. (Calculated using trapped water molecules on the interface of the Binding site)	124

Table 3.2.24 $\Delta SASA$ calculations for N-Hsp90-geldanamycin complex. (Calculated using trapped water molecules on the interface of the Binding site)	124
Table 3.2.25 Nearest protein atoms located in close proximity to the buried crystal water molecules between N-Hsp90 and ADP.	132
Table 3.2.26 Nearest protein atoms located in close proximity to the buried crystal water molecules between N-Hsp90 and Geldanamycin.	132
Table 3.2.27 Water residence time of different water molecules in the N-Hsp90-ADP binding interface.	136
Table 3.2.28 Water residence time of different water molecules in the N-Hsp90-geldanamycin binding interface.	137
Table 3.3.1 Some of the expected thermodynamic signs for possible contributions to thermodynamic process.	142
Table 3.3.2 X-ray crystal structure of N-Hsp90-ADP showing presence of Magnesium predicted by GRID (green) compared with crystal position of Magnesium (red).	145
Table 3.3.3 Comparison of binding thermodynamics for binding of Mg^{2+} -AMPPNP and Ca^{2+} -AMPPNP to N-Hsp90 at 8 °C (pH 8.00).	148
Table 3.3.4 Comparison of binding thermodynamics for binding of Mg^{2+} -AMPPNP and Mn^{2+} -AMPPNP to N-Hsp90 at 8 °C (pH 6.00). Binding was carried out in 100 mM ACES, 50 mM Tris, 50 mM Ethanolamine buffer.	148
Table 3.3.5 Summary of the thermodynamic parameters for the binding interaction of N-Hsp90-AMPPNP in 100 mM ACES, and 5 mM Manganese as a function of temperature (pH 6.00).	149
Table 3.3.6 Summary of the thermodynamic parameters for the binding interaction of N-Hsp90-AMPPNP in 20 mM Tris base, and 5 mM Calcium as a function of temperature (pH 8.00).	150
Table 3.3.7 Summary of the thermodynamic parameters for the binding interaction of N-Hsp90-AMPPNP in 100 mM ACES, 50 mM Tris base, 50 mM Ethanolamine and 5 mM Manganese as a function of temperature (pH 6.00).	150
Table 3.3.8 Coordination number and Ionic radii of divalent metal cations.	163
Table 3.3.9 Comparison of thermodynamical parameters for binding of various divalent metal cation binding to EDTA at 20 °C. Titration carried out in triple buffer pH 8.00.	164
Table 3.3.10 Summary of the thermodynamic parameters for the binding interaction of 100 μ M EDTA with 1 mM Magnesium in 20 mM Tris buffer as a function of temperature (pH 8.00).	165
Table 3.3.11 Summary of the thermodynamic parameters for the binding interaction of 100 μ M EDTA with 1 mM Manganese in 20 mM Tris buffer as a function of temperature (pH 8.00).	165
Table 3.3.12 Summary of the thermodynamic parameters for the binding interaction of 100 μ M EDTA with 1 mM Calcium in 20 mM Tris buffer as a function of temperature (pH 8.00).	166

Table 3.3.13 Summary of the thermodynamic parameters for the binding interaction of 158 μ M EDTA with 1.8 mM Manganese in 100 mM PIPES, 50 mM Tris base, 50 mM Ethanolamine (Triple Buffer) as a function of temperature (pH 6.00).	166
Table 4.2.1A Substituents used for substitution along with their appropriate positions on 2,4-bis anilino pyrimidine along with their positions	178
Table 4.2.1B Substituents used for substitution along with their appropriate positions on 4,6-bis anilino pyrimidine along with their positions	178
Table 4.2.2 Thermodynamic binding parameters for M387441 and M407492.	181
Table 4.2.3 Thermodynamic binding parameters for various Y-monosubstituted 2,4-bis anilino pyrimidine analogues.	182
Table 4.2.4 Thermodynamic binding parameters for various disubstituted 2,4-bis anilino pyrimidine analogues.	183
Table 4.2.5 Structure and thermodynamic parameters for various monosubstituted 4,6-bis anilino pyrimidine analogues.	187
Table 4.2.6 Figure 4.2.6 Structure and thermodynamic parameters for disubstituted 4,6-bis anilino pyrimidines analogues.	189
Table 4.2.7 Structure and thermodynamic parameters for M410038 and M389750.	190
Table 4.2.8 Structure and thermodynamic parameters for M365370 and M386872.	192
Table 4.3.1 The data are collected from a 30 ps. Simulation after a 15 ps. equilibration. Each ligand shows the LIE component for bound-free state.	200
Table 4.3.2 Table showing differences in ΔG calculated from calorimetry and ΔG calculated from LIE.	202

ABSTRACT

Most characterised protein-small molecule interactions that display a change in heat capacity (ΔC_p) occur with a negative ΔC_p value. This is often attributed to solvent reorganisation from reduction in solvent accessible apolar surface area accompanying complex formation. Positive ΔC_p values have not been widely reported and could typically be attributed to an increased solvent accessible apolar surface area, desolvation of polar surface area or structural transitions in the biomolecular complex.

Heat shock protein-90 (Hsp90) is one of the abundant and important molecular ATP-dependent chaperones. The N-terminal domain of Hsp90 contains ATP/ADP binding site, where Hsp90-ADP interactions proceed with a large positive ΔC_p of $2.35 \pm 0.46 \text{ kJ}\cdot\text{mol}^{-1}\cdot\text{K}^{-1}$. Interestingly geldanamycin, an Hsp90 inhibitor which binds to the same N-Hsp90-ADP/ATP binding site, interacts with a negative ΔC_p of $-0.39 \pm 0.04 \text{ kJ}\cdot\text{mol}^{-1}\cdot\text{K}^{-1}$. The semi-empirical correlation of the solvent accessible surface area change does not match well with the observed ΔC_p . This prompted us to investigate various factors affecting the thermodynamics of protein-small molecule binding including varying buffers, differing salt concentration, altering pH, substitution of different metal cations and performing interactions in heavy water. Molecular dynamics simulation and NMR studies have allowed us to disregard structural changes of N-Hsp90-ADP molecule from giving rise to positive ΔC_p .

From a combination of these calorimetric, simulation and structural studies we have gathered a considerable body of evidence suggesting that the change in accessible surface area, ionic interactions and resultant desolvation of water molecules from the surface of a Mg^{2+} ion can contribute substantially to a positive ΔC_p . We conclude that this unique result appears to come from extensive disruption of the tightly bound water molecules present around Mg^{2+} -ADP after binding to Hsp90, which then gives rise to a positive ΔC_p .

In addition to these findings, the thermodynamics of 18 structurally related CDK2 inhibitors were investigated using ITC. CDK2 is a member of cyclin dependent kinases implicated in eukaryotic cell cycle progression and control. This investigation showed that even conservative changes in small molecule structure can reveal large variation in thermodynamic signature, while simple concepts such as van der Waals interactions, steric hindrance, and hydrophobicity are insufficient to explain it.

1. Chapter

Introduction

In the past two decades, knowledge of the relationship between molecular structure and biological effect has prompted a fundamental change of the methods used in modern drug discovery. Methods such as molecular biology can identify receptor dysfunction or failures in regulation as possible causes of a disease. Protein engineering can help to isolate proteins in a purified form, which can be then be subjected to three dimensional structure elucidation by X-ray crystallography and/or NMR spectroscopy. Resultant three dimensional structures provide a platform for the development of improved techniques to predict and design newer and better ligands by structure based drug design (SBDD), which can subsequently be marketed as drugs.

However, on its own, structure elucidation gives very little or no information about the role played by various energetic components in biomolecular interaction. Additionally, binding or thermodynamic data in isolation is of little use in the absence of structural information. As a result, the question arises of how to correlate thermodynamic parameters with structural details on the change from one equilibrium state to another equilibrium state and occupies a central position in biophysical studies. Therefore, prediction of the thermodynamic consequences of structural variation induced by binding of two molecules can have far-reaching consequences on the whole drug development cycle. Additionally, establishing a direct link between the three dimensional structure of protein-ligand complexes and their respective binding thermodynamics will help in circumventing the need for synthesizing molecules and performing binding studies, as these are financially expensive and time consuming processes (*1*).

A number of different types of computational approaches have been developed in the past for predicting binding energies. These range from purely empirical or statistical ones, such as QSAR, to more or less rigorous methods based on evaluation of the physical energies involved in the binding process (MM-PBSA, MD and MC simulation). However none of these methods can predict the complete thermodynamics (ΔC_p , ΔS , ΔH , and ΔG) of a binding system except the method derived from correlation of change in heat capacity (ΔC_p) and change in solvent accessible surface area ($\Delta SASA$) on going from one equilibrium state to another. In fact several different equations have been proposed that allow calculation of the individual thermodynamic parameters and these have been successfully applied in a number of studies involving the prediction of binding energetics including protein-ligand, protein-protein and protein-peptide interactions (2-4).

However, the prediction of binding energetics from structure is still an area of some disagreement, which can mainly be attributed to factors such as trapped water molecules on the protein-ligand interface and presence of various external cofactors like salts and metals (5-8). As a result, development of a universally acceptable model has been held back. Therefore in this work, we have decided to investigate the role of water molecules present on the protein-ligand interface for its effect on the ΔC_p . For this we have adopted the Hsp90-ADP/ATP and Hsp90-geldanamycin binding system, since this system satisfies the various important criteria required for successful investigation such as: (1) accessibility of the high resolution free and bound data for Hsp90, Hsp90-ADP and Hsp90-geldanamycin and (2) easy availability of Hsp90 protein, along with various ADP and geldanamycin analogues.

Additionally, this work started with investigating ΔC_p in protein-ligand interactions; however the aim of the research has deviated a little due to observance of positive ΔC_p in Hsp90-ADP interaction and is discussed in this research work.

1.1 Role of Thermodynamics in Protein-Ligand Interactions

The binding of a ligand to a target protein is normally driven by the decrease in the free energy of the protein-ligand complex compared to the free energy of both the ligand and the protein existing independently in solution and can normally be represented by following equation 1.1.1.



The Gibbs free energy change (ΔG), for interaction of the macromolecule-ligand complex is related to the standard Gibbs free energy change ($\Delta G^\circ_{\text{bind}}$), under defined conditions (25 °C and 1 M of both target and ligand) and can be represented as

$$\Delta G = \Delta G^\circ_{\text{bind}} - RT \ln \frac{[\text{Protein:Ligand}]}{[\text{Protein}][\text{Ligand}]} \quad 1.1.2$$

where R is the universal gas constant and T denotes the absolute temperature. At equilibrium and at standard conditions, the $\Delta G^\circ_{\text{bind}}$ will be 0, and thus the equation 1.1.2 can be rewritten as,

$$\Delta G = -RT \ln \frac{[\text{Protein : Ligand}]}{[\text{Protein}][\text{Ligand}]} = -RT \ln K_b \quad 1.1.3$$

The difference in free energy between the bound and unbound state can also be rewritten in terms of the enthalpy and entropy changes by equation 1.1.4.

$$\Delta G = \Delta H - T\Delta S = -RT \ln K_b \quad 1.1.4$$

where ΔH denotes a difference in enthalpy between two states and ΔS denotes difference in entropy between the two states. This thermodynamic equation 1.1.4 reveals several relationships, of which the first is intuitive: the tighter the binding of the ligand to the target, the greater must be the differences in free energy between bound and unbound states, with the bound state being the lowest in free energy. Additionally, the differences in free energy are made up of, and driven by, both the difference in enthalpy (ΔH) and entropy (ΔS) between the bound and unbound states.

1.2 Forces Involved in Protein-Ligand Interactions

Understanding the forces involved in the binding of proteins or macromolecules to ligands is of prime importance for two major reasons. Firstly, the design of specific ligands having the requisite affinity for proteins requires knowledge of how the structure of the ligand is related to the specificity/affinity of binding and what structural modifications could result in a drug with the desired qualities. Secondly, identifying the forces/energetics involved in such processes is fundamental to unravelling the mystery of molecular recognition in general and ligand binding in particular.

Some of the forces that are known to contribute protein-ligand binding are H-bonding, the hydrophobic effect, electrostatic interactions, van der Waals/packing interactions, complex hydration/dehydration contributions composed of a hydrophobic component, ion effects and entropy terms.

Also, the binding process could be associated with some structural revision/deformation of the protein as well as of the ligand molecule in order for the two to accommodate each other. All these events are associated with some energetic gains and losses, the comprehensive evaluation of which is difficult to estimate (10).

1.2.1 The Hydrophobic Effect (Interaction)

The hydrophobic effect is normally defined as reduction in one of the relatively unfavourable interactions happening between water and nonpolar atoms, such as the hydrophobic residues in proteins. The hydrophobic effect happens mainly because nonpolar atoms are excluded from forming H-bonds in an aqueous environment and it seems that this lack of formation of H-bond between nonpolar molecules and water, rather than attractive interactions between nonpolar groups, is responsible for it (11).

1.2.1.1 Structure of Water

The geometry and structure of a water molecule is illustrated in Figure 1.2.1. It consists of two O-H bonds of 0.96 Å length and is arranged with an angle of about 104.5° rather than being placed on directly opposite sides of the oxygen atom (12). The asymmetric shape of the water molecule arises from a tendency of the four electron pairs in the valence shell of oxygen to arrange themselves symmetrically at the vertices of a tetrahedron around the oxygen nucleus. Nonetheless, the two non-bonding pairs remain closer to the oxygen atom and exert a stronger repulsion against the two covalent bonding

pairs. This effectively pushes the two hydrogen atoms closer together and results in a distorted tetrahedral arrangement of the H-O-H angle to 104.5° (13), rather than 109° for a regular tetrahedron.

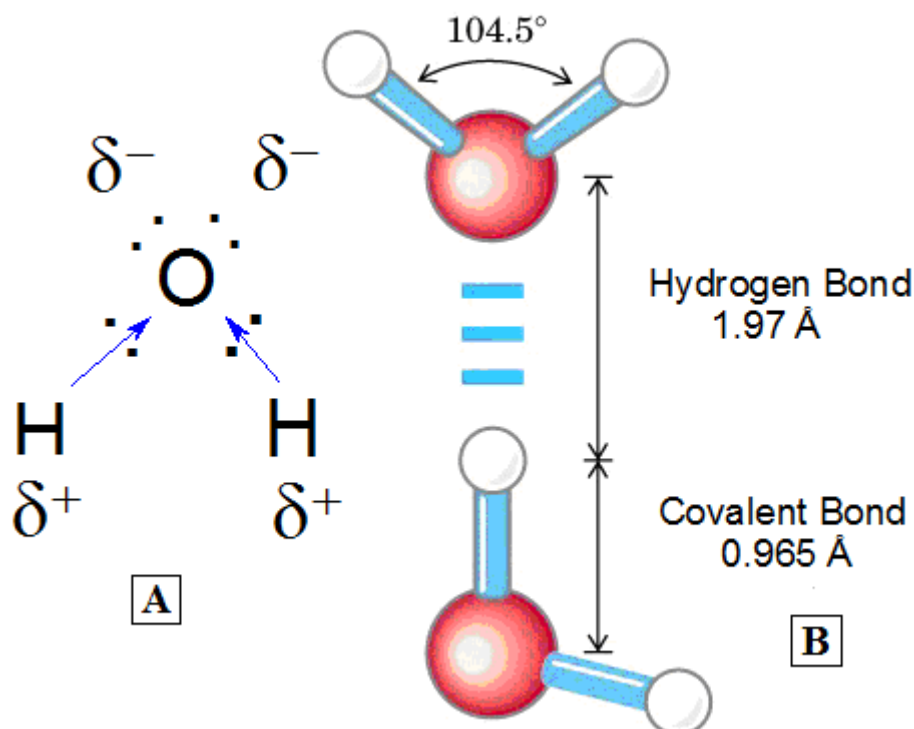


Figure 1.2.1 A: Water structure depicting four electron pairs, which arrange themselves symmetrically at the vertices of a tetrahedron around the oxygen nucleus. B: Structure of water molecule depicting the H-bond and covalent bond length, along with bond angle (104.5°) (13).

Nevertheless, this kind of molecular arrangement and the high electronegativity of the oxygen atom makes water a highly polar molecule. As this leads to creation of a net negative charge towards the oxygen end (the apex) and the creation of net positive charges at the hydrogen end of the V-shaped water molecule (14). Formation of this electric dipole also gives rise to attractions between neighbouring opposite ends of water molecules, with each oxygen atom attracting two nearby hydrogen atoms of two other water molecules, resulting in formation of H-bonds. These bonds allow water to display properties which are anomalous, based on its size and composition. For example, water has a higher melting and boiling point than hydrogen sulphide (H₂S) even though sulphur lies immediately below oxygen on the periodic table and is heavier than oxygen (13). As a result of this crosslinked H-bonding, water molecules remain in the liquid phase at ordinary temperature and pressure, even though its low molecular weight would normally be expected to make it a gas at such temperatures (14).

1.2.1.2 Hydrophobic Interactions and Role of Water as a Solvent

The hydrophobic effect can ideally be studied by considering the mode of insertion of simple nonpolar molecules into pure water molecules. In water, each water molecule is surrounded by four other water molecules (Figure 1.2.2A) and the geometry around each water molecule can be approximated as a tetrahedron (Figure 1.2.3A). Additionally, the water molecule in the center of a tetrahedron can arrange itself in 6 different ways to form a hydrogen bond (H-bond) with two of its nearest neighbours. This central water molecule can form hydrogen bonds with the water molecule at bottom left and bottom right. This configuration can be uniquely identified as it forms a triangle outlined by two hydrogen bonds and edge no. 1 of the tetrahedron (Figure 1.2.3A).

Each other edge corresponds to the available 6 different ways of hydrogen bonding configuration with two of its nearest neighbors. However, once the nonpolar solute is inserted into this cavity, the 3-dimensional organisation of the water molecules will change in order to decrease the ΔG of the system (14). For a polar molecule, hydrogen bonds and electrostatic interactions between solute and water will compensate for the energy required to create the cavity, whereas only weak Van der Waals attractive forces will occur between a nonpolar molecule and the solvent. As a result, the water molecules surrounding the nonpolar solute will gain strength in terms of intermolecular hydrogen bonds in order to compensate for the lack of favourable interactions between solute and solvent (12).

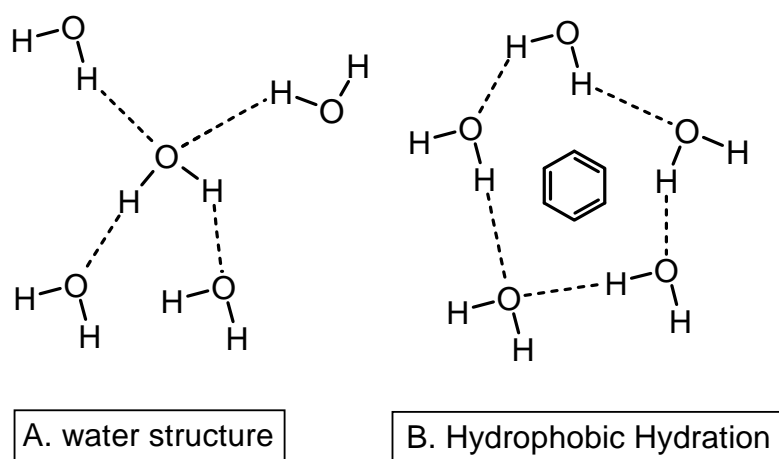


Figure 1.2.2 A: Water forms hydrogen bonds with other water molecule. B: Insertion of a nonpolar solute results in formation of a cage like structure around the nonpolar solute.

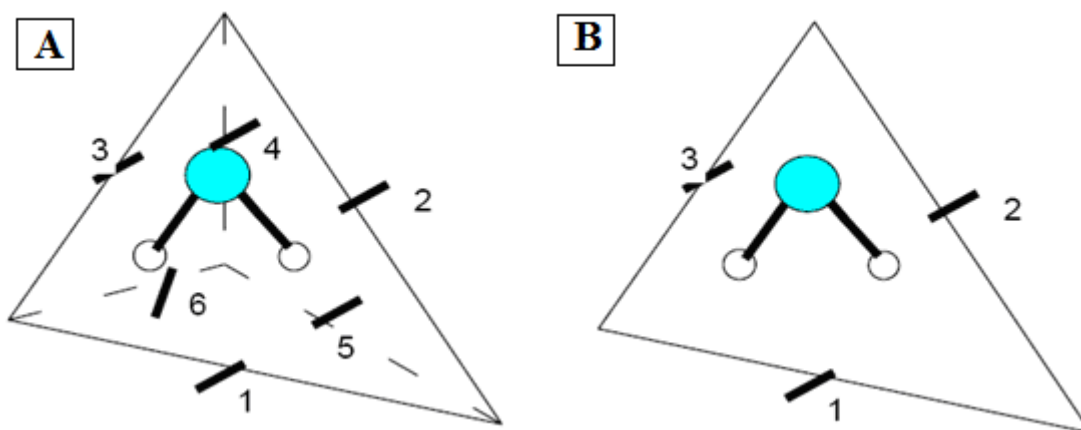


Figure 1.2.3 A: A water molecule (centre) can arrange itself in six different ways to form hydrogen bonds with two of its nearest neighbours. B: The water molecule is replaced with a non polar solute which cannot form hydrogen bonds, resulting in eliminating one of the edges of the tetrahedron reducing the number of possible hydrogen bonding configuration from 6 to 3. (Reviewed by Dill and Bromberg (14))

1.2.1.3 Thermodynamics of Hydrophobic Interaction

The apparent attractive force driving nonpolar molecules to stay together in water is not attractive in nature. On the contrary these nonpolar molecules stay together to minimize water-exposed accessible surface area as exposure of small surface area results in a lesser number of water molecules suffering from loss of conformational entropy and an energetic penalty (15). Reducing this exposed water/hydrophobic interface by the aggregation of the hydrophobic surfaces with one another is the most efficient mechanism. Therefore the hydrophobic effect is an entropy-driven process, which seeks to decrease the ΔG of a system by minimizing the surface interface between hydrophobic molecules and water. This aggregation of hydrophobic molecules apparently represents some sort of ordering, but the entropic cost of separating water and hydrophobic molecules is smaller than the entropic cost of ordering water molecules on the large hydrophobic-water interfaces, which would have resulted in mixing non-polar solutes with water (15). However once assembled into clusters, hydrophobic molecules are held together by weak van der Waals interactions, especially London dispersion forces (16).

1.2.2 Hydrogen Bonding

Hydrogen bonding is an attractive interaction between a hydrogen donor A-H and a hydrogen acceptor B (17). Atoms A and B are usually the highly electronegative N, O, and F, for which dipole moments are large. For example, a hydrogen bond can form between

an amide and carbonyl group, $\text{N-H}\cdots\text{O}=\text{C}$. In this case the, N-H group is called the hydrogen bond donor and $\text{C}=\text{O}$ is called the hydrogen bond acceptor. Hydrogen bonds are extremely important in influencing the structure and chemistry of most biological molecules. Hydrogen bonds of water give rise to unique physical properties that make it ideal as the medium for life processes, because solvents like water can serve as both hydrogen bond donor and acceptor. Each water molecule is capable of donating two H atoms to form hydrogen bonds, while each O atom is capable of accepting two hydrogen bonds (18).

Hydrogen bonds are directional. The strength of hydrogen bonds depends on bond length, bond angle, temperature, pressure and environment (usually characterised by local dielectric constant). The typical length of a hydrogen bond in water ($\text{H}\cdots\text{O}-\text{H}$) is 1.97 Å (17). The minimum distance between the heavy atom (non-hydrogen) positions is 1.6 Å and as the distance increases strength of hydrogen bonding falls off rapidly. The strength of the interaction falls to negligible value at a distance of 5 Å (17). The maximum stability (lowest energy) occurs when the three atoms $\text{A}-\text{H}\cdots\text{B}$ lie on a straight line. Bent hydrogen bonds occur, but they usually have decreased stability. In addition, the local microenvironment can greatly control the hydrogen bond strength (for example, whether the hydrogen bond is solvent exposed versus buried). Hydrogen bonds can vary in strength from very weak ($1\text{-}2\text{ kJ}\cdot\text{mol}^{-1}$) to extremely strong ($40\text{ kJ}\cdot\text{mol}^{-1}$), as in the ion HF_2^- . Generally in protein-ligand interactions hydrogen bonding contributes between 6.27 to $20.9\text{ kJ}\cdot\text{mol}^{-1}$ of binding energy (19).

In proteins and nucleic acids, hydrogen bonding plays an important role in determining their native three-dimensional structure. In these macromolecules, H-bonding between parts of the same macromolecule causes it to fold into a specific shape, helping to determine the molecule's physiological or biochemical role. The double helical structure of DNA, for example, is largely due to hydrogen bonding between the base pairs, which link one complementary strand to the other and enable replication.

In proteins, hydrogen bonds are formed between the backbone carbonyl oxygens and amide hydrogens. When the spacing of the amino acid residues participating in a hydrogen bond occurs regularly between positions i and $i + 4$, an alpha helix is formed. When the spacing is less, between positions i and $i + 3$, then a 3_{10} helix is formed. When two strands are joined by hydrogen bonds involving alternating residues on each participating strand, a β -sheet is formed. Hydrogen bonds also play an important role in forming the tertiary structure of protein through interaction of side-chains (20).

1.2.3 Charge-Charge (Electrostatic) Interactions

The electrostatic effect plays a very important role in many properties of proteins such as protein folding and protein-ligand interactions. These charges determine to a great extent the long-range interactions and the electrostatic field around protein molecules which are important for protein-protein and protein-substrate interactions. It has been shown, for example, that the distribution of the charged groups on the surface of cytochrome *c* is essential for the orientation and complexation with its redox partners (21).

Electrostatic interactions can schematically be represented by the Figure 1.2.4. The basic equation for all electrostatic interactions is Coulomb's law (Eq. 1.2.1), which states that potential energy falls as distance increases ($1/r$) between two point charges.

$$V = \frac{q_1 q_2}{4 \pi \epsilon_0 \epsilon_r r_{12}} \quad 1.2.1$$

where q_1 and q_2 are the magnitude of the charges, r_{12} is the separation, ϵ_0 is the permittivity of free space and ϵ_r is the relative dielectric constant of the medium in which the charges are placed.

Interactions that vanish with certain powers of $1/r$ are named long range interactions and usually have an attractive nature. The contribution of charge-charge interactions can be positive or negative based on the sign of the involved charges.

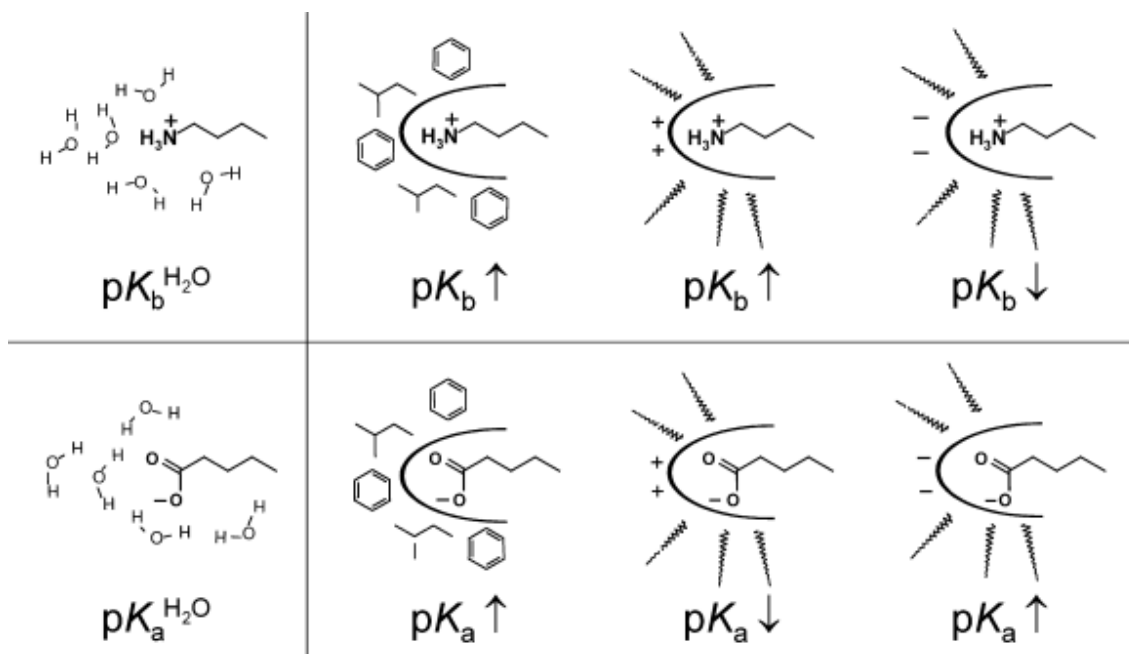


Figure 1.2.4 Impact of the protein environment on the pK_b values of a basic ligand group (upper row) and pK_a values of an acidic ligand group (lower row) compared to aqueous solution.

At physiological pH values (ca. 7.40), it is assumed that in proteins the guanidine side-chain of arginine ($pK_a = 12.5$) and the terminal amino group of lysine ($pK_a = 10.8$) are protonated, whereas the carboxy groups of aspartic ($pK_a = 3.9$) and glutamic acid ($pK_a = 4.1$) are deprotonated. Prediction of protonation state of histidine residues is more difficult to predict ($pK_a = 6.5$). Their exact protonation state depends upon the dielectric condition imposed by the local environment. This local environment changes upon ligand binding. Typically each electrostatic interaction provides an estimated 16.72 to 20.90 $\text{kJ}\cdot\text{mol}^{-1}$ of energy in protein-ligand interactions (22).

1.2.4 van der Waals Forces (Induced Dipole-Induced Dipole Interactions)

Molecules can attract each other at moderate distances and repel each other at close range. These forces are collectively called "van der Waals forces" and differ from covalent and ionic bonding in that they are caused by correlations in the fluctuating polarizations of nearby particles. Generally the Lennard-Jones potential (L-J potential, 6-12 potential) a simple mathematical model (23) is used to represent this behaviour and is represented by equation 1.2.2.

$$Vr = 4\epsilon \left[\left(\frac{\sigma}{r} \right)^{12} - \left(\frac{\sigma}{r} \right)^6 \right] \quad 1.2.2$$

where ϵ is the depth of the potential well, σ is the finite distance at which the interparticle potential is zero and r is the distance between the particles.

These forces operate only when molecules pass very close to each other, during collisions or near misses and are much weaker than chemical bonds. A random thermal motion around room temperature can usually overcome or disrupt them. Nonpolar molecules can also exhibit London forces, as electron density is often not distributed evenly throughout a nonpolar molecule. When uneven distribution occurs, a temporary multipole gets created, which can interact with other nearby multipoles. London forces are also present in polar molecules, but they usually form a very small part of the total interaction force. Additionally, electron density in a molecule may be redistributed by proximity to another multipole; as a result electrons will gather on the side of a molecule that faces a positive charge and retreat from a side facing negative charge.

Energetics of induced dipole-induced dipole interactions are similar to those of charge-charge interactions with the exception that the strength of the interaction falls off

rapidly with distance (contributing approximately 1.04 to 2.09 kJ·mol⁻¹ of binding energy for each atom involved) because they only involve transient partial charges (24). These dispersive interactions are long range and can occur at a distance of several Å. These induced dipole-induced dipole interactions are also known as London dispersion forces.

1.2.5 π - π Ring Stacking Interactions

Non bonded interactions which are attractive in nature can also be observed between two aromatic rings (Figure 1.2.5) and are normally called π - π ring stacking interactions. In biology, aromatic-aromatic interactions play a crucial role in protein-ligand interactions, and a prominent example of such π - π interactions on binding of an aromatic amino acid and adenine ring can be observed in an aminoglycoside phosphotransferase enzyme (APH(3')-IIIa). Tyr42 and the adenine ring of the bound nucleotide can be observed making a π - π interaction (25). This kind of ring stacking interaction contributes nearly 4.18 to 20.9 kJ·mol⁻¹ of binding energy in biological systems (24).

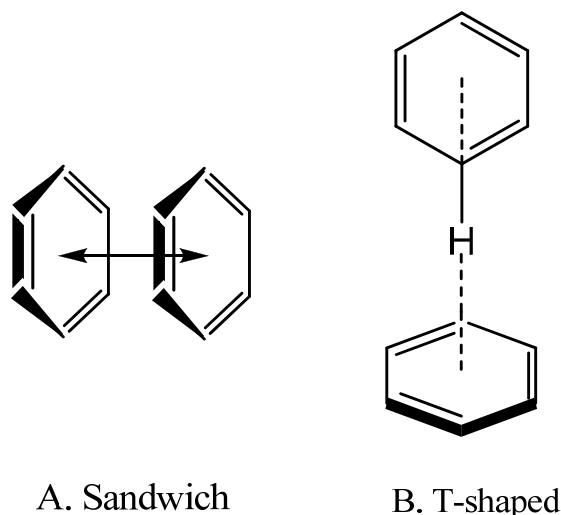


Figure 1.2.5 A: Sandwich and B: parallel-displaced, π - π interaction shown by an aromatic ring.

In π - π ring stacking interactions, the nature of the interaction can be vastly influenced by the chemical makeup of the aromatic groups and any functional groups bonded to the aromatic groups. Normally stacking interactions are observed occurring in two primary orientations, the first termed sandwich, has two aromatic rings positioned parallel to one another (Figure 1.2.5A). The second termed T-shaped (26), has the edge of one ring positioned perpendicular to the face of the other, with their geometric centres pointing perpendicular to each other (Figure 1.2.5B). However, the distance considerations are too complex to list here (26).

1.2.6 Cation- π Interaction

Interactions arising from an aromatic group (Phe, Tyr, Trp or ligand) and a cation (Arg, Lys or ligand) are normally categorised as Cation- π interactions (27). This interaction is electrostatic in nature and occurs between the positively charged cation and the negatively charged, electron rich π -cloud of the aromatic group. Within a protein, cation- π interactions can occur between the cationic side-chains of either lysine (Lys, K) or arginine (Arg, R) and the aromatic side-chains of phenylalanine (Phe, F), tyrosine (Tyr, Y) or tryptophan (Trp, W). Histidine can participate in cation- π interactions as either a cation or as a π -system, depending on its protonation state. These cation- π interactions typically contribute between 8.36 to 25.08 kJ·mol⁻¹ of binding energy in biological systems, with an average strength of 12.54 kJ·mol⁻¹ (24).

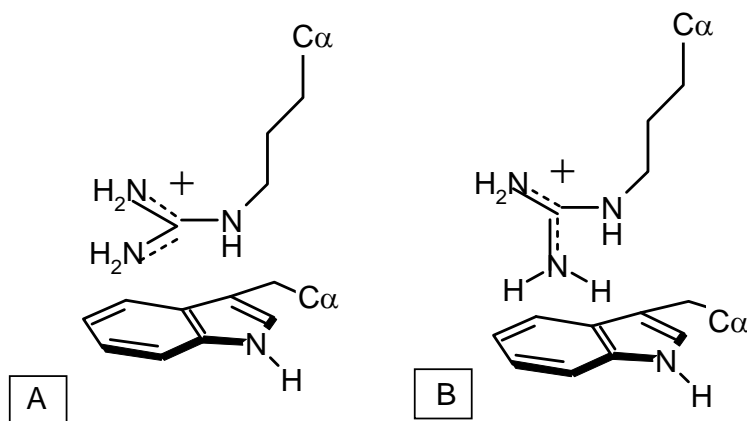


Figure 1.2.6 Figure depicts cation- π interactions involving arginine. Computationally the parallel geometry has been preferred in liquid phase (A), while T-shaped geometry has been favoured in gas phase (B) (27).

Figure 1.2.6A shows the cation- π interaction, where the cation lies perpendicular to the aromatic plane and the cation's van der Waals surface. If the cation lies further away from the aromatic group, the interaction will be subject to screening of water and other solvent molecules, which can significantly attenuate the strength of these interactions. Increasingly, the cation- π interaction is recognized as an important noncovalent binding interaction relevant to structural biology. A number of studies have established a role for cation- π interactions in biological recognition, particularly in the binding of acetylcholine (28).

1.3 Importance of Change in Heat Capacity (ΔC_p) in Protein-Ligand Interactions

One of the advantages of using calorimetry is the direct determination of ΔH , for a given biomolecular interaction. Additionally, if ΔH is determined at a range of temperatures, the change in heat capacity at constant pressure upon binding (ΔC_p) can then be obtained by the equation 1.3.1 given by Tame et al. (29):

$$\Delta C_p = \frac{\Delta H_{T_1} - \Delta H_{T_2}}{T_2 - T_1} = \frac{\Delta S_{T_1} - \Delta S_{T_2}}{\ln\left(\frac{T_2}{T_1}\right)} \quad 1.3.1$$

where T_1 and T_2 are two different absolute experimental temperatures.

Similarly from equation 1.3.1 it is clear that, if the value of ΔC_p is known; complete thermodynamic parameters such as ΔH , ΔS and ΔG can be obtained for that specific biomolecular interaction. Additionally, it has also been shown that the binding processes involving proteins results in decreasing of ΔC_p and solvent accessible surface area ($\Delta SASA$), showing a strong correlation between them (30; 31). This correlation can be used to provide a link between the thermodynamic data and the structural detail, i.e. if one has the knowledge of the structure of a biomolecule and its ligand to calculate $\Delta SASA$ on forming a complex, one should be able to predict ΔC_p . Alternatively it is also possible, from available ΔC_p data, to infer the structural effects occurring on binding, without requiring detailed structural information. In the past decade, various attempts to correlate ΔC_p with $\Delta SASA$ have been widely reported (30-33) and have achieved relative success in the prediction of thermodynamics of an interacting system. A comparison of some of these methods is discussed in the next section.

1.3.1 Correlations Between Changes in Surface Area (SASA) Exposed to Water and ΔC_p

Edsall (34) was the first person to notice that transfer of aliphatic compounds into water is accompanied by an increase in heat capacity and effectively founded the basis for studying the correlation between $\Delta SASA$ and ΔC_p . Later on, Kauzman (35) and Ooi et al. (36) showed that unfolding of proteins is also accompanied by an increase in ΔC_p . Together these observations led to a hypothesis that the ΔC_p upon protein unfolding is defined by the nonpolar groups of the protein that are buried in the native state and become solvent exposed in the unfolded form. It was also noted that in the native protein structure, not only nonpolar groups, but also polar groups are buried and they could also be affecting ΔC_p (37). Subsequently, model compound studies indicated that the ΔC_p upon transfer of polar groups into water will have negative ΔC_p , which has a sign opposite to that for the transfer of nonpolar groups (38). It also appeared that the use of both polar and nonpolar SASA exposure can describe adequately the ΔC_p upon unfolding of a large number of proteins that differ in size, structure and amino acid composition (30; 31; 33; 38).

Correlation between ΔC_p and $\Delta SASA$ was based initially on calorimetrically determined data from heats of transfer of organic compounds to aqueous solvents and was later extended to include studies of protein folding/unfolding equilibria. By fitting these data for the transfer of model compounds from the liquid state to water, Spolar et al (31) determined an equation (1.3.2) to estimate the ΔC_p from nonpolar and polar values of $\Delta SASA$

$$\Delta C_p = 1.34 \Delta A_{np} - 0.59 \Delta A_p \quad \text{J}\cdot\text{mol}^{-1}\text{K}^{-1} \quad 1.3.2$$

Also, by nonlinear fitting of data for the dissolution of solid model compounds, Murphy and Freire (30) give the equation 1.3.3

$$\Delta C_p = 1.88 \Delta A_{np} - 1.08 \Delta A_p \quad \text{J}\cdot\text{mol}^{-1}\text{K}^{-1} \quad 1.3.3$$

Equation 1.3.4, proposed by Myers et al. (33) is based on results by the non-linear fitting of experimental data for folding/unfolding of around 45 different proteins of various molecular weights

$$\Delta C_p = 1.17 \Delta A_{np} - 0.38 \Delta A_p \quad \text{J}\cdot\text{mol}^{-1}\text{K}^{-1} \quad 1.3.4$$

Lastly, Makhatadze and Privalov (32) have also fitted the experimental data for a folding/unfolding of various proteins to present equation 1.3.5

$$\Delta C_p = 2.14 \Delta A_{np} - 0.88 \Delta A_p \quad \text{J}\cdot\text{mol}^{-1}\text{K}^{-1} \quad 1.3.5$$

where ΔA_{np} represents change in nonpolar surface area, while ΔA_p describes change in polar surface area.

Interestingly, all these equations differ significantly from one another in the way they are derived and the percentage of polar and nonpolar contribution to the total ΔC_p calculation. This difference arises mainly from the fact that these equations (Equations 1.3.2, 1.3.3 and 1.3.5) are derived using different datasets. These datasets are in themselves composed of different sets of protein unfolding and transfer of different types of model compound data, whereas equation 1.3.4 was obtained mainly by fitting experimental ΔC_p data for a number of protein molecules.

It has often been seen that there is a significant discrepancy between the experimental and $\Delta SASA$ based values of ΔC_p (39). In fact there are many cases where it appears that large discrepancies exist between predicted and experimentally derived values of ΔC_p (40). In many cases it appears that water molecules are trapped at the binding interface (41). It has also been hypothesized that the restriction of these water molecules by H-bonds within the biomolecule can give rise to an additional contribution to the negative ΔC_p through changes in the soft vibrational modes (42).

1.3.2 Factors Affecting ΔC_p in Protein-Ligand Interactions

1.3.2.1 The Hydrophobic Effect

Mixing of nonpolar solute with water differs considerably from the polar solvation process, as it results in a large unfavourable ΔG , which is accompanied by a large positive ΔC_p (Table 1.3.1). This implies that a nonpolar solute surrounded by water has a greater ability to absorb heat energy from the surroundings than the corresponding pure component alone. Interestingly, ΔC_p increases with the molecular size of the solute and in proportion to the number of water molecules in the first hydration shell of the solute. According to Frank and Evans (43), at low temperature, the first-shell water molecules are ordered (low entropy) and form hydrogen bonds with other water molecules (low enthalpy). Heating results in weakening of this ordered water structure. Thus, any process involving breaking of ordered water structure will involve an increase in entropy and enthalpy. Similarly, increasing the temperature of water increases the enthalpy by weakening or breaking of water-water hydrogen bonds in the first solvation shell around the solute. As a result, water will also gain entropy from this increased bending and loosening of water-water hydrogen bonds.

Compounds	ΔG° (kJ·mol ⁻¹)	ΔH° (kJ·mol ⁻¹)	$T\Delta S^{\circ}$ (kJ·deg ⁻¹ ·mol ⁻¹)	ΔC_p° (kJ·mol ⁻¹ ·K ⁻¹ × 10 ³)
Benzene	19.33	2.08	-17.22	0.22
Toulene	22.82	1.73	-21.06	0.26
Ethyl benzene	26.19	2.02	-24.16	0.31
Propyl benzene	28.8	2.3	-26.49	0.39
Pentane	28.62	-2.0	-30.60	0.40
Cyclohexane	28.13	-0.1	-28.22	0.36
Hexane	32.54	0.0	-32.51	0.44

Table 1.3.1 Thermodynamic properties for the transfer of small hydrocarbons from their pure liquid state to water, based on solubilities at T=25 °C. Adapted from Gill and Wadso (44).

According to Sturtevent (42), data from Table 1.3.1 and other available literature can be used to correlate change in entropy (ΔS_{hydro}) with change in heat capacity ($\Delta C_{p\text{hydro}}$) arising due the hydrophobic effect and can be represented by equation 1.3.6.

$$\Delta S_{\text{hydro}} = -0.26 \pm 0.046 \Delta C_{p\text{hydro}} \quad \mathbf{1.3.6}$$

1.3.2.2 Electrostatic Interactions

Ions, like nonpolar solutes, can also order water molecules. However, the ordering of water molecules induced by ions is different from that induced by nonpolar solutes. The structure of nonpolar solutes in water is driven by maximization of water-water hydrogen bonds, whereas the water structure around ions is driven by the electrostatic interaction of ions with the immediate water molecules. Oxygen present in the water molecule is at the negative end of a dipole, so it is attracted to positive ions; whereas hydrogens are at the positive end of a dipole and get attracted towards negative ions. However, inserting nonpolar solute can strengthen water-water hydrogen bonds, while inserting ions can either strengthen or weaken them.

Charge density, and not simply the charge of an ion, is responsible for the electrostatic mechanism of water ordering. High charge density results from the presence of a large amount of charges on an ion with a small ionic radius. As a result, the electrostatic potential at the surface of the spherical ion is proportional to the charge present on the ion and inversely proportional to its radius. Water molecules bind to small

or multivalent ions very tightly and this is normally reflected in their enthalpies of solvation.

Sturtevant (42) indicates that the creation of a positive and negative pair of charges in aqueous solution leads to ΔS of -63 to -126 J·K⁻¹·mol⁻¹ and ΔC_p of -84 to -209 J·mol⁻¹·K⁻¹.

1.3.2.3 Hydrogen Bonds

In protein molecules, water is often trapped at the protein-ligand interface. This water is highly ordered, enthalpically favourable and is extensively hydrogen bonded. However, with an increase in temperature, breaking of hydrogen bonds will occur, which will affect the overall enthalpy of the binding reaction. Thus it is expected that a change in the net extent of hydrogen bonding occurring within the binding interaction will be reflected in a ΔC_p , with a decrease in hydrogen bonding resulting in negative ΔC_p and vice-versa.

1.3.2.4 Intramolecular Vibrations

1.3.2.4.1 Defining Intramolecular Vibrations

Intramolecular vibration occurs when atoms in a molecule are in periodic motion, while the molecule as a whole is in constant translational and rotational motion. The frequency of this periodic motion is normally called the vibration frequency and shows $3n-6$ (n = no. of atoms) normal modes of vibration for a non-linear molecule. A water molecule thus will have 3 normal modes of vibration.

The coordinate of a normal vibration is a combination of changes in the positions of atoms in the molecule and these normal vibrations normally belong to the stretching, bending, rocking, wagging and twisting kind of intramolecular interactions (13).

1.3.2.4.2 Intramolecular Vibrations in Protein-Ligand Interactions

Proteins have many soft intramolecular vibrations and have weak force constants. Naturally these intramolecular vibrations will be affected significantly after unfolding or ligand binding to the proteins. Therefore it is necessary to include changes in the number

of easily-excitabile internal vibrational modes (intramolecular interactions) as a possible source for ΔC_p , as constraining translational and soft vibrational modes of bound water compared to bulk solvent water will have a dramatic effect on the entropic contribution to the overall free energy of the interaction. Thus in the case of water-mediated interactions, the entropic cost of constraining a water molecule at the interface will be overcome by the enthalpic gain from reducing the energetic potential for a non-covalent interaction.

According to Morton and Ladbury (41), reduction of soft vibrational modes upon ligand binding can be observed at the intermolecular interface of crystallographic structures in the change of temperature (B) factors of the atoms in the binding site. When B factors are reduced on binding of a ligand, it is indicative of tightening of the structure and can be observed as significant net reductions in the B factor of those residues involved in the interaction with ligand. Morton and Ladbury (41) also assumed that the general restriction of the motion of bonds in interfaces will also extend to the water molecules mediating the intermolecular interactions.

According to Sturtevant (42), correlation of the change in entropy (ΔS_{vib}) with change in heat capacity ($\Delta C_{p_{\text{vib}}}$) can be represented by equation 1.3.7.

$$\Delta S_{\text{vib}} = 1.05 \Delta C_{p_{\text{vib}}} \quad (273\text{-}373 \text{ K}) \quad 1.3.7$$

1.3.2.5 Conformational Entropy

An increase in the number of approximately iso-energetic conformations available to a molecule results in an increase in its entropy without a directly related ΔC_p . So, the conformational entropy does not play a significant role in ΔC_p , but can modulate entropy (42).

For an Increase in	ΔS	ΔC_p
Exposure of nonpolar groups	-	+
Exposure of electrostatic charges	-	-
Hydrogen bonds	+	+
Conformations (Isoenergetics)	+	0
Soft internal modes	+	+

Table 1.3.2 Expected signs of ΔS and ΔC_p in Protein-ligand reactions. Adapted from Sturtevant (42).

In general, protein ligand interactions have been demonstrated to occur with a large negative ΔC_p . It has also been proposed that a large negative ΔC_p is a distinctive feature of site specific binding (31; 42), and the sign of ΔC_p is determined mainly by the removal of large amounts of nonpolar surface from water on complex formation.

1.4 Structure and Function of Hsp90

The research work described in Chapter 3, deals with understanding the role of water and ΔC_p in protein-ligand interactions. To accomplish this work, Hsp90 is being used as a model protein. Consequently, this section briefly introduces structure and function of Hsp90.

1.4.1 Function of Hsp90

Heat shock response was first described by Ritossa (45), and Heat Shock Proteins (HSPs) are named for their increased synthesis after heat shock. This is contrary to the reduced synthesis of most cellular proteins under stress conditions. In addition to heat, HSPs are modulated by nutrient deprivation, and oxidative and other stresses where protein denaturation might otherwise occur (46; 47). Many HSPs act as molecular chaperones by forming multi-molecular complexes by binding to other proteins, these proteins are denoted as client proteins. These complexes play a regulatory role in the fate of proteins in several different ways including: folding of proteins in the cytosol, endoplasmic reticulum and mitochondria; intracellular transport of proteins; repair or degradation of proteins partially denatured by exposure to various environmental stresses; control of regulatory proteins; and refolding of misfolded proteins (46; 47). HSPs differ in their cellular localisation and functions and mammalian HSPs have been classified into several families according to their molecular weight: Hsp90, Hsp70, Hsp60, Hsp40 and small HSPs such as Hsp27 (46-48).

Out of all HSPs, Hsp90 is the most abundant cellular chaperone protein and comprises as much as 1–2% of total cellular protein content, which increases about two-fold under stress conditions (48). Hsp90 functions in a multi-component complex of chaperone proteins that includes p60/Hop, p50^{cdc37}, Hsp40/HDJ2, p23, Hsp70 and one of a variety immunophilins (49; 50). Hsp90 differs from other chaperones as most of its known clients are protein kinases or transcription factors involved in signal transduction. These include ligand-dependent transcription factors such as steroid hormone receptors, ligand-independent transcription factors such as MyoD, tyrosine kinases such as p185^{erbB2} (Her-2/neu), serine/threonine kinases such as CDK-4 and Raf-1, and mutant transcription factors such as p53 (48).

Hsp90 is known to have numerous client proteins, although the Hsp90 binding process has only been studied with a few of these proteins. A model showing important

functions of molecular chaperones in mediating post-translational protein homeostasis, summarized by Whitesell and Lindquist (48), is described schematically in Figure 1.4.1. In this stepwise multi-protein process, where newly synthesized, conformationally labile client proteins associate with a multi-protein complex that contains various chaperones, co-chaperones and accessory molecules (different colored shapes). The particular components of a complex vary according to the client and also help specify the function of a particular complex. Dynamic association of a client with chaperone complexes can prevent its aggregation (Figure 1.4.1A) and assist in its intracellular trafficking, especially its translocation across membranous structures such as the endoplasmic reticulum (ER) (Figure 1.4.1B). For many clients involved in signal transduction pathways, association with the chaperone machinery maintains the protein in a meta-stable state that allows it to be activated by specific stimuli such as ligand binding, phosphorylation or assembly into multi subunit signalling complexes (Figure 1.4.1C). In the absence of appropriate stimuli, chaperone complexes can target the client for degradation through the ubiquitin-proteasome pathway, thereby regulating its steady-state cellular level (Figure 1.4.1D).

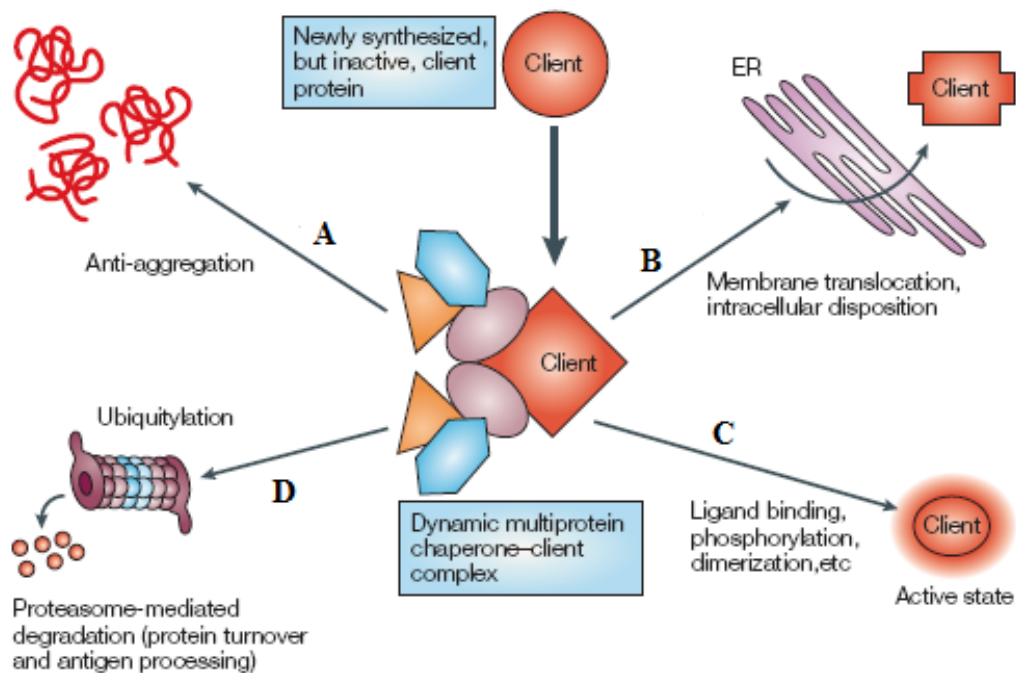


Figure 1.4.1 Molecular chaperones participate in regulating many aspects of posttranslational protein homeostasis. (Adapted from Whitesell and Lindquist (48)). A: Association of client proteins with HSPs complexes can result in preventing their aggregation B: assist in its intracellular trafficking, especially its translocation across membranous structures such as the endoplasmic reticulum (ER) C: association with the HSPs maintains the proteins in a meta-stable state and allows them to be activated by specific stimuli such as ligand binding, phosphorylation or assembly into multisubunit signalling complexes D: Without appropriate stimuli, HSPs can target the client proteins for their degradation through the ubiquitin-proteasome pathway and in the process regulates its steady-state cellular level.

In humans, there are two Hsp90 isoforms in the cytosol, Hsp90 α and Hsp90 β . Both these isoforms are closely related and are induced by stress, however no differences in their activities have been identified to date (51). Although chaperones are relatively abundant in nature, they rarely function alone. Instead, they typically function as components of larger machines that contain other chaperones, co-chaperones, modulators of ATPase activity and various accessory proteins. Also, in contrast to the kinases and other proteins, which are being targeted for the development of new anti-cancer therapy, chaperones do not covalently modify the substrates on which they act to prevent/resolve aggregation or alter conformation. Instead, chaperones typically interact with their clients in a cyclical, iterative fashion. Such chaperone cycling is driven by multiple rounds of ATP hydrolysis. As a result, targeting the nucleotide-binding pockets of chaperones with small molecules can provide an effective mean of changing chaperone protein interactions.

1.4.2 Structure of Hsp90

Hsp90 contains a highly conserved ATP binding domain in the N-terminus and the chaperoning activity of Hsp90 requires both the binding and hydrolysis of ATP at this site (52; 53). The C-terminus is less well characterised and is the main region for dimer interaction and for the binding of p60^{HOP} and immunophilins (51). The binding of ATP at the N-terminal region alters the conformational state of Hsp90 and affects its interactions with client proteins and co-chaperones and is discussed in detail below.

1.4.2.1 Structure of the ATP-binding N-terminal domain of Hsp90

The structures of the ATP-binding N-terminal domain of Hsp90 (N-Hsp90) for yeast (54) and human (55) proteins have been determined by X-ray crystallography. The N-terminal domain is highly conserved among both the Hsp90 domains with sequence identity of 69%, from yeast to human species. The tertiary structures of these two domains are extremely similar, consisting of an α/β sandwich of eight β -sheets, covered on one face by nine α -helices and loops, (Figure 1.4.2). At the centre of this helical face, a deep pocket about 15 Å deep with an entrance width of 8 Å to 12 Å exists. The buried β -sheet forms the bottom of the pocket and binding site for nucleotides. Nucleotides bind to the pocket centred at the middle of the N-Hsp90 as observed in the X-ray crystal structure solved and characterised by Prodromou et al. (54). Figure 1.4.3 shows the X-ray crystal structures of the yeast N-Hsp90 with bound ADP (blue) and geldanamycin (yellow).

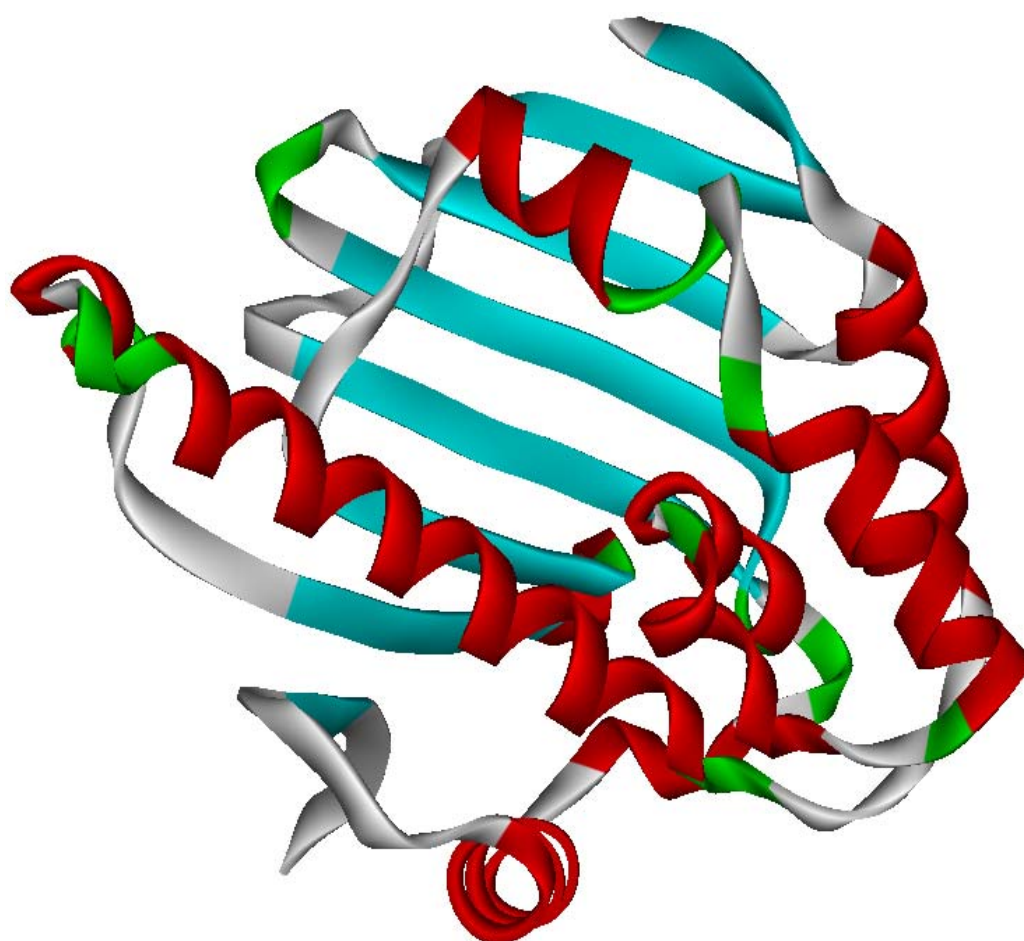


Figure 1.4.2 Cartoon representing structure of N-Hsp90 (Figure generated using DS ViewerPro 5.0 (56)).

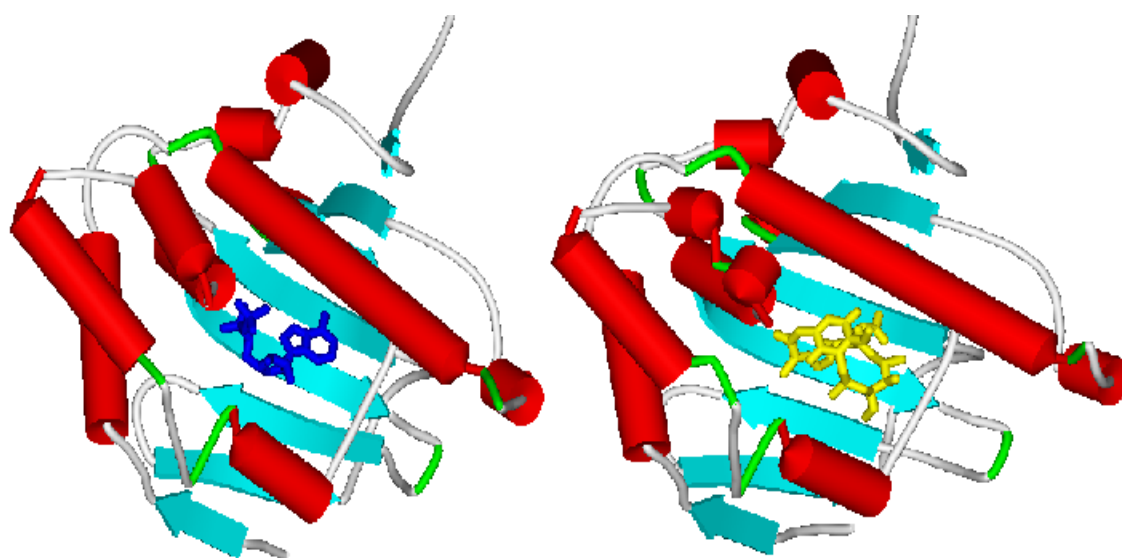


Figure 1.4.3 Two views of the structure of N-Hsp90 (helices in red, β -sheets in green) bound to ADP (blue) and Geldanamycin (yellow) (Figure generated using DS ViewerPro 5.0 (56)).

1.4.2.1.1 The ADP/ATP Binding Site Location in The N-Hsp90

ADP/ATP makes substantial interactions with the protein and bound water molecules in the binding pocket. ADP/ATP binds to the N-Hsp90 with a single direct hydrogen bond between the adenine base, from the exo-cyclic N6 of ADP/ATP to the carboxyl side-chain of Asp79 at the bottom of the pocket. All other hydrogen bonds of the adenine base take place through water-mediated interactions (Figure 1.4.4). Among these are residues Leu34 which binds to adenine N6, the side-chains of Asp79 and Thr171 hydrogen bonded to adenine N1 and Gly83 peptide nitrogen hydrogen bonded to adenine N1, all bonded through water molecules. The residue Asn92 is bound through water molecules to N3 of the adenine and O2' of the ribose, with a second connection to

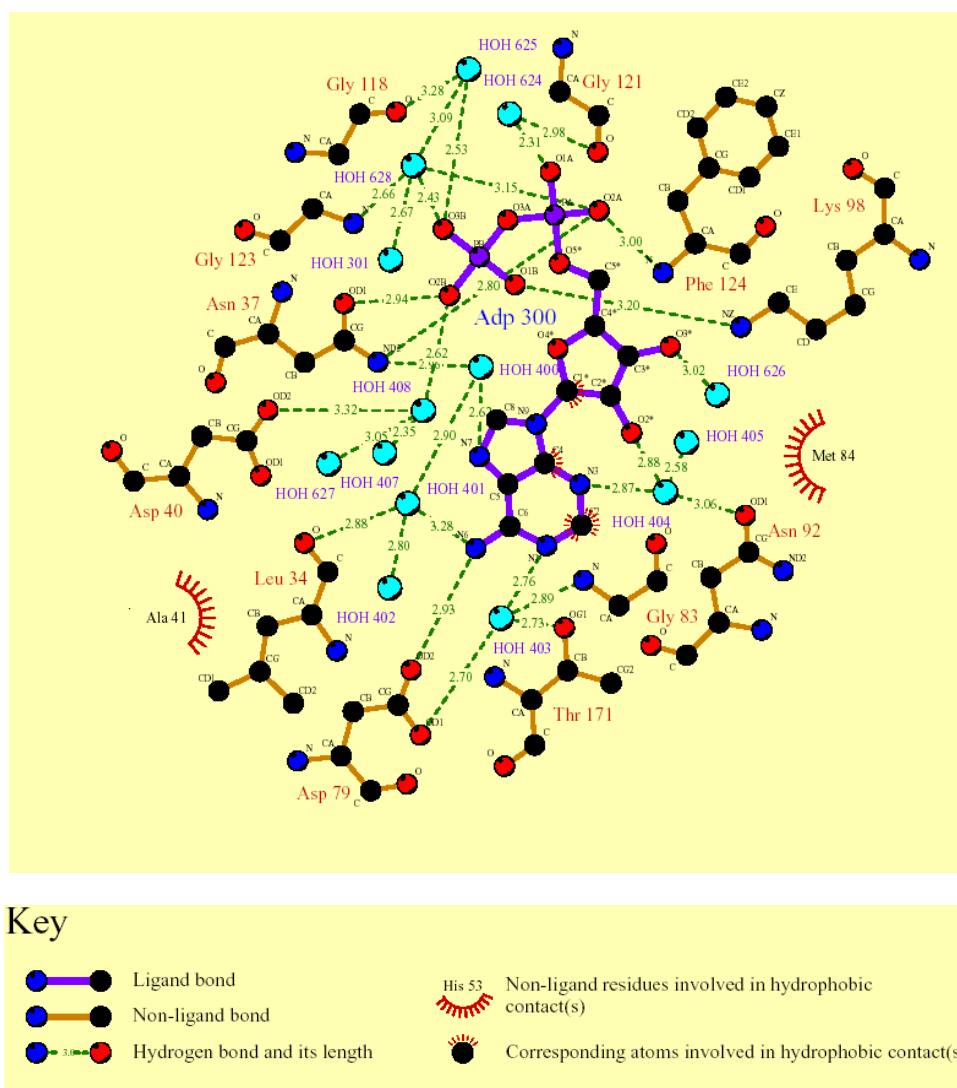


Figure 1.4.4 Schematic diagram of ADP interacting with the N-Hsp90. (Figure generated with ligplot (57))

O2' of the ribose directly connected to its side-chain (Figure 1.4.4). The side-chain of residue Asn37 is bound to the N7 of the adenine, again through water interaction. One hydrophobic face of the adenine ring has a van der Waals contact with the side-chain of Met84 while other face is exposed to solvent. At the top of the pocket, the α -phosphate group forms hydrogen bonds with the side-chain of Asn37 and the peptide nitrogen of Phe124. The β -phosphate group forms an ion-pair hydrogen-bonding interaction with the side-chain of Lys98 and interacts with several solvent molecules bound at the mouth of the pocket.

The base of the pocket in yeast N-Hsp90 is formed by residues Ile77, Asp79, Val136, Ser138, Thr171, and Ile173, whose side-chains project up from the buried face of the β -sheet. In the X-ray crystal structure, the electron density maps for nucleotides bound to the yeast N-Hsp90 were clear for the base, sugar, and α -phosphate groups, but were weaker for the β -phosphates with fewer contacts. No significant electron density was observed for the γ -phosphate in complex with ATP (54). Structural studies carried out on the N-Hsp90 suggest that despite binding Mg^{2+} -ADP/ATP, it has no inherent Mg^{2+} -binding site.

1.4.2.1.2 The Geldanamycin Binding Site Location in N- Hsp90

The ATP-ADP binding site also accommodates the antitumour agent geldanamycin on the N-Hsp90 (Figure 1.4.3). Geldanamycin consists of an ansa ring closed by an embedded benzoquinone, with attached carbamate group.

Prodromou et al. (54) have suggested that geldanamycin acts as an ADP/ATP mimetic and almost all of the interactions described between geldanamycin and human N-Hsp90 have a explicit equivalent in yeast N-Hsp90 with ADP/ATP (Table 1.4.1). The most significant interaction was between the carbamate nitrogen of geldanamycin and the carboxyl side-chain of Asp93 in human N-Hsp90, which corresponds to the direct hydrogen bond between the adenine N6 and Asp79 in yeast N-Hsp90. In addition, the hydrogen bond between the carbamate oxygen of geldanamycin and the buried water bound by Asp93, Gly97, and Thr184 in human N-Hsp90 corresponds to the interaction between the adenine N1 and the buried water bound by Asp79, Gly83 and Thr171 in yeast N-Hsp90. The hydrogen bond observed between the amide carbonyl of geldanamycin and the main-chain nitrogen of Phe124 in yeast N-Hsp90 corresponds to the hydrogen bond between oxygen of the α -phosphate of ADP/ATP and main-chain nitrogen of the Phe124 in yeast N-Hsp90. However, the hydrogen bond of the ϵ -amino of Lys58 to the methoxy and carbonyl oxygen on geldanamycin have no direct equivalent in yeast N-Hsp90 (54; 55).

N-Hsp90 Residues	ADP/ATP Interaction	Geldenamycin Interaction
Asp79	Direct H-bond to adenine N6	Direct H-bond to carbamate nitrogen
Asp79	Water-mediated interaction adenine N1	Water-mediated interaction with carbamate
Gly83	Water-mediated interaction adenine N1	Water-mediated interaction with carbamate
Thr171	Water-mediated interaction adenine N1	Water-mediated interaction with carbamate
Phe124	H-bond to oxygen in α -phosphate	H-bond to amide carbonyl
Lys98	H-bond ion pair to β -phosphate	H-bond to benzoquinone oxygen
Lys44	No direct equivalent, binds to O2' and O3' oxygens of the ribose sugar	H-bond to methoxy and carbonyl oxygens

Table 1.4.1 Amino acid residues involved in the binding of ADP/ATP compared with those involved in binding geldanamycin to N-Hsp90.

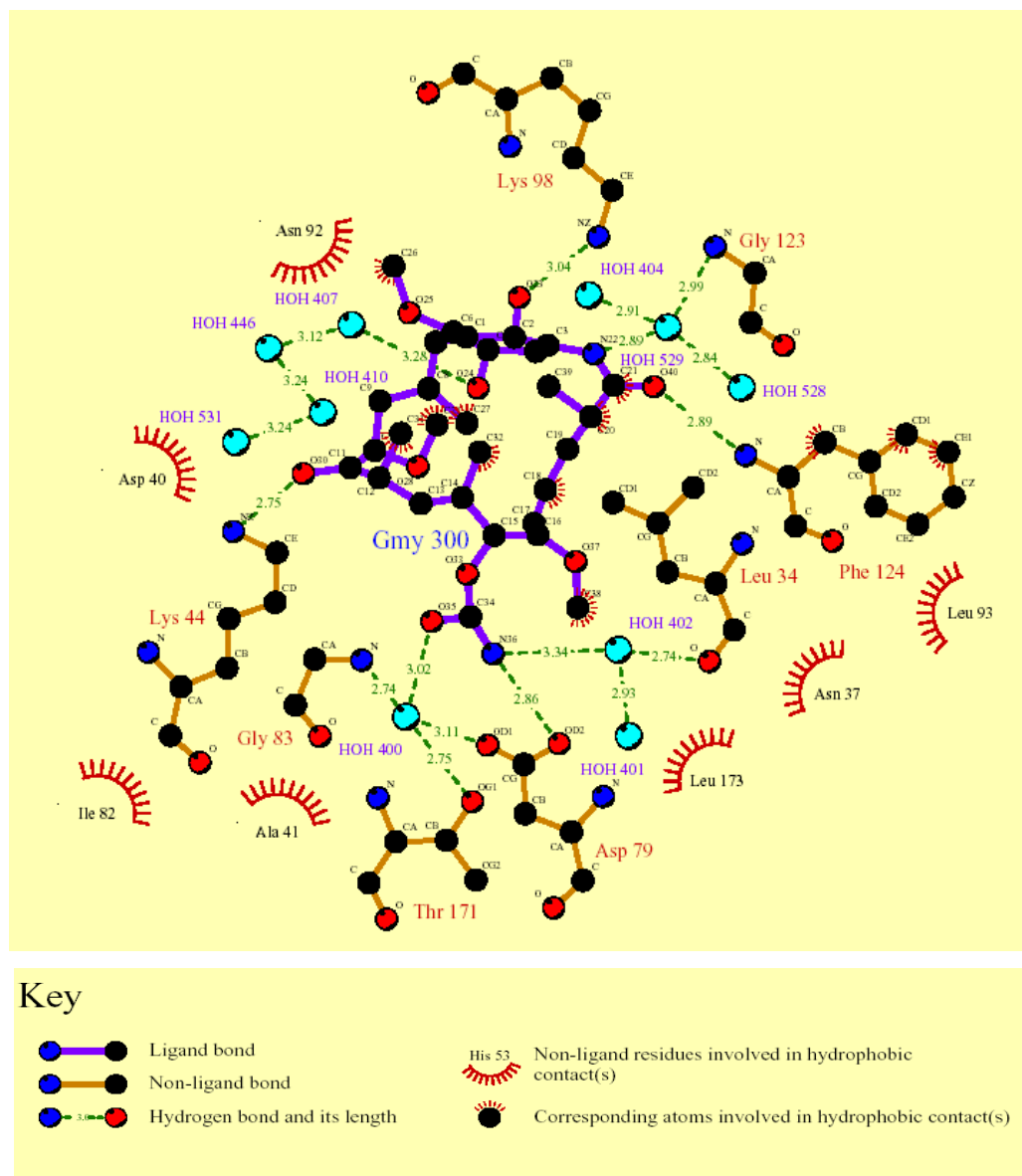


Figure 1.4.5 Schematic diagram of geldanamycin interacting with the N-Hsp90. (Figure generated with ligplot (57))

1.5 Structure of CDK2 and Function of Cyclin-Dependent Kinases (CDKs)

The research work described in Chapter 4, deals with the effect of minor substitutions in a series of bis-anilino pyrimidine compounds binding to CDK2. Consequently, a brief introduction to structure and function of CDK2 is provided in this section.

1.5.1 Function of CDKs

In all family of nine Cdc2-like proteins or Cyclin-Dependent Kinases (CDKs) as they are more generically known has been identified in humans. The human homologue of Cdc2 is normally referred to as HsCdc2 or CDK1. The sequence and function of these CDKs is highly conserved across evolution in common with many other cell-cycle regulatory proteins.

CDKs are necessary for the correct timing and sequential activation of the cell cycle to achieve required cell growth and cell division (Figure 1.12) (58). Disrupted cell-cycle control due to aberrant CDK activity has been linked directly to the molecular pathology of cancer (59). For example, loss of function of endogenous inhibitors such as p16^{INK4A}, over-expression of Cyclin D1 and CDK4, and alterations to CDK substrates such as the retinoblastoma gene product (pRb) are frequently observed in human tumours (60; 61).

CDKs require phosphorylation by ATP on their serine and/or threonine, and this is one of the essential criteria for the activation. CDK activity is highly regulated by association with regulatory subunits (Cyclins) and specific phosphorylation at the positive site (Thr160) or negative site (Thr14 and/or Thr15), or by association with native inhibitors. CDK2 and its related family members are active at distinct points in the cell cycle (Figure 1.5.1) (62).

In the past decade, the biochemical analysis of a small group of CDKs, their regulators and their substrates has provided a general framework for understanding how the mammalian cell cycle is regulated. After cytokinesis is completed, the newly generated cells can either continue cell division or stop proliferating. Cells that do not proliferate enter into a state that is generally known as 'quiescence' or G₀, while the cells that continue to cell division advance to the G₁ phase of the new cycle (Figure 1.5.1).

Cell cycle progression through to G₁ phase or G₀/G₁ transition is characterised by increased transcription of Cyclin D, giving rise to activation of CDK4 and CDK6, whose

primary target is pRb. pRb, in its hypophosphorylated state, binds to the E2F transcription factor, repressing its activity at promoter sites. pRb hyperphosphorylation disrupts these complexes, permitting the transcription of several genes whose products are associated with S-phase progression. Alterations in the level of CDK4 or CDK6 activity in malignant cells have suggested these kinases are important targets for therapeutic discovery (60).

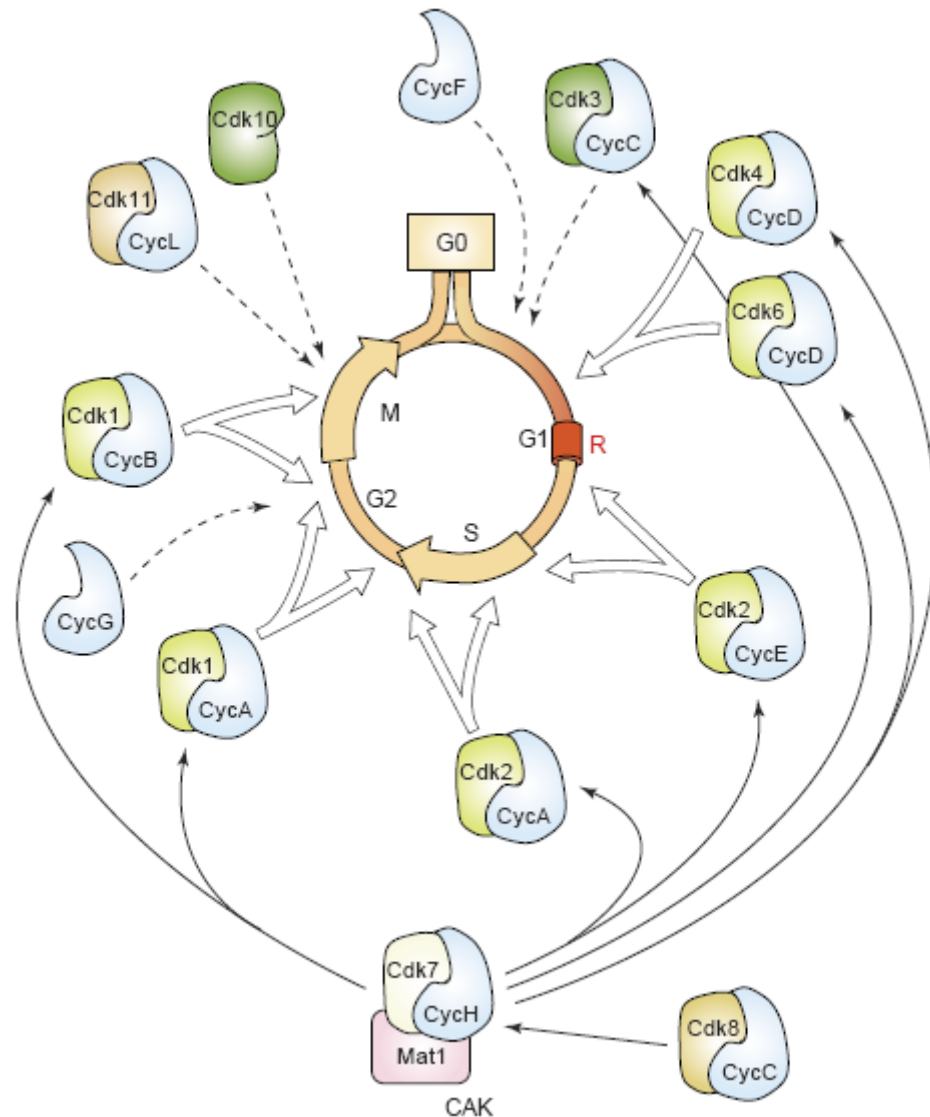


Figure 1.5.1 Roles played by different CDK-Cyclin complexes in mammalian cell cycle. CDK2-Cyclin E complexes have been proposed to complete phosphorylation of pRb, an event that is thought to convey mitogenic independence (passage through the restriction point, R) to dividing cells. CDK2-Cyclin E complexes have been also implicated in the G1-S transition by licensing DNA origins of replication. CDK2 later gets associates with Cyclin A during progression through S phase. CDK3, CDK10, CDK11, Cyclin F and Cyclin G are represented by dotted arrows to indicate that the data implicating them in cell cycle is very preliminary. (Reviewed by Malumbres and Barbacid (62))

Overall, human cell cycle progression is controlled by five CDKs and nine cyclins (Figure 1.5.1). Out of these five CDKs, CDK2 is essential for G1 progression and S-phase entry. Complexed with Cyclin E, it sustains pRb hyperphosphorylation to support

progression through G1 into S-phase. Once cells enter the S-phase, CDK2-Cyclin E complex needs to be controlled to avoid the replication of DNA (63). In the S-phase, CDK2 binds with Cyclin A, where it plays a role in inactivating E2F*, and is also required for the completion of the S-phase. Persistence of E2F activity during the S-phase leads to apoptosis (60; 64), and therefore selective inhibition of CDK2-Cyclin A may achieve cytotoxicity instead of cell-cycle arrest. Inhibition in S-phase may also be a strategy to which transformed cells are particularly sensitive due to their higher levels of E2F (65). CDK2-Cyclin A complexes have also been reported to phosphorylate numerous proteins that are thought to be required for proper completion and exit from S-phase.

These proteins include an upstream regulator of Cyclin A (pRb), transcription factors (E2F1, B-Myb), proteins involved in DNA replication (Cdc6, HSSB and MCM4), DNA repair (BRCA1, Ku70), histone modification (HIRA), ubiquitin mediated proteolysis (Rad6 and Cdc20), and cell-cycle checkpoints (p53, p21^{cip1}, MDM2) (62; 66). At the end of S-phase, Cyclin A attached to CDK2, switches partner and gets attached to CDK1 to continue in the G2 phase. CDK2-Cyclin A shares several of its substrates such as proteins involved in DNA replication (Cdc7) and various proteins participating in cell-cycle progression such as pRb, p53, BARD1 and BRCA2, with CDK1-Cyclin A (62; 66).

1.5.2 Structure of CDK2

Human CDK2 is about 35 kDa in size and encodes little more than the conserved catalytic core domain, which contains the classic bi-lobal kinase fold (67). The structure of cAMP[†]-dependent protein kinase (cAPK) (68) was the first to reveal the bilobal architecture of this domain, now confirmed by the determination of structures for more than twenty protein kinases including CDK2 (67) (Figure 1.5.2), CDK5 and CDK6 (69).

The CDK2 N-terminal domain comprises a five-stranded β -sheet that includes the glycine-rich ATP-binding loop (Ile10 to Val18 in CDK2, highlighted in dark green in Figure 1.5.2A), and a single helix, α C (Val44 to Glu57 in CDK2, highlighted in pink in Figure 1.5.2B). This helix contains the PSTAIRE sequence (boxed and labelled in Figure 1.5.2B), a motif that is highly conserved amongst CDKs and is involved in contacts with the cyclin subunit. In the human CDK2, the PSTAIRE sequence is contained within the

* E2F is a group of genes that codifies a family of transcription factors (TF) in higher eukaryotes.

† Cyclic AMP is denoted as cAMP.

α -1 helix, which undergoes a conformational change in the Cyclin A-CDK2 complex that is critical to kinase activation. An amino acid change from serine to cysteine, or to phenylalanine, in this signature sequence is responsible for the nomenclature of the human PCTAIRE-1 (residues 205-211) and murine PFTAIRE (residues 129-135) proteins, respectively.

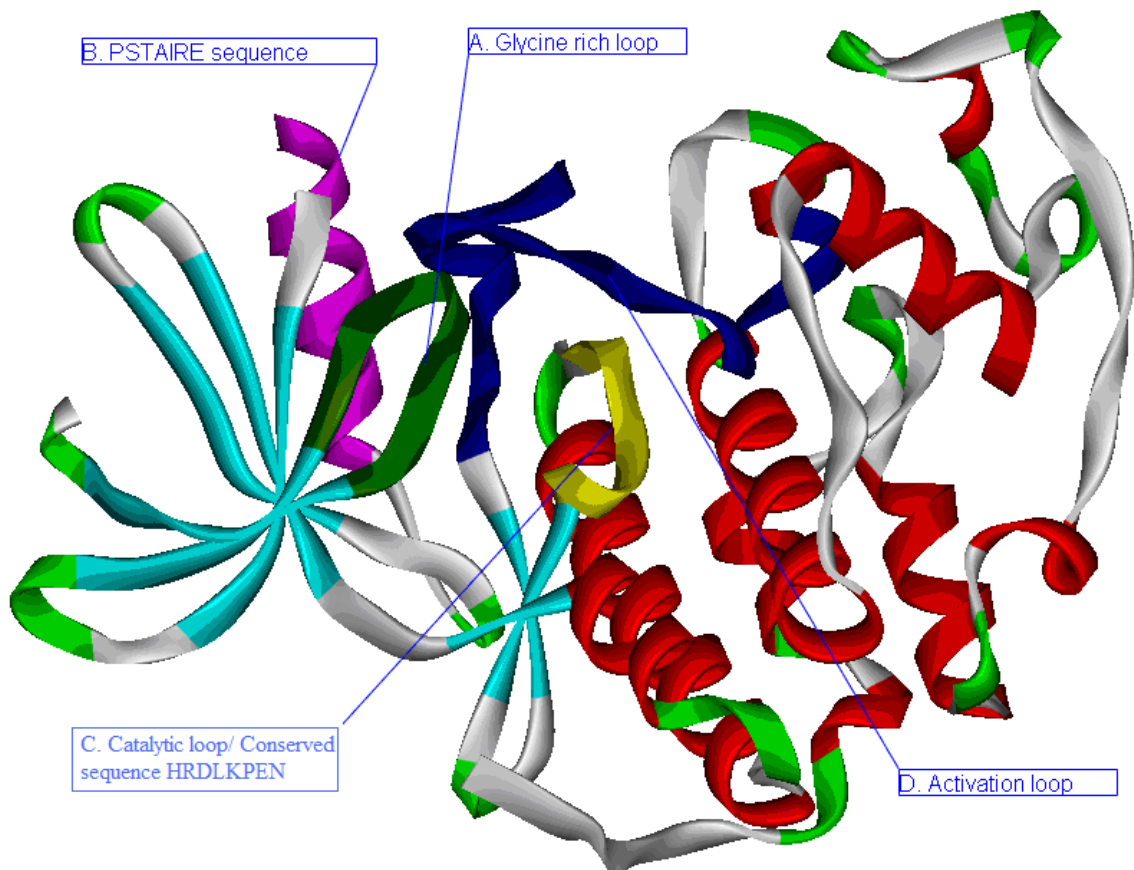


Figure 1.5.2 Cartoon representing structure of full length CDK2. (Figure generated using DS ViewerPro 5.0 (56))

The C-terminal domain is mainly α -helical in nature and contains the catalytic loop and the activation loop. The catalytic loop includes the residues required for catalysis of the phosphotransfer reaction and is defined by the conserved sequence HRDLKPEN (His125 to Asn132 in CDK2, highlighted in yellow in Figure 1.5.2C). The activation loop spans the residues lying between the highly conserved DFG and APE motifs (Asp145 to Glu172 in CDK2, highlighted in blue in Figure 1.5.2D). The activation loop in CDK2 contains a phosphorylation site, which is a common feature it shares with many other regulated kinases (70).

The ATP binding site is situated next to the cleft formed by the N- and C- terminal lobes, contacting residues from both lobes and a linking hinge. The adenine backbone of

the ATP fits well into this hydrophobic cavity close to the hinge and is held together by two hydrogen bonds formed between the peptide backbone of residues Glu81 and Leu83. The ribose and triphosphate groups project along the cleft, towards the protein substrate-binding site, and are held in place by interactions with the glycine-rich loop, the catalytic loop, and Lys33 from strand β -3 of the N-terminal lobe.

Comparison of the catalytic cleft architecture in CDK2 with that of the active kinases such as cAPK and phosphorylase kinase (PhK) highlights two major differences, explaining the failure of the unmodified CDK2 kinase core to catalyse the phospho-transfer reaction. Firstly, the activation loop adopts a conformation that obstructs access to both the ATP and the protein substrate-binding sites. Secondly, a short helix (α L12) is formed by residues Gly147 to Ala151 of the activation loop, forcing the α C helix to rotate away from the active site cleft relative to its position in the active kinase structures. In the structure of monomeric CDK2, the side-chain of Glu51 (the E of PSTAIRE) is directed out of the active site cleft, and Lys33 forms a charge-charge interaction with Asp145 from the DFG sequence at the start of the activation loop. Asp145 and Asn132 from the catalytic loop, bind to an essential Mg^{2+} ion that co-ordinates the α - and β -phosphates of ATP in the structures of active kinases. In the structure of monomeric CDK2, Asp145 is positioned such that productive binding of Mg^{2+} to the triphosphate moiety is disrupted.

1.5.3 Using Inactive or Active CDK2 as a Design Template

CDK2 interacts with Cyclin A and forms a CDK2/Cyclin A complex. There is no change in structure of Cyclin A, but CDK2 shows a lot of structural and conformational changes and creates an ATP recognition site. The CDK2-Cyclin A binding interface exhibits an unusually large surface area (71). Several helices in Cyclin A contact both lobes of CDK2 in the region adjacent to the active site cleft. Major contributions to binding are provided by interactions between the large PSTAIRE helix in CDK2 and helices 3 and 5 of Cyclin A; another major interaction involves the C-terminal lobe of CDK2 and the non-conserved N-terminal helix of Cyclin A. CDK2/Cyclin A exhibits ~0.2% of the activity of the fully activated phosphorylated binary complex (71). Full activity is achieved only by phosphorylation on Thr160, which is contained within the activation segment.

Phosphorylation causes a repositioning of this structural element into an orientation that allows for productive substrate binding.

Activation of CDK2 has two main effects on the ATP-binding site. The N- and C-terminal domains rotate by $\sim 5^\circ$ about the hinge region, leading to a slight widening or opening of the ATP cleft (72). In addition, the movement of the PSTAIRE helix and Glu51, and the subsequent reorganisation of the residues responsible for coordinating the ATP phosphates, leads to reshaping of the phosphate-binding site. In particular, the movement of Lys33 leads to the deepening of the ATP cleft and the formation of an additional pocket (73-75).

These complicated binding events in CDK2/Cyclin A suggest that design of inhibitors to target active kinase and the interpretation of the structure-activity correlation arising from biological data on the active complex will be very hard to interpret. This is why the majority of structural studies in the past have focused on characterization and exploitation of interactions formed between inhibitors and monomeric CDK2 to increase potency and specificity. Consequently, we have also used the monomeric form of CDK2 as a design template in the present study.

1.6 Isothermal Titration Calorimetry (ITC)

A schematic of a typical modern calorimetric instrument is shown in Figure 1.6.1. This type of calorimeter is based on a cell feedback principle that measures the differential heat effects between a reference and sample cell. A constant power is applied to the reference cell, which activates the power feedback circuit maintaining the temperature in the sample cell and also slowly increasing the temperature during a measurement. The resting power applied to the sample cell is the baseline signal.

In an actual experiment of ligand (L) binding to macromolecule (P) (Figure 1.6.2), heat is released (exothermic reaction) or absorbed (endothermic reaction). This heat absorbed or evolved during a calorimetric titration is proportional to the fraction of bound ligand and can be represented by the following equation 1.6.1 described by Pierce et al. (76)

$$Q = \frac{V_0 \Delta H_b [M]_t K_b [L]}{(1 + K_b [L])} \quad 1.6.1$$

where V_0 is the cell volume, ΔH_b is the binding enthalpy per mole of ligand, $[M]_t$ is the total macromolecule concentration including bound and free fractions, K_b is the binding constant, and $[L]$ is the free ligand concentration.

As the ligand concentration increases, the macromolecule becomes saturated and subsequently less heat is evolved or absorbed on further addition of titrant. Consequently, the heat evolved for all cumulative titrations can be described by equation 1.6.2.

$$Q = \frac{V_0 [M]_t \sum n_i \Delta H_i K_{bi} [L]}{(1 + K_b [L])} \quad 1.6.2$$

In a typical ITC[‡] experiment, the sample cell is filled with the system of interest, leaving the reference cell untouched. The ligand is applied by injection syringes with long needles having a stirring paddle attached to the bottom end and is continuously rotated during an experiment (310 rotations/minute), leading to complete mixing in the cell within a few seconds after an injection. The mechanical heat of stirring is constant and becomes

[‡] Typical ITC instrument is called for VP-ITC calorimeter from Microcal Inc. (www.microcalorimetry.com)

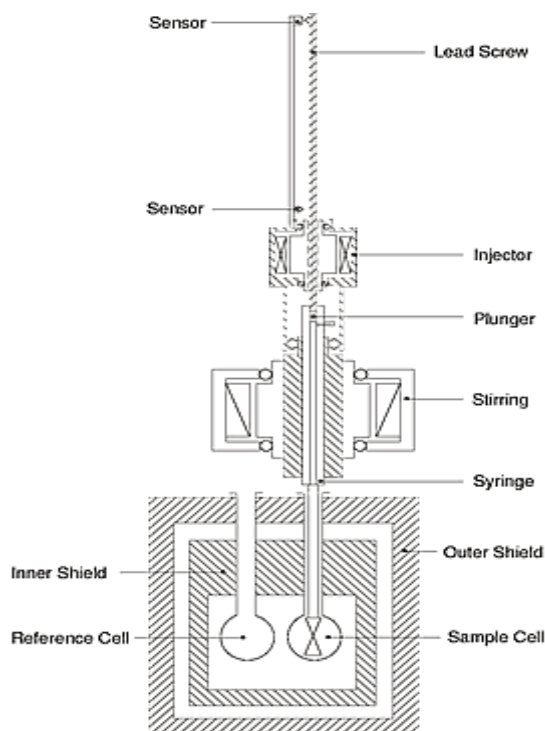


Figure 1.6.1 Diagram of ITC cells and syringe. The syringe rotates in place during the ITC experiment. The end of the syringe has been adapted to provide continuous mixing in the ITC cell. The plunger is computer-controlled and injects precise volumes of ligand. (Picture adopted from www.microcalorimetry.com)

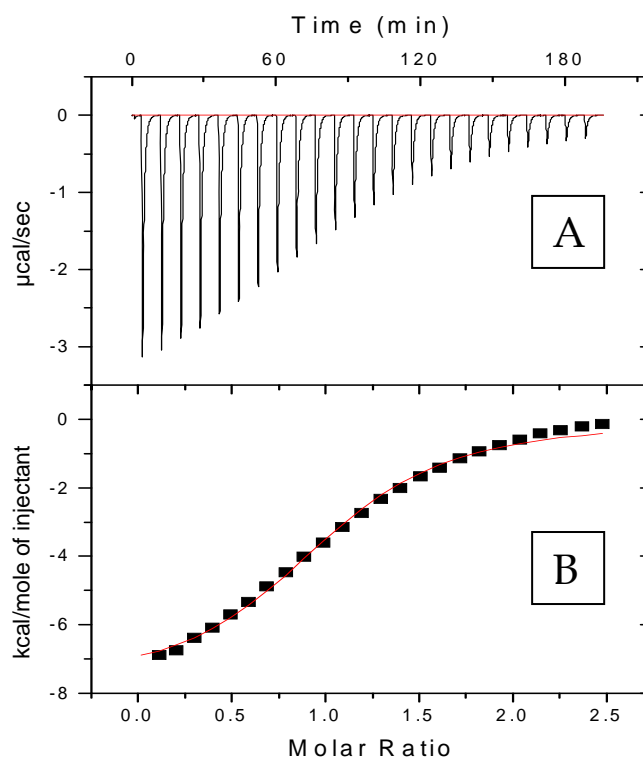


Figure 1.6.2 Raw data for the titration of AMPPNP into N-Hsp90 solution at 8 °C in Tris-base at pH 8.00. B: Binding isotherm derived from (A), corrected for the heats of dilution; the line represents the least squares fit to the single site binding model.

part of the resting baseline. With optimal performance (short equilibration time) a complete binding isotherm may be determined within 1 to 2 hours.

Calorimetric binding experiments are very testing, since noncovalent binding heats are intrinsically small, typically in the range of 21 to 42 kJ·mol⁻¹. In addition, the heat must be liberated in a stepwise manner during the binding experiment to fit a binding isotherm optimally. However, stepwise ligand addition also produces additional heat effects arising from dilution and mixing, which are frequently subtracted by conducting separate heats of dilution.

During the past few years, significant advances in ITC instrumentation, data analysis and the structural interpretation of binding thermodynamic data have taken place (77; 78). Together, these developments have permitted the implementation of accurate experimental protocols aimed at measuring the binding energetics of protein-ligand and protein-protein interactions, and at dissecting ΔG into the fundamental thermodynamic components: ΔH and ΔS . Consequently, the range of application of ITC has been extended considerably, including systems that could not be studied by ITC before.

1.7 Linear Interaction Energy (LIE) Free Energy Change Calculation

The linear interaction energy approximation (LIE) is a way of combining molecular mechanics or molecular dynamics calculations with experimental data to build a model scoring function for the evaluation of protein-ligand binding free energies. LIE type methods were first suggested by Aqvist and Hansson (79). Since then, the LIE method has been pursued by a number of research groups with promising results for a number of ligand binding data sets (80-83).

The LIE approach is a semi-empirical method for estimating absolute binding free energies and requires just two simulations, one of the ligand in solvent and other of the ligand bound to the protein molecule. The interactions that are accumulated consist solely of electrostatic and van der Waals interactions between the ligand and its environment. Only interactions between the ligand and either the protein or the aqueous environment enter into the quantities that are accumulated during the simulation; the protein-protein and protein-water interactions are part of the "reference" Hamiltonian and hence are used to generate conformations in the simulation, via either Monte Carlo (MC) or molecular dynamics (MD), but are not used as descriptors in the resulting model for the binding free energy. This eliminates a considerable amount of noise and systematic uncertainties in the calculations.

The LIE method employs experimental data on binding free energy values for a set of ligands (referred as the training set) to estimate the binding affinities for a set of novel compounds. The method is based on the linear response approximation (LRA), which dictates that the binding free energy of a protein-ligand system is a function of polar and nonpolar energy components that scale linearly with the electrostatic and van der Waals interactions between a ligand and its environment. The ΔG for the complex is derived by considering only two states: (1) free ligand in the solvent and (2) ligand bound to the solvated protein. The conformational changes and entropic effects pertaining to unbound receptor are taken into account implicitly and only interactions between the ligand and either the protein or solvent are computed during molecular mechanics calculations. Among the various formulations of the LIE methodology developed in the past, the SGB-LIE method, implementing a surface generalized Born (SGB) model for the solvation has been shown to be an order of magnitude faster than the methods based on explicit solvent with the same order of accuracy (82; 84). The SGB-LIE method also offers better

accuracy in treating the long-range electrostatic interactions. The SGB-LIE method implements the original formulation proposed by Carlson and Jorgensen (85) for the case of continuum solvent replacing the solvent accessible surface area term by a cavity term as follows

$$\Delta G = \alpha(\langle U_{vdw}^b \rangle - \langle U_{vdw}^f \rangle) + \beta(\langle U_{elec}^b \rangle - \langle U_{elec}^f \rangle) + \chi(\langle U_{cav}^b \rangle - \langle U_{cav}^f \rangle) \quad 1.7.1$$

where bracketed terms represent the ensemble average of the energy terms, such as van der Waals (U_{vdw}), electrostatic (U_{elec}), or cavity (U_{cav}) energy. The energy terms involved can be computed using energy minimization, molecular dynamics, or Monte Carlo calculations. All the terms are evaluated for interaction between ligand, both in the free (f) and bound (b) state, and its environment. The α , β and χ are LIE fitting parameters. The transferability and dependence of LIE parameters on force fields and interacting protein-ligand system is still the subject of debate (82).

In the SGB model of solvation, there is no explicit van der Waals or electrostatic interaction between the solute and solvent. The contribution for net free energy of solvation comes from two energy terms, namely, reaction field energy (U_{rxn}) and cavity energy (U_{cav}):

$$U_{SGB} = U_{rxn} + U_{cav} \quad 1.7.2$$

The cavity and reaction field energy terms implicitly take into account the van der Waals and the electrostatic interactions, respectively, between the ligand and solvent. The application of the SGB-LIE method for a given protein-ligand system essentially involves computing four energy components, i.e., the van der Waals and coulombic energy between the ligand and protein and the reaction field and cavity energy between the ligand and continuum solvent. The total electrostatic energy in the SGB-LIE method is the sum of coulombic and reaction field energy terms.

1.8 Aims of The Project

- To investigate the role of water in a protein-ligand interaction, using Hsp90-ADP/ATP and Hsp90-Geldanamycin as a model interacting system. Additionally, examination of positive ΔC_p in Hsp90-ADP/ATP interaction will also be investigated.
- To delineate a general strategy for the design of drug molecules that is more specific and highly selective towards the target. By combining high resolution structural data with binding thermodynamic results for closely related bis-anilino pyrimidine inhibitors with CDK2, we attempt to understand the mechanism by which an inhibitor can achieve specificity and high affinity binding. In the process, various tools such as LIE (79; 86) and GRID force fields (87; 88) will be used.

2. Chapter

Materials and Methods

2.1 Expression, Purification and Characterization of N-Hsp90

2.1.1 Expression System

The plasmid pET3a vector (Novagen) encoding a 1 to 207 insert was used. This expression system is under the control of the T7 promoter, which is not recognized by the *E. coli* strain Plyss(DE3) α host cells, which contain a chromosomal copy of the T7 RNA polymerase gene under lacUV5 control. This system provides high selectivity and high expression yields upon induction with isopropyl- β -D-thiogalactopyranoside (IPTG; Melford Laboratories Ltd.). The sequence of residues 1 to 207 for the N-Hsp90 protein is shown in Figure 2.1.1 below.

```
      10      20      30      40      50      60
MASETFEFQA EITQLMSLII NTVYSNKEIF LRELISNASD ALDKIRYKSL SDPKQLETEP
      70      80      90     100     110     120
DLFIRITPKP EQKVLEIRDS GIGMTRAEI L NLGTIAKSG TKAFMEALSA GADVSMIGQF
      130     140     150     160     170     180
GVGFYSLFLV ADRVQVISKS NDDEQYIWES NAGGSFTVTL DEVNERIGRG TILRLFLKDD
      190     200
QLEYLEEKRI KEVIKRHSEF VAYPIQL
```

Figure 2.1.1 Primary amino acid sequence, using the single letter abbreviations, for the 207 amino acid yeast N-Hsp90 protein.

2.1.2 Preparing Competent Cells

A single colony of BL21(DE3)PlysS cells was plated out from a glycerol stock of *E. coli* BL21(DE3)PlysS onto LB (Luria Bertani) and agar plates (15 g of agar per litre) which contained 34 µg/ml chloramphenicol (CAP-Melford Laboratories Ltd, MIL) and previously incubated at 37 °C over night. These cells were then inoculated in 5 ml of LB with CAP and grown overnight at 37 °C in a shaking incubator. This was then transferred to a flask containing 50 ml of fresh LB with CAP and incubated at 37 °C with shaking until the OD₆₀₀[§] reached between 0.2 to 0.5. The flask was kept on ice for 20 min and centrifuged at 2500 to 3000 rpm for 10-15 min at 4 °C, after which the pellet was suspended in 20-40 ml ice cold CaCl₂ (50 mM). This was kept on ice for 20 min and once again centrifuged (at 2500 rpm for 15 min at 4 °C) before resuspending in 1 ml ice cold 50 mM CaCl₂ and kept on ice.

2.1.3 Transformation

1 to 10 µl of plasmid DNA carrying a His-tagged version of the N-Hsp90 (25 kDa), was placed in an aliquot of 100 µl *E. coli* BL21(DE3)PlysS CaCl₂ competent cells in an Eppendorf tube on ice for 15-30 minutes. Heat shock was performed for 5 minutes at 37 °C in a water bath and returned to ice for 2 minutes. The sample was then incubated at 37 °C for 60 minutes with 900 µl LB media without antibiotics for recovery and subsequently plated out on LB and agar plates with CAP and 100 to 150 µg/ml carbenicillin and then incubated overnight at 37 °C.

2.1.4 Expression of Protein in LB

A single colony of the transformed *E. coli* BL21(DE3)PlysS was inoculated in 50 ml LB with antibiotics and then incubated at 37 °C with continuous stirring. Once the OD₆₀₀ had reached 0.6, 1 litre LB culture containing antibiotics was inoculated and then incubated at 220 rpm and 37 °C until the OD₆₀₀[§] reached 0.8 to 1.0. The T7 promoter was then induced by addition of IPTG to a final concentration of 0.1 mM and incubated at 220 rpm and 37 °C for four hours. The cells were then harvested by centrifugation at 5000 rpm

[§] Optical Density measured at 600 nm.

for 20 min using a SORVALL RC5B-GS3 super light rotor and the resulting pellets were stored at -20 °C.

2.1.5 Expression of Protein in Minimal Media

A single colony of the transformed *E. coli* BL21(DE3)PlsysS was inoculated in 50 ml LB with antibiotics and then incubated at 37 °C with continuous stirring. Once the OD₆₀₀ had reached 0.6 to 1, LB culture containing antibiotics was spun down and washed twice with M9 Media. These *E. coli* BL21(DE3)PlsysS cells were then transferred to M9 media and incubated at 220 rpm and 37 °C until the OD₆₀₀ reaches 0.8-1.0. M9 media was prepared with 0.2 % glucose (Cambridge Isotope Laboratories; CIL) as a carbon source and 0.2% ammonium chloride (CIL) as the nitrogen source. The M9 media was also supplemented with vitamin and mineral concentrates. Uniformly enriched ¹⁵N samples were obtained by growing on ¹⁵NH₄Cl as the sole nitrogen source. The N-Hsp90 production was induced by inducing T7 promoter by addition of IPTG (MIL) to a final concentration of 0.5 mM and incubated at 220 rpm and 37 °C for six-eight hours. The cells were then harvested by centrifugation at 5000 rpm for 20 min using a SORVALL RC5B-GS3 super light rotor and the resulting pellets were stored at -20 °C.

2.1.6 Purification of N-Hsp90

Frozen cells were disrupted by sonication, using a Sanyo Soniprep 150 Ultrasonic disintegrator, in the presence of protease inhibitors (Roche Biosciences-COMLETETM protease inhibitor tablets without EDTA), and the cell-lysate spun at 25,000 rpm at 4 °C for 25 min using Beckman L7-65 ultra centrifuge with 70Ti rotor. Protein was purified by loading on a 30 ml Talon His-tag metal affinity column, equilibrated in 20 mM Tris-base (pH 8.00) containing 100 mM NaCl and 0.1 mM NaN₃ (Buffer A) using AKTA FPLC system. The column was then washed extensively with Buffer A, followed by Buffer A containing 10 mM imidazole (pH 8.00) and eluted with Buffer A containing 300 mM imidazole, pH 7.00. The protein was subsequently concentrated by using VivaspinTM protein concentrators with 10 kDa molecular weight retention. Concentrated protein was further purified using size exclusion chromatography columns (SuperdexTM-75 preparation grade, GE Lifesciences). The gel-filtration column was connected to the AKTATM FPLCTM and equilibrated in 20 mM Tris-base, 500 mM NaCl, 5 mM EDTA and 0.1 mM NaN₃,

adjusted to pH 8.00 and filter sterilized. The protein sample was concentrated to 2 ml and injected into the column.

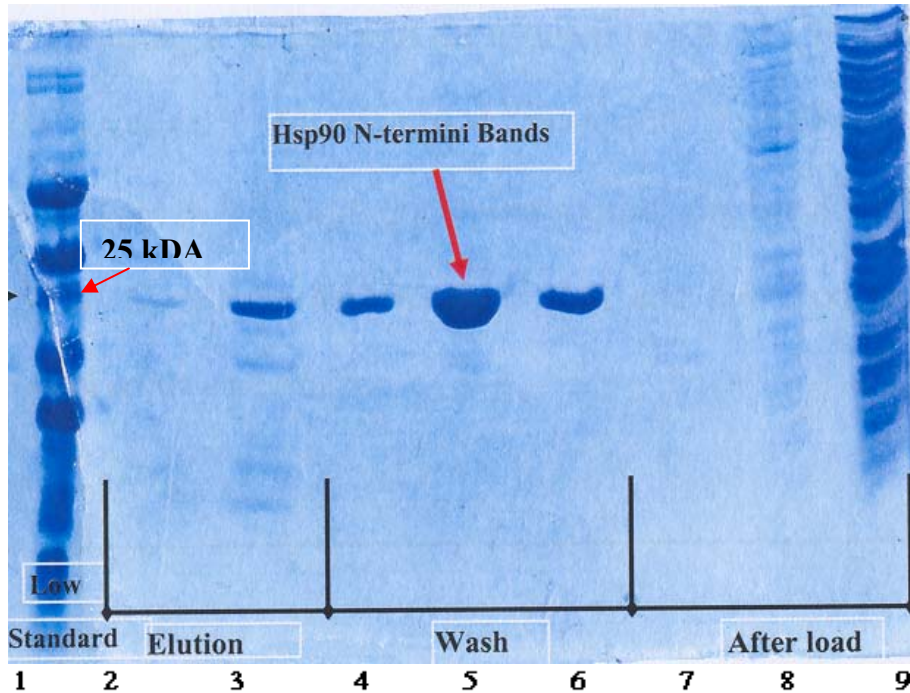


Figure 2.1.2 SDS PAGE gel shows aliquots collected during purification of the N-Hsp90. Lane 1 Standard molecular weight marker showing a relative 25 kDa band, Lane 2-3 shows small protein fractions eluted with buffer A containing 300 mM imidazole pH 7.00, Lane 4-6 various fraction of N-Hsp90 protein, Lane 8 shows bands for the loading of cell lysate on the Talon His-tag metal affinity column, Lane 9 homogenized and sonicated lysate after denaturation. (gel stained with comassie blue).

The protein was eluted following the absorbance at 280 nm. The fractions collected were screened by SDS-PAGE chromatography. All His-tagged proteins were finally dialyzed against 2 × 2 litres of 20 mM Tris-Base, 0.1 NaN₃ mM (pH 8.00) and concentrated using Vivaspin™ protein concentrators with 10 kDa molecular weight retention. N-Hsp90 expression in *E. coli* has produced a yield of about ~20 mg/L.

2.1.7 Protein Concentration Measurements

Protein concentration was measured using absorbance at 280 nm by scanning between 340 to 240 nm wavelength using a Varian Cary 100 spectrometer with baseline correction using a blank buffer (Figure 2.1.3). The extinction coefficient of the N-Hsp90 was calculated from the amino acid sequence [$\epsilon_{280} = 13370 \text{ M}^{-1} \cdot \text{cm}^{-1}$].

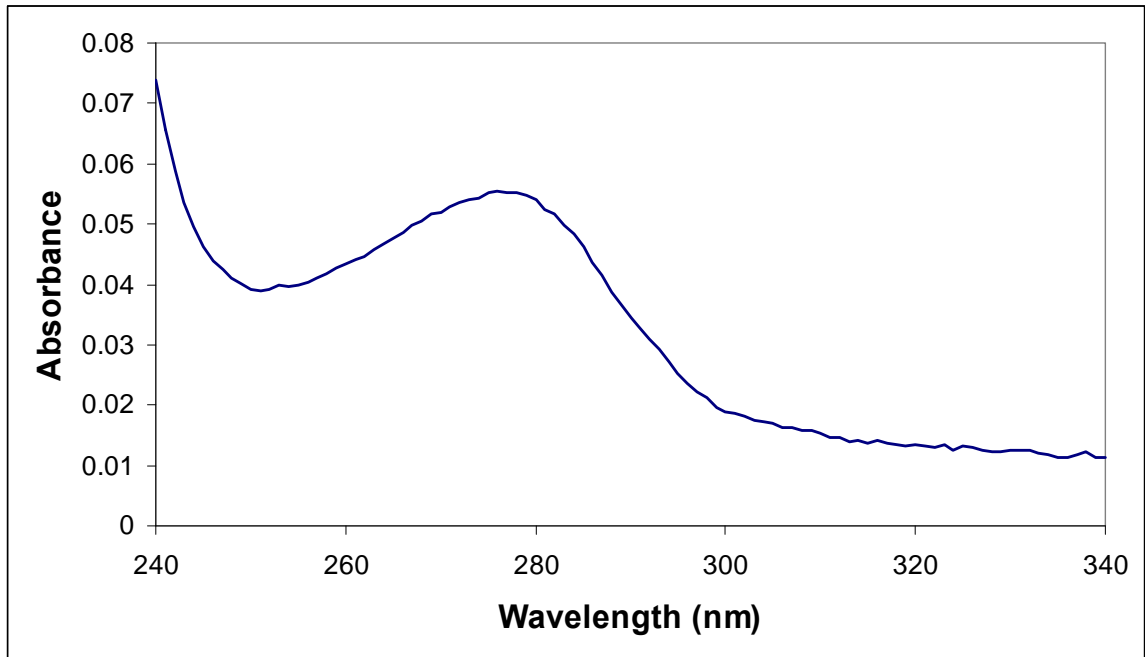


Figure 2.1.3 UV/Vis spectrum of purified N-Hsp90 (Residues 1-207). Spectra were recorded using 57 μm protein solution in 20 mM Tris (pH 8.00) on a Varian Cary 100 UV/Vis spectrometer and using a 1 cm path length quartz cuvette.

2.2 Purification and Characterization of CDK2

CDK2 was expressed in insect cells and harvested cell pellets were supplied by AstraZeneca, Alderely Park, Macclesfield, Cheshire.

Harvested cell pellets were resuspended in 30 ml of lysis buffer (10 mM Tris-HCl, pH 7.40, 25 mM NaCl, 1mM EDTA). After dounce homogenization, the lysate was clarified by centrifugation at 40,000 rpm for 40 min. The supernatant was loaded over a DEAE sepharose fast flow column pre-equillibrated with lysis buffer. The flowthrough was collected and was loaded onto an ATP affinity column pre-equilibrated with 10mM HEPES, 10 % glycerol, 1mM DTT, 1mM EDTA (pH 7.40). This column was composed of ATP coupled through ribose hydroxyl linkers to 4% agarose (Sigma). After washing, bound protein was eluted with 40 ml linear salt gradient buffer solution.

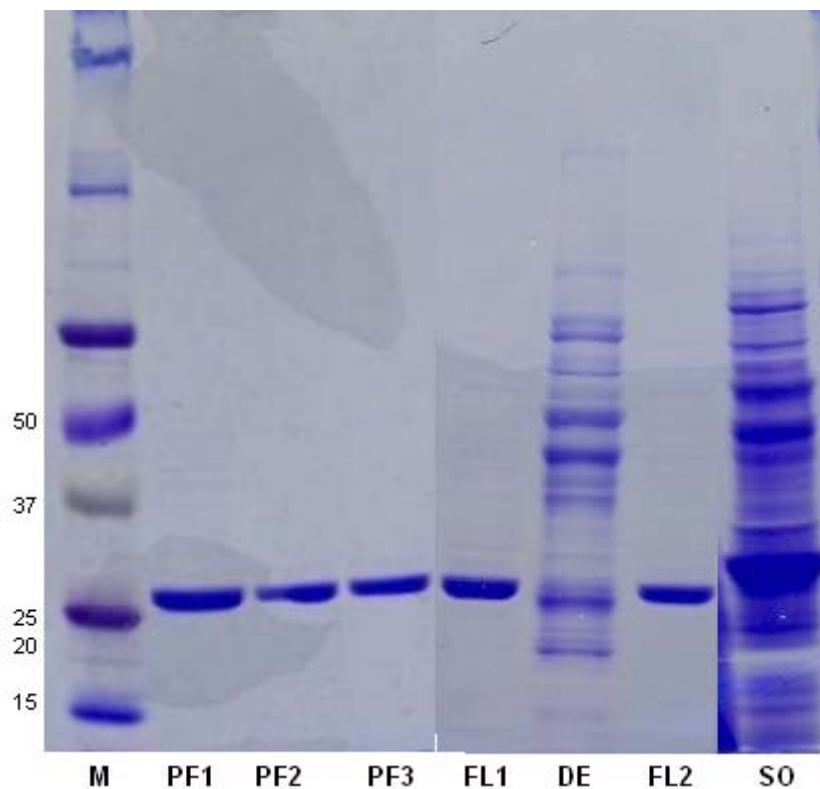


Figure 2.2.1 SDS PAGE gel electrophoresis of human CDK2. Purification of CDK2 was done by a two-step chromatography process. (see Experimental Procedure). Lane M, protein size marker (Biorad); PF1, PF2 and PF3, various protein fractions obtained from ATP agarose column. FL1 and FL2, flowthrough from DEAE sepharose column. DE, DEAE sepharose column wash. SO, homogenized and sonicated cells after denaturation. (gel stained with Comassie blue)

Fractions containing CDK2 were identified, pooled and concentrated by VivaspinTM with a molecular weight cutoff of 10 kDa. Finally CDK2 was dialyzed against

2 × 4 litre 10 mM HEPES, 1 mM DTT, 1 mM EDTA buffer (pH 7.40). The resulting CDK2 was pure and monomeric as checked with mass spectroscopy. The quality of the CDK2 preparation was checked with Circular Dichroism (CD) spectroscopy for secondary structure content and dynamic light scattering (DLS) for aggregation. CDK2 was also shown to be fully functional in various studies conducted previously at AstraZeneca, Macclesfield, Cheshire.

The far-UV CD spectrum was recorded (Figure 2.2.2) with 10 μ M CDK2 at 25 °C. The far-UV CD spectrum shows a predominantly α -helical structure, which matches well with the X-ray crystallographic structure (89).

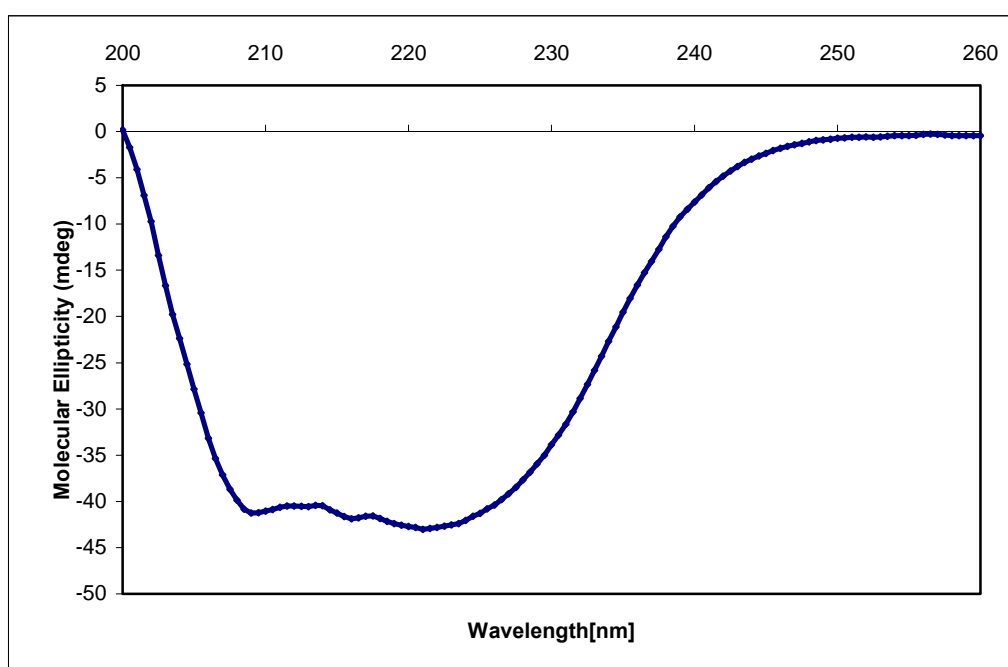


Figure 2.2.2 UV/Vis spectrum of purified Human CDK2 recorded at 25 °C. The protein concentration was 10 μ M and the cell path length was 1.0 mm. The reported CD spectrum is an average of four smoothed scans and was recorded on a JASCO J-810 CD spectrophotometer.

To characterise the molecular weight of the CDK2 preparation, a DLS study was carried out using DynaPro MS800 Light Scattering apparatus operating at a wavelength of 824 nm equipped with temperature control (Wyatt Technology, Santa Barbara, CA). Prior to measurement, protein solutions (1 mg/ml) were centrifuged at 5000 rpm for 10 min and filtered with a Whatman anatop 0.1 mm filter membrane. Data were collected for at least 200 seconds.

2. Materials and Methods

Sample	R _h (nm)	Mr (kDa)	% Mass intensity
Full length Human-CDK2	2.85	36.7	99

Table 2.2.1 Dynamic Light Scattering (DLS) analysis of full length CDK2. Protein samples were analyzed by use of Protein Solutions DynaPro Molecular Sizing Instrument and Dynamics 6 software. For each sample, the hydrodynamic radius (R_h) was determined from the measured translation diffusion coefficient by application of the Stokes-Einstein equation, and the molecular mass (Mr) was estimated with the supplied standard curve of Mr vs. R_h data. % Mass intensity for each sample was calculated after subtraction of solvent noise peaks. Polymer standard (Duke Scientific) was used as a standard with the known radius of 30 nm.

DLS data exhibited a diffusion coefficient of $815 \times 10^{-9} \text{ cm}^2 \cdot \text{s}^{-1}$, a hydrodynamic radius of $\sim 2.85 \text{ nm}$ (Table 2.2.1) and was virtually monodisperse. Assuming the protein has a spherical shape; the molecular mass was 36.7 kDa (Table 2.2.1) and was close to that expected from the amino acid composition.

2.3 Isothermal Titration Calorimetry (ITC)

2.3.1 ITC of ADP/ATP and its Analogues Binding with N-Hsp90

All the titration experiments were performed using the VP-ITC system (MicroCal Inc., Northampton, MA). In each experiment, 19 aliquots of 15 μL of 1.5 mM ATP/ADP and their analogues were injected into 1.45 ml of N-Hsp90 protein (150 μM in 20mM Tris-Base, pH 8.00) over temperature ranges of 8 to 30 $^{\circ}\text{C}$. Resulting data were fitted after subtracting the heats of dilution. Heats of dilution were determined in separate experiments from addition of ADP/ATP and its analogue into buffer, and buffer into protein. Titration data were fitted using a nonlinear least squares curve fitting algorithm with three floating variables: stoichiometry (n), binding constant (K_b) and change of enthalpy (ΔH) of interaction. All ADP/ATP analogues bind to N-Hsp90 with stoichiometry of close to 1.

2.3.2 ITC of Geldanamycin and its Analogues Binding with N-Hsp90

In each experiment 19 aliquots of 15 μL of geldanamycin (13 μM in 2% DMSO), 17-DMAG (20 μM in 2% DMSO) and 17-AAG (10 μM in 2% DMSO) were injected into 1.4 ml of N-Hsp90 protein (130 μM , 202 μM and 105 μM in 20mM Tris-Base, pH 8.00) respectively, over a temperature range of 8 to 30 $^{\circ}\text{C}$. Resulting data were fitted after subtracting the heats of dilution. Heats of dilution were determined in separate experiments from addition of geldanamycin and its analogue into buffer, and buffer into protein. Calorimetric results showed no evidence for binding of dimethyl sulfoxide (DMSO) to the nucleotide binding site. Titration data were fitted using a nonlinear least squares curve fitting algorithm with three floating variables: n , K_b and ΔH . All geldanamycin analogues bind to N-Hsp90 with stoichiometry of close to 1.

2.3.3 ITC of 2,4 and 4.6-bis anillino Pyrimidine and its Analogues with CDK2

For each series of experiments, ITC measurements were carried out against the same preparation of CDK2. Protein stored at -80 $^{\circ}\text{C}$ was thawed and dialyzed overnight at 4 $^{\circ}\text{C}$ against 2 L of buffer containing 10 mM Hepes, 8% Glycerol, 1 mM DTT and 1 mM EDTA (pH 7.40). After dialysis, the protein was filtered through a Whatman 0.02 μ filter and then adjusted to a final concentration of 100 μM with dialysis buffer. Ligand samples were dissolved in dialysis buffer with the help of 2% DMSO. The ITC

measurements were carried out at 25 °C using 30-100 μM CDK2 in the calorimeter and 0.3-1 mM ligand in the injection syringe. The injection sequence consisted of an initial injection of 2 μL to prevent artifacts arising from the filling of the syringe, followed by 24 injections of 12 μL each at 360s intervals until final saturation was observed. To correct for the heats of dilution and mixing, blank titrations of inhibitor into buffer were conducted. After subtraction of the dilution heats, calorimetric data were analyzed using the evaluation software MicroCal Origin v5.0. For these experiments, independent measurements were made at least twice for each ligand. There was less than 15% variation between readings.

2.4 The GRID Force Field and GRID MIFs

In the program GRID (88), a regular grid is built over the molecular region of interest or inside a protein cavity. Probes, i.e., functional groups that represent different physicochemical properties, are moved stepwise from grid point to grid point. For each probe/point, the interaction energy is computed using the GRID force field. The force field is based on a Lennard-Jones potential, a distance-dependent electrostatic function, and a hydrogen-bond term. The force field has been parameterised from crystal structure data. Thus, for each grid point, the energy of interaction is obtained, which together form a molecular interaction field (MIF) that represents the potential interaction of the compound/protein with a certain chemical group (probe).

The probes selected for this study were the DRY probe representing steric and hydrophobic interactions, the N1 (amide nitrogen) and N1⁺ (sp³ amine NH cation) probes to represent hydrogen-bond-donor groups, and the O⁻ (sp² carbonyl oxygen) and O⁻ (sp² phenolate oxygen) probes to represent hydrogen-bond-acceptor groups with different formal charges. In Grid force fields, the nonbonded interaction energy E_{xyz} of the probe at each xyz position of the GRID is calculated as the sum of three different components

$$E_{xyz} = \sum E_{lj} + \sum E_{el} + \sum E_{hb} \quad 2.4.1$$

where lj is the Lennard Jones potential; el is the Electrostatic interaction; and hb is the Hydrogen bonding potential.

Each individual term in the summation relates to one pairwise interaction between the probe at position xyz and single extended atom of the protein. The summation extends over all protein atoms.

2.5 Nuclear Magnetic Resonance (NMR) spectroscopy

NMR spectra were acquired on Varian UNITY plus 500 MHz and a Varian UNITY plus 600 MHz at 25 °C spectrometer were used for recording ^1H - ^{15}N HSQC. All samples were dissolved in 90% H_2O and 10% D_2O , containing 20 mM Tris-base, 5 mM MgCl_2 and 0.1 mM NaN_3 at pH 8.00. The concentration of protein ranged between 0.6 to 0.8 mM (Measured using UV absorption at 280 nm with $\epsilon_{280} = 13370$). Spectra were processed with NMRPipe/NMRDraw (90) and ANSIG (91).

2.6 Generation of N-Hsp90 Mutants

N-Hsp90 mutants were made using the QuikChange[®] Site-Directed Mutagenesis Kit (Stratagene, La Jolla, CA, USA). Plasmid pRSETA encoding the 25 kDa N-Hsp90 was used as a template in PCR with suitable primers for each mutation. Primers containing the desired mutation (Table 2.6.1) were sourced from MWG biotech. PCR amplifications were performed in 50 μL reaction volumes containing 1x reaction buffer (20 mM Tris HCl, 10 mM KCl, 10 mM $(\text{NH}_4)_2\text{SO}_4$, 0.2 mM MgSO_4 , 0.1% Triton X-100, 0.1 mg/ml BSA, pH 8.80), 125 ng forward primer, 125 ng reverse primer, 200 μM dNTP mix, 2.5 enzyme units *Pfu Turbo* DNA polymerase and 10 ng plasmid DNA.

PCR amplification was performed using a Thermo Hybaid thermal cycler set to hold for 5 min at 95 °C before performing a cycle consisting of 95 °C for 1 min, 55 °C for 1 min and 68 °C for 16 min, repeated 20 times. Once the PCR reaction is complete, 10 enzyme units of Dpn1 restriction endonuclease were added to each reaction and incubated at 37 °C for 1 hour to digest methylated template DNA. 5 μL of Dpn1-treated reaction product was then used to transform 50 μL *E. coli* XL1-Blue super competent cells. Transformation was performed in prechilled Falcon tubes by incubating the cells with PCR product for 30 mins on ice before heat shock at 42 °C for 45 seconds. After heat shock, cells were placed on ice for 2 minutes before adding 450 μL NZY broth (10 g/L caesin hydrolysate, 5 g/L yeast extract, 5 g/L NaCl, 20 % (w/v) glucose, 12.5 mM MgCl_2 , 12.5 mM MgSO_4) preheated at 42 °C. Cells were then incubated for 1 hour at 37 °C with shaking. 250 μL of transformation reaction was spread on LB agar plates containing 200 $\mu\text{g}/\text{ml}$ CAB and 34 $\mu\text{g}/\text{ml}$ CAP before incubating at 37 °C overnight. Mutated plasmid DNA was then purified from single colonies and the sequence was confirmed by DNA sequencing. The plasmid encoding various mutants was then transformed into *E. Coli* BL21(DE3)PlsysS.

Mutation	Primers	
	Forward	Reverse
N37H	5'-GAG AGA ACT GAT TCA TGC CTC GGA TGC GTT G-3'	5'-CAA CGC ATC CGA GGC ATG TAT CAG TTC C-3'
N37Q	5'-CTT GAG AGA ACT GAT ATC TCA GGC CTC GGA TGC GTT G-3'	5'-CAA CGC GGC CTG AGA TAT CAG TTC TCT CAA G-3'
N92Q	5'-CCA AGG CTG AAT TGA TTA ATC AGT TGG GTA CCA TTG CCA AG-3'	5'-CTT GGC AAT GGT ACC CCA CTG ATT AAT CAA TTC AGC CTT GG-3'
T171Q	5'-GAA GTT AAT GAA AGA ATT GGT CAG ATC TTG AGG TTA TTC TTG AAA GAT GAC-3'	5'-GTC ATC TTT CAA GAA TAA CCT CAA GAT CTG ACC CCT ACC AAT TCT TTC ATT AAC TTC-3'

Table 2.6.1 Sequence of various primers used in N-Hsp90 mutations.

2.7 Circular Dichroism (CD) Spectroscopy of N-Hsp90

All CD experiments were performed using the AVIV-202SF circular dichroism spectrometer with constant N₂ flushing (AVIV Associates Inc., NJ). A Neslab circulating water bath was used to control the temperature of the optic cell chamber. Each experiment used a 0.01 cm cuvette filled with 20 μM N-Hsp90 protein in 20 mM Tris-Base, pH 8.00 buffer at 25 °C. Protein scans were collected between 190 to 260 nm wavelengths at 1 nm intervals and were subjected to further deconvolution after subtracting buffer scans. Buffer scans were determined in separate experiments from scans at 190 to 260 nm of the buffer (20mM Tris-Base, pH 8.00). The scans between 200 to 260 nm were then converted into mean residue ellipticity, ([θ]_{mrw}) by using equation 2.7.1 and plotted against wavelength. The mean residue ellipticity was calculated using 218 as the number of amino acids residues, as the N-Hsp90 construct used in the present study contained an 11 residue His-tag sequence on the N-terminal end.

$$[\theta]_{mrw} = \frac{\theta_{\gamma}}{(n \times d \times c \times 10)} \quad 2.7.1$$

where θ is the observed ellipticity in degrees at each wavelength, n is the total number of amino acid residues, d is the path length of the cuvette (0.01 cm), c is the concentration of the protein in mg/ml.

Deconvolution of CD spectra of N-Hsp90 in the presence or absence of AMPPNP was achieved using the program CONTIN-CD (92).

2.8 Determination of Melting Temperatures (T_m) by CD Spectroscopy

All CD protein melting experiments were performed using the AVIV-202SF CD spectrometer with constant N_2 flushing (AVIV Associates Inc., NJ). A Neslab circulating water bath was used to control the temperature of the optical cell chamber. For thermal melting experiments, data points were taken at 1°C intervals at a scan rate of 30 °C per hour. The sample cuvette (pathlength 0.01 cm) contained 50 μ M N-Hsp90 in 20 mM Tris buffer, pH 8.00. Protein stability was determined by thermal denaturation by monitoring the decrease in α -helical content at a wavelength of 218 nm with increasing temperature. The melting point (T_m) for N-Hsp90 in the presence or absence of AMPPNP was determined over the temperature range of 20 to 80 °C. The raw data obtained for the temperature dependence of the ellipticity were fitted using a nonlinear least squares algorithm using Origin 5.0 (OriginLab Corporation, Northampton, MA) to obtain the melting point (T_m).

2.9 Solvent Accessible Surface Area (SASA) Calculations

The SASA of N-Hsp90, N-Hsp90-ADP and N-Hsp90-geldanamycin were calculated by the procedure implemented in the VEGA suite of programs (93; 94) with default water radius of 1.4 Å. The polar surface portion included all nitrogen and oxygen atoms, whereas the non-polar surface area was constructed from the exposed sulphur, aliphatic and aromatic carbon atoms. The solvent accessible surface removed upon complex formation was determined as the difference between the surface of the complex and the sum of the surface of ligand and free protein based on the crystal structure.

$$\Delta SASA = SASA_{\text{complex}} - SASA_{\text{protein}} - SASA_{\text{ligand}} \quad 2.9.1$$

where SASA is defined as the solvent accessible surface area.

2.10 Molecular Dynamics (MD) simulations

2.10.1 Preparation of N-Hsp90-ADP Structure for MD simulation

An N-Hsp90-ADP simulation was started using the X-ray crystal structure of ADP bound to N-Hsp90 (PDB: 1AMW), solved by Prodromou and co-workers (54). The ADP topology files, as needed in GROMACS (95; 96), were prepared using the PRODRG server (97). The downloaded crystal structure of N-Hsp90-ADP (PDB: 1AMW) did not contain the Mg^{2+} coordinates and were added during the structure preparation step by predicting its most energetically favorable position with GRID (88). This structure has a total charge of -12. To achieve electroneutrality, 12 Na^+ counterions were added using the GENION module of GROMACS 3.2.1 (95; 96). The protein and ligand were embedded in a box containing an SPC model water (98) that extended to at least 5 Å between the complex and the edge of the box. Subsequently solvation of the N-Hsp90-ADP complex in a cubic box type periodic boundary condition with a pre-equilibrated SPC water requiring a 5 Å solvent shell in all directions resulted in a system with dimensions $63.65 \times 63.65 \times 63.65 \text{ \AA}^3$ containing 7,450 water molecules (Figure 2.10.1).

2.10.2 Preparation of N-Hsp90-geldanamycin Structure for MD simulation

N-Hsp90-geldanamycin simulation was started using the X-ray crystal structure of geldanamycin bound to N-Hsp90 (PDB: 1A4H), also determined by Prodromou and co-workers (54). The geldanamycin topology files, as needed in GROMACS, were prepared using the PRODRG server (97).

This structure has a total charge of -9. To achieve electroneutrality, 9 Na^+ counterions were added using GENION(95). The protein and ligand were embedded in a box containing an SPC model water (98) that extended to at least 5 Å between the complex and the edge of the box. Subsequently solvation of the N-Hsp90-geldanamycin complex with pre-equilibrated SPC water in a cubic box style periodic boundary condition with a 5 Å solvent shell in all directions resulted in a system with dimensions of $69.44 \times 69.44 \times 69.44 \text{ \AA}^3$ encompassing 9,912 water molecules.

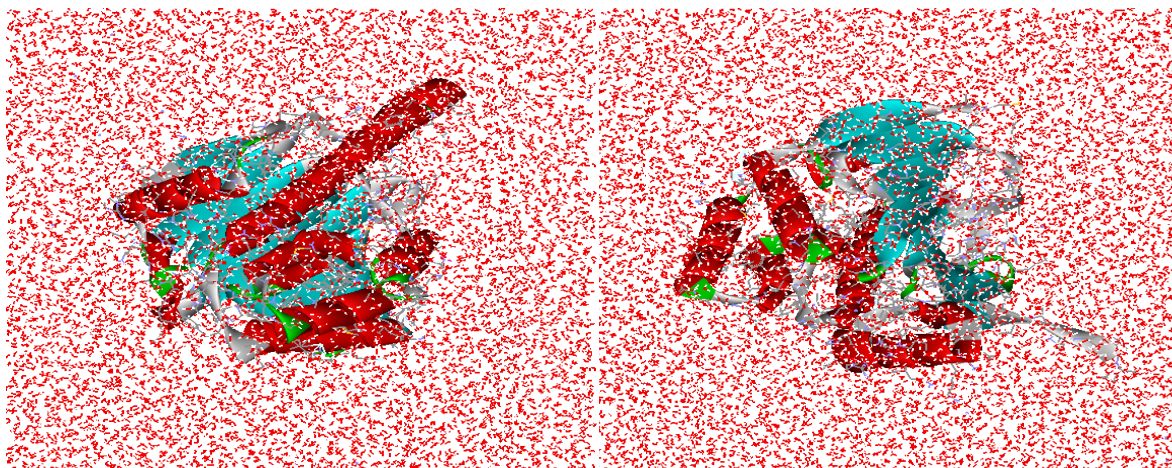


Figure 2.10.1 Front view of the N-Hsp90-ADP placed in a cubic box of pre-equilibrated SPC water molecules. α -helices and β -sheets of the N-Hsp90 are emphasized. (Figure generated using VMD (99))

2.10.3 Minimization/Equilibration and MD simulation

The simulations were run at constant temperature (298.15 K) and pressure (1 atm) by using the GROMACS simulation package (95; 96). MD calculations employed the united atom force-field described by van Burren et al. (100). The Reaction-Field summation method was used for the treatment of long-range electrostatic interactions. The chosen charge grid spacing is close to 1 Å and a cubic interpolation scheme was used. A cut-off of 13 Å for the van der Waals interactions and the Berendsen coupling scheme were used. The system was prepared through a series of energy minimization and heating steps. The heating stage was followed by equilibration at 298 K for 100 ps. The trajectory was

Neighbor-searching parameters	
nstlist	10
nstype	Grid
pbc	xyz
rlist	1 nm
Parameters for calculation of electrostatics and vdW interactions	
Coulomb-type	Reaction_field
vdW-type	Cut-off (r : 1.3 nm)
T-coupling	Berendsen (298.15 K, τ : 0.1)
p-coupling	Berendsen (isotropic, 1 bar, τ : 1)
Constraints	Hydrogen bonds (LINCS)

Table 2.10.1 GROMACS parameters for the normal simulation setup.

continued for a total of 20 ns, of which the first 12 ns were chosen for analysis. The trajectory was recorded with 2 ps intervals.

Further analysis of the simulations was performed by the tools available in the GROMACS package and was partially aided by in-house scripts. Resulting trajectory and snapshots were investigated with different visualization programs, i.e., VMD (99) and XMGRACE (101). These were used for the determination of the water residence times and for visualization in the form of graphs. All simulations were performed on 3 individual dual processor AMD based linux workstations.

2.10.4 Determination of RMSD and RMSF

The root mean square deviation (RMSD) for the simulation structures at time T relative to the starting structure was calculated using equation 2.10.1.

$$RMSD = \sqrt{\frac{\sum_{i=1}^T (x_i - X)^2}{n - 1}} \quad 2.10.1$$

where x_i refers to the position of residue i at time T . X defines the position of the corresponding residue i in the starting structure at time $t=0$ and n refers to the total number of residues in the protein molecule. For root mean square fluctuation (RMSF) calculations, X is replaced by the average position of residue i during the simulation, where the value of X is calculated by the following equation

$$X = \frac{1}{n} \sum_{T=1}^n x_{i,T} \quad 2.10.2$$

where $x_{i,T}$ is the position of residue i at time T during the simulation and n corresponds to the total number of time points.

2.10.5 Determination of Water Residence Times

The average site occupancy is defined as the fraction of time the site is occupied by any water molecule. A site is considered occupied if a water molecule is found in a spherical volume with a radius of 1.4 Å. This distance was chosen because the radius of a water molecule is approximately 1.4 Å. The residence time was evaluated from a survival

time correlation function $C(t)$, which represents the average number of water molecules that remain in the hydration site for a duration of time (102). The survival function is defined as

$$C\alpha(t) = \sum_{j=1}^{N_w} \frac{1}{T_{run} - t + 1} \sum_{t_0}^{T_{run}-t} P_{\alpha j}(t_0, t_0 + t) \quad 2.10.3$$

where $P_{\alpha j}(t_0, t_0+t)$ is a binary function that takes the value of 1 if the j th water molecule occupies the α th site from t_0 to t_0+t ; otherwise, the function is 0; N_w is the total number of water molecules; T_{run} is the length of simulation. Water occupancies were then converted into water residence times and calculated by the method described by Spoel et al. (103).

2.11 Linear Interaction Analysis (LIE) Calculation

2.11.1 Protein Preparation and Identification of Binding Site

Initial coordinates for CDK2 co-crystallized with compound 1 were downloaded from the RCSB Protein Data Bank (PDB: 1H00) and imported into SYBYL 7.0 (Tripos Associates: St. Louis, MO, 2005) and ligand (M365370) was removed to make a empty binding site. The Molcad (program in SYBYL, Version 7.0; Tripos Associates: St. Louis, MO, 2005) site detection software was then used to identify potential binding sites.

Overall four X-ray crystal structures of CDK2 are available in the Protein Data Bank with assigned ids of 1H00, 1H01, 1H07 and 1H08. However, for the present analysis and the validation study of the computer aided drug design algorithm that we employ, the crystal structure with PDB code 1H01 was used as a starting structure. 1H01 contains a CDK2 bound with M395323. This crystal structure was determined to a resolution of 1.79 Å by Breault et al. (104) and consists of two overlapping orientation of the M395323 molecule. Both of these orientations have the possibility of interacting with CDK2 through H-bonding with water. However these two orientations vary in the position of the flexible tail, as it does not form any direct H-bond with any of the protein residues.

2.11.2 Molecular Docking By GOLD

Molecular docking of compounds was performed by the GOLD 2.1.2 package (105) with the default speed setting. For each of the 10 independent genetic algorithm (GA) runs, a maximum number of 100000 GA operations were performed on a single population of 100 individuals. Operator weights for crossover, mutation, and migration in the entry box were set to 95, 95 and 10, respectively. The maximum distance between hydrogen donors and fitting points was set to 2.5 Å, and nonbonded van der Waals energies were cutoff at a value equal to $4 k_{ij}$ (well depth of the van der Waals energy for the atom pair i and j). To speed up the calculation, the GA docking was stopped when the top 3 solutions were within 1.5 Å root-mean square deviation (rmsd) of each other.

2.11.3 LIE Free Energy Change Calculation

The free energy calculations were carried out using the Liaison 3.0 package from Schrödinger Inc (106). Liaison 3.0 is an LIE implementation and uses a surface-generalized Born (SGB) continuum solvation model (84). All charges used in MD calculations were treated using the OPLS-AA force field (107). A non bonded cutoff distance of 10 Å was used. The maximum number of minimization steps was 1000 steps and molecular dynamics simulation data collection was performed after 20 ps initial equilibration (before collecting the LIE energies), a sample target temperature of 298.15 K and 100 ps of sampling for the LIE energies (total simulation time = 120 ps) was used. For all MD simulations, the time step was fixed at 0.002 ps and energies were sampled every 10 steps.

3. Chapter

3.1 Thermodynamics and Structural Properties for Binding of ADP/ATP and Geldanamycin to N-Hsp90

To gain an insight into the ΔC_p of ligand binding to the N-Hsp90 (residues 1-207), the thermodynamic parameters of the N-Hsp90 in complex with ADP, ATP and geldanamycin and their analogues were compared by ITC. X-ray structures and NMR assignments for the N-Hsp90 from yeast and human in complex with ADP, ATP, radicicol, and geldanamycin are already known (54; 55). All these ligands had been shown to use a similar deep binding pocket made up of two α -helices with the central β -sheet at its base, making this system unique and ideal for understanding various theories and conjectures surrounding the evaluation of ΔC_p . Additionally, extensive availability of structural and proteomic data available within the group (52; 54; 108) played an important role in affirming this decision.

This section describes the investigation of ΔC_p for protein-small molecule interactions, along with the investigation of the positive ΔC_p in the N-Hsp90-ADP/ATP interaction.

3.1.1 Thermodynamics of ADP/ATP Binding to N-Hsp90

The physiological substrate for N-Hsp90 is ATP, however ITC experiments using this ligand showed a lack of reproducibility compared to other compounds. This is likely to be the result of a low level of background hydrolytic activity by the domain toward the γ -phosphate of ATP over the course of the titration. As a result ADP was also used in these experiments.

The binding energetics of ADP and ATP to N-Hsp90 was characterised in the temperature range of 11 °C to 29 °C by ITC. All thermodynamic measurements were conducted in 20 mM Tris, pH 8.00 to correlate with the structural data presented elsewhere (108). As an example of the experimental results, Figure 3.1.1. shows the raw calorimetric binding isotherm obtained at 20 °C from the progressive titration of N-Hsp90 with ADP. The corresponding heat of dilution experiment consisting of the injection of ligand solution into buffer is also shown. In all experiments ligand solution heats were very small in relation to actual binding heats. After subtraction, n (the number of binding sites of protein, stoichiometry), ΔH and K_b were obtained from nonlinear fitting of an identical and independent binding sites model to the normalized titration curve.

Calorimetric results obtained for ADP and ATP binding to N-Hsp90 are presented in Table 3.1.1 and 3.1.2. At 25 °C, ADP binds to Hsp90 with a K_d^{**} of around 9.47 μM with highly favourable ΔH of $-42.00 \pm 0.63 \text{ kJ}\cdot\text{mol}^{-1}$ and highly unfavourable $T\Delta S$ of about $-13.36 \text{ kJ}\cdot\text{mol}^{-1}$. While, binding of ATP to Hsp90 at 25 °C leads to an increase in K_d to 60.35 μM , with a reduction of $19.96 \text{ kJ}\cdot\text{mol}^{-1}$ in ΔH and $T\Delta S$ being $15.36 \text{ kJ}\cdot\text{mol}^{-1}$ more favourable (Table 3.1.2). From the calorimetric data obtained, it is also clear that at 25 °C the entropy term contributes unfavourably to the ease of ADP and ATP binding to N-Hsp90.

The X-ray crystal structure of Hsp90 with ADP and ATP, solved by Prodromou et al. (54) does not show any substantial difference in structure, except for the ordering of the side-chain of Lys98, which might be providing a steric hindrance to the ATP binding to N-Hsp90. This steric hindrance for the binding of ATP is reflected in its lower enthalpy of binding (about $19.96 \text{ kJ}\cdot\text{mol}^{-1}$), compared with the binding of ADP. The n values indicate

** dissociation constant

that the stoichiometry is 1:1 in agreement with the crystal structure of the N-Hsp90-ADP complex.

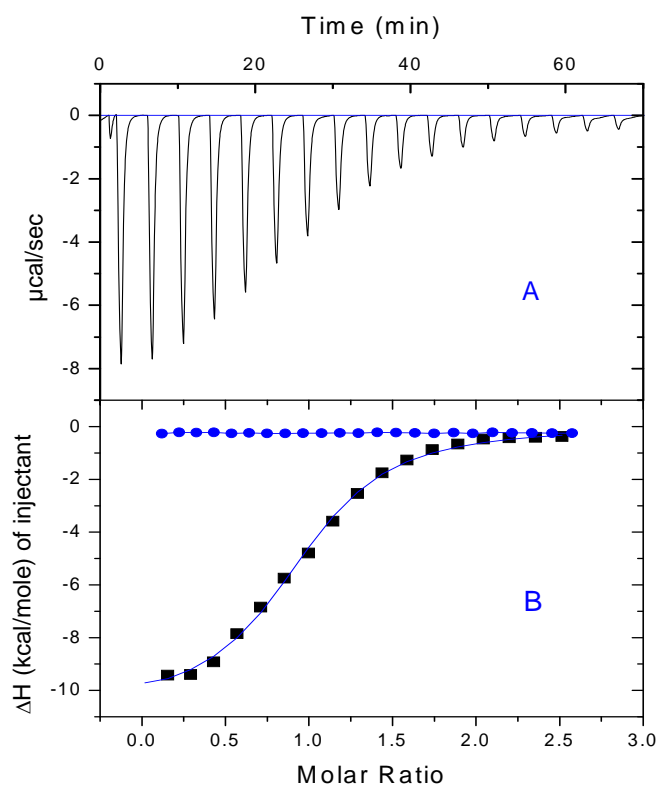


Figure 3.1.1 A: Raw data for the titration of ADP into N-Hsp90 solution at 20 °C in 20 mM Tris-base at pH 8.00. **(B)** Binding isotherm derived from (A), corrected for the heats of dilution shown as diamonds in B; the line represents the least squares fit to the single site binding model.

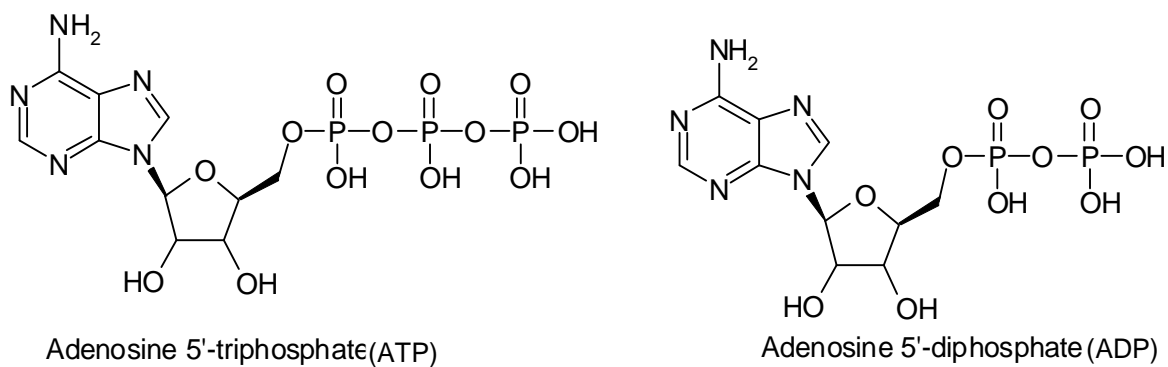


Figure 3.1.2 Structure of ADP/ATP.

3. Results and Discussion

Ligand	Temp (°C)	Stoichiometry (n)	$K_b \times 10^4$ (M ⁻¹)	$K_d^{(2)}$ (μM)	ΔH_{obs} (kJ·mol ⁻¹)	$T\Delta S_{\text{obs}}$ (kJ·mol ⁻¹)	ΔG_{obs} (kJ·mol ⁻¹)	ΔC_p (kJ·mol ⁻¹ ·K ⁻¹)
ADP	11	0.89 ± 0.02	8.92 ± 0.85	11.20	- 72.56 ± 2.92	-45.62	- 26.93	2.35 ± 0.46
	16	1.03 ± 0.00	7.86 ± 0.15	12.72	- 63.28 ± 0.35	- 36.20	- 27.07	
	20	0.95 ± 0.01	6.14 ± 0.44	16.28	- 45.52 ± 0.71	- 18.66	- 26.85	
	25	1.12 ± 0.01	10.55 ± 1.26	9.47	- 42.00 ± 0.64	- 13.36	- 28.63	

Table 3.1.1 Summary of the thermodynamic parameters for the binding interaction of N-Hsp90 with ADP as a function of temperature in 20 mM Tris buffer (pH 8.00).

Ligand	Temp (°C)	Stoichiometry (n)	$K_b \times 10^4$ (M ⁻¹)	$K_d^{(2)}$ (μM)	ΔH_{obs} (kJ·mol ⁻¹)	$T\Delta S_{\text{obs}}$ (kJ·mol ⁻¹)	ΔG_{obs} (kJ·mol ⁻¹)	ΔC_p (kJ·mol ⁻¹ ·K ⁻¹)
ATP	19	0.98 ± 0.02	2.84 ± 0.18	35.13	- 31.22 ± 0.95	- 6.33	- 24.88	2.28 ± 1.95
	20	0.64 ± 0.01	1.06 ± 0.04	93.89	- 41.36 ± 0.88	- 18.	- 24.04	
	25	1.19 ± 0.05	1.65 ± 0.18	60.35	- 22.04 ± 1.44	2.00	- 24.04	

Table 3.1.2 Summary of the thermodynamic parameters for the binding interaction of N-Hsp90 with ATP as a function of temperature in 20 mM Tris buffer (pH 8.00).

¹ Data was fitted to a one-set-of-sites model.

² Dissociation constant values (K_d) were calculated as the reciprocal of the observed equilibrium binding constant ($K_d = 1 / K_{\text{obs}}$)

Using MCS-ITC, Prodromou et al. (54) characterised the binding of ADP to N-Hsp90 in 20 mM Tris buffer, pH 7.40 and 25 °C. Analysis of ATP and ADP binding to the N-Hsp90 in solution indicates a K_d of 132 ± 47 and 29 ± 3 μM , respectively, with binding stoichiometries close to 1 per N-Hsp90 monomer. As seen in Table 3.1.1 and Table 3.1.2, their measured K_d values are within an acceptable level of agreement with our results. Discrepancy between their values and the present calorimetric results can also be attributed to the difference in pH and to the unstable nature of ADP/ATP in aqueous solvents.

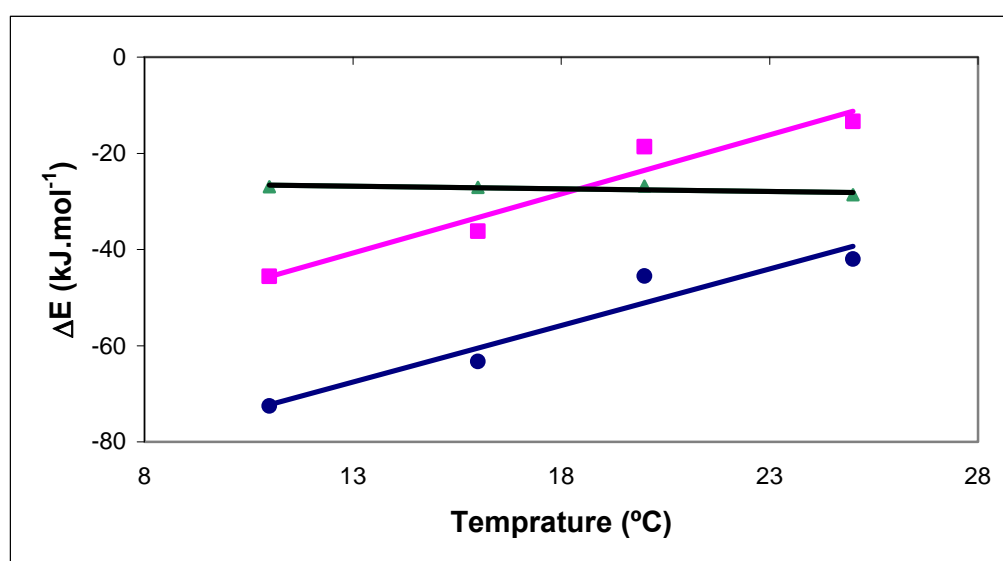


Figure 3.1.3 Thermodynamic parameters of the binding of ADP to N-Hsp90 at pH 8.00 as a function of temperature: ΔH (blue circles); $T\Delta S$ (pink square); ΔG (green triangles).

Assuming ΔC_p to be temperature independent, linear regression analysis of enthalpy data versus temperature in Tables 3.1.1 and 3.1.2 gave ΔC_p values of 2.35 ± 0.46 and 2.28 ± 1.95 $\text{kJ}\cdot\text{mol}^{-1}\cdot\text{K}^{-1}$ for ADP and ATP complexes respectively. The results are also shown in Figure 3.1.3. The blue closed circles in Figure 3.1.3 are the net enthalpy change obtained experimentally at each temperature (Table 3.1.1) for N-Hsp90-ADP binding. From equation 1.3.1, $T\Delta S$ is known to be 0 at 43 °C. Below this temperature, the entropy term contributes unfavourably, formation of N-Hsp90-ADP complex is driven by enthalpy term alone and the binding is still very tight. At 25 °C, the enthalpy change becomes much more unfavourable to the extent of 30.56 $\text{kJ}\cdot\text{mol}^{-1}$ than at 11 °C. The contribution of the enthalpy term still overcomes that of the entropy value up to 43 °C. However, it is obvious that, like many other protein-ligand interaction systems, N-Hsp90-ADP/ATP is not characterised by a negative ΔC_p .

Molecular interactions involving protein-ligand, protein-DNA and antigen-antibody recognition are usually characterised by substantial negative values of the standard ΔC_p (41; 109-112).

So, to understand this positive ΔC_p effect in ADP/ATP interaction with N-Hsp90 and to investigate whether other ADP/ATP analogues show the same thermodynamic signature, a study was conducted to investigate effects of various closely related ADP/ATP analogues on modulating ΔC_p .

3.1.2 Comparative Analysis of the Nucleotide Specificity of N-Hsp90 Nucleotide Binding Sites

Since the K_b of ADP and ATP shows a wide difference in affinity and also shows a positive ΔC_p upon binding, we decided to initiate a detailed study to obtain thermodynamic parameters for similar ADP/ATP analogues. Additionally, this study was also aimed at getting a detailed understanding of the nature of the specific interactions between ligand functional groups and specific N-Hsp90 subsites. To achieve this objective, ITC was used to probe binding of various ADP/ATP analogues such as adenylyl imidodiphosphate tetralithium salt (AMPPNP), cyclic-AMP (cAMP), cytidine-5-diphosphate, xanthosine diphosphate, guanosine 5-monophosphate, guanosine-5-diphosphate, guanosine 5-triphosphate, xanthosine 5-triphosphate, 8-bromoadenosine-5-diphosphate, 8-bromoadenosine-5-triphosphate, inosine 5-diphosphate and inosine 5-triphosphate.

We found that the ΔH for binding of AMPPNP to N-Hsp90 in 0.02 M Tris-base buffer is $-33.39 \text{ kJ}\cdot\text{mol}^{-1}$ (25 °C). The binding of ADP in 20 mM Tris-Base buffer shows a 30% higher ΔH than the AMPPNP. The thermodynamic parameters of binding for AMPPNP and cAMP are reported in Tables 3.1.3 and 3.1.4. Since all the compounds described contained a purine ring, it was necessary to study the binding of adenine and adenosine (Figure 3.1.4) in order to evaluate the role of adenine (purine) moiety in the binding of ADP and its analogues. Accordingly, binding titrations were carried out for adenine and adenosine binding to N-Hsp90. However accurate binding thermodynamics were difficult to estimate, due to the relative weakness of the bindings and also limits on increasing the concentration of N-Hsp90 protein.

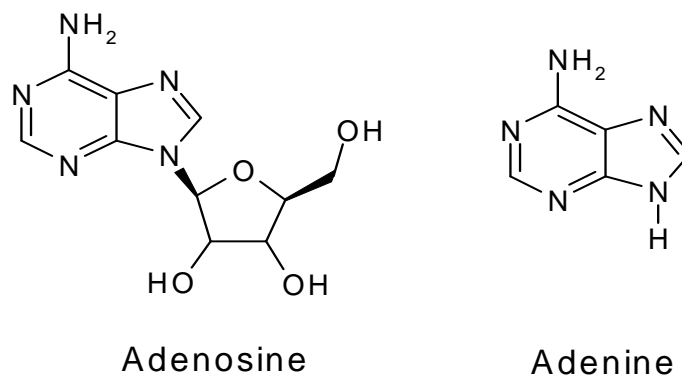


Figure 3.1.4 Structure of Adenine and Adenosine.

Binding of adenine, adenosine, cAMP, ADP and ATP to N-Hsp90 as a function of the number of phosphate groups in each small molecule was measured by ITC and the thermodynamic parameters are compared graphically in Figure 3.1.5. Each thermodynamic parameter is discussed in turn for each of these analogues.

Adenine, adenosine, cAMP and ADP show a small regular increment in ΔG , while ΔG for ATP binding to N-Hsp90 drops down almost to that of adenosine (Figure 3.1.5). Adenine shows the weakest binding of all the ligands in the series. Interestingly, ΔG does not show any large variation in each of the series of analogues, with all values falling in the range of $8.74 \text{ kJ}\cdot\text{mol}^{-1}$ of each other.

AMPPNP and cAMP bind with positive ΔC_p of 0.28 ± 0.03 and $0.59 \pm 0.15 \text{ kJ}\cdot\text{mol}^{-1}\cdot\text{K}^{-1}$ respectively. This positive ΔC_p in both AMPPNP and cAMP binding to N-Hsp90 confirmed our earlier finding of positive ΔC_p in ADP/ATP-Hsp90 interactions.

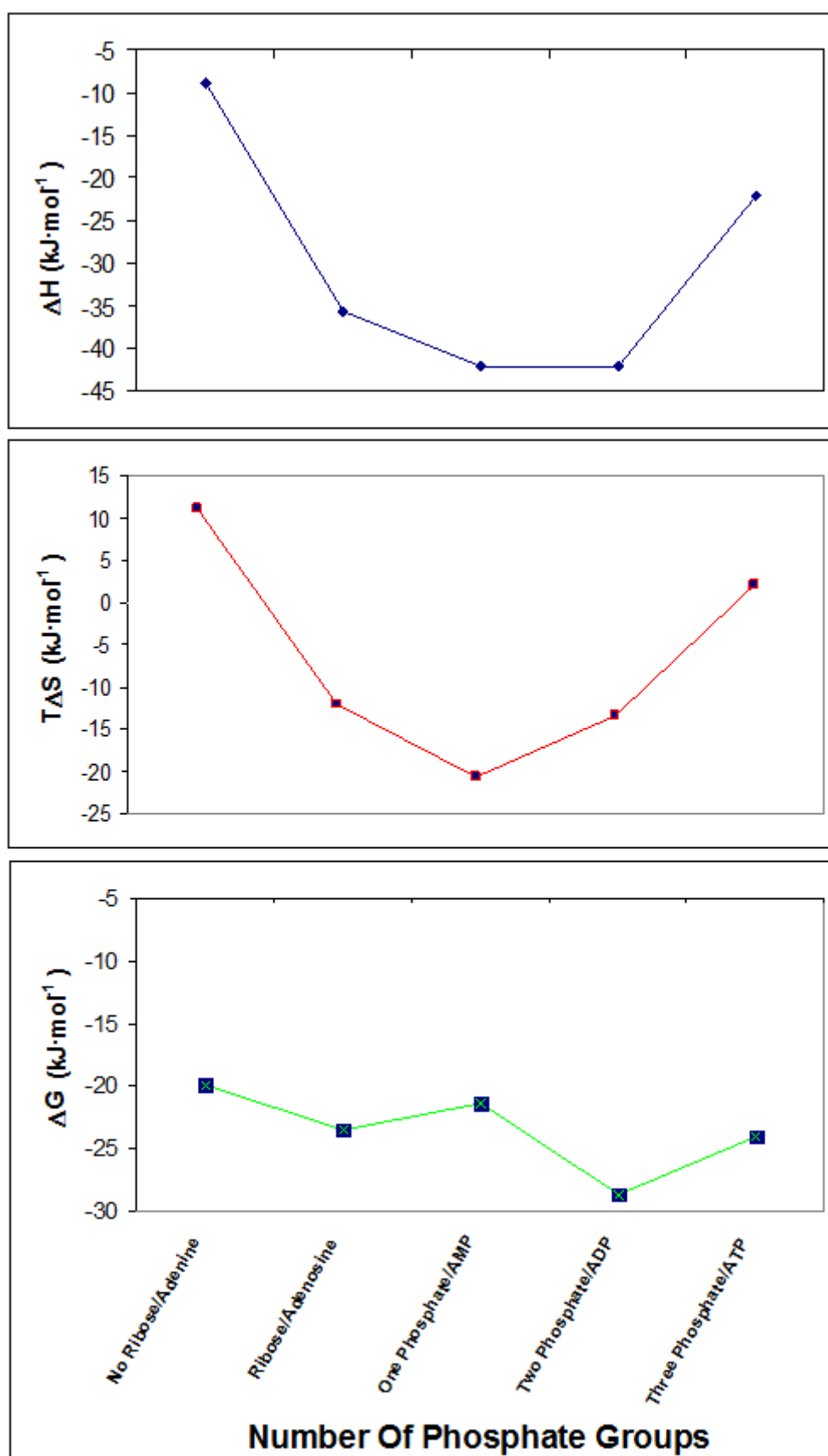


Figure 3.1.5 Thermodynamic parameters for the binding of the adenosine series of small molecules to N-Hsp90 at 25 °C.

3. Results and Discussion

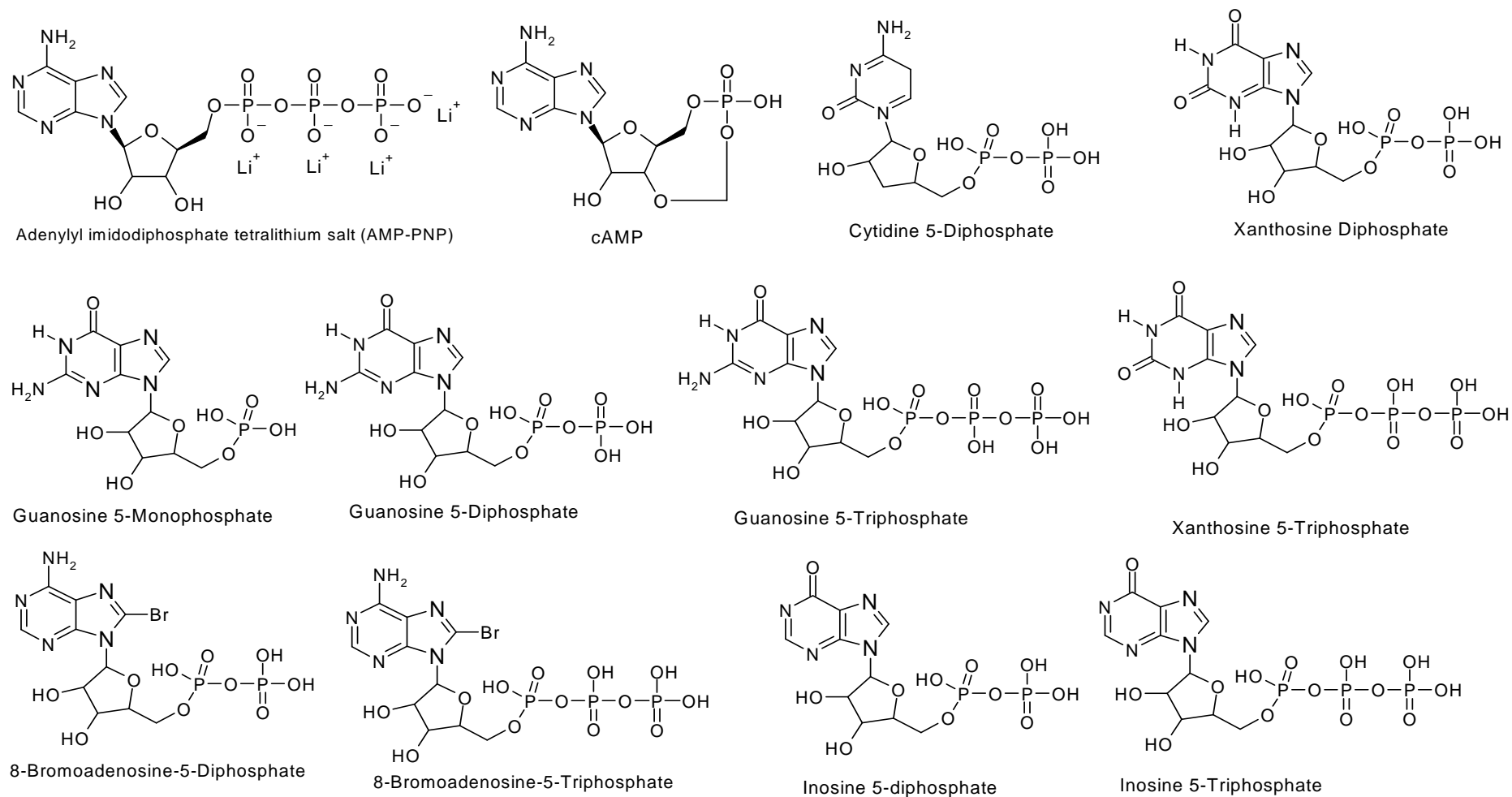


Figure 3.1.6 Structure of various ATP/ADP analogues used in the study.

3. Results and Discussion

Ligand	Temp (°C)	Stoichiometry (n)	$K_b \times 10^4$ (M ⁻¹)	$K_d^{(2)}$ (μM)	ΔH_{obs} (kJ·mol ⁻¹)	$T\Delta S_{\text{obs}}$ (kJ·mol ⁻¹)	ΔG_{obs} (kJ·mol ⁻¹)	ΔC_p (kJ·mol ⁻¹ ·K ⁻¹)
AMPPNP	8	1.10 ± 0.00	2.32 ± 0.04	42.9	- 38.38 ± 0.24	- 14.89	-23.49	0.28 ± 0.03
	12	1.12 ± 0.00	1.86 ± 0.04	53.5	- 36.26 ± 0.27	- 12.97	- 23.29	
	16	1.10 ± 0.00	1.34 ± 0.02	74.4	- 35.89 ± 0.29	-13.05	- 22.84	
	20	1.12 ± 0.00	1.05 ± 0.02	94.6	- 34.21 ± 0.31	- 11.65	- 22.56	
	25	1.07 ± 0.02	0.77 ± 0.04	129.6	- 33.39 ± 1.07	- 11.22	- 22.17	

Table 3.1.3 Summary of the thermodynamic parameters for the binding interaction of N-Hsp90 with AMPPNP as a function of temperature (pH 8.00).

Ligand	Temp (°C)	Stoichiometry (n)	$K_b \times 10^4$ (M ⁻¹)	$K_d^{(2)}$ (μM)	ΔH_{obs} (kJ·mol ⁻¹)	$T\Delta S_{\text{obs}}$ (kJ·mol ⁻¹)	ΔG_{obs} (kJ·mol ⁻¹)	ΔC_p (kJ·mol ⁻¹ ·K ⁻¹)
cAMP	9	1.00 ± 0.00	2.23 ± 0.03	44.70	- 47.77 ± 0.48	- 24.21	- 23.55	0.59 ± 0.15
	15	0.82 ± 0.00	1.24 ± 0.03	80.45	- 47.98 ± 0.68	- 25.41	- 22.57	
	25	0.95 ± 0.04	0.54 ± 0.02	182.50	- 42.13 ± 2.63	- 20.78	- 21.34	
	29	0.85 ± 0.00	0.42 ± 0.02	103.45	- 40.40 ± 4.23	- 19.45	- 20.94	

Table 3.1.4 Summary of the thermodynamic parameters for the binding interaction of N-Hsp90 with cAMP as a function of temperature (pH 8.00).

¹ Data was fitted to a one-set-of-sites model.

² Dissociation constant values (K_d) were calculated as the reciprocal of the observed equilibrium binding constant ($K_d = 1 / K_{\text{obs}}$)

3. Results and Discussion

Ligand used	K_d (μM)	ΔH_{obs} ($\text{kJ}\cdot\text{mol}^{-1}$)	$T\Delta S_{\text{obs}}$ ($\text{kJ}\cdot\text{mol}^{-1}$)	ΔG_{obs} ($\text{kJ}\cdot\text{mol}^{-1}$)
Adenine	323.10	-8.83 ± 1.17	11.06	-19.89
Adenosine	74.18	-35.64 ± 2.53	-12.09	-23.55
cAMP	182.50	-42.13 ± 2.63	-20.78	-21.34
ADP	9.47	-42.00 ± 0.64	-13.36	-28.63
ATP	60.35	-22.04 ± 1.44	2.00	-24.04

Table 3.1.5 Thermodynamic parameters for binding of various Purine analogues arranged in increasing number of phosphate groups at 25 °C.

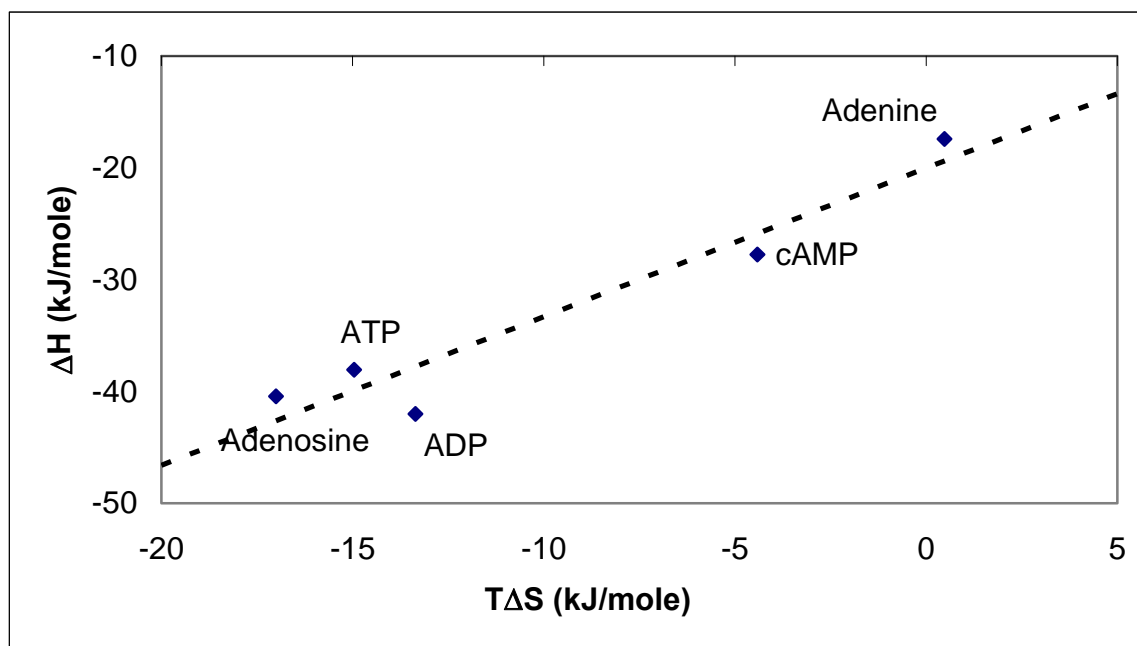


Figure 3.1.7 Plot of ΔH versus $T\Delta S$ for the binding of adenosine series of ligands to the N-Hsp90 at 25 °C.

ΔH shows much larger differences between individual ligands and has a marked differential appearance which is in contrast to the ΔG plot also shown in Figure 3.1.5. The complexity of interactions, which are not revealed by the ΔG measurements, can be ascertained by the ΔH measurements. This can be seen through comparison of ΔH and $T\Delta S$ plots in Figure 3.1.5. These two plots are almost mirror images of one another, while the ΔG plot is relatively flat and results from the equal but opposite compensating changes in the other two thermodynamic parameters i.e. ΔH and $T\Delta S$. This behaviour is a striking

example of the phenomenon of “enthalpy-entropy” compensation and has been discussed extensively by Dunitz, Lachenmann et al., and Lumry (113-115).

From Table 3.1.4 and Figure 3.1.5 it is apparent that the ΔH and ΔG of the binding of adenine to N-Hsp90 are markedly less than that of other ligands in the series. Possibly, adenine engages in the same exothermic interactions utilized by the other ligands in the series. Such interactions are always available to adenosine, cAMP, ADP and ATP, which in turn shows much higher ΔH of binding to N-Hsp90. ATP shows decreased affinity than ADP, as the γ -phosphate of ATP shows a steric hindrance caused by the third phosphate (54), which can be bypassed by ADP as it can form a more productive set of interactions than ATP.

The ribose hydroxyl group of adenosine contributes about $-3.66 \text{ kJ}\cdot\text{mol}^{-1}$ to its ΔG of binding and is composed of favourable enthalpic and unfavourable entropic contributions as compared to adenine (Table 3.1.5). The ribose hydroxyl groups of both adenosine and other ligands (cAMP, ADP and ATP) engage in significant exothermic interactions and these interactions contribute mainly to the ΔG of adenine binding.

Aside from these results, a study to determine the thermodynamic signatures of ten compounds (described in Figure 3.1.6) namely cytidine-5-diphosphate, xanthosine diphosphate, guanosine-5-monophosphate, guanosine-5-diphosphate, guanosine-5-triphosphate, xanthosine-5-triphosphate, 8-bromoadenosine-5-diphosphate, 8-bromoadenosine-5-triphosphate, inosine 5-diphosphate and inosine 5-triphosphate was also carried out. All these compounds have shown little or undetectable levels of binding with N-Hsp90, suggesting that the purine ring is absolutely necessary for binding to N-Hsp90 and even a slight modification in the purine ring can decrease or wipe out binding affinity.

Nonetheless, all the ligands binding to N-Hsp90 are assumed to be binding through strong interactions involving the purine ring of the adenine moiety. The ribose hydroxyl groups of the adenosine, cAMP, ADP and ATP, each appear to engage in distinctly different individual interactions with the binding site of N-Hsp90, as discussed above. Actually the binding of adenosine analogues to N-Hsp90 has been developed in such a manner that a comparatively strong ADP binding is due to summation of a number of small interactions, none of which involves more than a few kilojoules.

3.1.3 Thermodynamics of Geldanamycin and its Analogues Binding to N-Hsp90

Natural ansamycin antibiotics such as geldanamycin and its analogues (17-(allylamino)-17-demethoxy-geldanamycin, 17-AAG; and 17-*N,N*-dimethylaminoethylamino-17-demethoxy-geldanamycin, 17-DMAG; Figure 3.1.8) investigated in this work are structurally very different from the adenosine phosphate (ADP/ATP) molecules. They are macrocyclic compounds which contain neither the adenine-sugar nucleoside nor a linear phosphate chain. These compounds also bind to the N-Hsp90 with high affinity and could inhibit the ATPase activity of Hsp90 (116).

We have used ITC to characterise the binding of geldanamycin and its analogues (structure shown in Figure 3.1.8) to the N-Hsp90. In general, geldanamycin analogues are much more hydrophobic in nature than the water soluble ATP/ADP analogues. As a result, the low solubility of the geldanamycin analogues required 2% DMSO as a co-solubilising agent. The effect of addition of 2% DMSO to N-Hsp90 was investigated separately with NMR. ^1H - ^{15}N HSQC of 2% DMSO with N-Hsp90 showing no interaction between DMSO and N-Hsp90 (Figure 3.1.11).

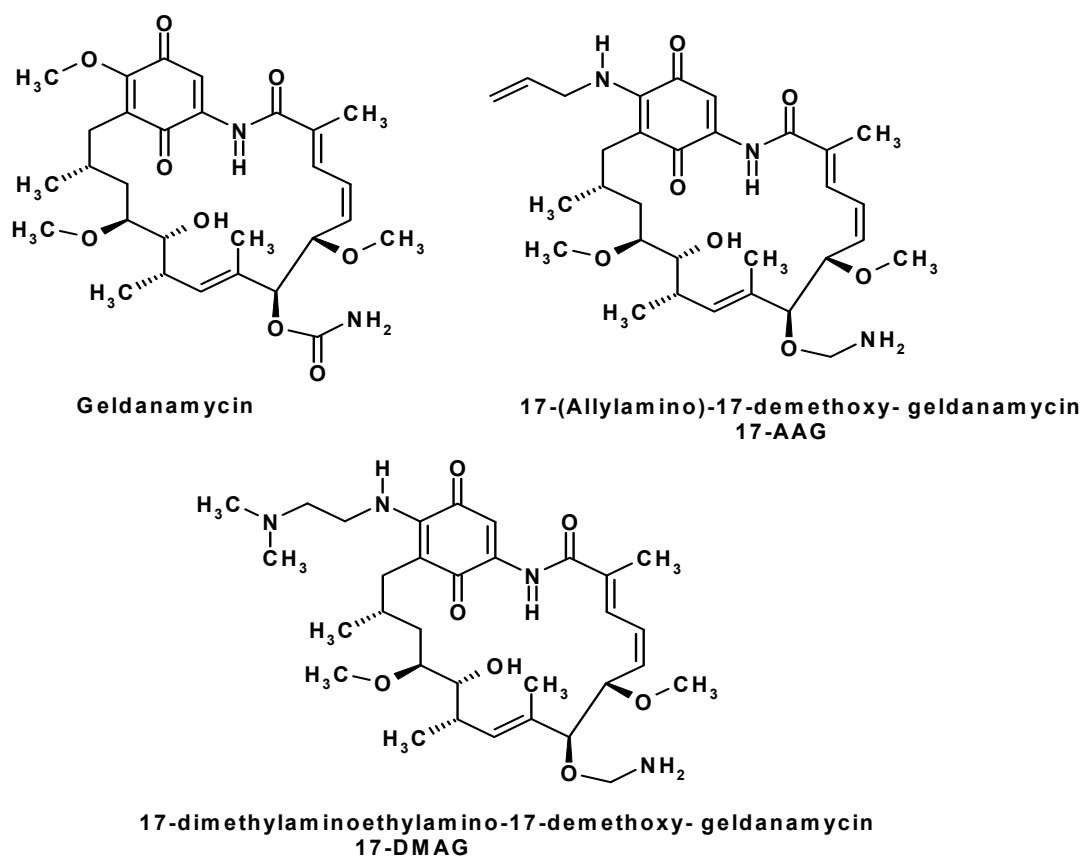


Figure 3.1.8 Chemical structures of geldanamycin, 17-AAG and 17-DMAG, used in the present study.

This hydrophobicity of geldanamycin analogues is reflected in the thermodynamic parameters obtained for the titration, where geldanamycin and its analogues bind with more favourable entropy than observed for the binding of ADP analogues. At 25 °C, geldanamycin binds to N-Hsp90 with a K_d of around 1.05 μM with ΔH being highly favourable at $-34.35 \pm 0.53 \text{ kJ}\cdot\text{mol}^{-1}$ and a negligible $T\Delta S$ of $-26 \text{ kJ}\cdot\text{mol}^{-1}$. A major potential source of negative ΔH values is usually considered to be van der Waals and hydrogen bonding interactions (42). The binding of geldanamycin, 17-AAG and 17-DMAG is enthalpically favourable at all temperatures studied, for which it can be suggested that van der Waals and hydrogen bond interactions will be the major contributors to the binding energetics of these ligands.

Binding of 17-AAG and 17-DMAG to N-Hsp90 at 25 °C leads to an increase in K_d to 2.48^{††} and 2.2 μM respectively. In 17-AAG, ΔH becomes $-6.38^{\dagger\dagger} \text{ kJ}\cdot\text{mol}^{-1}$ less favourable and $T\Delta S$ becomes more favourable by $4.28^{\dagger\dagger} \text{ J}\cdot\text{mol}^{-1}$. Binding of 17-DMAG proceeds with a less favourable ΔH of $9.75 \text{ kJ}\cdot\text{mol}^{-1}$ and favourable $T\Delta S$ of $7.81 \text{ kJ}\cdot\text{mol}^{-1}$. Interestingly, these analogues show increasing $T\Delta S$ as their hydrophobicity decreases. Geldanamycin, which is more hydrophobic than the other two analogues, shows negligible $T\Delta S$. 17-DMAG which is much more soluble in water, binds to N-Hsp90 with a favourable $T\Delta S$ of $7.55 \text{ kJ}\cdot\text{mol}^{-1}$ at 25 °C.

Also, the experimental binding constant decreases systematically as the steric bulk at the first carbon atom situated on the 17 position of the ansa-ring in geldanamycin is increased: $K_{\text{CH}_3\text{-O-}}$ (geldanamycin) > $K_{\text{CH}_2=\text{CH-CH}_2\text{-NH-}}$ (17-AAG) > $K_{(\text{CH}_3)_2\text{-N-CH}_2\text{-CH}_2\text{-NH-}}$ (17-DMAG). One explanation might be that increasing the steric bulk of the substituents leads to progressive distortion of the binding pocket and its surroundings, which is reflected in increasing $T\Delta S$ of these ligands and is not entirely compensated by the ΔH contribution, which ultimately affects ΔG (Table 3.1.6). However on close examination of the X-ray crystallographic structure of geldanamycin and 17-DMAG bound to N-Hsp90 (Figure 3.1.9), it is evident that the structure of the backbone of the N-Hsp90 remains relatively unaffected after the substitution with an all-atom RMS deviation of only 1.29 Å (117). This is also in line with crystallographic studies of the trypsin complex (118; 119), where substitution of the ligand with even conservative modifications showed large differences in the thermodynamic signature.

^{††} Obtained from determination of the straight line of best fit to the observed data.

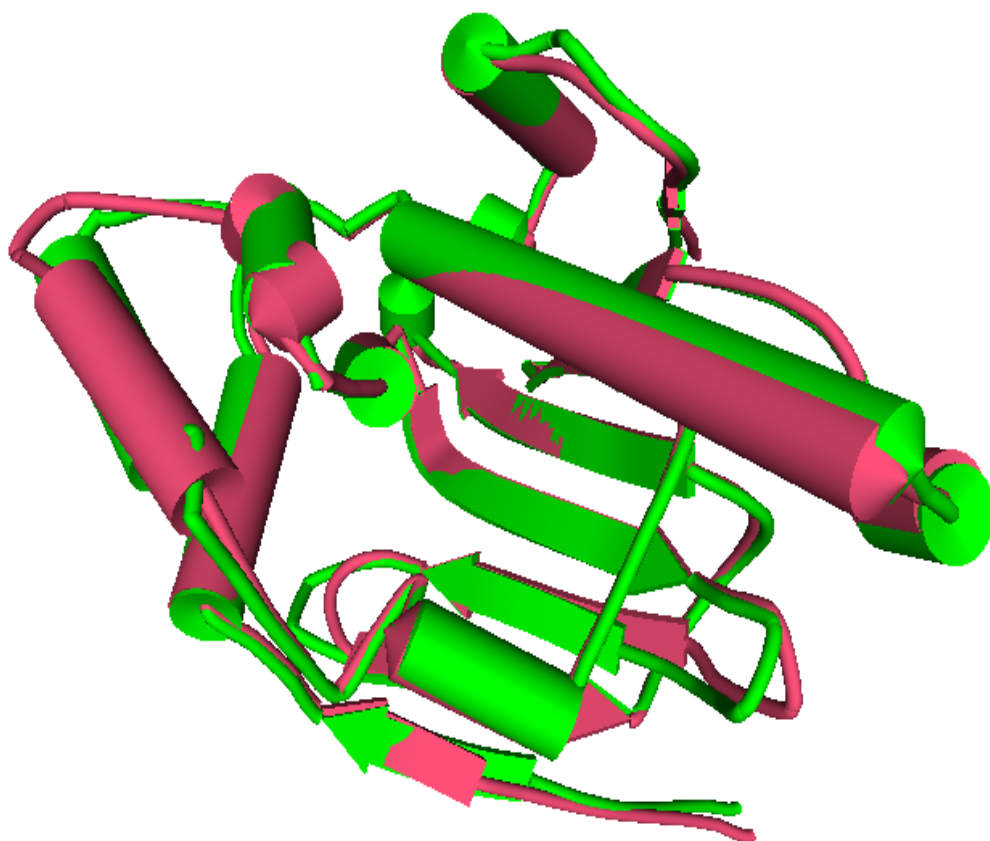


Figure 3.1.9 Overlay of geldanamycin over 17-DMAG bound to N-Hsp90. (pink-geldanamycin bound Hsp90 and green 17-DMAG bound). 17-DMAG and geldanamycin bound structures show an all-atom RMS deviation of 1.29 Å. (Figure generated using DS ViewerPro 5.0 (56))

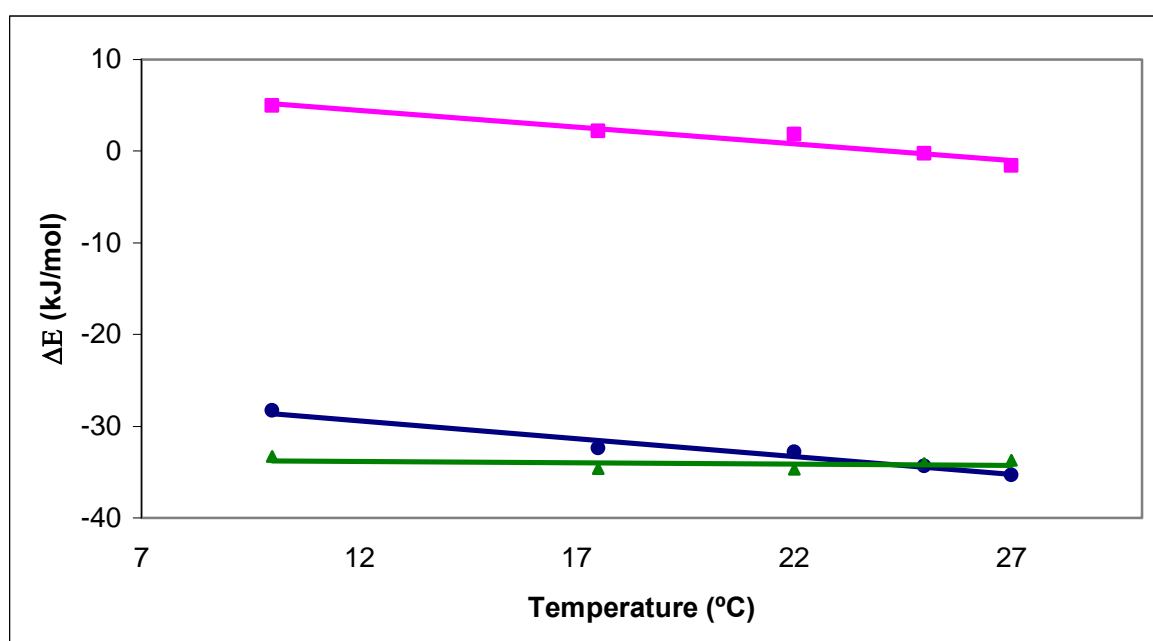


Figure 3.1.10 Thermodynamic parameters of the binding of geldanamycin to N-Hsp90 at pH 8.00 as a function of temperature: ΔH (blue circles); $T\Delta S$ (pink square); ΔG (green triangles).

3. Results and Discussion

Ligand	Temp(°C)	Stoichiometry (n)	$K_b \times 10^4$ (M ⁻¹)	$K_d^{(2)}$ (μM)	ΔH_{obs} (kJ·mol ⁻¹)	$T\Delta S_{\text{obs}}$ (kJ·mol ⁻¹)	ΔG_{obs} (kJ·mol ⁻¹)	ΔC_p (kJ·mol ⁻¹ ·K ⁻¹)
Geldanamycin	10	1.00 ± 0.00	141.9 ± 16.1	0.70	- 28.29 ± 0.21	5.01	- 33.3	- 0.39 ± 0.04
	17.5	0.74 ± 0.00	168.2 ± 8.65	0.59	- 32.43 ± 0.27	2.17	- 34.6	
	22	1.02 ± 0.00	139.7 ± 10.67	0.71	- 32.85 ± 0.39	1.83	- 34.68	
	25	0.89 ± 0.01	95.17 ± 7.44	1.05	- 34.35 ± 0.53	- 0.26	- 34.09	
	27	1.04 ± 0.01	75.54 ± 5.21	1.32	- 35.35 ± 0.49	- 1.60	- 33.75	
17-AAG	8	1.04 ± 0.00	106.80 ± 7.13	0.93	-19.34 ± 0.19	13.06	- 32.40	- 0.36 ± 0.16
	13	1.05 ± 0.00	75.17 ± 4.54	1.3	- 26.03 ± 0.29	6.12	- 32.15	
	20.2	1.06 ± 0.01	53.66 ± 3.92	1.8	- 27.24 ± 0.59	4.89	- 32.13	
	30	1.03 ± 0.02	32.04 ± 2.86	3.1	- 28.69 ± 1.07	3.22	- 31.91	
17-DMAG	15	0.97 ± 0.00	62.84 ± 2.35	1.5	- 20.38 ± 0.14	11.56	- 31.94	- 0.48 ± 0.06
	20	1.00 ± 0.00	44.72 ± 1.80	2.2	- 23.59 ± 0.21	8.08	- 31.67	
	25	1.04 ± 0.01	43.73 ± 3.04	2.2	- 24.60 ± 0.37	7.55	- 32.15	
	30	1.01 ± 0.01	37.91 ± 2.97	2.63	- 28.06 ± 0.54	4.28	- 32.34	

Table 3.1.6 Summary of the thermodynamic parameters for the binding interaction of N-Hsp90 with different Geldanamycin analogues as a function of temperature in 20 mM Tris buffer (pH 8.00).

¹ Data was fitted to a one-set-of-sites model.

² Dissociation constant values (K_d) were calculated as the reciprocal of the observed equilibrium binding constant ($K_d = 1 / K_{\text{obs}}$).

The results are also shown in Figure 3.1.10. The blue closed circles are the net ΔH obtained experimentally at each temperature (Table 3.1.6). From equation 1.3.1, $T\Delta S$ is known to be 0 at 24.8 °C. Below this temperature, the entropy term contributes favourably to complex formation. However compared with formation of N-Hsp90-geldanamycin, N-Hsp90-ADP binding is mainly driven by ΔH . At 27 °C, the enthalpy change for geldanamycin binding becomes much more favourable ($-7.06 \text{ kJ}\cdot\text{mol}^{-1}$) than at 10 °C, the contribution of the entropy term still adds to the total ΔG of the binding below 25 °C. However, it is evident that like many other protein-ligand interactions, the present process is characterised by a negative ΔC_p . This is contrary to the positive ΔC_p observed in ADP/ATP binding. The negative ΔC_p causes the net thermodynamic driving force for association to shift from an entropic to an enthalpic contribution with increasing temperature.

Since geldanamycin, 17-AAG and 17-DMAG bind to N-Hsp90 with a similar binding mode, with the modified side-chain of 17-AAG and 17-DMAG playing no significant role in ordering of water molecules, this results in similar negative ΔC_p of about -0.36 to $-0.48 \text{ kJ}\cdot\text{mol}^{-1}\cdot\text{K}^{-1}$. The behaviour described is usual for molecular associations, which are characterised by a negative ΔC_p and indicates significant burial of the hydrophobic surface area. Additionally, this surface area burial correlates well with the reduction in solvent accessible surface area calculated from the crystallographic structure of geldanamycin bound to N-Hsp90 and discussed further in Section 3.2.7.

Binding of geldanamycin was also studied by NMR. In NMR titrations, geldanamycin shows strong chemical shift perturbations. The shift changes within the binding pocket are large, with signals of residues 81G, 189R, 94G, 130V, 122V and 123G being strongly affected. N-Hsp90 also shows significant ordering of secondary structure upon titrating with geldanamycin and ADP/ATP analogues in NMR; this indicates significant secondary structure ordering (stiffness) after ligand binding (Williams M., Unpublished data).

Geldanamycin shows negative ΔC_p upon binding to N-Hsp90, while ADP/ATP shows a positive ΔC_p of binding. Geldanamycin, ADP and ATP bind in the same nucleotide binding pocket of N-Hsp90. Moreover, it is interesting to note that the negative ΔC_p shown by the geldanamycin and its analogues is opposite to the positive ΔC_p shown by the ADP/ATP analogues (Figure 3.1.14), as all of these analogues bind in the same binding pocket (Figure 3.1.13) and in similar binding conformation (Figure 3.1.12).

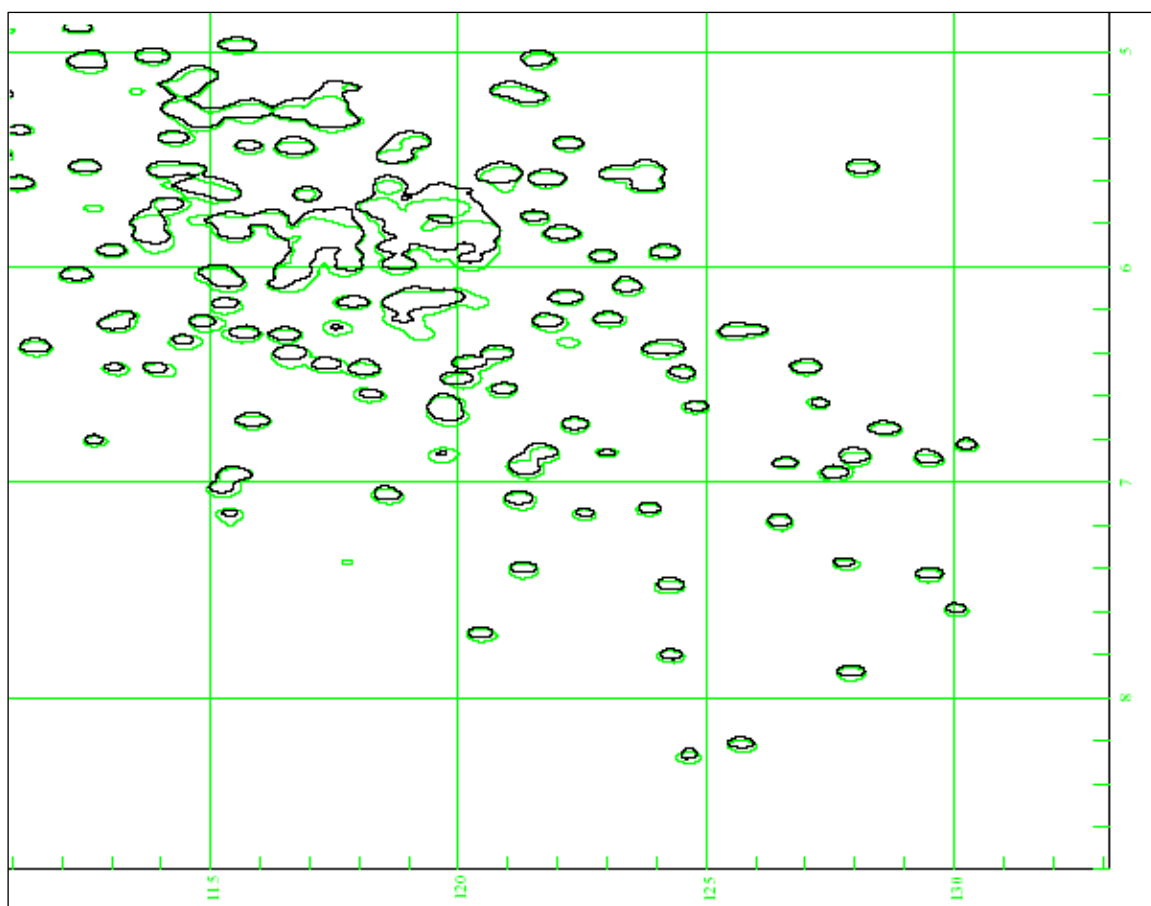


Figure 3.1.11 ^1H - ^{15}N HSQC experiment showing effect of addition of DMSO on N-Hsp90. (Green-Apo, Black-Apo+DMSO)

This property of positive ΔC_p in N-Hsp90-ADP/ATP interactions and negative ΔC_p in N-Hsp90-geldanamycin make this system thermodynamically unique, and specially suitable for further development of quantitative interpretation of intermolecular interactions in protein-ligand systems. It was therefore, decided to investigate further the positive ΔC_p in N-Hsp90-ADP/ATP interactions.

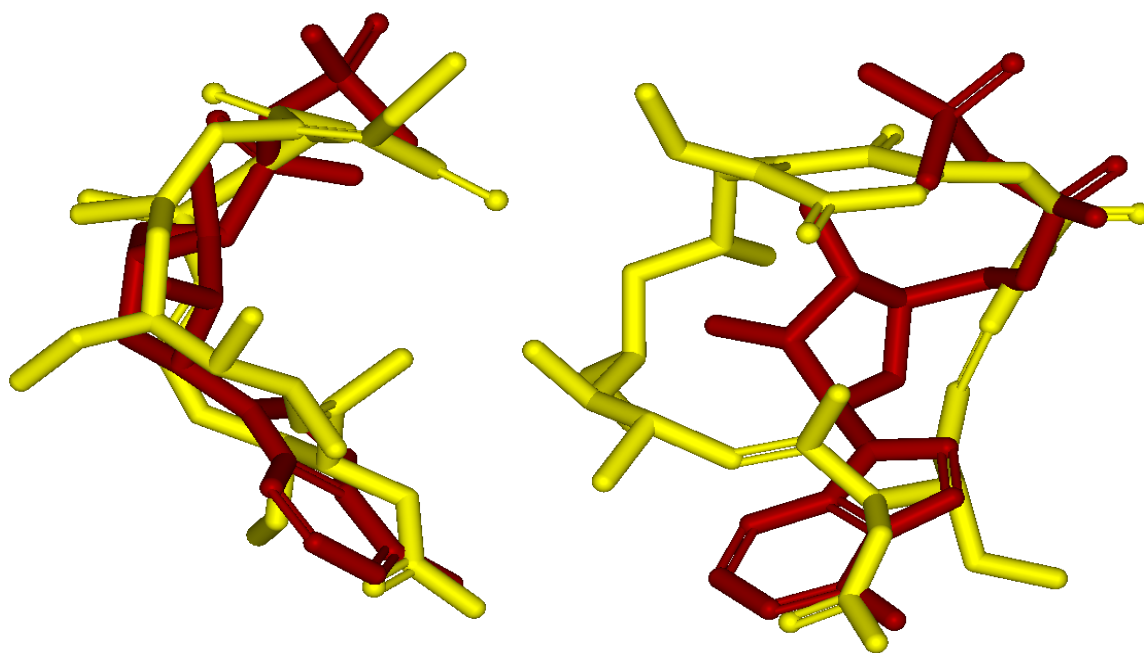


Figure 3.1.12 Two different views of geldanamycin (yellow) over ADP (red) in bound conformation to N-Hsp90, showing similar conformation for the bound form. (Figure generated using DS ViewerPro 5.0 (56))

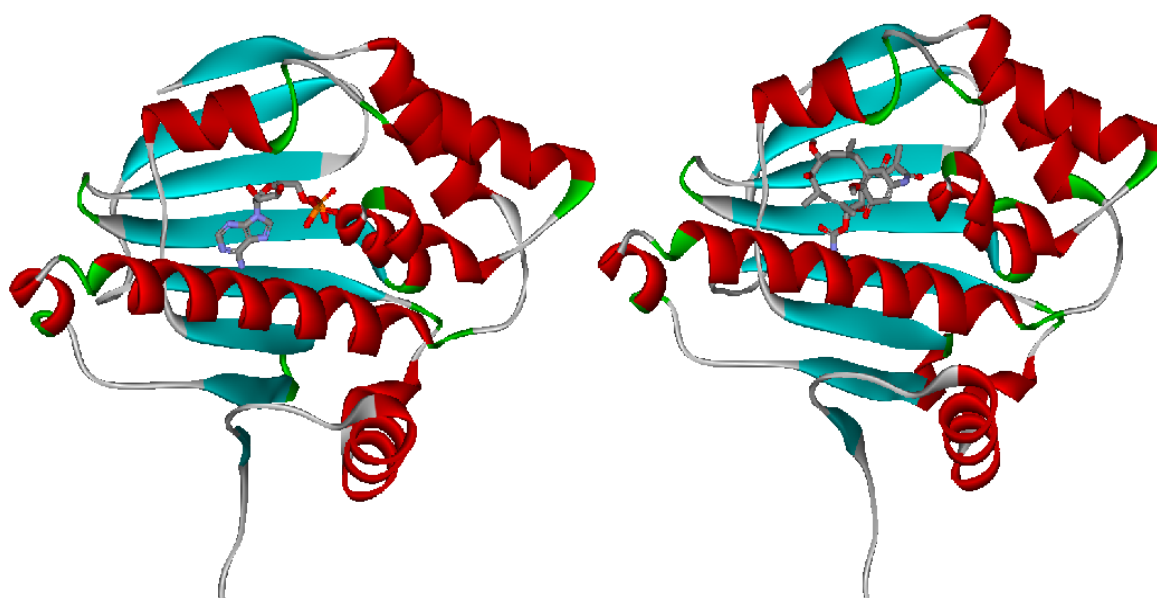


Figure 3.1.13 Two views of the structure of yeast N-Hsp90 (helices in red, β -sheets in green) bound to ADP (left) and geldanamycin (right). (Figure generated using DS ViewerPro 5.0 (56))

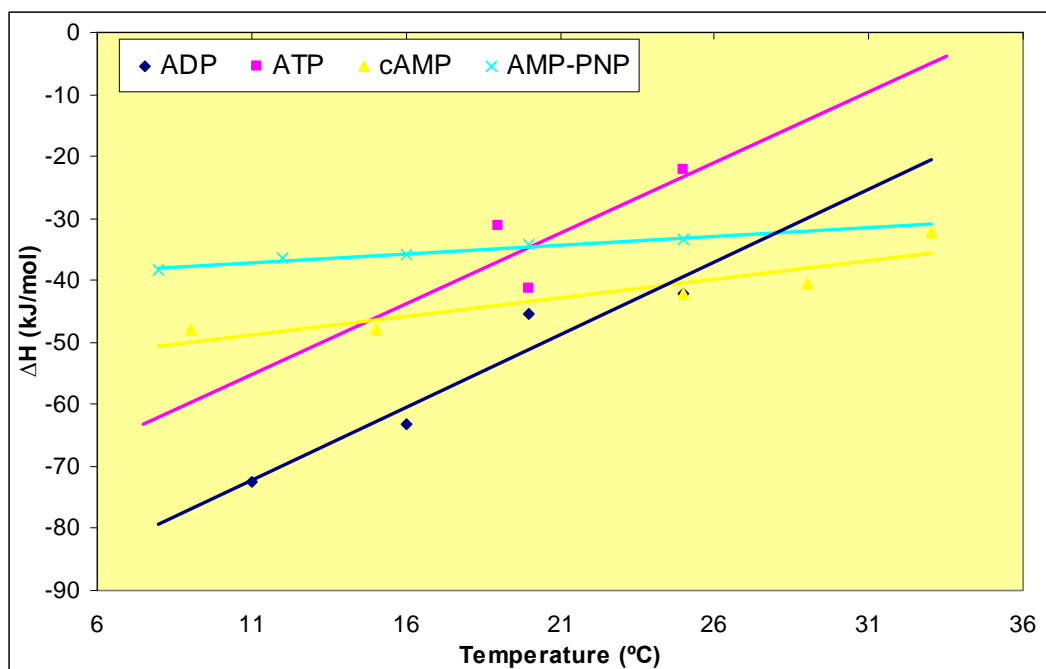


Figure 3.1.14 Temperature dependence of the enthalpy change upon binding of ADP, ATP, AMP-PNP and cAMP binding to N-Hsp90 at pH 8.00. The data are summarized in Table 3.1.1, 3.1.2, 3.1.3 and 3.1.4. The continuous line is the least squares fit of the data, while the slope of the linear regression yields the ΔC_p upon binding.

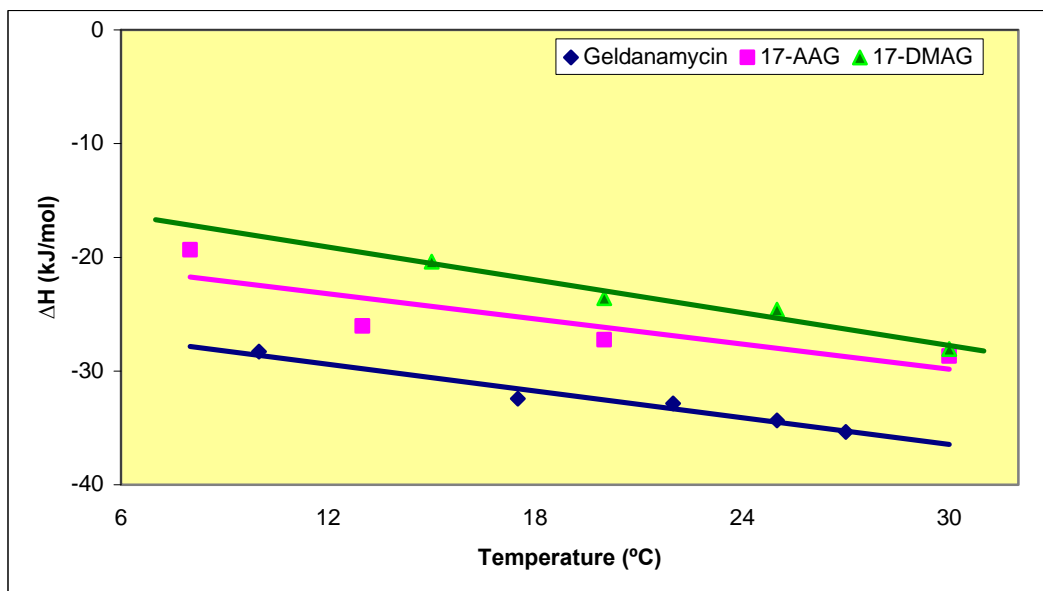


Figure 3.1.15 Temperature dependence of the enthalpy change upon binding of Geldanamycin, 17-AAG and 17-DMAG binding to N-Hsp90 at pH 8.00. The data are summarized in Table 3.1.6. The continuous line is the least squares fit of the data, while the slope of the linear regression yields the ΔC_p upon binding.

3.1.4 Conclusion: Understanding/Interpretation of Positive ΔC_p

The binding of adenosine-based ligands to N-Hsp90 is generally weak, typically $>9 \mu\text{M}$. The binding is mainly enthalpy driven and proceeds with a positive ΔC_p under the observed temperature conditions. The ansa-ring compounds bind more tightly (by approximately an order of magnitude) and with a favourable entropic contribution. However, the interactions exhibit a negative ΔC_p , as compared to the adenosine-based ligands.

In most characterised protein-ligand association reactions that display a ΔC_p , interactions occur with negative ΔC_p values and has been discussed extensively by Cooper, Freire, along with Spolar and Record (31; 120; 121). These negative ΔC_p values are often attributed to water reorganisation arising from a reduction in the accessible hydrophobic surface (as depicted in Figure 3.1.16) in areas accompanying complex formation (i.e., the hydrophobic effect). Usually these negative values of the standard ΔC_p denotes specific hydrophobic binding between protein and ligand in rigid body interactions (31; 42).

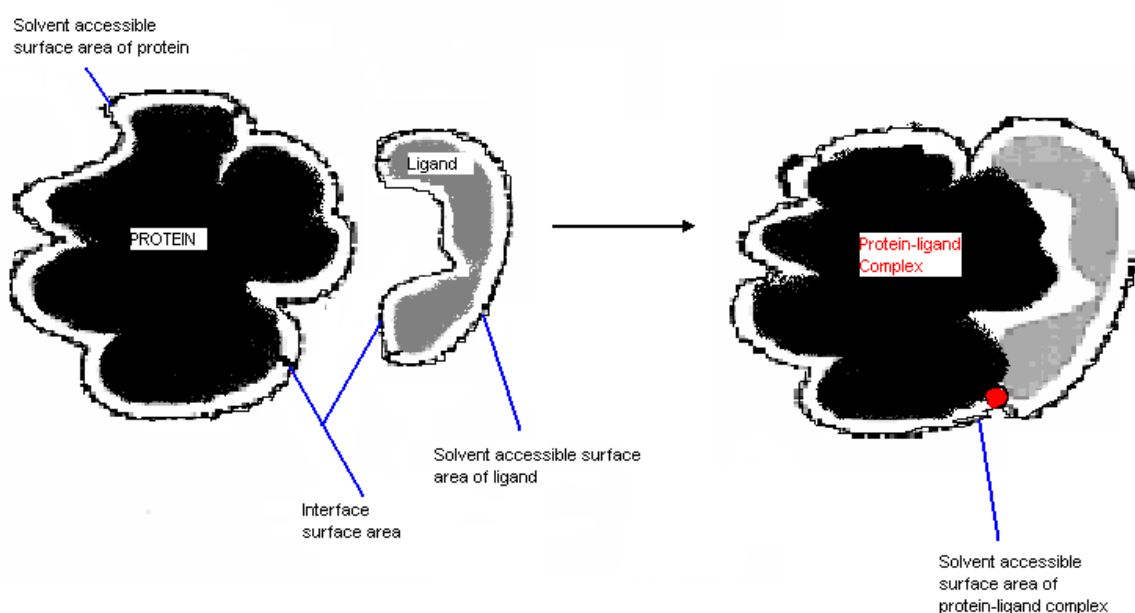


Figure 3.1.16 Figure showing reduction in solvent accessible surface area of protein-ligand complex upon ligand binding to protein.

As suggested above, the main negative contribution to ΔC_p comes from the hydrophobic effect, i.e. the removal of nonpolar surface from water upon complex formation. On the contrary, the reduction of the polar surface area gives a positive

contribution to ΔC_p , although to a lesser extent compared with the reduction in nonpolar surface area: 2.3 fold (Spolar, et al.(31)) or 1.7 fold (Murphy and Freire (30)) depending upon the proposed model. Other noticeable contributions are comprised of electrostatic interactions, changes in soft internal vibration modes and conformational changes (42).

Generally, unfolding of proteins results in a large positive ΔC_p of 6.5 to 13 $\text{kJ}\cdot\text{mol}^{-1}\cdot\text{K}^{-1}$, which is mainly attributed to the exposure of hydrophobic groups from the inside of the protein core to the aqueous environment (122). In contrast, most ligand binding processes result in a negative ΔC_p value of -0.35 to -1.7 $\text{kJ}\cdot\text{mol}^{-1}\cdot\text{K}^{-1}$ (122). However, the binding of ADP/ATP analogues shows a ΔC_p of between 0.28 to 2.28 $\text{kJ}\cdot\text{mol}^{-1}\cdot\text{K}^{-1}$, which is in the intermediate range of molecular association and protein unfolding.

To confirm causes of our unusual calorimetric results, it was decided conduct additional experiments and is described in detail in the next section.

3.2 Effect of Various Contributions To The ΔC_p

The heat capacity of the system, for any given interaction will have a number of events involving different components. The observed ΔC_p reports on the cumulative effect of these. The structural basis of the ΔC_p for macromolecular interactions is a matter for conjecture, however it can generally be correlated with gross changes in order of the system going from the free to the bound state. Thus, on complex formation the more commonly observed negative ΔC_p is thought to arise from the system moving to a state of greater order (120; 123). Intuitively, the simple process of formation of a complex between two molecules should produce greater order, however, concomitant contributions from the release of solvent molecules from, or sequestration of solvent molecules into the complex interface, changes in protonation, ion binding or solute conformational change can all affect the observed ΔC_p ($\Delta C_{p_{\text{obs}}}$) (124). By considering the potential contributions from these phenomena independently, we can assess which factor is likely to have an effect on producing the distinct differences in $\Delta C_{p_{\text{obs}}}$ for the ADP/ATP and geldanamycin-based compounds and is covered in this section.

3.2.1 Mapping Interfacial Water Molecules in the Protein-Ligand Binding Sites

Water molecules trapped at the interface of a protein-ligand complex can play a very important role in modulating ΔC_p (41; 125). Water molecules which form hydrogen bonds directly bridging between the protein and ligand, or are involved in a network of water molecules at an interface, reduce the value of the ΔC_p (125; 126) through a net reduction in rotational and vibrational modes (42). Shown in Figure 3.2.1 is the N-Hsp90-ADP binding site (left), which is highly hydrated compared with N-Hsp90-geldanamycin binding site (right). To obtain some information about the influence of water molecules on the interaction between the protein and the ligand, an analysis of the competition of the various (water, dry) probes with water molecules was performed.

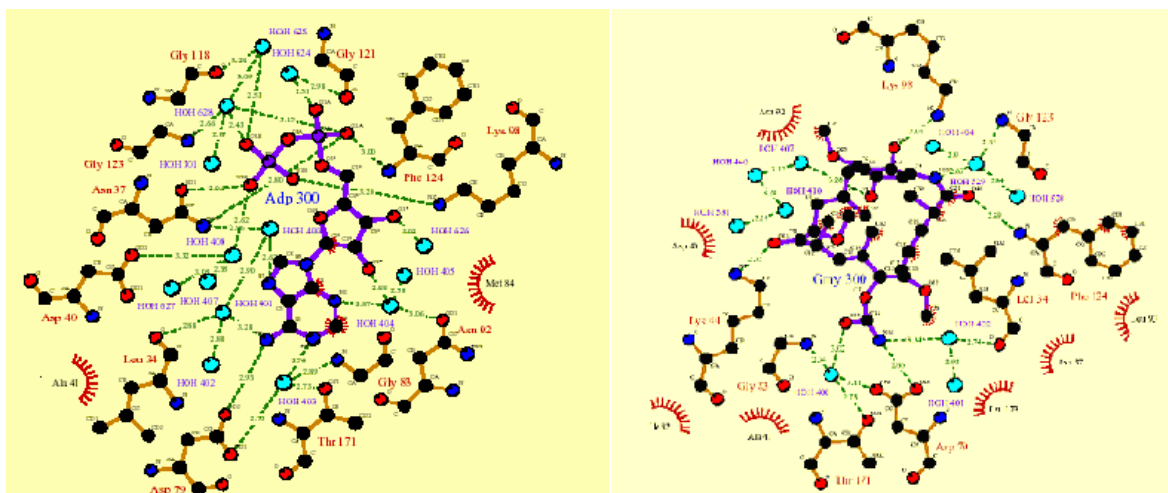


Figure 3.2.1 Schematic diagram of ADP (Left) and geldanamycin (Right) interacting with the N-Hsp90. (Figure generated with ligplot (57))

The GRID program (87; 88) was used to calculate the interactions between the GRID water probe and the N-Hsp90-ADP (1AM1) crystal structure (54). For N-Hsp90-geldanamycin, the 1A4H crystal structure was used (54). The LEAU option in the GRID program was kept equal to 3, which means that GRID would compute the interaction energy taking into account the competition between probe and water. When used in this mode, the program calculates at each grid point whether water or the probe itself had the stronger interaction with the protein. The separation of planes of GRID points was set to 0.2 Å (NPLA = 5); increasing NPLA gives better resolution of the GRID. An entropy factor was introduced by the program in the water calculation, to account for the

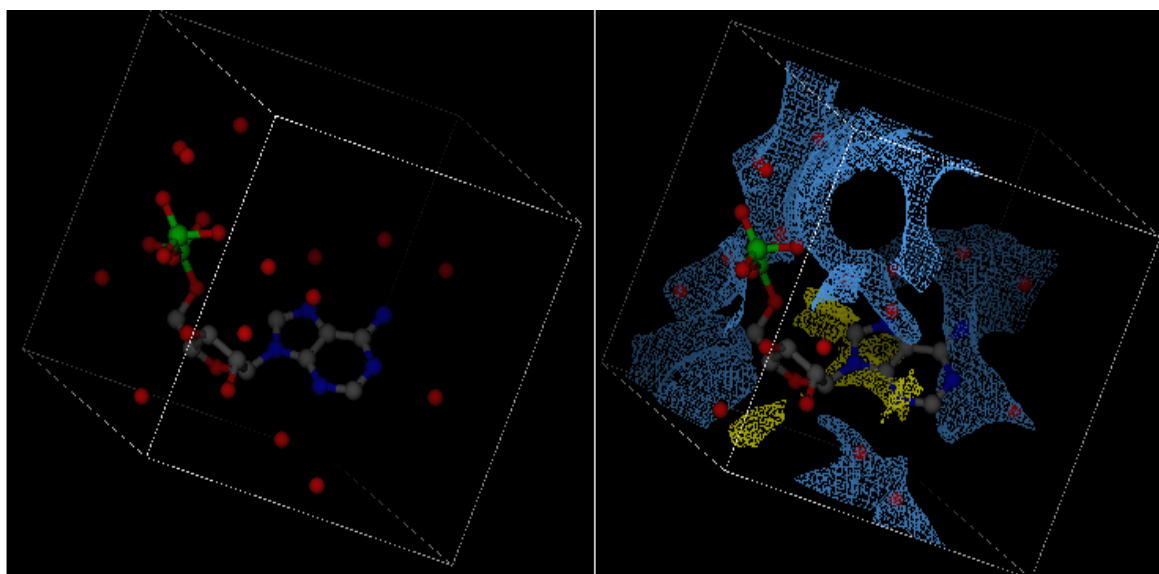


Figure 3.2.2 Left: Position of ADP in N-Hsp90-ADP binding site. Right Position of ADP in N-Hsp90-ADP binding site along with surrounding area depicted with the hydrophobic and hydrophilic energy surface derived from the program GRID. The contour maps marked as yellow correspond to most favourable hydrophobic position. (Contours derived at $-8.73 \text{ kJ}\cdot\text{mol}^{-1}$ on a scale of 0 to $-11.70 \text{ kJ}\cdot\text{mol}^{-1}$), while contour maps marked as blue correspond to most favourable hydrophilic position (Contours derived at $-20.09 \text{ kJ}\cdot\text{mol}^{-1}$ on a scale of 0 to $-67.29 \text{ kJ}\cdot\text{mol}^{-1}$). Red-water molecules. The hydrophilic contours fit very well with positions of water molecules experimentally found in N-Hsp90-ATP/ADP binding site. Water molecules are positioned in an energetically favourable position, where enthalpic contribution to binding is highest. (Figures generated with Gview (88))

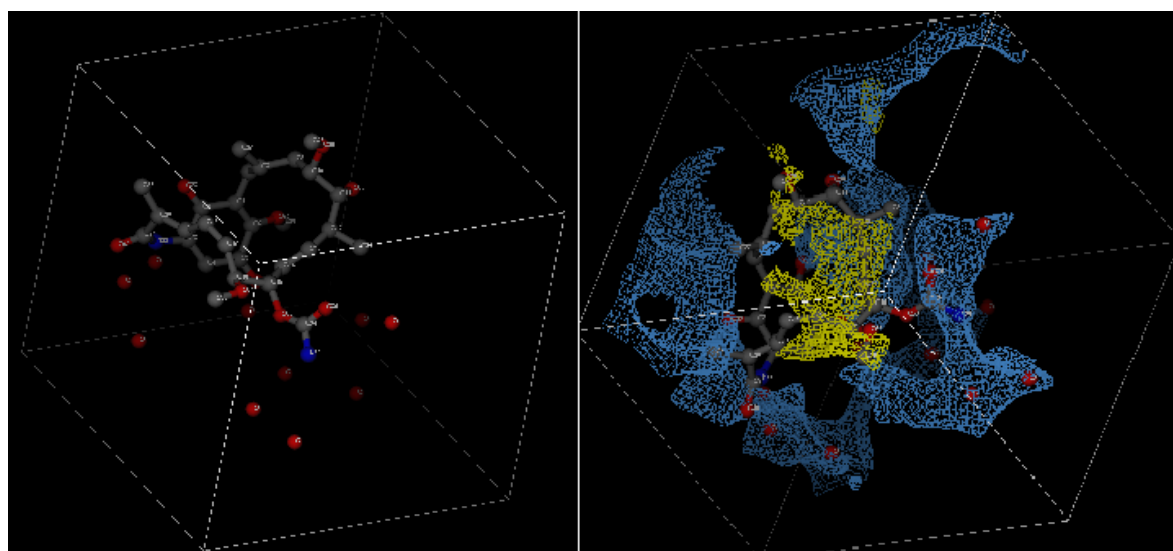


Figure 3.2.3 Left: Position of geldanamycin in N-Hsp90-Geldanamycin binding site. Right: Position of geldanamycin in N-Hsp90-Geldanamycin binding site along with surrounding area depicted with the hydrophobic and hydrophilic energy surface derived from the program GRID. The contour maps marked as yellow correspond to most favourable hydrophobic position. (Contours derived at $-2.09 \text{ kJ}\cdot\text{mol}^{-1}$ on a scale of 0 to $-11.36 \text{ kJ}\cdot\text{mol}^{-1}$), while contour maps marked as blue correspond to most favourable hydrophilic position (Contours derived at $-20.9 \text{ kJ}\cdot\text{mol}^{-1}$ on a scale of 0 to $-69.01 \text{ kJ}\cdot\text{mol}^{-1}$). Red-water molecules. The hydrophilic contours fit very well with positions of water molecules experimentally found in N-Hsp90-Geldanamycin binding site. Water molecules are positioned in an energetically favourable position, where enthalpic contribution to binding is highest. (Figures generated with Gview (88))

possible formation of an interaction between water and the protein. This water interaction energy was then used in the decision as to whether water made a stronger interaction than the probe at a specific grid point. The water molecules found in the crystal structure, which correspond to the position of the grid points where the water molecules had stronger interactions than the probes, were kept in the next GRID analysis.

The GRID fields with the probes DRY (LEAU = 0) were also computed for N-Hsp90-ADP (PDB: 1AM1) and N-Hsp90-geldanamycin (PDB: 1A4H), and the preselected water molecules were included in the calculation. MINIM calculations were performed for each probe field in order to identify the minima in the GRID interaction field.

All the computed GRID fields (WATER and DRY) were superimposed over one another with the help of the program GVIEW (87; 88). GRID maps were derived at $-20.09 \text{ kJ}\cdot\text{mol}^{-1}$ on a scale of 0 to $-67.29 \text{ kJ}\cdot\text{mol}^{-1}$ (Figure 3.2.2) for N-Hsp90-ADP and on a scale of 0 to $-69.01 \text{ kJ}\cdot\text{mol}^{-1}$ (Figure 3.2.3) for geldanamycin. Computed GRID fields for trapped water molecules for both Hsp90-ADP and Hsp90-geldanamycin show equivalent positions (favourable) for water molecules in the binding site. Interestingly geldanamycin with its hydrophobic character (limited to the inside of the geldanamycin molecule), shows that waters around it are not influenced by its hydrophobic character. According to Morton and Ladbury (41), these water molecules in the binding interface can modulate the ΔC_p to a more negative value than those computed from solvent accessible surface area calculations.

The results obtained show that the water molecules at the binding interface of N-Hsp90-Mg²⁺-ADP and Hsp90-geldanamycin are very similar in energetic profiles and the role of water molecules in N-Hsp90-Mg²⁺-ADP interaction can be ruled out in modulating ΔC_p to a more positive ΔC_p value.

3.2.2 Investigating The Effect of Mutations in Hsp90-ADP/ATP Binding Site on AMPPNP and 17-DMAG Binding

In order to analyze the energetic contribution of the water mediated interactions to the thermodynamic properties, including $\Delta C_{p,obs}$, site directed N-Hsp90 mutants were made that were designed to displace interfacial waters yet maintain hydrogen bonding capability. Mutations to glutamine were made of the conserved residues Asn37, which makes a hydrogen bond to a water molecule mediating an interaction with adenine N7, and Thr171, which binds to a water linking Gly83 and Asp79 and the adenine N1. Additionally N37H, N92Q and T171 (Figure 3.2.4) mutants were also generated in order to investigate rest of the water mediated hydrogen bonds in N-Hsp90-ADP/ATP interactions.

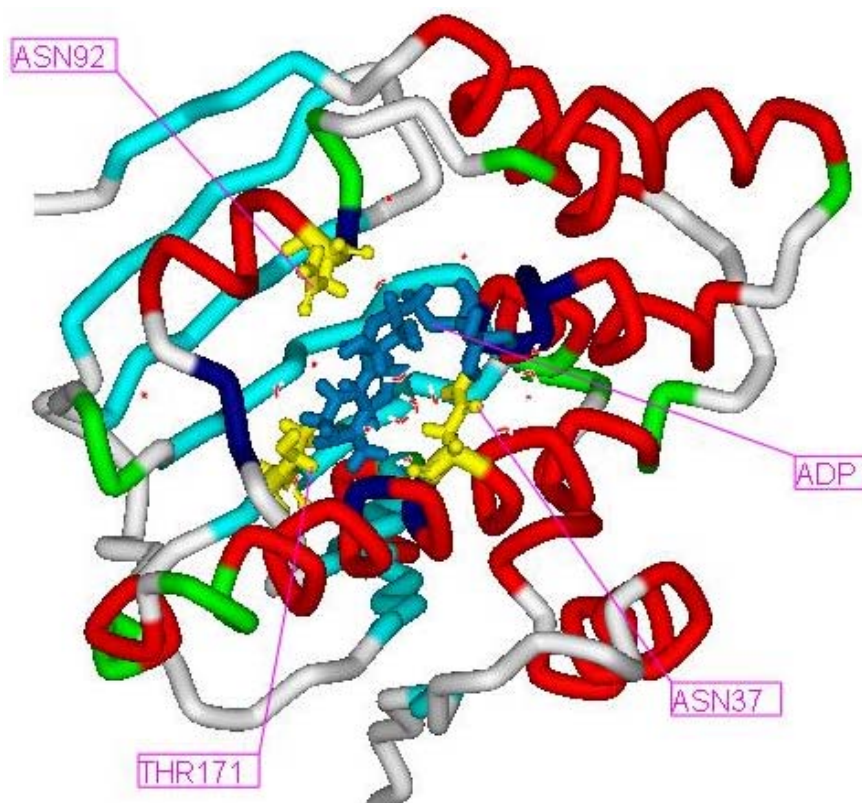


Figure 3.2.4 Crystal structure of N-Hsp90-ADP complex with residues selected for mutations labeled. (Figure generated using DS ViewerPro 5.0 (56))

Using CD, all the mutants and the wild-type construct were analyzed between 190 and 260 nm, which corresponds to the region in which the CD spectrum of a protein reflects its secondary structure content (127). The main observed spectral characteristic of the N-Hsp90 CD curve is the presence of two broad negative bands centred at 210 to 211

3. Results and Discussion

and 217 to 218 nm; according to Manavalan and Johnson (128), this characteristic spectrum is consistent with the backbone-folding pattern of a predominantly α -helix rich structure. The secondary structure content (Table 3.2.1) obtained from the deconvolution of the CD spectrum supports this proposal showing 36% α -helix content which matches well with 39 % shown by the crystal structure. Results of the deconvolution of the CD-spectra showed significant changes in secondary structure content for N37H and N37Q mutants, while T171Q was unaffected compared with wild type N-Hsp90 protein. However comparison of α -helical content for the mutants T171Q and N37H showed near identity with wild type N-Hsp90.

Protein	α -Helix (%)	β -Sheet (%)	Coil (%)
Wild Type N-Hsp90	0.36 (0.39)	0.26 (0.22)	0.37 (0.39)
N37H	0.33	0.16	0.51
N37Q	0.30	0.24	0.45
T171Q	0.37	0.20	0.42

Table 3.2.1 Secondary structure prediction of wild type and mutant N-Hsp90 as determined from CONTIN-CD. While values in bracket shows amount calculated from the X-ray crystal structure.

The result for AMPPNP and 17-DMAG binding to various N-Hsp90 mutants (Tables 3.2.2 and 3.2.3) showed undetectable binding in ITC experiments. A number of factors could be responsible for loss of binding in ADP/ATP and 17-DMAG binding to N-Hsp90 mutants. This includes loss of native structure and disruption to key molecular interactions within the binding pocket. If native structure is lost, the residues that make key molecular interactions are likely to be disrupted, affecting ligand binding. If the extent of the structural deformation is minimal then binding may occur, but proteins have extremely complex structures and have strict functional requirements, allowing minimal margin for flexibility.

3. Results and Discussion

Ligand	N-Hsp90 Variants	K_d (μM)	ΔH_{obs} ($\text{kJ}\cdot\text{mol}^{-1}$)	$T\Delta S_{\text{obs}}$ ($\text{kJ}\cdot\text{mol}^{-1}$)	ΔG_{obs} ($\text{kJ}\cdot\text{mol}^{-1}$)
AMPPNP	Wild type	46.04	-20.76	3.96	-24.72
	N37Q	No binding	NA	NA	NA
	N37H	No binding	NA	NA	NA
	N92Q	No binding	NA	NA	NA
	T171Q	No binding	NA	NA	NA

Table 3.2.2 Thermodynamic Parameters for the binding of AMPPNP with different mutants of N-Hsp90.

Ligand	N-Hsp90 Variants	K_d (μM)	ΔH_{obs} ($\text{kJ}\cdot\text{mol}^{-1}$)	$T\Delta S_{\text{obs}}$ ($\text{kJ}\cdot\text{mol}^{-1}$)	ΔG_{obs} ($\text{kJ}\cdot\text{mol}^{-1}$)
17-DMAG	Wild type	1.64	-23.24	9.73	-32.98
	N37Q	No binding	NA	NA	NA
	N37H	No binding	NA	NA	NA
	N92Q	No binding	NA	NA	NA
	T171Q	No binding	NA	NA	NA

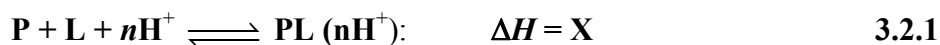
Table 3.2.3 Thermodynamic Parameters for the binding of 17-DMAG with various mutants of N-Hsp90.

Generated mutants were designed to dislodge water molecules from the active site, which indicates that water mediated interactions plays a key role in binding of ADP and geldanamycin analogues. There is also a chance that mutations might be providing a steric hindrance to water molecules present in the wild-type Hsp90-ADP/ATP binding site. Removing these water molecules deletes H-bonds formed in binding of ATP/ADP.

3.2.3 Effect of the Protonation/Deprotonation on the ΔH of AMPPNP Binding to N-Hsp90 and its Effect on Positive ΔC_p

In our studies of binding of N-Hsp90 to ADP/ATP, we were intrigued by the positive ΔC_p effect, which could be due to the protonation/deprotonation effects in N-Hsp90-AMPPNP interactions. Since the calorimetric measurements of a reaction system involving proton release/uptake takes place simultaneously and a sum of enthalpy changes occurring due to the reaction and the change in protonation state of the buffer components is measured.

The protein-ligand interactions can be expressed by the following scheme:



where P and L denote protein and ligand respectively, and n represents the number of protons taken up during the process of complex formation.

Therefore, the observed enthalpy of interaction may be expected to depend upon the enthalpy of ionization (proton uptake upon complex formation) or protonation (proton release upon complex formation) of the buffer.

Therefore in this study, we have decided to use two different buffers with different enthalpies of ionization to study this effect. The enthalpies of ionization of the buffer used were: Tris 47.44 kJ·mol⁻¹; TAPS 41.49 kJ·mol⁻¹ (129-131). Representative data for individual reactions with each buffer system at pH 8.00 are given in Figure 3.2.5, and a summary of the results obtained is given in Tables 3.1.3, 3.2.4 and 3.2.5. The observed enthalpy (ΔH_{obs}) can be corrected for the enthalpy of ionization of the buffer (ΔH_{ion}) in order to obtain the enthalpy of binding, (ΔH_{bind}) according to equation 3.2.2:

$$\Delta H_{\text{obs}} = \Delta H_{\text{bind}} + N_{\text{H}} \Delta H_{\text{ion}} \quad 3.2.2$$

where N_{H} represents the number of protons released by the protein and taken up by the buffer as a result of complex formation. The value of N_{H} depends on the difference between the pK_a of the ionisable group and the pH of the binding experiment.

Similarly, the observed value of ΔC_p can also be corrected for the effect of protonation of the buffer = $\Delta C_{p_{\text{ion}}}$, according to equation 3.2.3.

$$\Delta C_{p_{\text{obs}}} = \Delta C_{p_{\text{bind}}} + N_{\text{H}} \Delta C_{p_{\text{ion}}} \quad 3.2.3$$

where N_{H} represents the number of protons released by the protein and taken up by the buffer as a result of complex formation. $\Delta C_{p_{\text{bind}}}$ is the intrinsic ΔC_p .

3. Results and Discussion

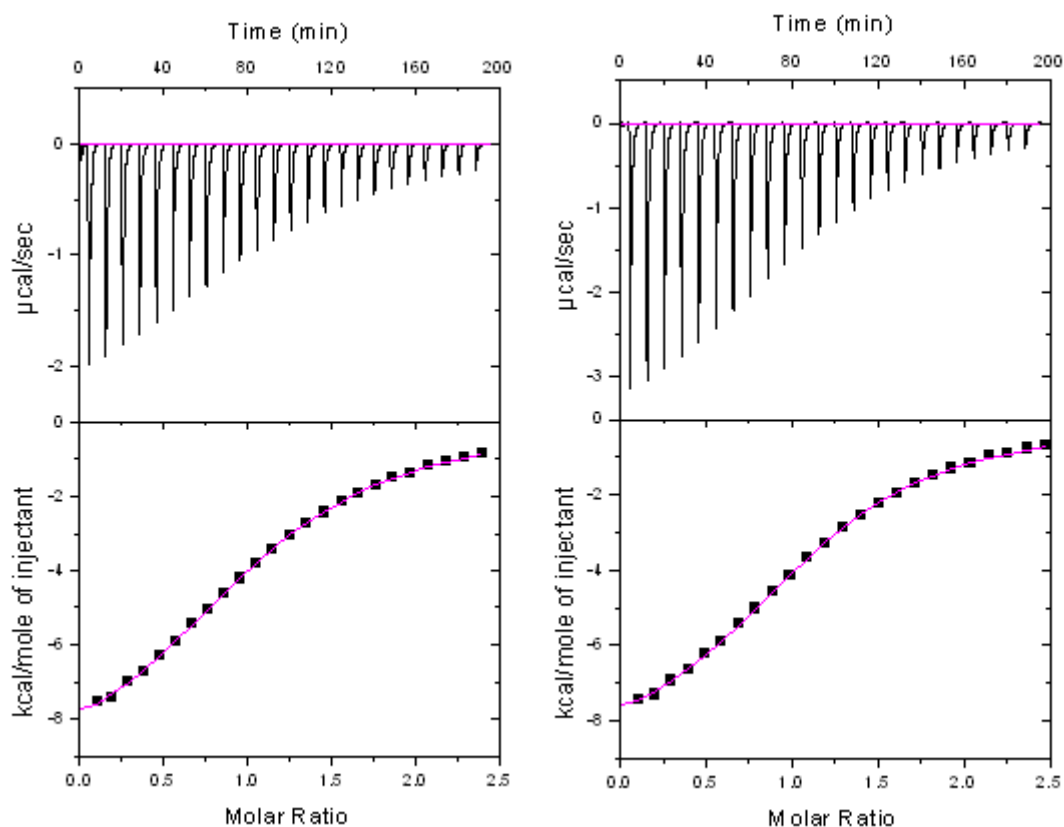


Figure 3.2.5 Binding isotherm for calorimetric titration of AMPPNP binding to N-Hsp90 in 20 mM Tris-base at pH 8.00 (Left) and similar experiment conducted in 20 mM Taps buffer at pH 8.00 (Right). (Experiments shown were carried out at 8 °C).

Buffer	AMPPNP (mM)	N-Hsp90 (μ M)	K_d (μ M)	ΔH (kJ·mol ⁻¹)	ΔC_p (kJ·mol ⁻¹ ·K ⁻¹)
Taps	1.321	0.104	80.7	- 29.95 \pm 4.40	0.59 \pm 0.14
Tris	2.116	0.186	129.6	- 33.39 \pm 1.07	0.28 \pm 0.03

Table 3.2.4 Thermodynamic data obtained from the titration of AMPPNP with N-Hsp90 at pH 8.00, 0.02 M ionic strength TRIS and TAPS buffer at 25 °C.

3. Results and Discussion

Ligand	Temp (°C)	Stoichiometry (n)	$K_b \times 10^4$ (M ⁻¹)	K_d ⁽²⁾ (μM)	ΔH_{obs} (kJ·mol ⁻¹)	$T\Delta S_{\text{obs}}$ (kJ·mol ⁻¹)	ΔG_{obs} (kJ·mol ⁻¹)	ΔC_p (kJ·mol ⁻¹ ·K ⁻¹)
AMPPNP	8	1.09 ± 0.00	2.88 ± 0.06	34.72	- 40.99 ± 0.34	- 17.00	-23.99	0.59 ± 0.14
	12	1.06 ± 0.00	2.21 ± 0.04	45.00	-39.60 ± 0.34	- 15.89	- 23.71	
	16	1.12 ± 0.01	1.76 ± 0.04	56.70	- 38.09 ± 0.53	- 14.60	-23.49	
	20	1.14 ± 0.01	1.23 ± 0.03	80.70	- 37.11 ± 0.63	- 14.17	- 22.94	
	25	1.22 ± 0.03	1.23 ± 0.11	80.70	- 29.95 ± 1.40	- 6.61	- 23.34	

Table 3.2.5 Summary of the thermodynamic parameters for the binding interaction of N-Hsp90 with AMPPNP in 20 mM Taps buffer function of temperature (pH 8.00).

¹Data was fitted to a one-set-of-sites model.

²Dissociation constant values (K_d) were calculated as the reciprocal of the observed equilibrium binding constant ($K_d = 1 / K_{\text{obs}}$).

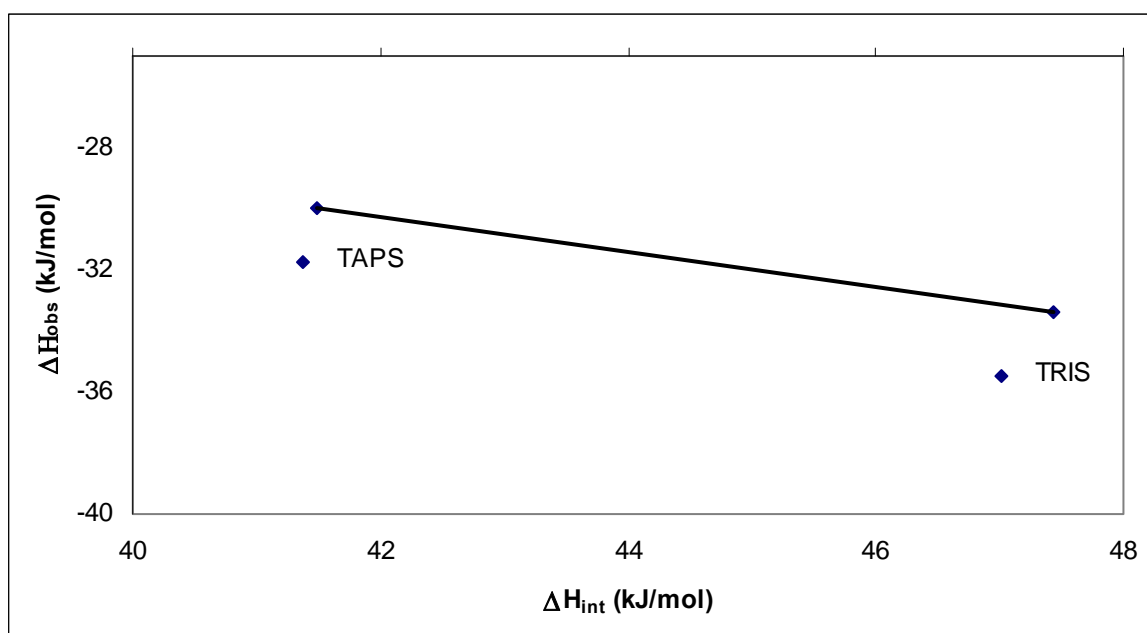


Figure 3.2.6 Proton linkage for AMPPNP binding to N-Hsp90 at pH 8.00 and 25 °C. The observed enthalpy of binding is plotted versus the enthalpy of ionization of the buffer. Buffers used for each value of ΔH_{buffer} are labelled. (Ionisation enthalpies of TRIS and TAPS are taken as 47.44 and 41.49 $\text{kJ}\cdot\text{mol}^{-1}$).

According to proton linkage theory (132), binding titrations should display a linear relationship between ΔH_{obs} and ΔH_{ion} . The slope of this line reflects the degree of protonation of the ligand (N_{H}), while the y -intercept represents the buffer corrected enthalpy of binding (ΔH_{bind}), (equation 3.2.2). From the slope of the line (Figure 3.2.6), the value of N_{H} was deduced to be -0.57 (protons released by the protein-ligand complex, per mole of site filled). The intercept (at buffer $\Delta H_{\text{H}} = 0$) is the intrinsic $\Delta H_{\text{bind}} = -7.9 \text{ kJ}\cdot\text{mol}^{-1}$ for the ligand binding reaction at pH 8.00, corrected for the identity of the buffer (assuming that buffer only contributes via this heat of proton dissociation effect).

This intrinsic ΔH_{bind} may itself depend upon pH, due to contributions from heats of protonation of protein or small molecule functional groups. Additionally, the value of Δn is likely to be lower and more positive at pH 7.50 and below, where the ΔG versus pH profile is flat: it can also be expected that N_{H} will be more negative at pH 8.50 and above. The expected magnitude for the proton transfer correction, the apparent ΔH for the AMPPNP binding to N-Hsp90 will be equal to the sum of the intrinsic ΔH of binding plus a contribution of $\Delta n \times \Delta H_{\text{ion}}$. At pH 8.00 with TRIS buffer, the magnitude of the term for proton transfer from buffer will be around $-27.04 \text{ kJ}\cdot\text{mol}^{-1}$, resulting in the actual intrinsic ΔH_{bind} of $-6.35 \text{ kJ}\cdot\text{mol}^{-1}$. Whereas for TAPS buffer, the correction will be $-71.36 \text{ kJ}\cdot\text{mol}^{-1}$; giving a matching intrinsic ΔH_{bind} of $-6.30 \text{ kJ}\cdot\text{mol}^{-1}$.

3. Results and Discussion

The ΔS values are listed in Table 3.1.3 and 3.2.5. They are large and negative at 8 °C and change to less negative values as temperature is increased in both the buffers.

For TAPS buffer between 5 and 45 °C, the value of $\Delta C_{p_{ion}}$ extrapolated to zero ionic strength is $0.023 \text{ kJ}\cdot\text{mol}^{-1}\cdot\text{K}^{-1}$ (129). Using this value and the determined value of $N_H\Delta C_{p_{bind}}$ is found to be $0.57 \text{ kJ}\cdot\text{mol}^{-1}\cdot\text{K}^{-1}$, which is not very different than $\Delta C_{p_{obs}}$ of $0.59 \text{ kJ}\cdot\text{mol}^{-1}\cdot\text{K}^{-1}$. In TRIS buffer, the value of $\Delta C_{p_{ion}}$ is around $-0.033 \text{ kJ}\cdot\text{mol}^{-1}\cdot\text{K}^{-1}$ (129), which results in a $\Delta C_{p_{bind}}$ of $0.30 \text{ kJ}\cdot\text{mol}^{-1}\cdot\text{K}^{-1}$. The intrinsic $\Delta C_{p_{bind}}$, at pH 8.00 (buffer $\Delta C_{p_H} = 0$) will be $0.47 \text{ kJ}\cdot\text{mol}^{-1}\cdot\text{K}^{-1}$.

An interesting feature of AMPPNP binding to N-Hsp90 is that binding proceeds with positive ΔC_p , even in different buffer systems.

3.2.4 Dissection of the pH Dependence of AMPPNP Binding Energetics to N-Hsp90

ΔG has been examined particularly frequently in characterizing the perturbations of protein groups produced by folding of a polypeptide chain or by interaction of a protein with ligands. However due to enthalpy-entropy compensation (10; 123; 133), ΔG is often less sensitive than the ΔH in the chemistry of a system. Also, it is of interest with regards to the experiments described here that several studies of the pH dependence of protein ligand interactions (4; 132; 134) have shown that compensation between large enthalpy and entropy changes results in relatively pH-invariant ΔG . However the effect of pH on positive ΔC_p in protein-ligand interaction has not been examined or observed previously and therefore in this section we decided to investigate the effect of pH on positive ΔC_p in N-Hsp90-ADP/ATP interactions. Generally protein-small molecule interactions show significant degrees of pH dependence, reflecting the binding of the small molecule and protons (proton linkage). This linkage is quantitated as a change in the small molecule binding constant with pH or as a change in the proton affinity (i.e. pK_a) of an ionisable group in the protein upon small molecule binding.

In this section, we carried out ITC measurements of the binding of AMPPNP to N-Hsp90 over a pH range of 5.00 to 10.00. Triple buffer (100 mM ACES, 50 mM Tris, 50 mM Ethanolamine) described by Good et al. (130) was used throughout the study, giving an excellent buffering capacity over the required pH range. The pH range was limited to pH 5.00 at the lower end due to the buffering capacity of triple buffer used in the measurements. The binding of AMPPNP was not extended to higher than pH 10.00, since weaker binding requires higher stock concentration of the protein.

Secondly, a prerequisite for a precise calorimetric determination of the binding enthalpy is a good signal to noise ratio and therefore, certain minimum sample concentrations would be required. In our case, N-Hsp90 solutions in the range from 100 to 150 μM resulted in a titration curve which allowed us to determine the binding enthalpy and binding constant with high accuracy. Figure 3.2.7 shows the binding enthalpy as a function of pH at 8 °C. Calorimetric measurements of ΔH_{obs} and K_a of the N-Hsp90-AMPPNP interaction at 25 °C resulted in ΔH_{obs} of $-32.64 \pm 1.59 \text{ kJ}\cdot\text{mol}^{-1}$ and a K_a of $(0.91 \pm 0.06) \times 10^{-4} \text{ M}^{-1}$ (pH 8.00). For all titrations, the calculated stoichiometry of binding was between 1.00 and 1.21, indicating a 1:1 binding.

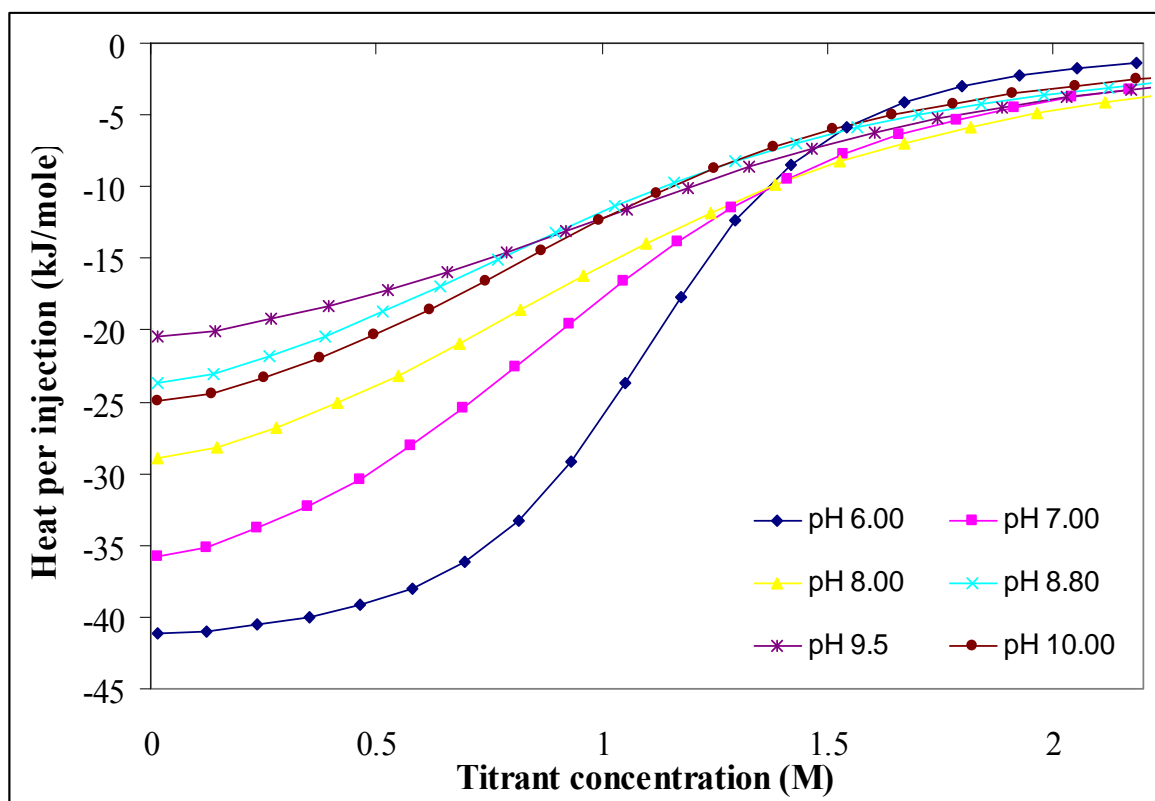


Figure 3.2.7 Uncorrected ITC data of AMPPNP binding with N-Hsp90 performed at six different pH values at 8 °C in Triple buffer. The AMPPNP solution was injected into the reaction cell containing protein solution. The heat evolved in $\text{kJ}\cdot\text{mol}^{-1}$, is shown as a function of titrant concentration for successive injection of ligand.

In order to evaluate the ΔC_p of binding, the temperature dependence of the binding enthalpy was also investigated. Binding experiments were performed at three to five different temperatures from 8 to 25 °C, under the same pH and buffer conditions. Observed ΔG , ΔS , ΔH and ΔC_p values determined at different pH are given in Tables 3.2.6, 3.2.7, 3.2.8, 3.2.9, 3.2.10, 3.2.11, 3.2.12, 3.2.13 and are derived by fitting a single site binding model. All the titrations in the experimental pH range were well described by the single site binding model (i.e. the binding isotherm were hyperbolic, with no indication of cooperative or non-cooperative binding). However many of the calorimetric titrations at and above 25 °C showed incorrect energetics, due to the temperature and pH dependent protein stability issues. These erratic titrations obtained have not been used in calculations or included in the ΔC_p tables.

3.2.4.1 AMPPNP Binding to N-Hsp90: pH Dependency of ΔH_{obs} and $\Delta G_{\text{obs}}/K_b$

As expected, the observed ΔH varies with pH. At 8 °C and as pH changes, the observed ΔH varies significantly (Table 3.2.6), indicating a linkage between the heat of protonation of the ligand and deprotonation of buffer. At pH 5.00, AMPPNP is fully protonated (no release/uptake occurs upon binding); the observed value is the intrinsic enthalpy, $-57.93 \text{ kJ}\cdot\text{mol}^{-1}$. (Discussed in detail in Section 3.2.3)

Table 3.2.6 gives values of $\log Ka$ and ΔG_{obs} measured for binding of AMPPNP to N-Hsp90. Table 3.2.6 also gives values for $T\Delta S_{\text{obs}}$, ΔH_{obs} at 8 °C, along with $\Delta C_{\text{p}_{\text{obs}}}$. Values for $\log Ka$ were determined calorimetrically. Figure 3.2.7 gives the ΔH_{obs} of binding of AMPPNP to N-Hsp90 as a function of pH. Binding of AMPPNP is significantly higher at pH 5.00. The binding reaction is exothermic and ΔH_{obs} is nearly constant within a pH range of 7.00 to 10.00. However, these values at any pH range are not corrected for protonic equilibria. This figure further suggests that the ionizing system may deviate from ideal behaviour between experimental pH of 8.70 to 10.00 and pH 5.00 to 6.00 suggesting that a group ionizing in this range may be perturbed by ligand binding. However, during evaluation of these trends, it should be noted that the differences are nearly all within the maximum error of the experiments.

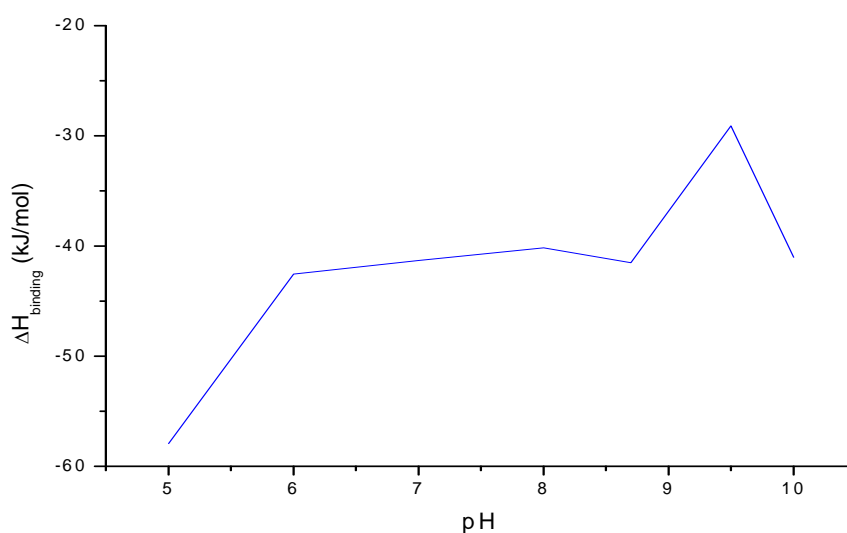


Figure 3.2.8 pH Dependence of ΔH_{obs} for the binding of AMPPNP to N-Hsp90 at 25 °C and in 100 mM ACES, 50 mM Ethanolamine and 50 mM Tris buffer.

3. Results and Discussion

pH	Log K_a	ΔH_{obs} (kJ·mol ⁻¹)	$T\Delta S_{\text{obs}}$ (kJ·mol ⁻¹)	ΔG_{obs} (kJ·mol ⁻¹)	ΔC_p (kJ·mol ⁻¹ ·K ⁻¹)
5.0	5.37	-57.93 ± 0.28	-29.01	-28.92	0.09 ± 0.10
6.0	4.97	-42.55 ± 0.20	-15.80	-26.75	0.00 ± 0.03
7.0	4.59	-41.30 ± 0.24	-16.57	-24.73	0.18 ± 0.06
8.0	4.37	-40.16 ± 0.26	-16.64	-23.52	0.37 ± 0.22
8.7	4.14	-41.51 ± 0.57	-19.22	-22.29	0.57 ± 0.21
9.5	4.27	-29.10 ± 0.60	-6.08	-23.02	0.18 ± 0.31
10.0	3.94	-41.01 ± 0.46	-19.76	-21.25	0.28 ± 0.15

Table 3.2.6 Summary of comparative thermodynamic parameters for the binding interaction of AMPPNP to N-Hsp90 between pH 5.00-10.00 and at 8 °C in 100 mM ACES, 50 mM Tris, 50 mM Ethanolamine buffer.

The AMPPNP binding interface of Hsp90 is similar to the ADP/ATP interface. Inspection of the ADP/ATP bound structures and from the structural information available (52; 54), allowed two ionizable groups at the active site that could cause a pK_a shift to be identified: two aspartic acid residues Asp79 and Asp40. These two aspartates situated in the ADP/ATP binding site of N-Hsp90 interact with the inhibitor by forming H-bonds. However between these two aspartates, Asp79 interacts with a specific and direct hydrogen bond with the purine ring of ADP/ATP, whilst Asp40 engages in a non-specific water-mediated hydrogen bond with the phosphate side-chain of ADP/ATP. The apparent pK_a value of less than 6, found in the ΔH -pH profile for AMPPNP (Figure 3.2.8.) likely reflects the protonation of one of these aspartate residues, along with AMPPNP (pK_a around 7.0). However the correct pK_a value is difficult to predict as the data from the ΔH -pH profile is difficult to fit with an appropriate global nonlinear least squares analysis algorithm, due to insufficient points available below pH 6.00.

3. Results and Discussion

Ligand	Temp (°C)	Stoichiometry (n)	$K_b \times 10^4$ (M ⁻¹)	$K_d^{(2)}$ (μM)	ΔH_{obs} (kJ·mol ⁻¹)	$T\Delta S_{\text{obs}}$ (kJ·mol ⁻¹)	ΔG_{obs} (kJ·mol ⁻¹)	ΔC_p (kJ·mol ⁻¹ ·K ⁻¹)
AMPPNP	8	1.00 ± 0.00	23.47 ± 1.11	4.26	-57.93 ± 0.28	-29.01	-28.92	0.09 ± 0.10
	12	1.02 ± 0.00	22.65 ± 0.96	4.45	-56.84 ± 0.25	-27.61	-29.22	
	16	1.02 ± 0.00	11.88 ± 0.55	8.41	-58.14 ± 0.36	-30.06	-27.48	
	20	1.01 ± 0.00	7.89 ± 0.38	12.67	-56.26 ± 0.45	-28.79	-27.47	

Table 3.2.7 Summary of the thermodynamic parameters for the binding interaction of N-Hsp90-AMPPNP in 100 mM ACES, 50 mM Tris, 50 mM Ethanolamine (Triple buffer) and 5 mM MgCl₂ as a function of temperature (pH 5.00).

Ligand	Temp (°C)	Stoichiometry (n)	$K_b \times 10^4$ (M ⁻¹)	$K_d^{(2)}$ (μM)	ΔH_{obs} (kJ·mol ⁻¹)	$T\Delta S_{\text{obs}}$ (kJ·mol ⁻¹)	ΔG_{obs} (kJ·mol ⁻¹)	ΔC_p (kJ·mol ⁻¹ ·K ⁻¹)
AMPPNP	8	1.09 ± 0.00	9.45 ± 0.36	10.57	-42.55 ± 0.20	-15.80	-26.75	0.00 ± 0.03
	12	1.07 ± 0.00	8.12 ± 0.34	12.30	-42.09 ± 0.22	-15.29	-26.80	
	16	1.05 ± 0.00	6.42 ± 0.28	15.57	-42.46 ± 0.26	-15.88	-26.58	
	20	1.15 ± 0.00	2.75 ± 0.70	36.32	-42.46 ± 0.24	-17.57	-24.89	

Table 3.2.8 Summary of the thermodynamic parameters for the binding interaction of N-Hsp90-AMPPNP in 100 mM ACES, 50 mM Tris, 50 mM Ethanolamine (Triple buffer) and 5 mM MgCl₂ as a function of temperature (pH 6.00).

3. Results and Discussion

Ligand	Temp (°C)	Stoichiometry (n)	$K_b \times 10^4$ (M ⁻¹)	$K_d^{(2)}$ (μM)	ΔH_{obs} (kJ·mol ⁻¹)	$T\Delta S_{\text{obs}}$ (kJ·mol ⁻¹)	ΔG_{obs} (kJ·mol ⁻¹)	ΔC_p (kJ·mol ⁻¹ ·K ⁻¹)
AMPPNP	8	1.01 ± 0.00	3.96 ± 0.90	25.20	-41.30 ± 0.24	-16.57	-24.73	0.18 ± 0.06
	12	1.01 ± 0.00	2.91 ± 0.57	34.32	-41.05 ± 0.24	-16.70	-24.35	
	16	1.02 ± 0.00	2.42 ± 0.79	41.18	-39.85 ± 0.44	-15.59	-24.46	

Table 3.2.9 Summary of the thermodynamic parameters for the binding interaction of N-Hsp90-AMPPNP in 100 mM ACES, 50 mM Tris, 50 mM Ethanolamine (Triple buffer) and 5 mM MgCl₂ as a function of temperature (pH 7.00).

Ligand	Temp (°C)	Stoichiometry (n)	$K_b \times 10^4$ (M ⁻¹)	$K_d^{(2)}$ (μM)	ΔH_{obs} (kJ·mol ⁻¹)	$T\Delta S_{\text{obs}}$ (kJ·mol ⁻¹)	ΔG_{obs} (kJ·mol ⁻¹)	ΔC_p (kJ·mol ⁻¹ ·K ⁻¹)
AMPPNP	8	1.13 ± 0.00	2.35 ± 0.40	42.48	-40.16 ± 0.26	-16.64	-23.52	0.37 ± 0.22
	16	1.13 ± 0.00	1.30 ± 0.22	76.62	-38.79 ± 0.37	-16.03	-22.76	
	20	1.10 ± 0.01	0.95 ± 0.25	104.63	-39.73 ± 0.74	-17.41	-22.32	
	25	1.11 ± 0.03	0.91 ± 0.06	109.09	-32.64 ± 1.59	-9.72	-22.92	

Table 3.2.10 Summary of the thermodynamic parameters for the binding interaction of N-Hsp90-AMPPNP in 100 mM ACES, 50 mM Tris, 50 mM Ethanolamine (Triple buffer) and 5 mM MgCl₂ as a function of temperature (pH 8.00).

3. Results and Discussion

Ligand	Temp (°C)	Stoichiometry (n)	$K_b \times 10^4$ (M ⁻¹)	$K_d^{(2)}$ (μM)	ΔH_{obs} (kJ·mol ⁻¹)	$T\Delta S_{\text{obs}}$ (kJ·mol ⁻¹)	ΔG_{obs} (kJ·mol ⁻¹)	ΔC_p (kJ·mol ⁻¹ ·K ⁻¹)
AMPPNP	8	1.12 ± 0.00	1.39 ± 0.38	71.94	-41.51 ± 0.57	- 19.22	- 22.29	0.57 ± 0.21
	12	1.09 ± 0.02	1.11 ± 0.53	90.09	-38.96 ± 1.12	-16.89	- 22.07	
	20	1.14 ± 0.02	0.83 ± 0.04	119.31	-38.30 ± 1.29	-16.82	- 21.48	
	25	1.18 ± 0.03	0.59 ± 0.23	169.26	-30.00 ± 1.13	-8.49	- 21.50	

Table 3.2.11 Summary of the thermodynamic parameters for the binding interaction of N-Hsp90-AMPPNP in 100 mM ACES, 50 mM Tris, 50 mM Ethanolamine (Triple buffer) and 5 mM MgCl₂ as a function of temperature (pH 8.70).

Ligand	Temp (°C)	Stoichiometry (n)	$K_b \times 10^4$ (M ⁻¹)	$K_d^{(2)}$ (μM)	ΔH_{obs} (kJ·mol ⁻¹)	$T\Delta S_{\text{obs}}$ (kJ·mol ⁻¹)	ΔG_{obs} (kJ·mol ⁻¹)	ΔC_p (kJ·mol ⁻¹ ·K ⁻¹)
AMPPNP	8	1.33 ± 0.01	1.89 ± 0.11	143.63	-29.10 ± 0.60	- 6.08	- 23.02	0.18 ± 0.31
	12	1.08 ± 0.02	2.29 ± 0.25	43.63	-22.84 ± 0.76	0.93	- 23.77	
	25	1.03 ± 0.02	0.76 ± 0.05	172.44	-24.23 ± 1.00	- 2.10	- 22.13	

Table 3.2.12 Summary of the thermodynamic parameters for the binding interaction of N-Hsp90-AMPPNP in 100 mM ACES, 50 mM Tris, 50 mM Ethanolamine (Triple buffer) and 5 mM MgCl₂ as a function of temperature (pH 9.50).

3. Results and Discussion

Ligand	Temp (°C)	Stoichiometry (n)	$K_b \times 10^4$ (M ⁻¹)	K_d ⁽²⁾ (μM)	ΔH_{obs} (kJ·mol ⁻¹)	$T\Delta S_{\text{obs}}$ (kJ·mol ⁻¹)	ΔG_{obs} (kJ·mol ⁻¹)	ΔC_p (kJ·mol ⁻¹ ·K ⁻¹)
AMPPNP	8	1.14 ± 0.00	0.88 ± 0.01	113.01	-41.01 ± 0.46	-19.76	- 21.25	0.28 ± 0.15
	12	1.13 ± 0.00	0.79 ± 0.01	126.39	-36.34 ± 0.21	- 15.06	- 21.28	
	20	1.21 ± 0.01	0.41 ± 0.09	243.24	- 35.16 ± 0.52	-14.85	- 20.31	
	25	1.09 ± 0.03	0.28 ± 0.01	347.22	- 35.58 ± 1.64	-15.84	- 19.74	

Table 3.2.13 Summary of the thermodynamic parameters for the binding interaction of N-Hsp90-AMPPNP in 100 mM ACES, 50 mM Tris, 50 mM Ethanolamine (Triple buffer) and 5 mM MgCl₂ as a function of temperature (pH 10.00).

¹ Data was fitted to a one-set-of-sites model.

² Dissociation constant values (K_d) were calculated as the reciprocal of the observed equilibrium binding constant ($K_d = 1 / K_{\text{obs}}$).

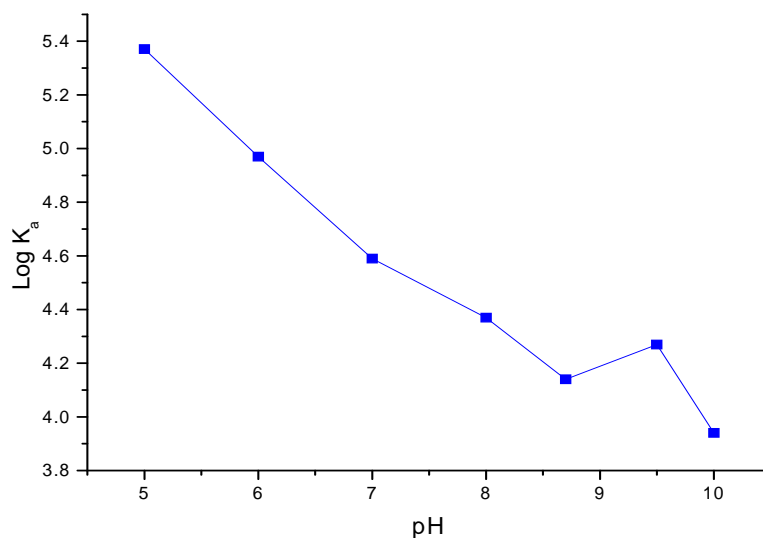


Figure 3.2.9 The pH dependence of the logarithm of the association constant of AMPPNP to N-Hsp90 at 8 °C and in 100 mM ACES, 50 mM Tris, 50 mM Ethanolamine (Triple buffer). The association or binding constant is maximal at pH 5.00. At this pH values, the affinity is close to $23.47 \pm 1.11 \text{ M}^{-1}$ ($K_d = 4.26 \text{ }\mu\text{M}$).

A separate calorimetric study (Section 3.2.3) showed that 0.57 protons were released from the complex upon binding of AMPPNP at pH 8.00. Since a proton is released, one of the aspartates or AMPPNP must have become ionized upon inhibitor binding. During complex formation, two aspartates (Asp40, Asp79) of N-Hsp90 are involved, however only one of the aspartates (Asp40) retains its solvent accessibility along with AMPPNP and could have released this proton.

The increase in pH of the solution induces a decrease in the K_b from around 23.47×10^4 at pH 5.00 to 0.88×10^4 at pH 10.00 (25 °C) (Figure 3.2.9). Furthermore at pH 8.00, the apparent enthalpy of binding strongly depends on the ionization enthalpy of the buffer in which the reaction takes place and amounts to $31.97 \text{ kJ}\cdot\text{mol}^{-1}$ when the buffer is Triple buffer (ΔH_{ion} value taken for Tris buffer pH=8.00, as at pH 8.00 Tris is the main buffering agent in triple buffer). This decrease in the observed K_b (Figure 3.2.9) upon increasing pH is a clear indication that the binding of AMPPNP is coupled to the binding of protons to the N-Hsp90.

3.2.4.2 AMPPNP Binding to N-Hsp90: pH Dependency of $\Delta C_{p_{obs}}$

According to Makhatadze and Privalov along with Nguyen et al. (32; 135), the $\Delta C_{p_{obs}}$ can be described as a collective contribution of several factors, and can be represented by equation 3.2.4 partially modified with added polar surface area and protonation/deprotonation terms added.

$$\Delta C_{p_{obs}} = \Delta C_{p_{sasa}} + \Delta C_{p_v} + \Delta C_{p_{nc}} + \Delta C_{p_p} + \Delta C_{p_{dp}} + \Delta C_{p_{ot}} \quad 3.2.4$$

where $\Delta C_{p_{sasa}}$ describes the hydrophobic effects associated with the burial of polar and nonpolar surface and can be evaluated from calculating solvent accessible surface area change ($\Delta SASA$). The terms ΔC_{p_v} and $\Delta C_{p_{nc}}$ describes the ΔC_p arising from internal vibrations/stretching of covalent bonds and vibrations of non-covalent interactions respectively. The term ΔC_{p_p} is from protonation of ligand, and $\Delta C_{p_{dp}}$ is from deprotonation of the buffer component.

The ΔC_p , that arises from the secondary structure effect, $\Delta C_{p_{nc}}$, is small and estimated at $-0.0087 \times (\Delta C_{p_{sasa}})$, (32) whereas the contribution from the deprotonation of buffer, $\Delta C_{p_{dp}}$, is $N_H \cdot \Delta C_{p_{ion}}$. Where N_H is the number of protons taken per mol of complex, and $\Delta C_{p_{ion}}$ is the ΔC_p of buffer deprotonation. The last term $\Delta C_{p_{ot}}$ is from other factors such as ion-pair, bound water and surface water.

The ΔC_p associated with the burial of nonpolar areas, $\Delta C_{p_{SASA}}$, was computed from the change in solvent accessible surface area ($\Delta SASA$) of the N-Hsp90/ADP complex, free N-Hsp90 and free ADP. More details on $\Delta SASA$ are given in Section 3.2.7. Results of the change in polar and nonpolar areas of the N-Hsp90 and its complex with the ADP using the water probe radii of 1.4 Å are summarized in Table 3.2.21 to 3.2.24, and an illustration of solvent-accessible surface area of the whole complex is shown in Figure 3.1.16.

The observed ΔC_p may be described as a collective contribution of several factors, as shown in equation 3.2.4. At 25 °C, the ΔC_p from the noncovalent interactions, $\Delta C_{p_{nc}}$, contributes around $-0.0002 \text{ kJ}\cdot\text{mol}^{-1}\cdot\text{K}^{-1}$ (30-32), which is very small and can be neglected. The ΔC_p from that of vibrating/stretching of covalent bonds is also presumably negligible ($\Delta C_{p_v} = 0$). At pH 5.00, the protonation upon binding is negligible and ΔC_{p_p} and $\Delta C_{p_{dp}}$ nearly approaches zero, as the free phosphate linker of AMPPNP will remain protonated. If we add these factors together, they contribute little to the observed intrinsic value of $0.09 \pm 0.10 \text{ kJ}\cdot\text{mol}^{-1}\cdot\text{K}^{-1}$ at pH 5.00. The ΔC_p from $\Delta SASA$ calculations (Table 3.2.21)

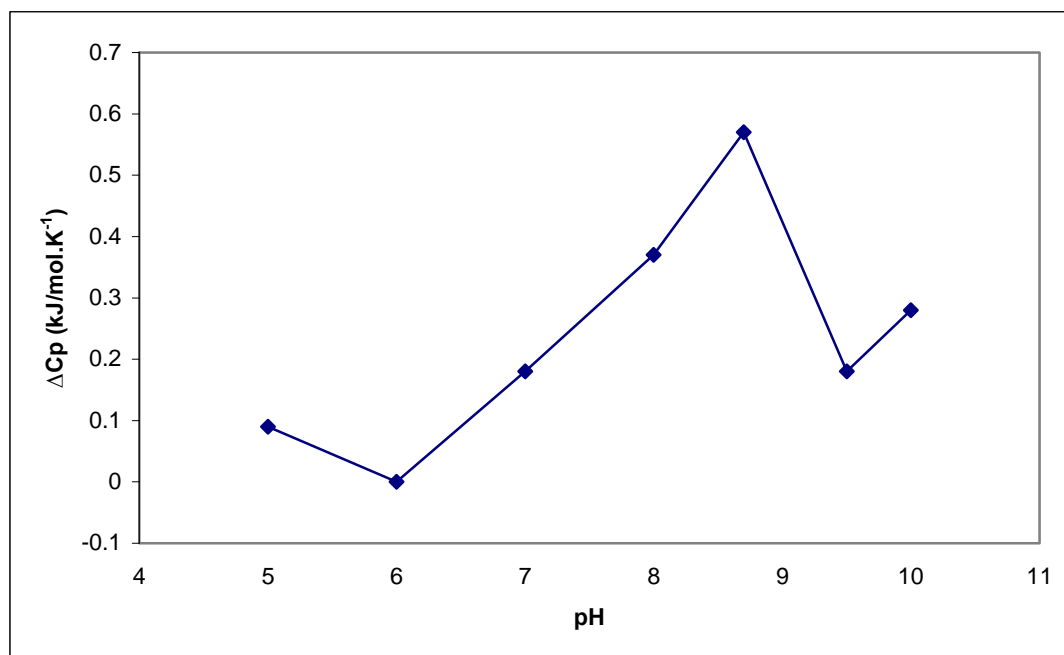


Figure 3.2.10 $\Delta C_{p_{\text{obs}}}$ as a function of pH using the values in Table 3.2.4.1. The ΔC_p is maximal at pH 8.70. At this pH values, the ΔC_p value is $0.57 \pm 0.21 \text{ kJ}\cdot\text{mol}^{-1}\cdot\text{K}^{-1}$.

accounts for 0-33% (-0.03 to $0.03 \text{ kJ}\cdot\text{mol}^{-1}\cdot\text{K}^{-1}$) of this intrinsic value, (considering structure change remains similar at pH 5.00 and pH 8.00) indicating that the contribution from other factors, $\Delta C_{p_{\text{ot}}}$, accounts for the remaining 33 to 66%. One of important factors that is not included specifically in the above analysis is the effect of the bound water (41), which could be playing an important role at this pH.

At pH 6.00, the ΔC_p from deprotonation of the buffer, $\Delta C_{p_{\text{dp}}}$ ($(\Delta C_{p_{\text{d,ACES}}} = -27 \text{ J}\cdot\text{mol}^{-1}\cdot\text{K}^{-1})$, will contribute less than $-0.015 \text{ kJ}\cdot\text{mol}^{-1}\cdot\text{K}^{-1}$ ($N_{\text{H}} = 0.57$) to the observed value of $0.00 \text{ kJ}\cdot\text{mol}^{-1}\cdot\text{K}^{-1}$. However, the ΔC_p from the noncovalent interactions, $\Delta C_{p_{\text{nc}}}$, will be negligible (30-32). Therefore, the total ΔC_p contributions from all the constituents including $\Delta C_{p_{\text{sasa}}}$ will be between -0.045 and $0.015 \text{ kJ}\cdot\text{mol}^{-1}\cdot\text{K}^{-1}$, which matches well with the observed of ΔC_p value of $0.00 \pm 0.03 \text{ kJ}\cdot\text{mol}^{-1}\cdot\text{K}^{-1}$.

However at pH 8.00 the $\Delta C_{p_{\text{obs}}}$ is around $0.37 \pm 0.22 \text{ kJ}\cdot\text{mol}^{-1}\cdot\text{K}^{-1}$ and is about 0.28 and $0.37 \text{ kJ}\cdot\text{mol}^{-1}\cdot\text{K}^{-1}$ more positive than at pH 5.00 and pH 6.00 respectively. At this pH, $\Delta C_{p_{\text{sasa}}}$, $\Delta C_{p_{\text{v}}}$, and $\Delta C_{p_{\text{nc}}}$ will contribute nearly -0.003 to $0.03 \text{ kJ}\cdot\text{mol}^{-1}\cdot\text{K}^{-1}$ to the $\Delta C_{p_{\text{obs}}}$. However, ΔC_p from deprotonation of the buffer component, $\Delta C_{p_{\text{dp}}}$ ($\Delta C_{p_{\text{dpTriple}}} = -33 \text{ J}\cdot\text{mol}^{-1}\cdot\text{K}^{-1}$) (129), will contribute about $-0.019 \text{ kJ}\cdot\text{mol}^{-1}\cdot\text{K}^{-1}$ to the observed value of $0.37 \text{ kJ}\cdot\text{mol}^{-1}\cdot\text{K}^{-1}$ (Table 3.2.10). Therefore, the rest of the $\Delta C_{p_{\text{obs}}}$

3. Results and Discussion

difference must be attributed to combined heat capacity changes, $\Delta C_{p_p} + \Delta C_{p_{ot}}$ and will have a value ranging between 0.32 to 0.38 $\text{kJ}\cdot\text{mol}^{-1}\cdot\text{K}^{-1}$. This differential value ($\Delta C_{p_p} + \Delta C_{p_{ot}}$) could be attributed to factors such as the bound water, complex dynamics or ion/metal effects (41; 42; 126) also it has been recently shown that a bound water molecule can contribute significantly to the overall ΔC_p ($-75 \text{ J}\cdot\text{mol}^{-1}\cdot\text{K}^{-1}$) (120).

However, an interesting point to note in this study is 0 $\text{kJ}\cdot\text{mol}^{-1}\cdot\text{K}^{-1}$ or negligible $\Delta C_{p_{obs}}$ at pH 6.00, which is about 0.37 $\text{kJ}\cdot\text{mol}^{-1}\cdot\text{K}^{-1}$ less than $\Delta C_{p_{obs}}$ at pH 8.00. These calorimetric data indicate that positive ΔC_p observed at pH 8.00 can be more or less minimized/reversed if pH is changed to pH 6.00.

3.2.5 Effect of Salt Concentration on AMPPNP Binding to N-Hsp90

The formation of complexes of charged molecules is, in general accompanied by changes to their local ionic environment, i. e. salt or buffer ions redistributing to lower the total energy of the solute-solvent system (124). In some cases, these effects of ionic environment can influence the $\Delta C_{p,obs}$ of the binding reaction. Where such an effect does contribute, it manifests as a salt concentration dependent $\Delta C_{p,obs}$ (136). To investigate this effect on the N-Hsp90-ADP/ATP interaction, calorimetric titrations were carried out at increasing salt concentrations in 20 mM Tris buffer (pH 8.00).

ITC results for individual titrations conducted at 0.0, 0.1 and 0.2 M salt (NaCl) are presented in Tables 3.1.3, 3.2.15 and 3.2.16 respectively. These data show that the attractive forces between N-Hsp90-AMPPNP molecules are slightly changed at the different ionic concentrations values studied. Specifically at 0.2 M, the ΔH between N-Hsp90 and AMPPNP is much more favourable than that at 0.0 M and 0.1 M.

Salt Concentration (M)	ΔH_{obs} (kJ·mol ⁻¹)	$T\Delta S_{obs}$ (kJ·mol ⁻¹)	ΔG_{obs} (kJ·mol ⁻¹)	ΔC_p (kJ·mol ⁻¹ ·K ⁻¹)
0.00	-33.39 ± 1.07	-11.22	-22.17	0.28 ± 0.03
0.10	-32.69 ± 3.74	-9.74	-22.95	0.28 ± 0.05
0.20	-39.23 ± 1.76	-18.36	-20.87	0.20 ± 0.01

Table 3.2.14 Comparison of thermodynamic parameters at different salt concentrations at 15 °C.

The molecular basis of the influence of NaCl on the binding of AMPPNP to N-Hsp90, could be due to several reasons and these include

- 1) Specific counterion binding to negatively charged aspartic acid residues which are known to interact directly with the purine ring of AMPPNP.
- 2) Simple counterion shielding of the electrostatic interactions between the phosphate side-chain of AMPPNP and N-Hsp90 binding site residues (Asp40, Lys98).
- 3) Ionic strength effects on the apparent pK_a values for the ionisable groups on the N-Hsp90 and AMPPNP, which are important in the binding reaction. However, such an effect could be coupled with a conformational change of the protein (137).

3. Results and Discussion

However a very interesting point to note in this titration, i.e. the large and positive ΔC_p observed in buffer devoid of salt, can still be observed even at increasing salt concentration. At zero salt concentration, interaction between N-Hsp90 and AMPPNP proceeds with a $0.28 \pm 0.03 \text{ kJ}\cdot\text{mol}^{-1}\cdot\text{K}^{-1}$, which remains virtually unaffected even after increasing salt concentration to 100 mM NaCl. However a further increase to 200 mM salt results in ΔC_p of about $0.20 \pm 0.01 \text{ kJ}\cdot\text{mol}^{-1}\cdot\text{K}^{-1}$, which is very insignificant and is around $0.08 \text{ kJ}\cdot\text{mol}^{-1}\cdot\text{K}^{-1}$ less than at 0 mM and 100 mM of salt concentration.

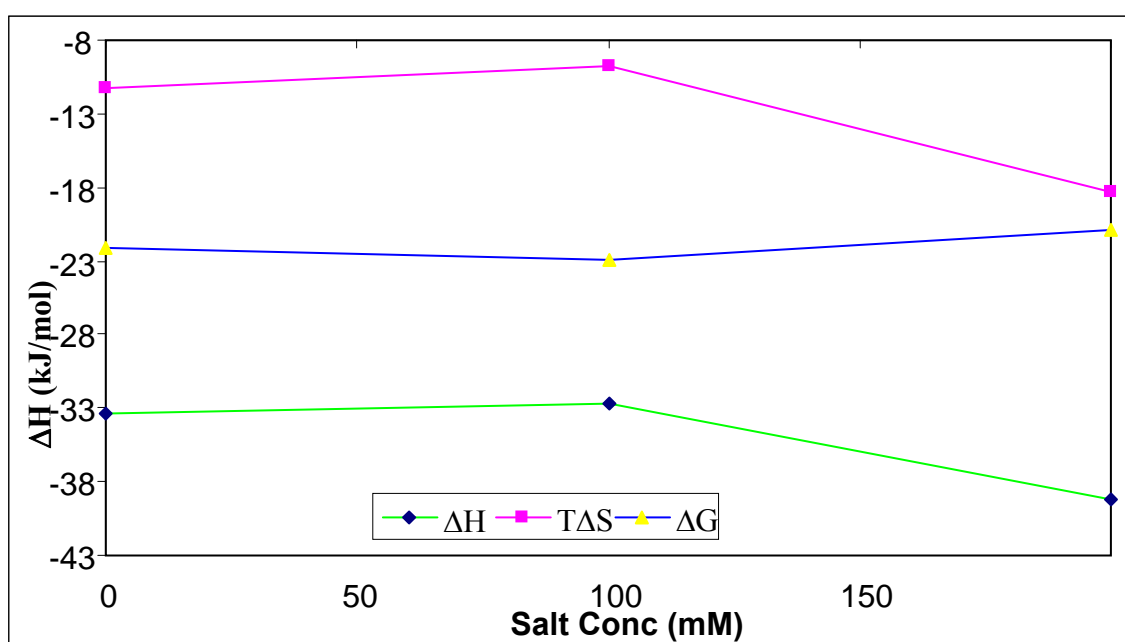


Figure 3.2.11 Salt dependence of the thermodynamic quantities of the N-Hsp90-AMPPNP interaction (0.0 to 0.2 M NaCl).

Nonetheless, it was also expected that monovalent salts, due to their charge stabilization effect, will affect desolvation of water molecules from divalent metal cations. As a result, we had expected a significant influence of salt on the positive ΔC_p in N-Hsp90- Mg^{2+} -AMPPNP interaction. However, observed results point towards the fact that the observed positive ΔC_p in the N-Hsp90-AMPPNP interaction is independent of the monovalent salt concentration and stabilization of charge-charge interactions.

On the contrary, calorimetric titrations carried out with 0.1 M salt (NaCl) as a monovalent cation substituent in place of divalent metal cations (Mn^{2+}), showed no binding between AMPPNP and N-Hsp90. This highlights the fact that metal-nucleotide binding pocket of N-Hsp90 is charge-selective and can discriminate between monovalent and divalent metal cations.

3. Results and Discussion

Ligand	Temp (°C)	Stoichiometry (n)	$K_b \times 10^4$ (M ⁻¹)	K_d ⁽²⁾ (μM)	ΔH_{obs} (kJ·mol ⁻¹)	$T\Delta S_{\text{obs}}$ (kJ·mol ⁻¹)	ΔG_{obs} (kJ·mol ⁻¹)	ΔC_p (kJ·mol ⁻¹ ·K ⁻¹)
AMPPNP	8	1.15 ± 0.00	2.24 ± 0.05	44.40	- 37.76 ± 0.30	- 14.34	- 23.42	0.28 ± 0.05
	12	1.14 ± 0.00	1.84 ± 0.03	54.30	- 35.69 ± 0.26	- 12.42	- 23.27	
	16	1.13 ± 0.01	1.39 ± 0.05	71.80	- 34.32 ± 0.76	-11.40	- 22.92	
	25	0.93 ± 0.07	0.85 ± 0.10	116.90	- 32.69 ± 3.74	- 9.74	- 22.95	

Table 3.2.15 Summary of the thermodynamic parameters for the binding interaction of N-Hsp90-AMPPNP with 20 mM Tris , 5 mM MgCl₂ and 100 mM Salt as a function of temperature (pH 8.00).

Ligand	Temp (°C)	Stoichiometry (n)	$K_b \times 10^4$ (M ⁻¹)	K_d ⁽²⁾ (μM)	ΔH_{obs} (kJ·mol ⁻¹)	$T\Delta S_{\text{obs}}$ (kJ·mol ⁻¹)	ΔG_{obs} (kJ·mol ⁻¹)	ΔC_p (kJ·mol ⁻¹ ·K ⁻¹)
AMPPNP	8	1.30 ± 0.00	1.92 ± 0.05	51.90	- 39.77 ± 0.29	- 16.72	- 23.05	0.20 ± 0.01
	12	1.29 ± 0.00	1.42 ± 0.01	70.10	- 38.83 ± 0.14	- 16.17	- 22.66	
	16	1.51 ± 0.00	1.04 ± 0.00	95.80	- 38.11 ± 0.22	- 15.88	- 22.23	

Table 3.2.16 Summary of the thermodynamic parameters for the binding interaction of N-Hsp90 with AMPPNP in 20 mM Tris, 5 mM MgCl₂ and 200 mM Salt as a function of temperature (pH 8.00).

¹Data was fitted to a one-set-of-sites model.

²Dissociation constant values (K_d) were calculated as the reciprocal of the observed equilibrium binding constant ($K_d = 1 / K_{\text{obs}}$).

3.2.6 Investigating The Effect of D₂O on ΔH and ΔC_p of 17-DMAG and AMPPNP Binding to N-Hsp90.

Deuterium Oxide (D₂O) is known to have similar properties to water (H₂O). However, there are small but definite differences in several physical properties (*138-140*). Some important properties of D₂O and H₂O are compared in Table 3.2.17.

	Unit	X _{H2O}	X _{D2O}
Molecular Weight	Daltons	18.015	20.028
Melting Point T _m	°C	0.00	3.81
Boiling point	°C	100	101.42
Hydrogen bond length	Å	2.765	2.766

Table 3.2.17 Some physical properties of H₂O and D₂O. Please note, H-bond length denoted here is used purely for comparison purpose with H-bond length in D₂O [Adopted from Nemethy and Scheregra (*140*)] and is different from that specified on page 8. Generally H-bond length can vary due to external factors such as temperature, pressure and polarity of the constituent atoms.

In this study, binding of two structurally different small molecules (AMPPNP and 17-DMAG) to N-Hsp90 in D₂O was investigated. Parallel measurements of the thermodynamics (ΔG , ΔH , ΔS and ΔC_p) of ligand binding to N-Hsp90 in H₂O and D₂O have been performed in an effort to probe the difference in energetic contributions. Both of these molecules bind to N-Hsp90 in a similar fashion (Figure 3.1.12 and 3.1.13) and in the same largely hydrophilic binding pocket situated on the N-Hsp90. Identification and exploitation of various energetic contributions of protein-small ligand binding in aqueous solution, and an evaluation of their structural basis, requires a direct account of changes in the interaction of protein with solvent, which accompanies the binding reactions.

3.2.6.1 Isothermal Titration Calorimetry for Association of AMPPNP and Geldanamycin to N-Hsp90 in D₂O

Enthalpies of association can be strongly influenced by pH. For this work, it is clearly imperative that protonation states of the interacting species are identical in H₂O and D₂O. Because solvent isotopic substitution also affects the ionization constant or pK_a values of ionizable groups, a second variable is introduced to the problem in order to achieve identical ionization states in the two solvents. It has long been recognized that at equal concentration of H⁺ and D⁺ in a glass electrode of a pH meter reading will be 0.30 units lower for D₂O because glass electrodes measure ion activities rather than actual concentrations (158); empirically, it has also been noted that the difference in pK values for deuterated acids versus the corresponding protonated derivative is 0.3 ± 0.02 pK_H . Thus for globular proteins, $pD = pH + 0.30$, should result in identical protonation states and this method is used for all the titrations reported in Table 3.2.18, 3.2.19 and 3.2.20.

Figure 3.2.12 shows a typical calorimetric titration of N-Hsp90 in tris buffer at pH 8.00 in H₂O and pD 8.00 in D₂O at 25 °C with 17-DMAG together with corresponding binding isotherm. The binding reaction is characterised by a significant exothermic heat effect, which remains constant while binding sites are still available and sharply drops to the dilution level once saturation has been achieved.

In order to evaluate ΔC_p upon binding, temperature-dependence of the binding enthalpy at various temperatures was also investigated. Binding experiments were performed at five different temperatures between 8 °C and 25 °C for AMPPNP and 17-DMAG binding to N-Hsp90 under the same pH and buffer conditions. The results for AMPPNP binding are presented in Figure 3.2.14 and summarized in Table 3.2.19, while results for 17-DMAG binding are presented in Figure 3.2.13 and summarized in Table 3.2.20.

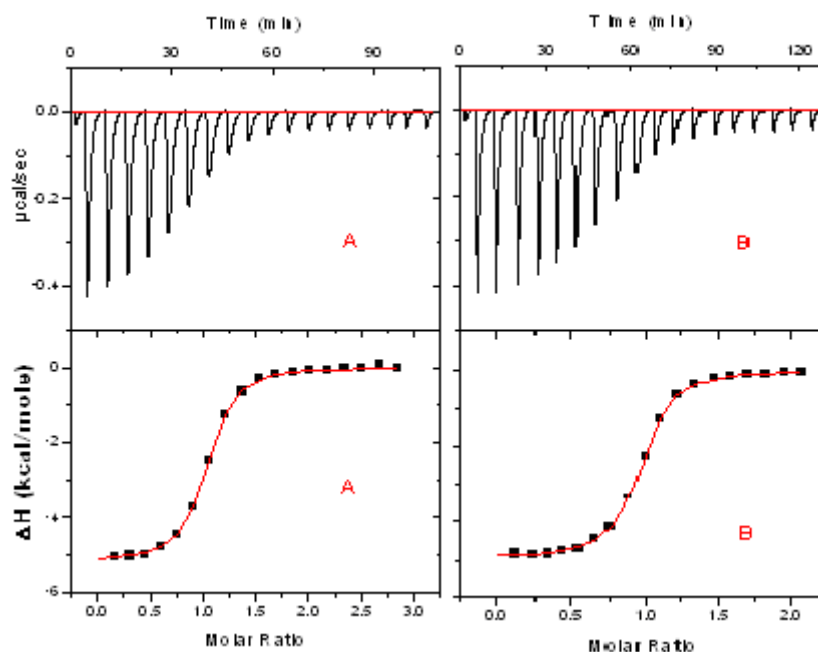


Figure 3.2.12 Typical calorimetric titration of N-Hsp90 with 17-DMAG in 20 mM Tris buffer (pH = 8.00 and pD = 8.00) in **A. D₂O** and **B. H₂O**.

The ΔH for the reaction of N-Hsp90 with 17-DMAG depends strongly on the temperature, indicating the large negative ΔC_p of $-0.77 \pm 0.12 \text{ kJ}\cdot\text{mol}^{-1}\cdot\text{K}^{-1}$ accompanying binding. The temperature dependence of the ΔH was described well, in all cases, by linear regression models assuming a constant ΔC_p in the temperature range of the experiment (Figure 3.2.13 and 3.2.14).

The interaction of N-Hsp90 with AMPPNP also depends strongly on temperature, however it indicates a strong positive ΔC_p of $0.57 \pm 0.15 \text{ kJ}\cdot\text{mol}^{-1}\cdot\text{K}^{-1}$. The temperature dependence of the ΔH was also well described in all cases by linear regression models. For each binding investigated, D₂O substitution resulted in a higher negative ΔH of binding, while offsetting $T\Delta S$ leads to unaltered or slightly higher ΔG energies in D₂O.

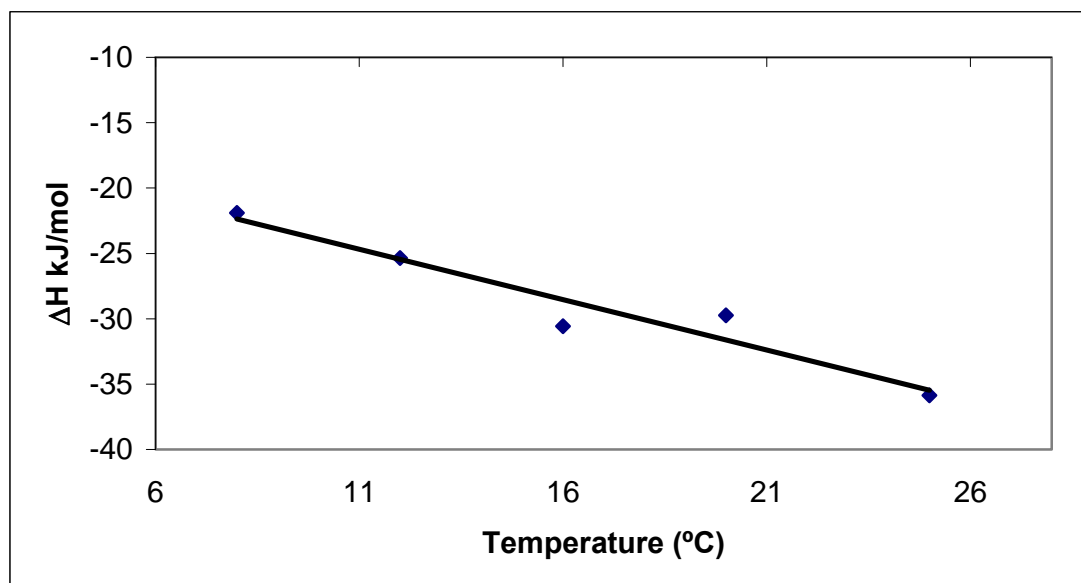


Figure 3.2.13 Temperature dependence of the enthalpy change upon binding (ΔH) of geldanamycin to N-Hsp90 at pH 8.00 in D_2O . The data are summarized in Table 3.2.20. The continuous line is the least squares fit of the data. The slope of linear regression yields the ΔC_p upon binding ($-0.77 \pm 0.12 \text{ kJ}\cdot\text{mol}^{-1}\cdot\text{K}^{-1}$).

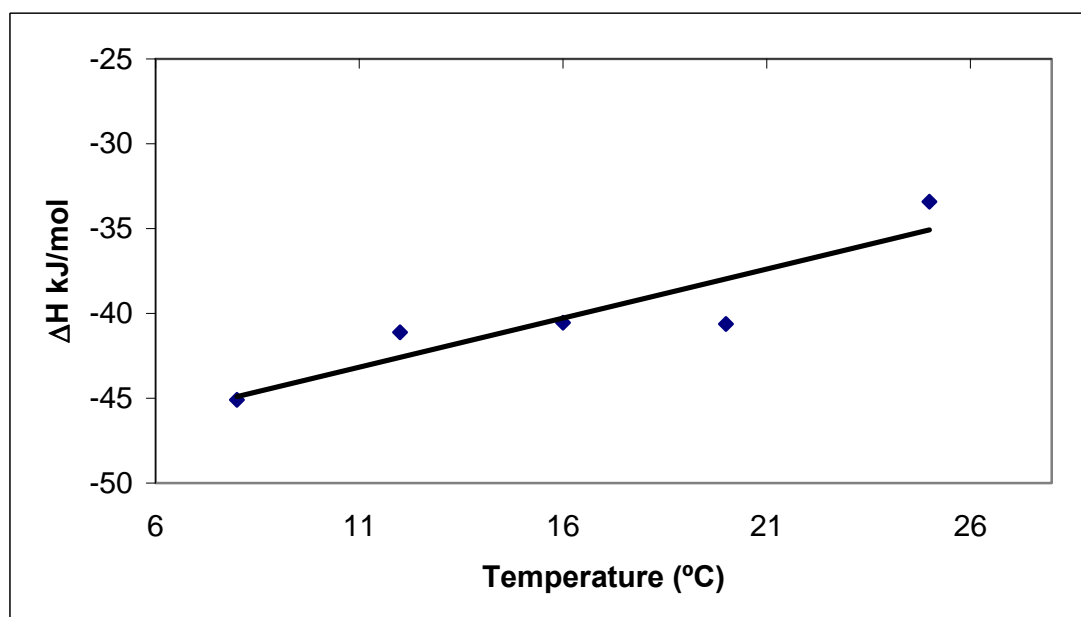
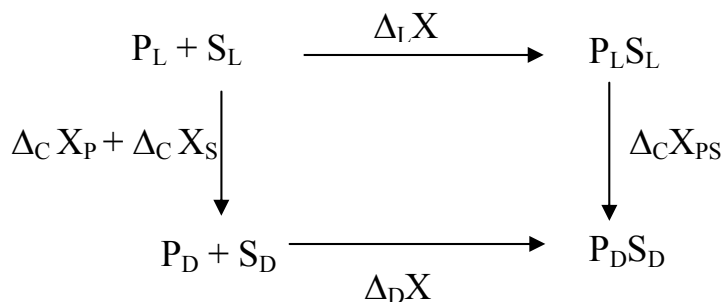


Figure 3.2.14 Temperature dependence of the enthalpy change upon binding (ΔH) of AMPPNP to N-Hsp90 at pH 8.00 in D_2O . The data are summarized in Table 3.2.19. The continuous line is the least squares fit of the data. The slope of linear regression yields the ΔC_p upon binding, ($0.57 \pm 0.15 \text{ kJ}\cdot\text{mol}^{-1}\cdot\text{K}^{-1}$).

3.2.6.2 Thermodynamic Difference for Titrations of N-Hsp90-ADP/ATP and N-Hsp90-17-DMAG Interactions Conducted in H₂O and D₂O

For a protein-small molecule interaction that takes place under constant pressure, thermodynamics of reactions in H₂O and D₂O can be represented by the following scheme II.



Scheme II. Thermodynamic cycle showing separation of partitioning of measured thermodynamics of binding in H₂O and D₂O.

In scheme II, the protein, the ligand and the protein-ligand complex in water (L) are represented as P_L, S_L, and P_LS_L respectively. The protein, the ligand and the protein-ligand complex, in heavy water (D) are represented by P_D, S_D and P_DS_D respectively. Horizontally, the thermodynamic cycle identifies the binding reaction carried out in light water (top) and heavy water (bottom). Whilst transferring protein and ligand (left) and protein-ligand complex (right) from H₂O to D₂O is represented in the vertical direction of the thermodynamic cycle. Δ_CX, Δ_CX_{PS}, Δ_CX_P and Δ_CX_S represent various thermodynamic parameters (X may be H, S, G or Cp) for transfer from H₂O to D₂O for protein-ligand complex, protein and small molecule, respectively. From the thermodynamic cycle, the difference in thermodynamics in D₂O relative to H₂O is equal to the thermodynamics of transfer of product and reactant from light to heavy water, and for any individual thermodynamic parameter can be represented by equation 3.2.5.

$$\Delta_D \Delta_L X = \Delta_C X_{PS} - \Delta_C X_P - \Delta_C X_S \quad 3.2.5$$

Similarly, the thermodynamic process which takes place at constant pressure Cp, can be further represented by a sum of three terms (141):

$$\Delta_L G = \Delta_L H^1 - T \Delta_L S^1 + \Delta_L C_p [(T^2 - T^1) - T \ln(T^2/T^1)] \quad 3.2.6$$

3. Results and Discussion

Where $\Delta_L H^1$ and $T\Delta_L S^1$ are measurable variables for a given reaction, and defined at a particular temperature T^1 . The third term contains a temperature function (in brackets) and a constant multiplier of this function, the ΔC_p on binding.

$$\Delta_D G = \Delta_D H^1 - T\Delta_D S^1 + \Delta_D C_p [(T^2 - T^1) - T \ln(T^2/T^1)] \quad 3.2.7$$

For a reaction carried out in D_2O relative to H_2O , equation 3.2.6 and 3.2.7 can be rearranged and represented as

$$\Delta_D \Delta_L G = \Delta_D \Delta_L H^1 - T\Delta_D \Delta_L S^1 + \Delta_D \Delta_L C_p [(T^2 - T^1) - T \ln(T^2/T^1)] \quad 3.2.8$$

where for a specific thermodynamic property X , $\Delta_D \Delta_L X$ is defined as

$$\Delta_D \Delta_L X = \Delta_D X - \Delta_L X \quad 3.2.9$$

From this equation 3.2.9, we can derive thermodynamic parameters (ΔH , ΔS , ΔG or ΔC_p) for transfer of protein-ligand complex from H_2O to D_2O as given in Table 3.2.18.

Thermodynamic Parameter (kJ·mol ⁻¹)	17-DMAG	AMPPNP
$\Delta_L H$	-24.60 ± 0.37	-33.39 ± 1.07
$\Delta_D H$	- 35.86 ± 0.26	- 33.41 ± 0.43
$\Delta_D \Delta_L H$	- 11.26	- 0.02
$T\Delta_L S$	7.55	- 11.22
$T\Delta_D S$	- 1.52	- 8.79
$T\Delta_D \Delta_L S$	- 9.07	2.43
$\Delta_L G$	-32.15	-22.17
$\Delta_D G$	- 34.34	- 24.62
$\Delta_D \Delta_L G$	- 2.19	- 2.45
$\Delta_L C_p^\#$	-0.48 ± 0.06	0.28 ± 0.03
$\Delta_D C_p^\#$	- 0.77 ± 0.12	0.57 ± 0.15
$\Delta_D \Delta_L C_p^\#$	- 0.29	0.29

Table 3.2.18 $T\Delta S$, ΔH , ΔG and ΔC_p for 17-DMAG and AMPPNP binding to N-Hsp90 at 25 °C.

ΔC_p values are given in kJ·mol⁻¹·K⁻¹.

The $\Delta_D\Delta_L H$, which can also be called the enthalpy of transfer ($\Delta_C H_{PS}$) from H_2O to D_2O shows a marked difference of about $-11.26 \text{ kJ}\cdot\text{mol}^{-1}$ for N-Hsp90-17-DMAG binding, while for N-Hsp90-AMPPNP binding, it shows a negligible value of $-0.02 \text{ kJ}\cdot\text{mol}^{-1}$. However, these $\Delta_D\Delta_L H$ values are marked by $T\Delta_D\Delta_L S$ values of 2.43 and $-9.07 \text{ kJ}\cdot\text{mol}^{-1}$ for AMPPNP and 17-DMAG binding to N-Hsp90, which in turn give rise to a $\Delta_D\Delta_L G$ of only $-2.45 \text{ kJ}\cdot\text{mol}^{-1}$ and $-2.19 \text{ kJ}\cdot\text{mol}^{-1}$ respectively (Table 3.2.18). Such enthalpy-entropy compensation is the hallmark of associations in aqueous solutions (10; 113; 115; 120), assuming a constant ΔC_p in the temperature range of the experiment (Figure 3.2.15).

Observed less negative ΔH of binding for AMPPNP and 17-DMAG to N-Hsp90 in water than in D_2O (Figure 3.2.15 and Table 3.2.18) is in disagreement with the result obtained for tacrolimus and rapamycin binding to FK506 (141) and also the binding of vancomycin to tripeptide α,ϵ -diacetyl-L-lysine-D-alanine-D-alanine (142; 143). Connelly and Thomson (141) in addition to Chervenak and Toone (143) had observed higher negative ΔH of binding in H_2O than in D_2O . This indicates that in their titrations, D_2O either stabilizes the unbound reactants or destabilizes the protein-ligand complex, relative to H_2O , as compared to our experiment. Where D_2O stabilizes the protein-ligand complex relative to H_2O or destabilizes the unbound reactants. However, previous X-ray crystallographic and FT-IR studies do not support the theory of destabilization of proteins or small molecules in D_2O (141). One of the significant contributions to observed enthalpic stabilization is the hydration of a significant amount of polar surface area upon small molecule binding in 17-DMAG binding and tighter H-bonds in D_2O .

Differences in the thermodynamics observed in H_2O versus D_2O can be explained entirely by changes in $\Delta_D\Delta_L H$. Assuming the structure of the ligand, the receptor and the complex is identical in both solvents (144; 145), then solvent isotopic substitution from hydrogen to deuterium should affect only the ΔH of binding contained in $\Delta_D\Delta_L H$. The $\Delta\Delta H$ versus ΔC_p plot (Figure 3.2.15) provides additional evidence that the origin of the solvent isotope effect originates in differential O-H versus O-D H-bond strengths. The slope of the $\Delta\Delta H$ versus ΔC_p plot is a temperature ($\text{kJ}\cdot\text{mol}^{-1}/\text{kJ}\cdot\text{mol}^{-1}\cdot\text{K}^{-1}$), which is defined as the offset temperature (T_0) or the temperature difference required to yield identical enthalpies of binding in light (H_2O) and heavy (D_2O) water. The $15 \text{ }^\circ\text{C}$ offset temperature observed for both AMPPNP and 17-DMAG binding to N-Hsp90, differs with the $5 \text{ }^\circ\text{C}$ T_0 observed by Chervenak and Toone (143).

3. Results and Discussion

However one of the most interesting results of these titrations was totally opposing observed $\Delta_D\Delta_L C_p$ values. The $\Delta_D\Delta_L C_p$ value for 17-DMAG binding to N-Hsp90 is around $-0.29 \text{ kJ}\cdot\text{mol}^{-1}\cdot\text{K}^{-1}$ and matches well with the results obtained by Chervenak and Toone (143). On the other hand, $\Delta_D\Delta_L C_p$ value for AMPPNP binding to N-Hsp90 is around $0.29 \text{ kJ}\cdot\text{mol}^{-1}\cdot\text{K}^{-1}$, which is opposite to the 17-DMAG results and differs by a wide margin of $0.58 \text{ kJ}\cdot\text{mol}^{-1}\cdot\text{K}^{-1}$. A ΔC_p of $0.58 \text{ kJ}\cdot\text{mol}^{-1}\cdot\text{K}^{-1}$ is equivalent to gaining about 77.14 \AA^2 of apolar surface area or a decrease of 33.94 \AA^2 of polar surface area (Equation 1.3.2).

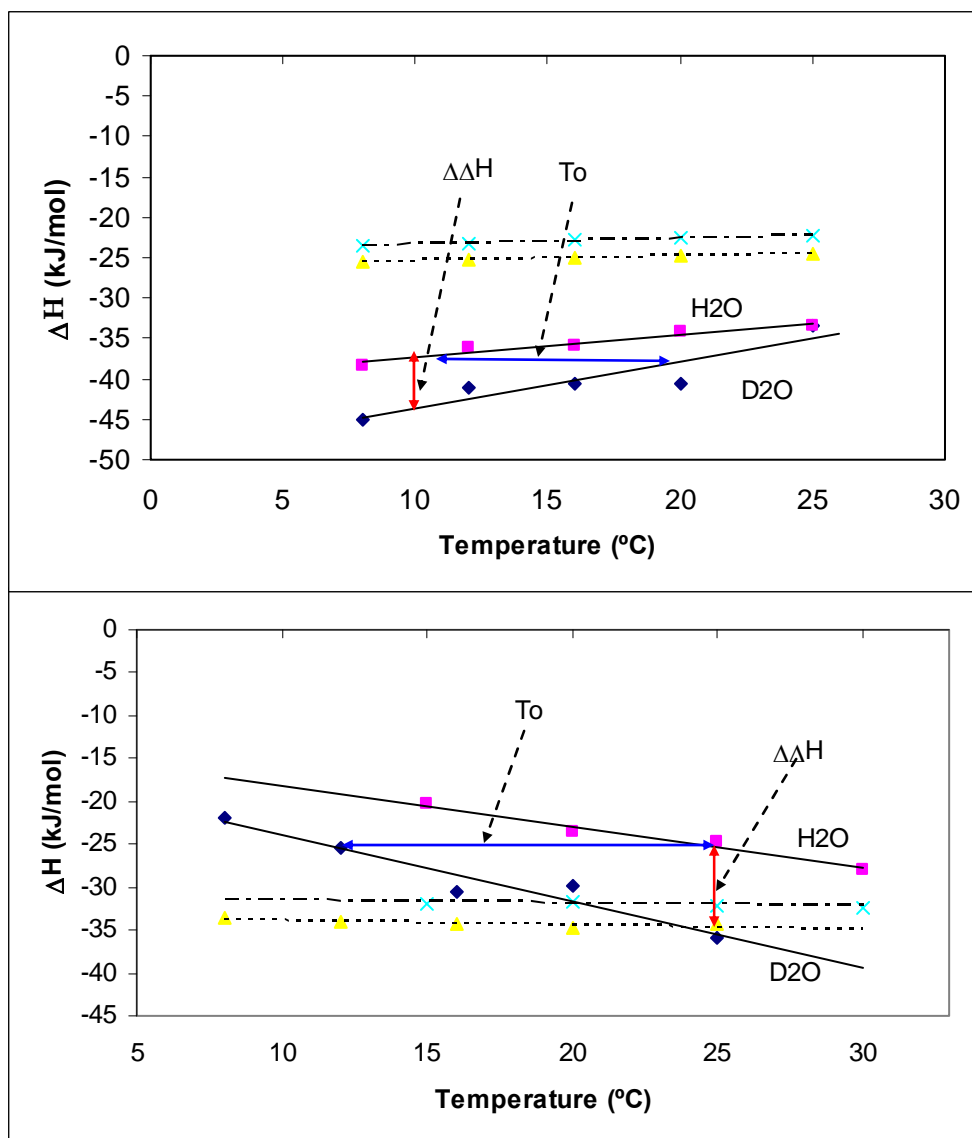


Figure 3.2.15 Change in enthalpies of binding AMPPNP (top) and 17-DMAG (bottom) in H₂O (square) and D₂O (♦) as a function of temperature. The solid lines were calculated from best-fit parameters obtained in the linear regression analysis. Best fit parameters are given in Table 3.2.6.2.

3. Results and Discussion

Ligand	Temp (°C)	Stoichiometry (n)	$K_b \times 10^4$ (M ⁻¹)	$K_d^{(2)}$ (μM)	ΔH_{obs} (kJ·mol ⁻¹)	$T\Delta S_{\text{obs}}$ (kJ·mol ⁻¹)	ΔG_{obs} (kJ·mol ⁻¹)	ΔC_p (kJ·mol ⁻¹ ·K ⁻¹)
AMPPNP	8	1.09 ± 0.00	5.50 ± 0.09	18.10	- 45.10 ± 0.14	- 19.58	- 25.52	0.57 ± 0.15
	12	1.07 ± 0.00	4.18 ± 0.08	23.80	- 41.11 ± 0.18	- 15.90	- 25.21	
	16	1.06 ± 0.00	3.32 ± 0.13	30.90	- 40.54 ± 0.42	- 15.59	- 24.95	
	20	1.13 ± 0.00	2.59 ± 0.08	38.40	- 40.62 ± 0.33	- 15.87	- 24.75	
	25	1.09 ± 0.00	2.07 ± 0.08	48.10	- 33.41 ± 0.43	- 8.79	- 24.62	

Table 3.2.19 Summary of the thermodynamic parameters for the binding interaction of N-Hsp90 AMPPNP with 20 mM Tris in Deuterium Oxide (D₂O) as a function of temperature (pD 8.0).

Ligand	Temp (°C)	Stoichiometry (n)	$K_b \times 10^4$ (M ⁻¹)	$K_d^{(2)}$ (μM)	ΔH_{obs} (kJ·mol ⁻¹)	$T\Delta S_{\text{obs}}$ (kJ·mol ⁻¹)	ΔG_{obs} (kJ·mol ⁻¹)	ΔC_p (kJ·mol ⁻¹ ·K ⁻¹)
17-DMAG	8	0.99 ± 0.00	175.30 ± 6.24	0.57	- 21.91 ± 0.07	11.66	- 33.57	- 0.77 ± 0.12
	12	0.97 ± 0.00	175.10 ± 6.09	0.57	- 25.36 ± 0.08	8.67	- 34.03	
	16	0.99 ± 0.00	150.60 ± 7.58	0.66	- 30.57 ± 0.22	3.59	- 34.16	
	20	1.00 ± 0.01	162.3 ± 28.82	0.61	- 29.74 ± 0.48	5.07	- 34.81	
	25	1.01 ± 0.00	105.2 ± 6.86	0.95	- 35.86 ± 0.26	- 1.52	- 34.34	

Table 3.2.20 Summary of the thermodynamic parameters for the binding interaction of N-Hsp90-17-DMAG in 20 mM Tris buffer in Deuterium Oxide (D₂O) as a function of temperature (pD 8.0).

¹ Data was fitted to a one-set-of-sites model.

² Dissociation constant values (K_d) were calculated as the reciprocal of the observed equilibrium binding constant ($K_d = 1 / K_{\text{obs}}$).

3.2.6.3 Differences in Structure of H₂O and D₂O Can Give Different values for ΔC_p

According to Connelly and Thomson (*146*), the thermodynamics of transfer of a protein or small molecular species from H₂O to D₂O may be broken up into four terms which correspond to

1. Hydrogen exchange or replacement of exchangeable hydrogen atoms by deuterium atoms.
2. Changes in the state of protonation of the protein and ligand due to the difference in the affinity of ionizable groups for H⁺ and D⁺.
3. Difference in the light and heavy water hydration of polar and nonpolar groups.
4. Other changes in the structure of the protein and ligand that occur as a consequence.

The thermodynamic difference due to H/D exchange is unlikely to contribute significantly to the difference in thermodynamics reported in Table 3.2.18. There are more than 400 exchangeable hydrogen atoms in N-Hsp90 and only a handful in 17-DMAG and AMPNP. The heat of exchange between bound and free N-Hsp90 is not likely to be large as it involves nearly similar number of exchangeable sites.

Additionally, from studies conducted by Habash et al., (*147*) and Finer-Moore et al., (*148*) there is little evidence to suggest that there is a large difference in the structure of a hydrogenated and a deuterated protein. In a separate study conducted by Timmins et al. (*145*) on different isotopic forms of the α E-crystallin, they have shown that in either solvent no major structural differences are observed (r.m.s. deviation of 0.27 Å between all isotopic forms) as has been seen on other hydrogenated and deuterated systems (*144; 149-151*). Interestingly, recent comparative FT-IR studies of hydrogenated and deuterated P450cam-C334A show that the structure and dynamics of proteins dissolved in H₂O and D₂O under ambient conditions of pressure are very similar (*152*). Thus deuteration also does not affect the position of atoms in space, but understandably, there are some effects from the isotopic change of non-exchangeable and exchangeable hydrogens with D atoms.

The hydration contributions to the difference in thermodynamic properties usually can be divided into changes in hydration of various polar and nonpolar atoms that occur upon binding. This can be measured in terms of changes in solvent accessible surface area ($\Delta SASA$) accompanying binding. Upon ADP binding, there is a net burial of 705.8 Å² of polar groups and also net burial of 200.7 Å² of apolar groups. For geldanamycin binding

822.7 Å² total surface area is buried, consisting of 410.0 Å² non-polar groups and 472.0 Å² of polar groups. From the last section, also it can be assumed that $\Delta SASA$ will not be altered for the transfer of protein-ligand complex from H₂O to D₂O.

From the data obtained in Section 3.2.3, it is clear that there is a release of 0.57 protons linked to the binding of AMPPNP to N-Hsp90 at pH 8.00. This release of protons would make a difference to the heats of ionization and will contribute marginally to $\Delta_D\Delta_L H$ along with $\Delta_D\Delta_L C_p$. However exact $\Delta_D\Delta_L H$ and $\Delta_D\Delta_L C_p$ are difficult to predict, due to unavailability of heats of ionisation data in D₂O.

3.2.6.4 Correlating thermodynamics to the data Obtained From Transfer of Model Compounds from H₂O to D₂O

The observed differences in ΔH of small molecule binding to N-Hsp90 can possibly be quantified and analyzed from the data obtained from transfer of model compounds from H₂O to D₂O. Arnett and McKelvey (153) as well as Krescheck et al.(154) had extensively studied transfer of alcohols, amino acids and alkylamides and the enthalpies of transfer of these compounds from H₂O to D₂O at 25 °C. Studying these enthalpies of transfer, we could make two significant observations by investigating a plot of enthalpy of transfer (ΔH) of these compounds from H₂O to D₂O, versus the non-polar water-accessible surface area, $\Delta SASA_{NP}$. First, the dependence of ΔH on $\Delta SASA_{NP}$ within each series of compounds is linear, indicating the additivity of the enthalpy of transfer. Secondly, the extrapolation to zero non-polar SASA yields values for the three sets of compounds that are close to zero. This indicates that polar surface area, at least to a first approximation, does not contribute significantly to the $\Delta_C H$ for this series of compounds from H₂O to D₂O at 25 °C. Additionally, polar groups form H-bonds with water, the enthalpies of these hydrogen bonds in both H₂O and D₂O are very similar and give small negative ΔG of transfer, which is due to the small positive ΔS of the solvent (155; 156).

From the data obtained in the present calorimetric titrations it appears that, in part, the difference in $\Delta_D\Delta_L H$ can be accounted by the changes in the hydration of non-polar groups in D₂O and H₂O. The difference in the binding enthalpy of 17-DMAG with N-Hsp90 is -11.26 kJ·mol⁻¹ at 25 °C. $\Delta SASA$ calculations (Section 3.2.7) show a decrease of 822.70 Å of accessible surface (472.60 Å polar and 410 Å of nonpolar). According to Makhatadze et al. (157), 1 Å non-polar surface area exposed can give rise to about

$10 \pm 2 \text{ J}\cdot\text{mol}^{-1}$ of enthalpy of transfer from H_2O to D_2O , which predicts an enthalpy change of $4100 \pm 820 \text{ J}\cdot\text{mol}^{-1}$. This suggests that, in the present titrations the rest of the $\Delta_D\Delta_L H$ of binding should be attributed to other unknown factors and requires further investigation. However Makhatadze et al. (157) have derived these data from unfolding of protein in two different isotopic solvents and understandably, their data cannot be transferred successfully to a protein-small molecule interaction like ours.

AMPPNP binding to N-Hsp90 gives rise to an enthalpy of transfer from H_2O to D_2O of about $-0.02 \text{ kJ}\cdot\text{mol}^{-1}$. Such a small difference in $\Delta_D\Delta_L H$ can be accounted for by $\Delta SASA$ calculations.

Nemethy and Scheraga along with Connelly et al. (140; 141) had acknowledged that bonds involving deuterium (instead of hydrogens) are stronger; which in turn can be attributed to the lower frequency of vibrations of these bonds (140; 158). This implicates that bonds involving deuterium will be less flexible than a hydrogen bond and thus deuteration and D_2O will increase the rigidity of the native structure of protein (159). It can also be noted that the presence of D_2O as solvent rather than deuteration should have the most striking effects as it is hydrogen (deuterium) bonds which are primarily responsible for the stability of secondary structure elements of a protein.

$\Delta_D\Delta_L C_p$ for 17-DMAG and AMPPNP binding to N-Hsp90 is -0.29 and $0.29 \text{ kJ}\cdot\text{mol}^{-1}\cdot\text{K}^{-1}$ respectively. These $\Delta_D\Delta_L C_p$ values contradict the values observed by Chervenak and Toone (143) by $\pm 0.29 \text{ kJ}\cdot\text{mol}^{-1}\cdot\text{K}^{-1}$. However it must be noted that the results obtained from calorimetry are subject to experimental errors, arising from sample concentrations and data fitting. In addition obtaining a $\Delta_D\Delta_L C_p$ value depends on conducting at least 8 to 10 individual calorimetric titrations, which makes obtaining accurate results very difficult. However if obtained, a $\Delta_D\Delta_L C_p$ value of $0 \text{ kJ}\cdot\text{mol}^{-1}\cdot\text{K}^{-1}$, emphatically describes the relationship between $\Delta\Delta H$ and ΔC_p . Even though substitution of deuterium in place of hydrogen will change several soft protein vibrational modes and ΔH , the change will occur in both the free and bound form: thus ΔC_p arising from loss of protein vibrational modes, hydrogen bonding, electrostatic effect and desolvation/solvation of the surface area will be identical in both H_2O and D_2O .

Lastly, an important point to note here is that the sign for ΔC_p still remained positive for binding of AMPPNP to N-Hsp90; as compared to negative ΔC_p for 17-DMAG. These results indicate that the difference in hydrophobic effects arising from changes in surface solvation does not play an important role in the positive ΔC_p observed.

3.2.7 Comparison of Experimental and Empirically Calculated ΔC_p

It is well established that conformational changes coupled to binding can make substantial contributions to the ΔC_p observed on complex formation (Section 3.1.4). These are derived from either changes in the order of the protein and/or ligand, or from changes in solvation (31; 120; 121; 123). Therefore in this section we decided to compare empirically derived ΔC_p with experimentally calculated ΔC_p .

Change in solvent accessible surface area ($\Delta SASA$) was calculated with a default water probe radius of 1.4 Å, using the method published by Eisenhaber et al. (160) and incorporated in the VEGA molecular modelling suite (93; 94). For $\Delta SASA$ calculation per residue, the DSViewerPro molecular modelling suite (56) was used and again a water probe of 1.4 Å radius was used.

Prior to calculations, crystal structures were initially processed with DSViewerPro (56). Water and other unknown atoms were removed. Carbon, carbon-bound hydrogen, and phosphorous atoms are designated as nonpolar atoms, and all other atoms are designated as polar. Consequently, N-Hsp90 has 1193 polar atoms and 903 nonpolar atoms (residues 2-208); ADP had 15 polar atoms and 16 nonpolar atoms and geldanamycin showed 12 polar atoms and 32 nonpolar atoms. The $\Delta SASA$ of the polar and nonpolar areas of the ADP-bound and geldanamycin-bound N-Hsp90 were calculated by using the following equation 3.2.10.

$$\Delta SASA = SASA_{\text{complex}} - SASA_{\text{protein}} - SASA_{\text{ligand}} \quad \mathbf{3.2.10}$$

The two three-dimensional crystal structures of the N-Hsp90-ADP (PDB: 1AMW) and geldanamycin-bound form (PDB: 1A4H) were used for the calculation of $\Delta SASA$. However close inspection of the ADP- and geldanamycin-bound N-Hsp90, shows that water molecules form an important part of the biomolecular interface. Normally $\Delta SASA$ calculations are done in the absence of interfacial water molecules. However due to the complexity of ΔC_p calculations in N-Hsp90-ADP binding, we decided to incorporate the presence and absence of bound water molecules in our calculations. Therefore results are compared for both of these instances and are presented in Tables 3.2.21 to 3.2.24. Incorporation of bound water molecules resulted in including 1 water in N-Hsp90-geldanamycin and 6 water molecules in N-Hsp90-ADP $\Delta SASA$ calculations. [For the unbound N-Hsp90 $\Delta SASA$ calculation, the orthorhombic form of the Hsp90 dimer was

used (PDB: 1AH8) (161)]. Prior to calculation, all water molecules, unknown ligands and one Hsp90 monomer were removed, so that the final structure consisted of just one truncated Hsp90 monomer (residues 2-208).

Bound complexes of N-Hsp90 with ADP and geldanamycin showed significant $\Delta SASA$ per residue for groups which form hydrogen bonding upon complexation. ADP binds to the N-Hsp90 in an unusual compacted conformation, which brings the sugar and α -phosphate groups into close proximity to the five-membered ring of the adenine (54). ADP binding to N-Hsp90 results in a net burial of 705.8 \AA^2 of polar groups ($\Delta SASA_P$) and 200.7 \AA^2 of apolar groups ($\Delta SASA_{AP}$) (Table 3.2.21). However after including 6 trapped water molecules in the binding interface, net burial of $\Delta SASA_P$ increases by 26.9 \AA^2 to around 732.7 \AA^2 , while the $\Delta SASA_{AP}$ number jumps by 34.3 \AA^2 to around 235 \AA^2 (Table 3.2.21). For the $\Delta SASA$ change per residue, large peaks are observed for residues Arg32, Lys54, Ile96, Ala97, Lys98, Ser99, Lys102, Met105, Gly153, Gly154, Glu165, Val163, Arg166, Ile167, Glu199, Phe200, Val201, Ala201 and Tyr203 (Figure 3.2.16). Most of these residues (namely Ile96, Ala97, Lys98, Ser99, Lys102 and Met105) are located in the vicinity of the ADP binding pocket. The adenine ring, which forms the basic skeleton of the ADP molecule and experiences a very different hydrophobic environment after binding to N-Hsp90, becomes substantially buried, against the hydrophobic surface provided by the side-chains of Met84, Leu93, Phe124, Thr171 and Leu173. All these residues show moderate $\Delta SASA$ peaks in Figure 3.2.16 with a maximum increase of 3.11 \AA^2 for Met84 and is followed by a burial of 0.50, 1.60 and 2.39 \AA^2 for Thr173, Thr171 and Leu 93 respectively. The other major specific interaction between the adenine base and the protein involves a direct hydrogen bond from the exocyclic N6 of adenine to the carboxylate side-chain of Asp79. This residue shows marginal burial of 1.06 \AA^2 in $\Delta SASA$ upon binding. The phosphate groups of bound ADP make only two direct contacts with the protein; the peptide nitrogen of Gly123 at the N-terminus of the α -helix (residue 123-130) donates a hydrogen bond to the α -phosphate group, while the β -phosphate is involved in an ion pair/hydrogen bond with the side-chain of Lys98. Lys98 and Gly123 also get exposed on complex formation with ADP to an extent of 10.66 and 2.93 \AA^2 , respectively (Figure 3.2.16).

3. Results and Discussion

N-Hsp90-ADP complex	Total Accessible surface area (Å ²)	Hydrophilic contribution (Å ²)	Hydrophobic contribution (Å ²)	Experimental ΔCp (kJ·mol ⁻¹ ·K ⁻¹)	Calculated ΔCp (kJ·mol ⁻¹ ·K ⁻¹)
Complete complex	10530.00	5446.00	5084.0		
N-Hsp90	10868.10	5745.30	5122.70	2.35 ± 0.46	0.21 (1.3.2)
ADP	568.50	406.50	162.00		0.03 (1.3.4)
Net change	- 906.60	- 705.80	- 200.70		0.19 (1.3.5)

Table 3.2.21 ΔSASA calculations for N-Hsp90-ADP complex.

N-Hsp90-Geldanamycin complex	Total Accessible surface area (Å ²)	Hydrophilic contribution (Å ²)	Hydrophobic contribution (Å ²)	Experimental ΔCp (kJ·mol ⁻¹ ·K ⁻¹)	Calculated ΔCp (kJ·mol ⁻¹ ·K ⁻¹)
Complete complex	10771.90	5534.00	5177.90		
N-Hsp90	10868.10	5745.30	5122.70	- 0.39 ± 0.04	-0.27 (1.3.2)
Geldanamycin	726.50	261.30	465.20		- 0.30 (1.3.4)
Net change	- 822.70	- 472.60	- 410.00		-0.46 (1.3.5)

Table 3.2.22 ΔSASA calculations for N-Hsp90-Geldanamycin complex.

(1.3.2) Data was fitted using equation $\Delta C_p = 1.34 \Delta A_{np} - 0.59 \Delta A_p$ J·mol⁻¹·K⁻¹ by Spolar and Record (31).

(1.3.4) Data was fitted using equation $\Delta C_p = 1.17 \Delta A_{np} - 0.38 \Delta A_p$ J·mol⁻¹·K⁻¹ by Myers et al. (33).

(1.3.5) Data was fitted using equation $\Delta C_p = 2.14 \Delta A_{np} - 0.88 \Delta A_p$ J·mol⁻¹·K⁻¹ by Makhatadze and Privalov (32).

3. Results and Discussion

N-Hsp90-ADP complex	Total Accessible surface area (Å ²)	Hydrophilic contribution (Å ²)	Hydrophobic contribution (Å ²)	Experimental ΔCp (kJ·mol ⁻¹ ·K ⁻¹)	Calculated ΔCp (kJ·mol ⁻¹ ·K ⁻¹)
Complete complex	10469.60	5419.10	5049.70		
N-Hsp90	10868.10	5745.30	5122.70	2.35 ± 0.46	0.11 (1.3.2)
ADP	568.50	406.50	162.00		0.01 (1.3.4)
Net change	- 967.00	- 732.70	- 235.00		0.14 (1.3.5)

Table 3.2.23 ΔSASA calculations for N-Hsp90-ADP complex. (Calculated using trapped water molecules on the interface of the Binding site)

N-Hsp90-Geldanamycin complex	Total Accessible surface area (Å ²)	Hydrophilic contribution (Å ²)	Hydrophobic contribution (Å ²)	Experimental ΔCp (kJ·mol ⁻¹ ·K ⁻¹)	Calculated ΔCp (kJ·mol ⁻¹ ·K ⁻¹)
Complete complex	10689.30	5523.30	5166.00		
N-Hsp90	10868.10	5745.30	5122.70	- 0.39 ± 0.04	-0.27 (1.3.2)
Geldanamycin	726.50	261.30	465.20		-0.30 (1.3.4)
Net change	- 905.30	- 483.30	- 421.90		-0.47 (1.3.5)

Table 3.2.24 ΔSASA calculations for N-Hsp90-geldanamycin complex. (Calculated using trapped water molecules on the interface of the Binding site)

(1.3.2) Data was fitted using equation $\Delta C_p = 1.34 \Delta A_{np} - 0.59 \Delta A_p$ J·mol⁻¹·K⁻¹ by Spolar and Record (31).

(1.3.4) Data was fitted using equation $\Delta C_p = 1.17 \Delta A_{np} - 0.38 \Delta A_p$ J·mol⁻¹·K⁻¹ by Myers et al. (33).

(1.3.5) Data was fitted using equation $\Delta C_p = 2.14 \Delta A_{np} - 0.88 \Delta A_p$ J·mol⁻¹·K⁻¹ by Makhatadze and Privalov (32).

3. Results and Discussion

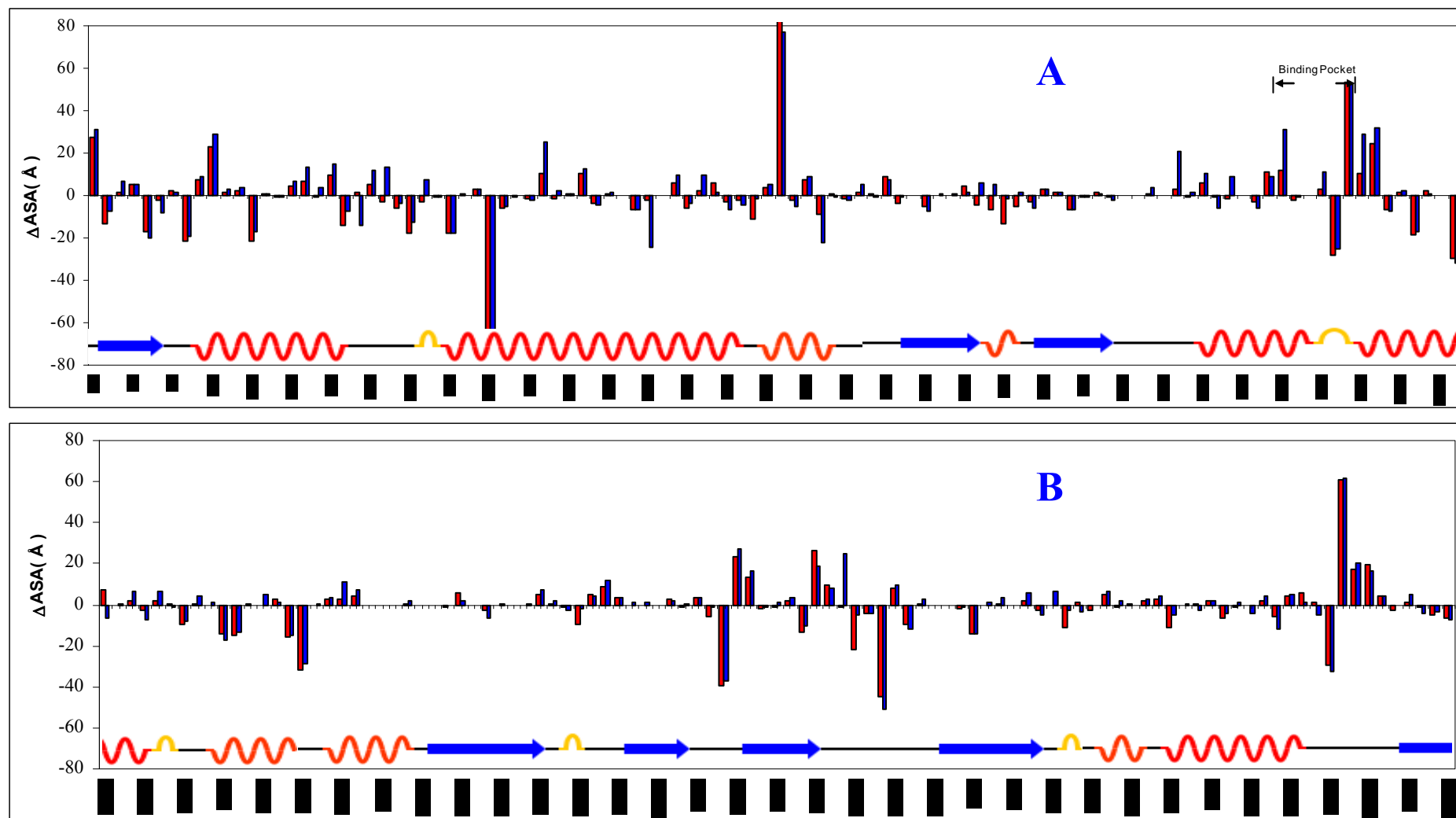


Figure 3.2.16 ΔASA upon complex formation for each residue, positive values on y-axis indicates increase in surface area for respective residue after binding. Red bars- ADP; Blue bars- geldanamycin binding; A. ΔASA per residue 2 to 105, B. ΔASA per residue 106 to 207.

3. Results and Discussion

Geldanamycin binding to N-Hsp90 results in a net burial of 472.60 \AA^2 of polar groups ($\Delta SASA_P$) and 410.00 \AA^2 of apolar groups ($\Delta SASA_{AP}$) (Table 3.2.22). $\Delta SASA$ calculation after including 1 trapped water molecule, results in a small $\Delta SASA_P$ increase of 10.70 \AA^2 to around 483.30 \AA^2 , while the $\Delta SASA_{AP}$ area increases by 34.30 \AA^2 to around 421.90 \AA^2 (Table 3.2.24). The largest negative peaks in Figure 3.2.16 for the N-Hsp90-geldanamycin complex, are given by residues Arg32, Ile96, Lys102, Met105, Gly153, Glu165 and Glu199, with a surface area exposure of 64.70, 25.08, 17.33, 31.92, 37.47, 51.06 and 32.85 \AA^2 respectively. These residues are however scattered in N-Hsp90 and are not segregated in a particular region. Binding of geldanamycin results in displacement of much of the surface bound water network, occupying the volume with part of the macrocycle, benzoquinone ring, quinone, and methoxy oxygens: which replace two or three of the water positions associated with the β -phosphate of a bound ADP. Protein groups forming the hydrophobic face of the adenine binding site make extensive hydrophobic interactions with the macrocycle of geldanamycin. Oxygen on the benzoquinone ring of the geldanamycin forms a direct hydrogen bond with Lys98, resulting in exposure of about 29.05 \AA^2 of solvent accessible surface. This exposed area is equivalent to 10.66 \AA^2 surface buried on ADP binding. Lys44 is involved in an interaction with the macrocycle hydroxyl of geldanamycin giving rise to a negative peak of 24.31 \AA^2 . In ADP, Lys44 makes no interactions, but still reduces its solvent accessibility by 2.46 \AA^2 , which differs by 21.95 \AA^2 compared with the geldanamycin. Interestingly, both ADP and geldanamycin after binding to N-Hsp90, show nearly the same $\Delta SASA$ area per residue, except for residues Glu162, Met84, Val163, Lys98, Ser36, Thr22 and Lys44. These residues show an increase of 25.80, 18.66, 18.39, 17.59, 15.23, -12.93 and -21.85 \AA^2 , respectively after geldanamycin binding compared with ADP.

Various empirical equations for the calculations of the ΔC_p upon ligand binding based on $\Delta SASA$ have been proposed by Makhatadze and Privalov (32), Myers et al. (33), and Spolar and Record (31), see Section 1.3.1. When the ΔC_p was estimated using these empirical relationships ($\Delta C_{p,cal}$), there is a striking lack of agreement in N-Hsp90-ADP calculations, while the Hsp90-geldanamycin calculation matches well with the experimental calculations. ΔC_p calculations according to equation 1.3.5 for N-Hsp90-geldanamycin interaction give a value of $-0.46 \text{ kJ}\cdot\text{mol}^{-1}\cdot\text{K}^{-1}$, which nearly matches the experimental value of $-0.39 \pm 0.04 \text{ kJ}\cdot\text{mol}^{-1}\cdot\text{K}^{-1}$ (Table 3.2.22). Equations 1.3.2 and 1.3.4 for N-Hsp90-geldanamycin binding give values of $-0.27 \text{ kJ}\cdot\text{mol}^{-1}\cdot\text{K}^{-1}$ and

-0.30 kJ·mol⁻¹·K⁻¹ respectively, which are within the accepted errors of experimental measurements. Calculated ΔC_p ($\Delta C_{p_{cal}}$) according to equation 1.3.2 for the N-Hsp90-ADP interaction gives a value of 0.21 kJ·mol⁻¹·K⁻¹; equations 1.3.4 and 1.3.5 give values of 0.03 kJ·mol⁻¹·K⁻¹ and 0.19 kJ·mol⁻¹·K⁻¹ respectively, which are significantly different from the experimental value of 2.35 ± 0.46 kJ·mol⁻¹·K⁻¹ and are 6 to 18 times higher than the calculated ΔC_p (Table 3.2.21). Comparing $\Delta C_{p_{cal}}$ values with observed ΔC_p ($\Delta C_{p_{obs}}$) for other ADP analogues like ATP and cAMP, shows a wide difference of around 3 to 10 times, however for AMPPNP the difference was small with a value of 0.0 to 0.36 kJ·mol⁻¹·K⁻¹. Nonetheless AMPPNP being a non-hydrolysable analogue of ADP, will not be ionized at experimental pH conditions. Therefore ADP bound $\Delta C_{p_{cal}}$, can not be compared with the $\Delta C_{p_{obs}}$ for AMPPNP binding, as AMPPNP will be present in non-ionized form unlike ADP.

Incorporation of trapped water molecules in $\Delta C_{p_{cal}}$ calculations resulted in identical values for the N-Hsp90-geldanamycin interaction except for equation 1.3.5; where $\Delta C_{p_{cal}}$ shows a difference of only 0.01 kJ·mol⁻¹·K⁻¹ (Table 3.2.24). Conversely for the N-Hsp90-ADP interaction, $\Delta C_{p_{cal}}$ values differ by around 0.02 to 0.10 kJ·mol⁻¹·K⁻¹, with the biggest difference of 0.10 kJ·mol⁻¹·K⁻¹, observed with equation 1.3.2 proposed by Spolar et al. (31). These results show that even after including trapped water molecules in the ΔC_p calculations, a marked improvement in the agreement between $\Delta C_{p_{obs}}$ and $\Delta C_{p_{cal}}$ can not be obtained. Nonetheless, a noticeable difference can be observed, if $\Delta C_{p_{cal}}$ involves a large number of water molecules as in the case of the N-Hsp90-ADP interaction.

What causes such a discrepancy in the $\Delta C_{p_{cal}}$ of N-Hsp90-ADP binding? The first possible explanation is that the calculation of ΔC_p using equation 1.3.2 is not applicable to a system that shows discrepancies (like the positive ΔC_p in this work) or there are some other responsible factors. The present calculations using equation 1.3.3 neglect the heat capacity changes associated with the internal interactions and assume that the effect is entirely because of hydration. However it has been shown that internal interactions contribute more than 5-10% to the observed ΔC_p of globular proteins (39; 162; 163). The second possible explanation of the observed discrepancies between the experimental and predicted changes in ΔC_p is water penetration (164). It has also been proposed from both experimental and theoretical studies that transient and permanent water molecules can be found in the protein ligand binding site, which can have a marked effect on the binding associated ΔC_p (7). Thirdly, all these $\Delta SASA$ calculations were developed using data from

the transfer of benzene and other small hydrocarbons and scaled up to predict ΔC_p in proteins, which are much more complex entities than small hydrocarbons. Also the role of metal in ΔC_p calculations, especially if the metal is present in the binding site, has not been discussed widely; however research done by Yamada et al. (122) using calorimetry points towards positive ΔC_p .

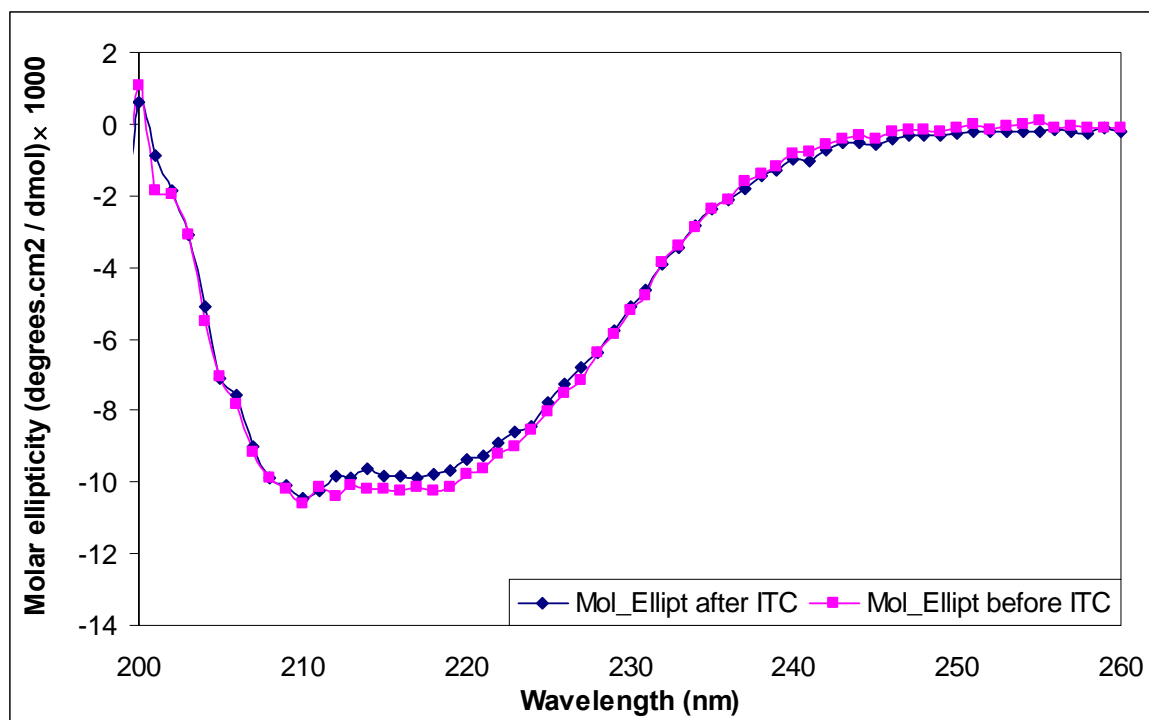


Figure 3.2.17 CD spectrum for N-Hsp90 bound to AMPPNP and on its own, measured at 25 °C in 20 mM Tris buffer pH 8.00. CD spectrum shows that protein is not unfolded after binding of AMPPNP in ITC.

Interestingly our data suggest that ΔS_{ASA} on binding can also result in a positive ΔC_p , which is unobserved and unreported in previous protein-ligand interactions. On the other hand, a positive ΔC_p can be observed in protein-ligand binding, if the protein is unfolding on binding of a ligand or undergoing structural transitions in the bimolecular complex (allosterism). However CD studies conducted on N-Hsp90, with and without AMPPNP showed very little difference (Figure 3.2.17) in the secondary structure of N-Hsp90; allaying this theory. The Hsp90-ADP/ATP binding site traps several water molecules, especially between the phosphate side-chain of ADP/ATP and N-Hsp90. These buried water molecules appear to be positionally ordered. Thus it is expected that release of buried water molecules from the binding site will affect the ΔC_p value. For example, Morton and Ladbury (41) estimated the ΔC_p of burying a water molecule to be between

-25 and $-50 \text{ J}\cdot\text{mol}^{-1}\cdot\text{K}^{-1}$, while Holdgate et al. (125) estimated the ΔC_p of burying a water molecule to be around $-200 \text{ J}\cdot\text{mol}^{-1}\cdot\text{K}^{-1}$. This indicates burial of water molecules will produce higher negative $\Delta C_{p_{\text{obs}}}$ values, than $\Delta C_{p_{\text{cal}}}$.

However, we have observed higher positive ΔC_p values than the calculated ΔC_p . To understand this discrepancy, we decided to study structural transitions in the bimolecular complex after binding of small molecules to N-Hsp90 by MD simulation, with special emphasis on the role of water (water residence time). This is discussed in detail in Section 3.2.8.

3.2.8 Molecular Dynamics (MD) Simulations Study of Ligand Binding to N-Hsp90

Water plays an important role in functioning of proteins and small molecule binding (165). Buried water molecules, especially those considered to be of structural importance, have been investigated by molecular dynamics simulations in recent years (166-168). Water also has a global influence on protein stability and protein folding through the hydrophobic effect (35) and also acts as a single molecule in biological events (125; 169). In a landmark study of internal water in bovine pancreatic trypsin inhibitor (BPTI), displacement of single water molecule resulted in protein destabilisation of $2.92 \text{ kJ}\cdot\text{mol}^{-1}$ (169) [This water molecule has been found to have the longest water residence time out of four buried water molecules in BPTI, determined to be $170 \pm 20 \mu\text{s}$ at $25 \text{ }^\circ\text{C}$ (168).

According to Williams et al. (170), water molecules present in protein solutions can broadly be classified theoretically into three major categories:

1. Strongly bound internal water molecules
2. Water molecules that interact with the protein surface
3. Bulk water

Bound water molecules occupying internal cavities and deep clefts can be identified crystallographically. Such water molecules, which are extensively involved in the protein-solvent H-bonding, often play a crucial role in maintaining protein structure. On the contrary, surface waters usually called 'hydration waters', exhibit a heterogeneous behaviour because of their interaction with solvent-exposed protein atoms having different chemical character and topography. Finally, water that is not in direct contact with the protein and continuously exchanging with surface bound water molecules, reveals properties that approach those of bulk water to the degree that solvent molecules at increasing distance from the protein surface are taken into account (171).

X-ray diffraction and NMR are two experimental techniques that have predominantly provided a better understanding of bound waters at the atomic level. Positionally ordered water molecules detected in crystal structures of proteins were suggested to reflect well-defined local free energy minima (172). NMR experiments reveal that the water molecules in the first protein hydration layer are exchanging rapidly with the solution with exchange times of less than 500 ps (173). Protein-solvent interaction can also be described effectively with molecular dynamics (MD) simulation, because it provides a

microscopic description of the protein water system on the picosecond time scale, allowing evaluation of the mean residence time of water molecules around a specific atom type.

In this work, we have investigated the role of buried water molecules found at the N-Hsp90-ADP/ATP and N-Hsp90-Geldanamycin interfaces by MD simulation. It is known from our earlier calorimetric experiments that N-Hsp90 binds to ADP/ATP with a positive ΔC_p and displays a negative ΔC_p after binding to geldanamycin. Molecular dynamics (MD) simulations can be helpful in providing a variety of detailed information regarding water residence times, hydrogen bonding, protein and ligand flexibility and dynamics of water molecules. These could be used to describe differences in the binding thermodynamics of two similar protein-ligand systems. Hence, we have decided to use MD simulations in conjunction with thermodynamic data to explain in detail the correlation between ΔC_p and various MD derived parameters.

3.2.8.1 Identification of Hydration sites in N-Hsp90-ATP/ADP and N-Hsp90-Geldanamycin Binding site

For the purpose of this work, protein hydration sites are defined as local maxima in the water oxygen density map that satisfy certain conditions. They should be no farther than 5 Å from any protein-ligand atoms and must be present between the N-Hsp90-ATP/ADP binding interface. As a result, the crystal structure of Hsp90 bound to ADP (PDB: 1AM1 and 1AMW) contained 8 trapped water molecules (Table 3.2.25). With a few exceptions, buried water molecules have been observed crystallographically in polar cavities in which they are seen to form hydrogen bonds with the protein atoms.

3. Results and Discussion

Crystal Water Molecule	ADP Atoms	N-Hsp90 Atoms
HOH400 (1AM1/1AMW)	ADP300 N7	ASN37 H26
HOH401 (1AM1/1AMW)	ADP300 N6	LEU34 O
HOH403 (1AM1/1AMW)	ADP300 N1	GLY83 H8, Asp79 OD1
HOH404 (1AM1/1AMW)	ADP300 H79, ADP300 N3	ASN92 OD1
HOH408 (1AM1/1AMW)	ADP300 O2B	ASP40 OD2
HOH624 (1AM1) / HOH625 (1AM1) / HOH664 (1AMW)	ADP300 O1A	GLY121 O
HOH628 (1AM1) / HOH406 (1AMW)	ADP300 O3B	GLY118 O
	ADP300 O2A	GLY123 N

Table 3.2.25 Nearest protein atoms located in close proximity to the buried crystal water molecules between N-Hsp90 and ADP. (PDB: 1AM1 and 1AMW shows highly similar positions for water)

Crystal Water Molecule	Geldanamycin Atoms	N-Hsp90 Atoms
HOH400 (1A4H)	GMY300 H178	THR171 OG1, GLY83 H8
HOH402 (1A4H)	GMY300 N36	LEU34 O
HOH407 (1A4H)	GMY300 O24	ASN92 (hydrophobic face)
HOH529 (1A4H)	GMY300 N22	GLY123 H8

Table 3.2.26 Nearest protein atoms located in close proximity to the buried crystal water molecules between N-Hsp90 and Geldanamycin.

3.2.8.2 General Structural Analysis

To analyze the structural behaviour of N-Hsp90, N-Hsp90-ADP and N-Hsp90-geldanamycin molecules during the simulations, the root-mean square deviation (RMSD) was calculated. Figure 3.2.18 shows the RMSD values calculated for each macromolecule system during the simulations. RMSD calculated from the initial X-ray structure has been computed for all MD trajectories.

The positional fluctuations of the C_{α} atoms have also been computed on the whole length of trajectories (12 ns.) and show a global behaviour similar in different trajectories with amplitude fluctuations ranging from about 0.1 to 0.2 nm for secondary structures. The conservation of the secondary structure is demonstrated by an analysis of the hydrogen bonds formed between the backbone Asp79 carbonyl group and the amine group present

on the adenine ring of ADP. The single N-Hsp90-water system reached a stable RMSD at 1.50 ns, with N-Hsp90-ADP and N-Hsp90-geldanamycin system requiring 0.80 ns and 1.00 ns respectively (Figure 3.2.18). At the end of the 12 ns simulation, N-Hsp90 did not exhibit significant changes in terms of the three-dimensional positioning of amino acid residues forming the secondary structure.

According to MD simulations studies carried out previously (174; 175), if the simulation reached an RMSD that oscillates around a constant value, it can be assumed that the system has converged to a stable or metastable state. In our simulations, calculated C_{α} RMSD values range between 0.1 and 0.2 nm and indicate rather stable geometries for the backbone.

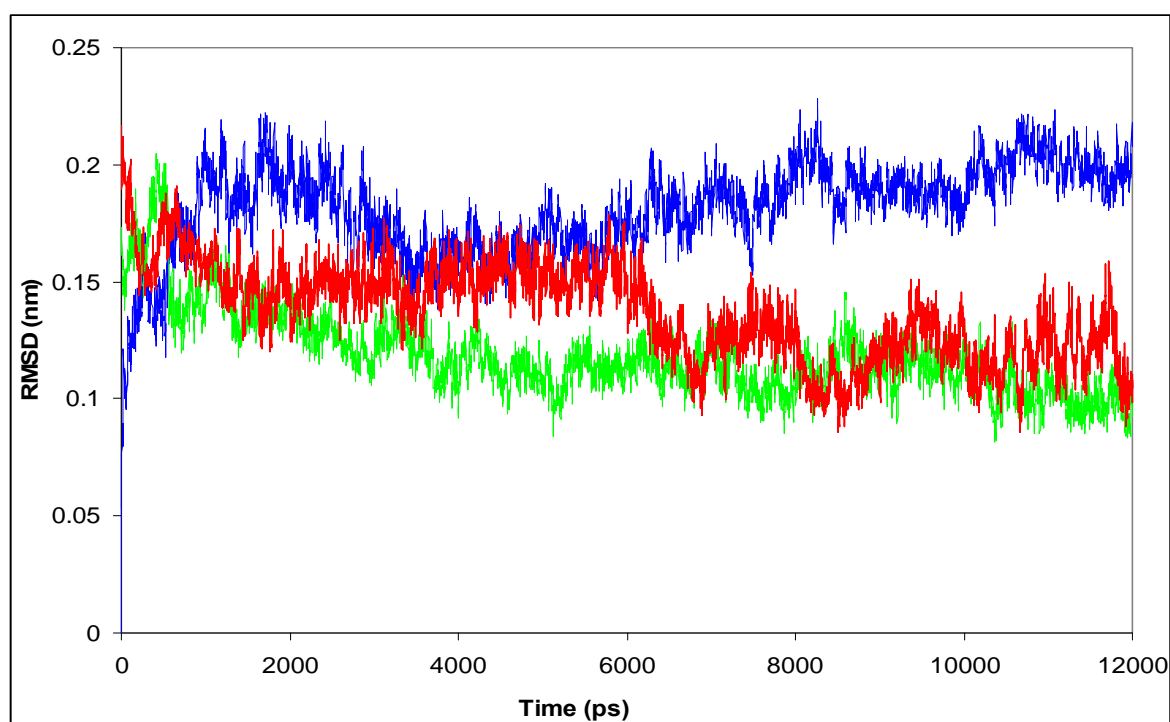


Figure 3.2.18 Root mean square deviation (RMSD) of the backbone atom positions from their starting positions as a function of time, for simulations of the N-Hsp90 (blue line), N-Hsp90-ADP (green line) and N-Hsp90-geldanamycin models (red line). (Trajectories are only shown for first 12 ns out of total 20 ns MD simulation run)

The C_{α} root mean-square fluctuations (RMSF) as a function of residue number have also been calculated to categorize the relative mobility of different regions of the protein as shown in Figure 3.2.19. The protein conformational stability was examined by a calculation of the backbone root mean-square deviations (RMSD) relative to the protein crystal structure throughout the simulations.

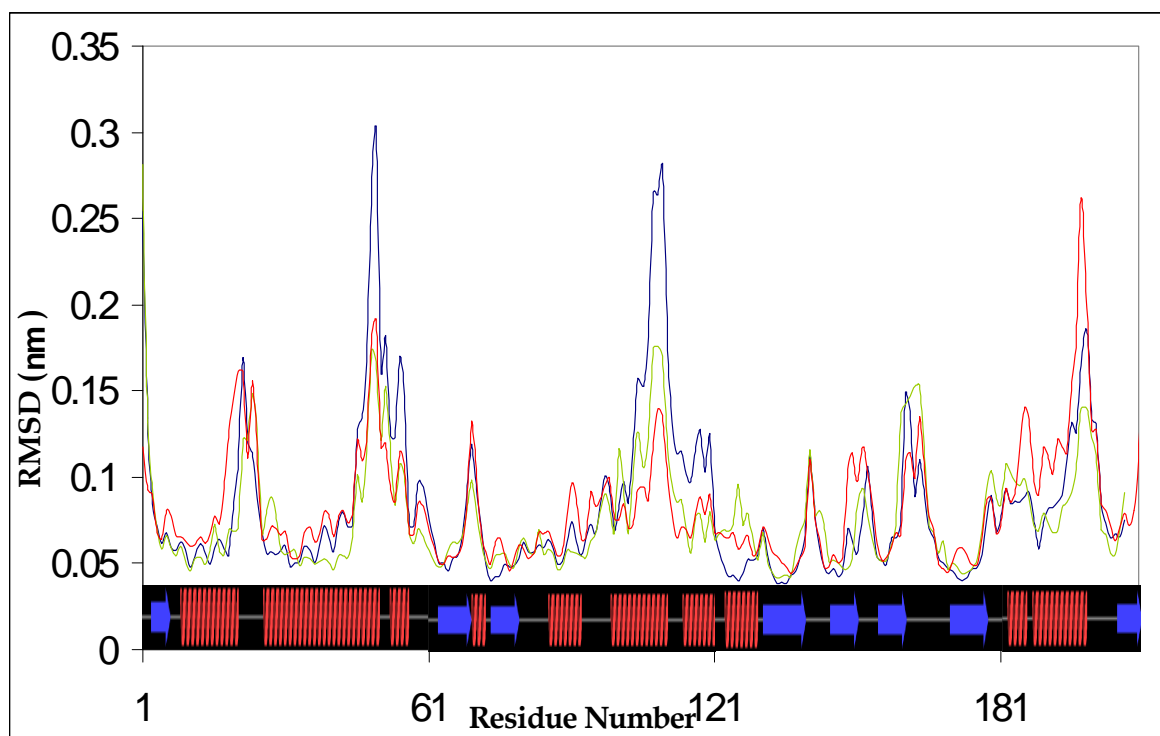


Figure 3.2.19 Residue-by-residue RMSF fluctuations around their average positions for N-Hsp90 (blue), N-Hsp90-ADP (Green) and N-Hsp90-Geldanamycin (Red).

Residues 0 to 207 have RMSF ranging from 0.04 to 0.31 nm for the free protein, 0.05 to 0.18 nm and 0.05 to 0.26 nm for the ADP and geldanamycin bound form, respectively. The RMSFs of all three systems are reasonable in comparison with the B-factors for each residue, with the maximum RMSF peaks at turns and loops in most of the apo and bound forms of proteins. In the regions of residues 48-52 and 106-121, the RMSF of the free protein is more mobile than that of the bound one by about 0.01 and 0.10 nm, respectively, indicating these are the regions where ADP and geldanamycin association with the protein affects dynamics and rigidity. While in the region 181 to 202 geldanamycin association results in higher RMSF of N-Hsp90 than on its own or in ADP-bound form.

Other than for the loop residues, the fluctuations are less than 0.1 nm, and for some α -helices they are nearly as low as 0.07 nm. In general, the maximal C_{α} RMSD and C_{α} RMSF values are between the accepted limits and indicate that N-Hsp90 did not undergo any significant conformational changes during the simulations.

3.2.8.3 Assessment of Water Residence Times In N-Hsp90-ATP/ADP and N-Hsp90-Geldanamycin Binding Site

Even though the Hsp90-ADP complex has many of the distinctive characteristics expected at the protein-ligand interface, like direct H-bonds, it also has a significant amount of water present at the interface when compared to other systems such as Hsp90-geldanamycin. In fact, the current X-ray crystallographic structure has eight water-mediated H-bonds within the Hsp90-ADP interface (54). These buried crystal water molecules would be permanently trapped inside the protein or at the protein-ligand interface, if the protein structure were static, but proteins are dynamic and assume a number of different conformations allowing the buried water molecules to exchange with the bulk water molecules (170; 176). The dynamics of eight crystal water molecules in yeast N-Hsp90 and human N-Hsp90 have been examined by monitoring their path along 12-ns trajectories of N-Hsp90-ADP in solution. All eight water molecules at the interface become fully solvent accessible at different times in the course of 12 ns of simulation. This also holds true for a 12-ns simulation of N-Hsp90-geldanamycin. Visual inspection of portions of the different trajectories confirms that these water molecules indeed exit the buried hydration sites and diffuse to bulk water.

To assess the potential exchange of water molecules in the eight different positions two criteria need to be fulfilled:

1. The water in the X-ray crystallographic structure must be present at the interface of protein and ligand (Mg^{2+} -ADP and geldanamycin).
2. These water molecules must form an H-bond with protein and ligand residues directly, and not form indirect H-bonds through another water molecule or to a water molecule.

After careful analysis, only 6 out of 8 water molecules fulfilled the criteria in the N-Hsp90-ADP interface and were subjected to further analysis. The average occupancy describes the equilibrium constant for a site. Ideally, it would be equal to 1 at a site in a perfect, crystalline system. Tables 3.2.27 and 3.2.28 illustrate the distributions of water residence times at the hydration sites for N-Hsp90-ADP and N-Hsp90-geldanamycin respectively, and values range from 51 to 879 ps. However, each one of the hydration sites shows a residence time which is far higher than the residence of bulk water. Chen et al. (177) predicted a residence of 1 ps or less for bulk water molecules. In this work, most residence times of water molecules in the cleft of the active site are about 350 to 450 ps,

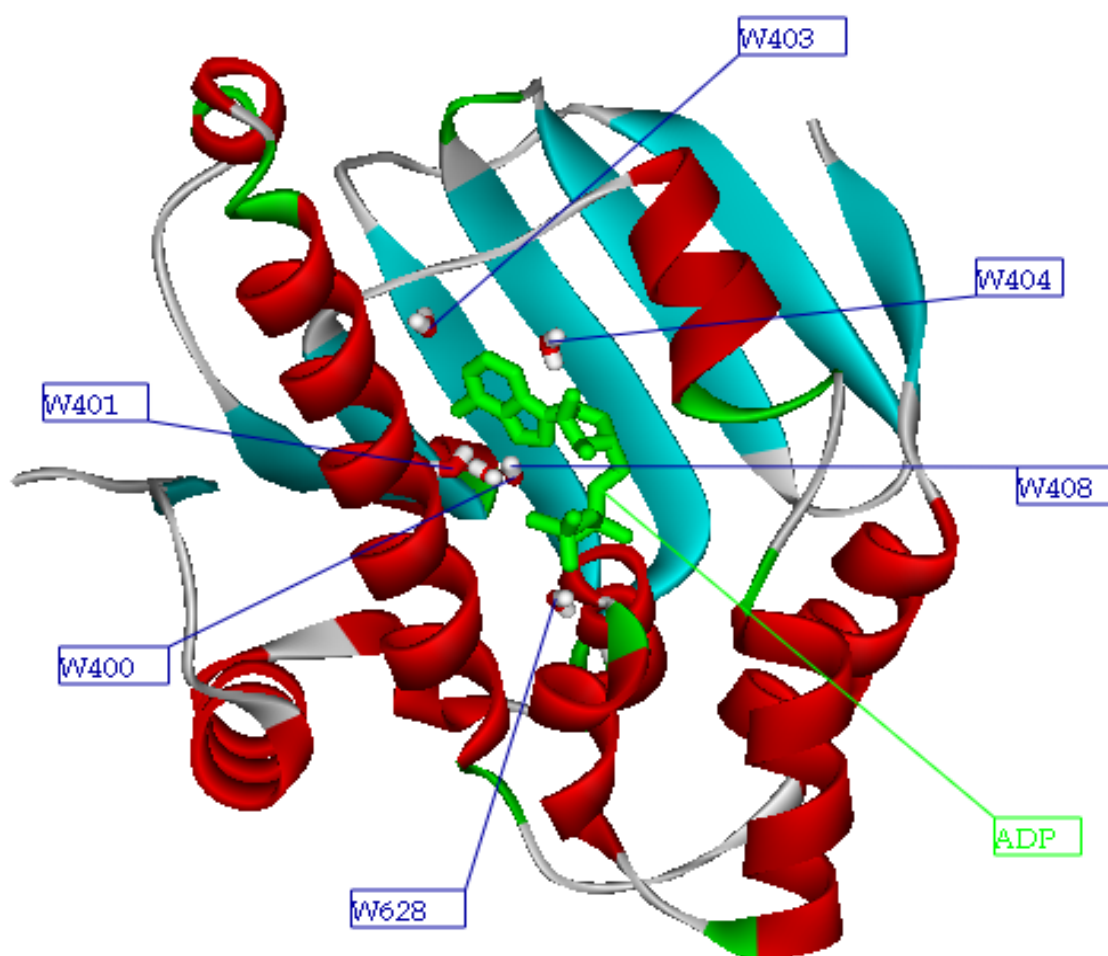


Figure 3.2.20 Structure of N-Hsp90 with ADP along with number of water molecule investigated. (Figure generated using DS ViewerPro 5.0 (56))

Water Number	Residence Time (ps)
W _A 400	577.4
W _A 401	132.2
W _A 403	879.2
W _A 404	345.3
W _A 408	322.7
W _A 628	359.6

Table 3.2.27 Water residence time of different water molecules in the N-Hsp90-ADP binding interface.

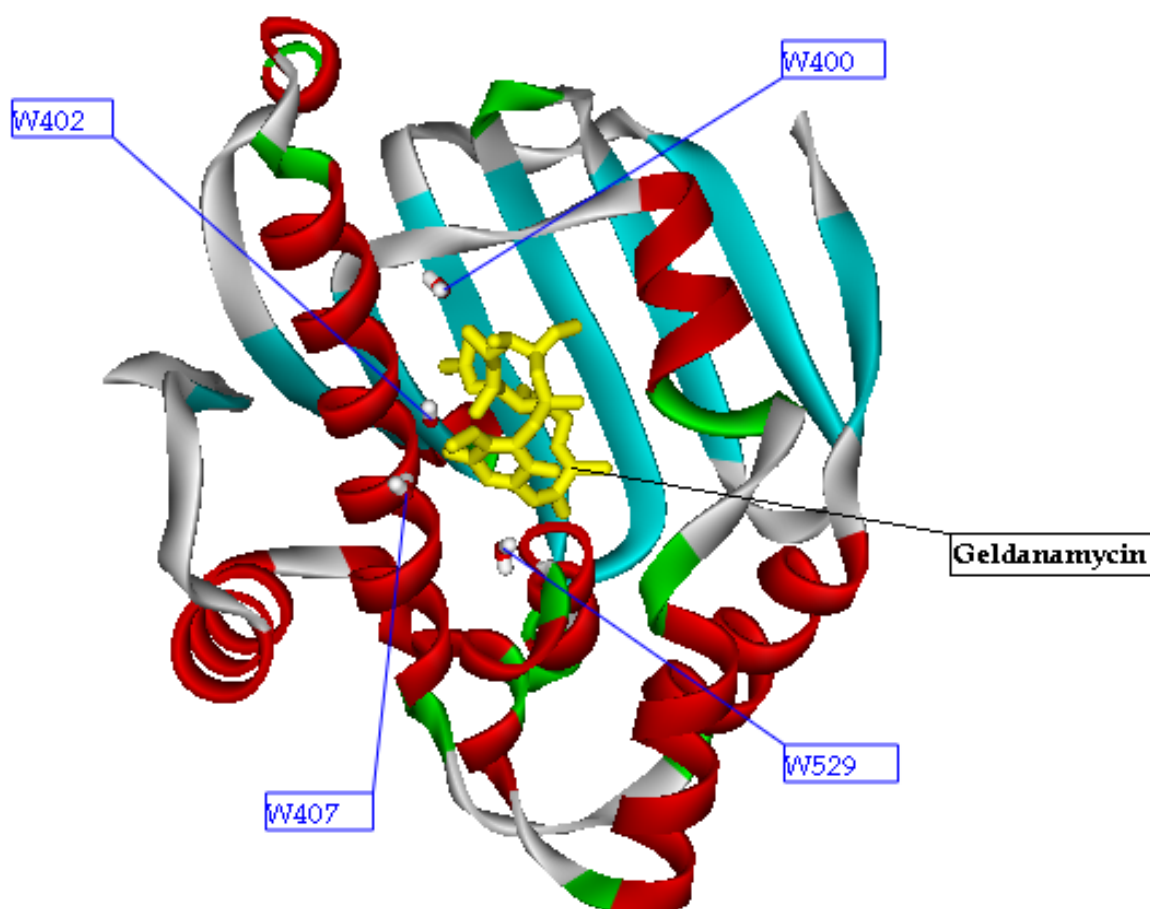


Figure 3.2.21 Structure of N-Hsp90 with geldanamycin along with number of water molecule investigated. (Figure generated using DS ViewerPro 5.0 (56))

Water Number	Residence Time (ps)
W _G 400	76.7
W _G 402	66.7
W _G 407	51.4
W _G 529	173.6

Table 3.2.28 Water residence time of different water molecules in the N-Hsp90-geldanamycin binding interface.

which matches well with the 400 ps observed in the protein myoglobin by Makarov et al. (102).

For the sake of simplicity, water numbers in the two different systems are denoted by subscript A in the N-Hsp90-ADP complex, while subscript G represents the N-Hsp90-geldanamycin system. In the N-Hsp90-ADP complex all of the water molecules except W_A401 show a water residence time higher than 300 ps (Figure 3.2.20 and Table 3.2.27). Site W_A400 and W_A403 are embedded deep inside the ADP binding pocket with no solvent accessibility, which results in maximum water residence times of 577.4 ps and 879.2 ps respectively. This higher residence time can also be attributed to water being confined to a deep cleft, from where it takes a long time to exchange with bulk water. Water W_A401 shows the lowest residence time among all the water molecules in the binding interface and results from easy solvent accessibility to bulk water, from where it can exchange rapidly. W_A404 H-bonds to Asn92 situated in an α -helix and also makes extensive H-bonds with ADP, giving it a higher residence time of 345.3 ps; even though it is fully solvent accessible to bulk water. W_A404 also forms an H-bond with another water molecule (W_A405), which shields it against exchange with other bulk water molecules.

Although water is continually exchanged from the Mg^{2+} ion, Mg^{2+} still keeps six ligands during the entire simulation. W_A408 and W_A628 are H-bonded and form a water shell around the Mg^{2+} . Interestingly both W_A408 and W_A628 show a similar residence time of 322.7 ps and 359.6 ps, respectively. These high residence times are attributable to the strong affinity of water molecules towards magnesium. Water residence time around Mg^{2+} can also be affected by the handling of ligation in the force field used. Such a polarization can be very important around highly charged ions like Mg^{2+} .

The hydration pattern of the water molecules at the N-Hsp90-geldanamycin interface is totally different from the hydration pattern observed in the N-Hsp90-ADP binding site (Figure 3.2.21 and Table 3.2.28). The location of water W_G402 is same as water site W_A401 in the N-Hsp90-ADP system, but has a residence time of 66.7 ps, a decrease of 65.5 ps relative to the N-Hsp90-ADP complex. It is noteworthy that all of the sites with residence times shorter than 76.7 ps are located in the protein interior or clefts of the protein. W_G529 is situated at the edge of the geldanamycin binding pocket and still shows a long lived water residence time of 173.6 ps. This long life of W_G529 can in part be attributed to extensive hydrogen bonding with protein and the geldanamycin molecule.

Interestingly, most of the water molecules in the N-Hsp90-geldanamycin interface are short lived and show a residence time of 80 ps or less, as opposed to about 300-900 ps observed for most of the water molecules in the N-Hsp90-ADP interface. This pattern of differing water residence times in two binding interfaces can be fully explained by the

hydrophobic character of geldanamycin, compared to the charged polar character of ADP. Normally in the literature, the noted trend of dependence of residence times on the amino acids is $\tau_{\text{charged}} > \tau_{\text{polar}} > \tau_{\text{apolar}}$ (102). However water residence times also depend upon several other properties of a protein. The topography of the protein surface and the identity of the amino acids are the two most important factors (102).

3.2.8.4 Assumption and limitations

From the results obtained from the two MD simulation studies, it could be assumed that the N-Hsp90-ADP complex shows relatively strong interactions between hydration sites as well as between the sites and biomolecules compared to N-Hsp90-geldanamycin. This strong attraction can in part be attributed to placement of a hydrophobic group in a predominantly hydrophilic binding site of N-Hsp90-ADP. In the calorimetry experiment, ADP binding to N-Hsp90 shows higher ΔH of $-7.65 \text{ kJ}\cdot\text{mol}^{-1}$ than observed for binding of geldanamycin to N-Hsp90. This higher ΔH can be attributed to stronger hydrogen bonding and/or higher water residence time.

Secondly, Mg^{2+} keeps six ligands during the entire simulation, upon binding to N-Hsp90. However it shows ligand exchange, as the water molecules around it exchange with bulk water. Interestingly, most of these water molecules show a similar but sometimes higher water residence time and can be credited in part to the charged interaction occurring between water and magnesium. These water molecules show about 300 to 360 times higher water residence time than the bulk water (102), even though these magnesium bound waters are almost exposed to the bulk waters.

The N-Hsp90-ADP and N-Hsp90-geldanamycin binding interfaces shows differing water residence times, nevertheless both ADP and geldanamycin bound structures show remarkable stability and integrity of fold. This integrity and stability rules out any possibility of allosteric effects in binding. Also from the results obtained by MD simulation, it is clear that neither structure plays any significant role in modulating ΔC_p .

3.2.9 Conclusion

In summary, an effort has been made to investigate the effect of various internal factors on the positive ΔC_p . As a result, a series of experiments involving varying buffer conditions, differing salt concentration, performing interactions in D₂O and MD simulation was performed. The results obtained clearly shows that, none of these factors is responsible for the observation of a positive ΔC_p of binding in the N-Hsp90 and AMPPNP interaction as compared to a negative ΔC_p of binding in the N-Hsp90 and geldanamycin interaction

Moreover in pH dependent binding titrations, at pH 8.00 the $\Delta C_{p_{obs}}$ is around $0.37 \pm 0.22 \text{ kJ}\cdot\text{mol}^{-1}\cdot\text{K}^{-1}$ (Section 3.2.4) and calculation of individual ΔC_p components with equation 3.2.4, shows that the rest of the $\Delta C_{p_{obs}}$ difference can be attributed to contributions coming from factors such as the bound water molecules, complex dynamics or ion/metal effects (41; 42; 126). Therefore, the explanation for positive ΔC_p may be lying in a strict requirement for divalent metal (Mg^{2+}) for binding of N-Hsp90 with AMPPNP, as compared to non-requirement in N-Hsp90-geldanamycin interactions. Consequently, further studies were carried out on the role of divalent metals on binding N-Hsp90 with AMPPNP and are discussed in the next section.

3.3 Role of Metal Ions in the N-Hsp90-AMPPNP Interaction

The thermodynamics of the protein-ligand binding process can be interpreted in terms of the following schematic model, proposed originally by Ross and Subramanian (178).

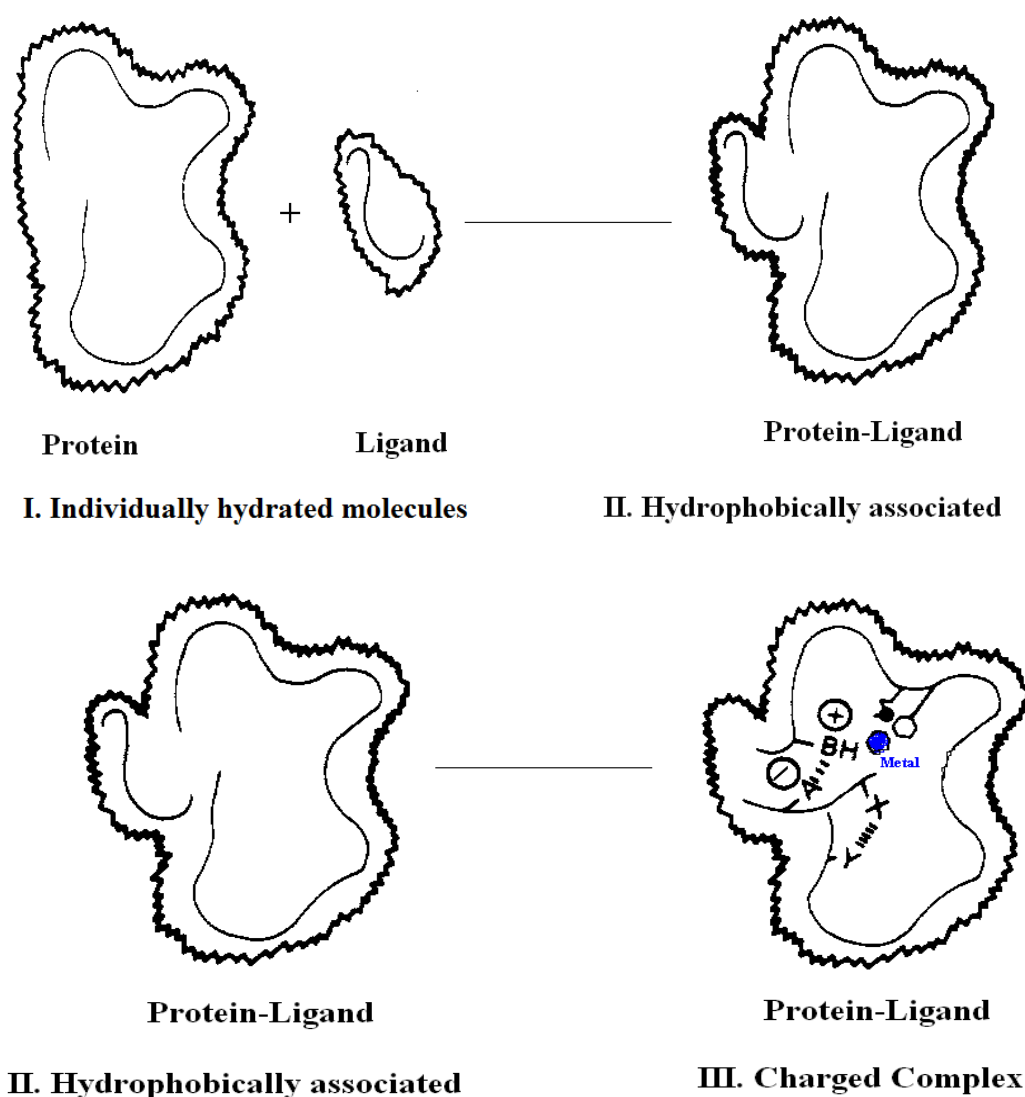


Figure 3.3.1 Schematic diagram showing protein-ligand binding. In the top diagram protein is shown reacting with ligand. The fuzzy outline surrounding protein, ligand and protein-ligand complex denotes water that is more ordered than the bulk solvent. Protein-ligand binding is depicted as occurring in two steps. I→II denotes hydrophobic association. II→III represents all other intermolecular interactions (Adapted with minor modifications from Ross and Subramanian (178)).

The protein-ligand binding process can be envisioned as proceeding from thermodynamic binding states I to II and then to III, as schematized in Figure 3.3.1. In this representation, state I represents isolated hydrated species, while in state II these isolated

3. Results and Discussion

hydrated species bind. In state II there is mutual penetration of hydration layers to form a hydrophobically bound complex. These hydrophobic interactions result because of the penchant of the waters to form a more ordered structure in the vicinity of nonpolar hydrocarbon groups (179-181). Theoretically, the hydrophobic effect in protein-ligand association simply means that hydrophobic amino acid side-chains, which were previously accessible to water in the isolated subunits; become buried after complex formation and produce a decrease in the number of ordered water molecules (182). In state III, these species are bound electronically or by charge-charge interactions.

Process	ΔH	ΔS	Reference
Hydrophobic association	Positive	positive	(183; 184)
van der Waals	Negative	Negative	
H-bond formation in low dielectric medium	Negative	Negative	(185)
Ionic (charge neutralization)	Slight positive or negative	positive	(186)
Protonation	Negative	Negative	(187)

Table 3.3.1 Some of the expected thermodynamic signs for possible contributions to thermodynamic process. Adapted from Ross and Subramanian (178).

Until now, we have studied different aspects of N-Hsp90-ADP/ATP and N-Hsp90-geldanamycin interaction taking these associations as a hydrophobic species. This approach proved mostly unsuccessful and failed to shed light on establishing the cause of positive ΔC_p effects in N-Hsp90-ADP/ATP interaction. Therefore we considered investigating the role of charge interactions as there is a considerable body of evidence (178; 188), which indicates that ionic interactions and formation of ion pairs (e.g., charge neutralization of ADP) can affect ΔC_p , ΔS and ΔH substantially (8). These types of interactions play an important part in binding resulting from the desolvation of charged surfaces and ions (178; 188). Additionally, charge interactions can also alter thermodynamic values of ΔH in both the directions (\pm) (Table 3.3.1) (178).

Mg^{2+} plays an important role in N-Hsp90-ADP/ATP interactions and in the N-Hsp90-ADP binding site, Mg^{2+} ion is octahedrally coordinated by the α - and β -phosphate groups of the ADP. Mg^{2+} also forms several water mediated H-bonds with protein backbone and side-chains. Without Mg^{2+} , N-Hsp90 loses its binding affinity for the ADP/ATP.

Normally in protein-ligand binding, metal ions can play at least three important roles namely:

1. To effectively bridge distances between residues or domains of the protein,
2. To act as a mediator in the interaction between the protein and the ligand,
3. To serve in the active site as either a nucleophilic catalyst or in an electron transfer role.

The thermodynamics aspects of divalent metal cations (Mg^{2+} , Ca^{2+} and Mn^{2+}) in protein-small molecule interactions is not properly understood. Here in this section, we investigated structural and thermodynamic aspects of divalent metal cations binding to N-Hsp90-ADP/ATP using both experimental (ITC and NMR) and theoretical methods, with special emphasis on ΔC_p in these interactions.

Investigating Thermodynamics of Divalent Metal-AMPPNP Binding to N-Hsp90

3.3.1 Prediction of Various Divalent Metal Binding and Divalent Metal Binding Site with GRID

We decided to probe substitution of various divalent metals cations like Mn^{2+} , Ca^{2+} in place of Mg^{2+} in the N-Hsp90-AMPPNP binding site. Modelling programs described by Gregory et al. (189), Schymkowitz et al. (190) and Sodhi et al. (191) are very successful in predicting these metal binding sites, however programs like GRID (88; 192) and modified GRID based methods (193; 194) are being increasingly used for predicting metal binding sites in proteins. It was therefore decided to predict metal binding sites with GRID, as it was very important that we do not obliterate the binding affinity between N-Hsp90 and AMPPNP.

Operating parameters used for GRID calculations are discussed in detail in Section 2.4 (Materials and Methods) and were used in this study. Human N-Hsp90- Mg^{2+} ADP structure (PDB: 1BYQ) refined by Obermann et al. (195) was used in the present study in place of yeast N-Hsp90-ADP crystal structure. The yeast N-Hsp90-ADP structure would have been ideal as we conducted all our experimental work with it, however the yeast N-Hsp90-ADP structure solved by Prodromou et al. (54) lacked a Mg^{2+} ion. The initial structure was processed by DS ViewerPro software (56) and the Mg^{2+} ion was removed. GRID calculations using a Mg^{2+} probe indicated the presence of one preferred binding site, with no other favourable binding sites observed. It correctly predicted five (ADP, Glu47, Asn51, Gly137, Phe138) out of six (ADP, Glu47, Asn51, Gly137, Phe138, Asp54) residues involved in contact with magnesium in the N-Hsp90-ADP binding site (Figure 3.3.2). At this position, the binding energy for a Mg^{2+} ion is around $-141.49 \text{ kJ}\cdot\text{mol}^{-1}$, which corresponds to the binding of a doubly positively charged ion to a highly negatively charged pocket and negatively charged phosphate side-chain of the ADP molecule.

However, the position predicted (most favourable position on the GRID map) was around 1.7 \AA away from the crystal structure position for the Mg^{2+} . One of the reasons for this different position of Mg^{2+} ion in the GRID map is Glu47. Glu47 with a negatively-charged carboxylic side-chain pulls the Mg^{2+} cation towards it, in competition

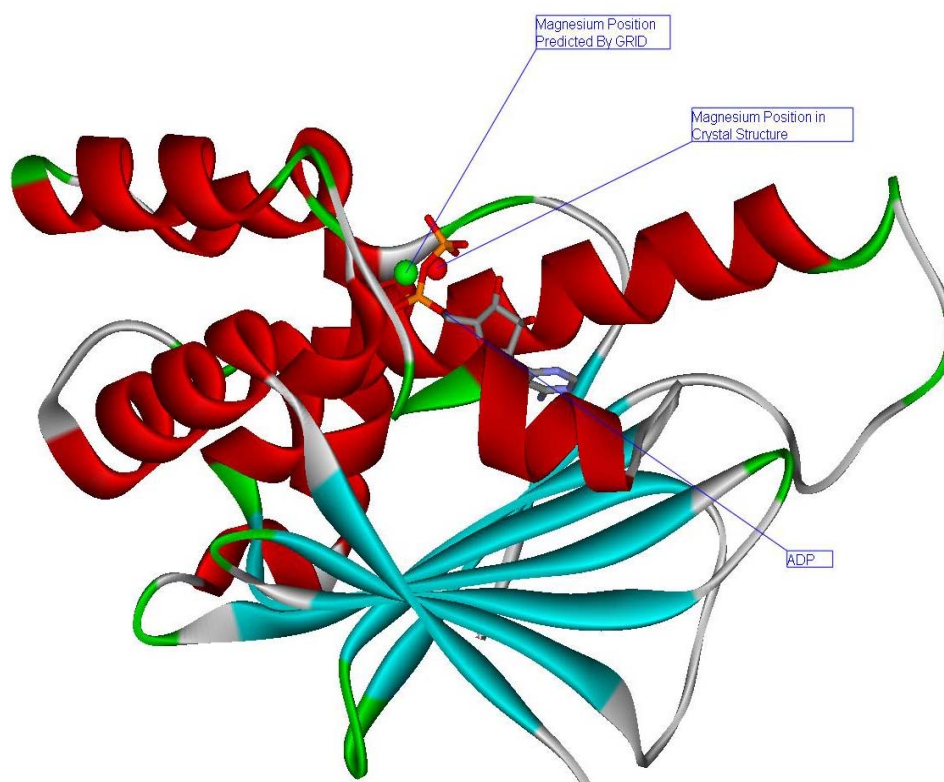


Table 3.3.2 X-ray crystal structure of N-Hsp90-ADP showing presence of Magnesium predicted by GRID (green) compared with crystal position of Magnesium (red). (Figure generated using DS ViewerPro 5.0 (56))

with the diphosphate side-chain of ADP. In the crystal structure, this cation is located next to the phosphate chain of ADP. The obtained results were however considered satisfactory in predicting the binding position of Mg^{2+} , and as a result predicting the position for Mn^{2+} and Ca^{2+} was continued.

GRID calculations using Mn^{2+} and Ca^{2+} groups as probes both resulted in one closely spaced minimum with no other favourable binding sites. The binding energies corresponding to these minima for Mn^{2+} and Ca^{2+} were -124.27 and -146.84 $\text{kJ}\cdot\text{mol}^{-1}$ respectively. The predicted position of the Ca^{2+} binding site was around 1.8 Å from the X-ray determined Mg^{2+} position and nearly matched the predicted Mg^{2+} position. For Mn^{2+} , the predicted binding site position was around 2.7 Å from the X-ray determined magnesium position and was placed much nearer Asn51, forming a H-bond with it. These results emphasise the preference of Mn^{2+} for nitrogen atoms compared to oxygen atoms and, as a result, water (196; 197). However it must be remembered that there is a large pocket between ADP and N-Hsp90, where water molecules and Mg^{2+} coexist. Prior to GRID calculations, these water molecules are removed. This creates a bigger space for

3. Results and Discussion

probe sampling and results in small inherent error in predicted position for divalent cations. Incidentally, magnesium is difficult to refine in crystal structure and as a result it has been added afterwards by modelling in most circumstances (Personal communication).

If one assumes that Mn^{2+} and Ca^{2+} metal bind to the phosphate side-chain in a similar way to that found in the GRID study, then clearly there will be a possible interaction for ADP with N-Hsp90 in an experimental binding assay.

3.3.2 Thermodynamics of Binding for Various Divalent Metal Cations

It is now well established that Ca^{2+} and Mn^{2+} can readily substitute for Mg^{2+} in biological environments. This is partially due to their preference for similar types of ligands, especially oxygen atoms (196). However Mn^{2+} has a slightly higher tendency to bind nitrogen ligands and is found particularly in its octahedral co-ordination environment.

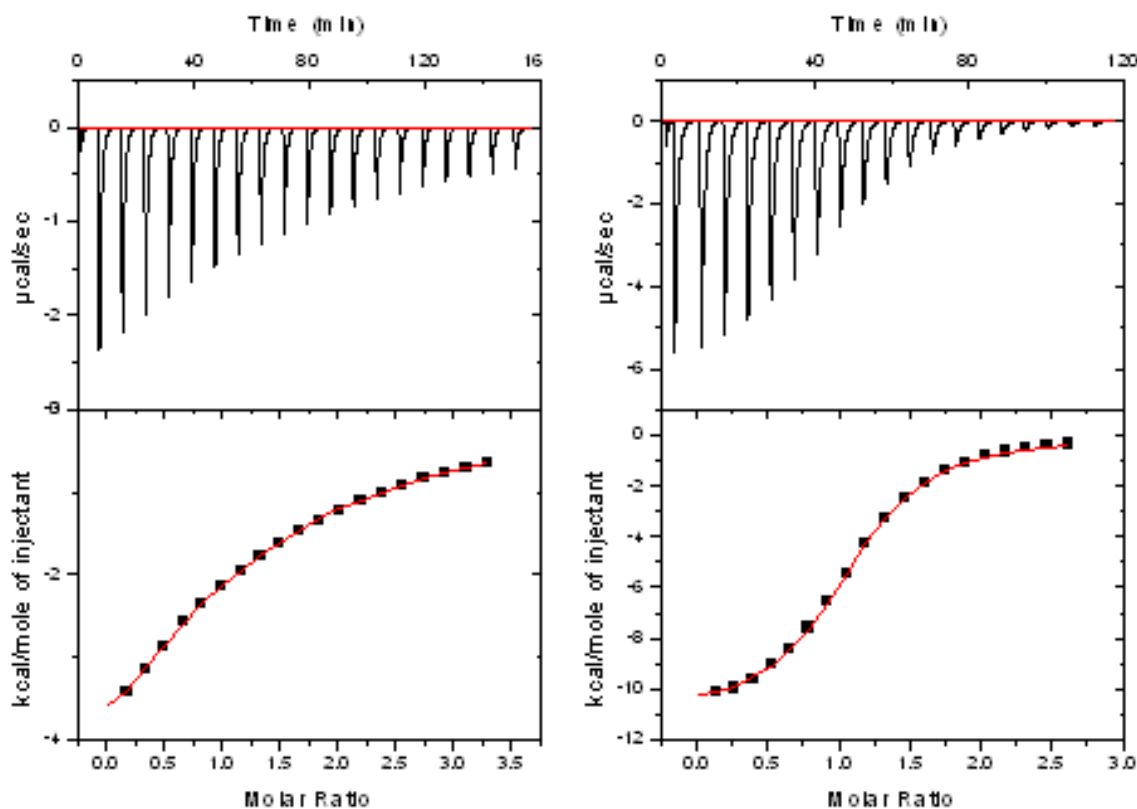


Figure 3.3.2 Isothermal titration calorimetric plot conducted at 12 °C for Ca^{2+} -AMPPNP binding to N-Hsp90 (left) and Mn^{2+} -AMPPNP binding to N-Hsp90 (Right).

Again, calorimetry was utilized to determine the binding affinity and binding enthalpy of AMPPNP binding to N-Hsp90 in the presence of Mn^{2+} and Ca^{2+} between 8 and 25 °C. The binding isotherm for calorimetric titrations of Mn^{2+} -AMPPNP and Ca^{2+} -AMPPNP binding to N-Hsp90 is displayed in Figure 3.3.2. The titrations for Ca^{2+} -AMPPNP binding to N-Hsp90 were carried out in 20 mM Tris buffer at pH 8.00. Whilst Mn^{2+} -AMPPNP titrations were carried out in 100 mM ACES buffer (pH 6.00), and were repeated in triple buffer (100 mM ACES, 50 mM Tris base, 50 mM Ethanolamine, pH 6.00) for comparison purposes. Change of pH from 8.00 to 6.00 for the Mn^{2+} titration was necessitated due to the unstable nature of Mn^{2+} at pH 8.00. For sake of clarity, the

3. Results and Discussion

Mg²⁺-AMPPNP-N-Hsp90 titration is compared with the Ca²⁺-AMPPNP-N-Hsp90 titration carried out in the same buffer and pH conditions. Mn²⁺-AMPPNP-N-Hsp90 titrations are compared with Mg²⁺-AMPPNP-N-Hsp90 titrations, also carried out in similar buffer and pH conditions. (Triple buffer pH 6.00)

Figure 3.3.3, 3.3.4 and Table 3.3.5, 3.3.6, 3.3.7 detail various thermodynamic parameters determined for the binding of Mg²⁺-AMPPNP, Mn²⁺-AMPPNP and Ca²⁺-AMPPNP to N-Hsp90. Table 3.3.3 and 3.3.4 detail comparative binding thermodynamics at 25 °C. Binding of Mn²⁺-AMPPNP to N-Hsp90 proceeds with a stoichiometry of close to 1, is exothermic, and unlike binding of the Mg²⁺-AMPPNP to the Hsp90 site, exhibits a small negative ΔC_p of $-0.18 \pm 0.01 \text{ kJ}\cdot\text{mol}^{-1}\cdot\text{K}^{-1}$.

Divalent metal cation	ΔH_{obs} (kJ·mol ⁻¹)	$T\Delta S_{\text{obs}}$ (kJ·mol ⁻¹)	ΔG_{obs} (kJ·mol ⁻¹)	ΔC_p (kJ·mol ⁻¹ ·K ⁻¹)
Mg ²⁺	-42.55 ± 0.20	- 15.80	- 26.75	0.00 ± 0.03
Ca ²⁺	$- 46.43 \pm 0.15$	- 19.49	- 26.94	$- 0.18 \pm 0.04$

Table 3.3.3 Comparison of binding thermodynamics for binding of Mg²⁺-AMPPNP and Ca²⁺-AMPPNP to N-Hsp90 at 8 °C (pH 8.00).

Divalent metal cation	ΔH_{obs} (kJ·mol ⁻¹)	$T\Delta S_{\text{obs}}$ (kJ·mol ⁻¹)	ΔG_{obs} (kJ·mol ⁻¹)	ΔC_p (kJ·mol ⁻¹ ·K ⁻¹)
Mg ²⁺	$- 38.38 \pm 0.24$	- 14.89	-23.49	0.28 ± 0.03
Ca ²⁺	$- 40.99 \pm 3.40$	- 20.68	- 20.31	1.04 ± 1.15

Table 3.3.4 Comparison of binding thermodynamics for binding of Mg²⁺-AMPPNP and Mn²⁺-AMPPNP to N-Hsp90 at 8 °C (pH 6.00). Binding was carried out in 100 mM ACES, 50 mM Tris, 50 mM Ethanolamine buffer.

3. Results and Discussion

Ligand	Temp (°C)	Stoichiometry (n)	$K_b \times 10^4$ (M ⁻¹)	K_d ⁽²⁾ (μM)	ΔH_{obs} (kJ·mol ⁻¹)	$T\Delta S_{\text{obs}}$ (kJ·mol ⁻¹)	ΔG_{obs} (kJ·mol ⁻¹)	ΔC_p (kJ·mol ⁻¹ ·K ⁻¹)
AMPPNP	8	0.96 ± 0.00	7.08 ± 0.13	14.10	-35.77 ± 0.13	- 9.66	- 26.11	
	12	1.08 ± 0.00	6.02 ± 0.12	16.60	- 46.27 ± 0.18	- 20.20	- 26.07	
	16	0.99 ± 0.00	3.43 ± 0.07	29.12	- 33.96 ± 0.18	- 8.87	- 25.09	
	20	1.08 ± 0.00	3.45 ± 0.08	28.90	- 46.06 ± 0.26	- 20.60	- 25.46	-0.16 ± 0.36
	21	1.17 ± 0.00	2.69 ± 0.05	37.05	- 44.76 ± 0.22	- 19.66	- 25.10	
	25	1.07 ± 0.01	1.45 ± 0.09	68.80	- 33.36 ± 0.82	- 9.74	- 23.62	
	29	1.04 ± 0.00	1.73 ± 0.03	57.80	- 45.47 ± 0.35	- 20.95	- 24.52	

Table 3.3.5 Summary of the thermodynamic parameters for the binding interaction of N-Hsp90-AMPPNP in 100 mM ACES, and 5 mM Manganese as a function of temperature (pH 6.00).

¹Data was fitted to a one-set-of-sites model.

²Dissociation constant values (K_d) were calculated as the reciprocal of the observed equilibrium binding constant ($K_d = 1 / K_{\text{obs}}$).

3. Results and Discussion

Ligand	Temp (°C)	Stoichiometry (n)	$K_b \times 10^4$ (M ⁻¹)	$K_d^{(2)}$ (μM)	ΔH_{obs} (kJ·mol ⁻¹)	$T\Delta S_{obs}$ (kJ·mol ⁻¹)	ΔG_{obs} (kJ·mol ⁻¹)	ΔC_p (kJ·mol ⁻¹ ·K ⁻¹)
AMPPNP	8	0.79 ± 0.05	0.59 ± 0.04	167.80	- 40.99 ± 3.40	- 20.68	- 20.31	2.10 ± 0.30
	12	1.11 ± 0.03	0.45 ± 0.01	217.62	- 29.73 ± 1.10	- 9.76	- 19.97	
	18	0.85 ± 0.04	0.62 ± 0.05	158.90	- 19.60 ± 1.34	1.54	- 21.14	

Table 3.3.6 Summary of the thermodynamic parameters for the binding interaction of N-Hsp90-AMPPNP in 20 mM Tris base, and 5 mM Calcium as a function of temperature (pH 8.00).

Ligand	Temp (°C)	Stoichiometry (n)	$K_b \times 10^4$ (M ⁻¹)	$K_d^{(2)}$ (μM)	ΔH_{obs} (kJ·mol ⁻¹)	$T\Delta S_{obs}$ (kJ·mol ⁻¹)	ΔG_{obs} (kJ·mol ⁻¹)	ΔC_p (kJ·mol ⁻¹ ·K ⁻¹)
AMPPNP	8	1.03 ± 0.00	10.27 ± 0.21	9.73	- 46.43 ± 0.15	- 19.49	- 26.94	- 0.18 ± 0.01
	16	1.03 ± 0.00	5.35 ± 0.10	18.68	- 48.11 ± 0.22	- 21.94	- 26.17	
	25	1.00 ± 0.00	2.52 ± 0.09	39.5	- 49.53 ± 0.60	- 24.41	- 25.12	

Table 3.3.7 Summary of the thermodynamic parameters for the binding interaction of N-Hsp90-AMPPNP in 100 mM ACES, 50 mM Tris base, 50 mM Ethanolamine and 5 mM Manganese as a function of temperature (pH 6.00).

¹ Data was fitted to a one-set-of-sites model.

² Dissociation constant values (K_d) were calculated as the reciprocal of the observed equilibrium binding constant ($K_d = 1 / K_{obs}$).

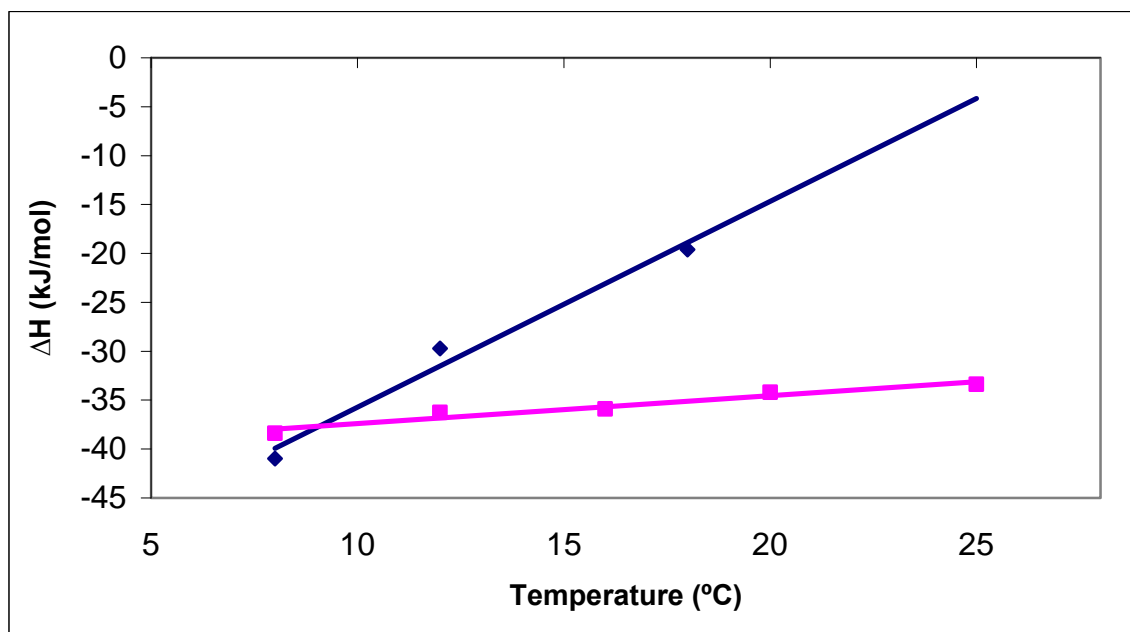


Figure 3.3.3 ΔH versus temperature plot for binding of Mg^{2+} -AMPPNP (pink square) and Ca^{2+} -AMPPNP (blue diamonds) binding to N-Hsp90 in 20 mM Tris-base at pH 8.00.

Ca^{2+} -AMPPNP also binds noticeably to N-Hsp90, however a weaker interaction occurs. The binding isotherm representing the binding of Ca^{2+} -AMPPNP to N-Hsp90 is hyperbolic (Figure 3.3.2), and as a result accurate estimation of stoichiometry and other thermodynamic parameters could not be obtained. This resulted in large errors in thermodynamic parameters obtained and is in turn reflected as a large variation in observed ΔC_p . The value of ΔH for the reaction is negative, suggesting that charge-charge interactions play an important role in the binding of Ca^{2+} -AMPPNP to N-Hsp90, in comparison to Mg^{2+} -AMPPNP. The K_d values of the Ca^{2+} -AMPPNP binding to N-Hsp90 are in the micromolar range, indicating weak affinity and is at least 4 times lower than that of the Mg^{2+} -AMPPNP binding to N-Hsp90.

Although no comparative thermodynamic values for binding of metal plus nucleotide to protein are quoted in the literature, intrinsic metal binding on its own to proteins is usually enthalpically driven ($\Delta H > 0$) because of the high dehydration enthalpies of divalent cations. However, the overall enthalpy of divalent cation binding to a protein can be exothermic ($\Delta H < 0$) if it is thermodynamically coupled to enthalpic equilibria such as a protein conformational change. Mn^{2+} -AMPPNP binds to N-Hsp90 with a large ΔH value of $-46.43 \text{ kJ}\cdot\text{mol}^{-1}$, compared to a ΔH of $-42.55 \text{ kJ}\cdot\text{mol}^{-1}$ for Mg^{2+} -AMPPNP binding to N-Hsp90 respectively. Higher ΔH values point towards higher attraction for

Mn²⁺-AMPPNP towards N-Hsp90. In addition, these calorimetric titration results indicate that Mg²⁺-AMPPNP, Mn²⁺-AMPPNP and Ca²⁺-AMPPNP bound N-Hsp90 structure may be different.

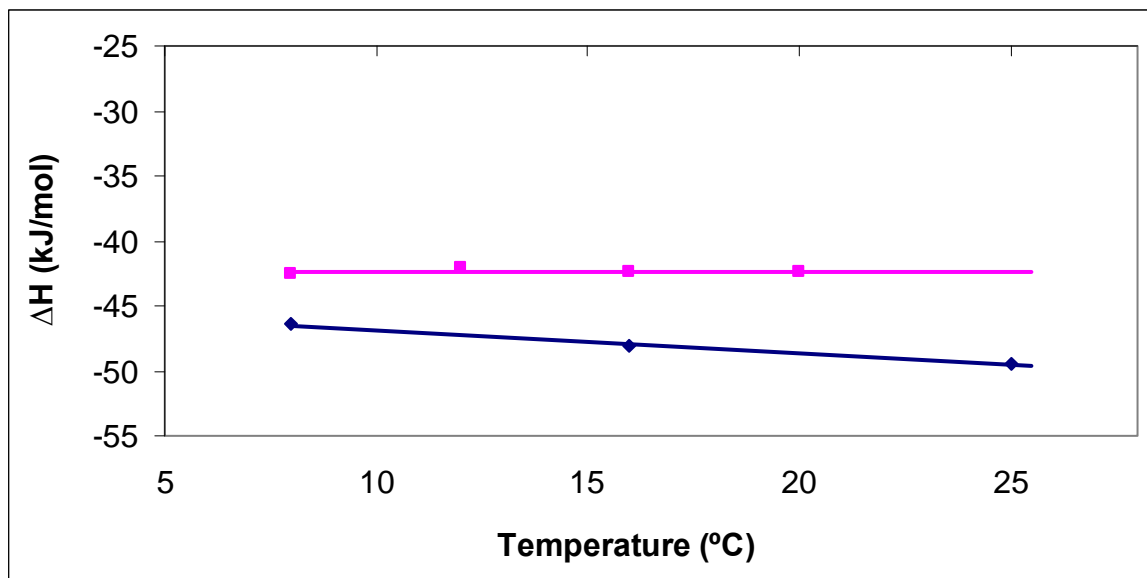


Figure 3.3.4 ΔH versus temperature plot for binding of Mg²⁺-AMPPNP (pink Square) and Mn²⁺-AMPPNP (blue diamonds) binding to Hsp90. Carried out at pH 6.00, in 100 mM ACES, 50 mM Tris, 50 mM Ethanolamine, 5 mM MgCl₂ or 5 mM MnCl₂.

In terms of ΔG , Ca²⁺-AMPPNP binds with an energy of $-20.31 \text{ kJ}\cdot\text{mol}^{-1}$, which is nearly $3.18 \text{ kJ}\cdot\text{mol}^{-1}$ less than the observed ΔG for Mg²⁺-AMPPNP binding to N-Hsp90. The ΔG of $-26.94 \text{ kJ}\cdot\text{mol}^{-1}$ for Mn²⁺-AMPPNP binding to N-Hsp90 nearly matches the observed ΔG value of $-26.75 \text{ kJ}\cdot\text{mol}^{-1}$ for Mg²⁺-AMPPNP.

However one of the most intriguing results comes from the comparison of ΔC_p for the binding of Mg²⁺-AMPPNP, Mn²⁺-AMPPNP and Ca²⁺-AMPPNP to N-Hsp90. Binding of Ca²⁺-AMPPNP to N-Hsp90 proceeds with a significant positive ΔC_p of $2.10 \pm 0.30 \text{ kJ}\cdot\text{mol}^{-1}\cdot\text{K}^{-1}$. However, binding of Mn²⁺-AMPPNP to N-Hsp90 proceeds with a small but significant negative ΔC_p of $-0.18 \pm 0.01 \text{ kJ}\cdot\text{mol}^{-1}\cdot\text{K}^{-1}$ at pH 6.00. This result contrasts with the results obtained for Mg²⁺-AMPPNP binding to N-Hsp90, which show a negligible ΔC_p value of $0.0 \pm 0.03 \text{ kJ}\cdot\text{mol}^{-1}\cdot\text{K}^{-1}$ (pH 6.00). However, it is worth noting that, at every other pH value (between 5.00 to 10.00), Mg²⁺-AMPPNP binding to N-Hsp90 proceeds with a positive ΔC_p value of between $0.09 \text{ kJ}\cdot\text{mol}^{-1}\cdot\text{K}^{-1}$ (pH 5.00) and $0.57 \text{ kJ}\cdot\text{mol}^{-1}\cdot\text{K}^{-1}$ (pH 8.70). This marked alteration in the binding thermodynamics,

especially ΔC_p , upon substituting the divalent metal cation in the N-Hsp90 indicates that altering the divalent metal cation has a marked effect on the binding thermodynamics between the protein and the nucleotide molecules.

Secondly, this large difference in binding thermodynamics, especially ΔC_p is also indicative of a conformational change involving changes in the interfacial surface areas between the protein and between the protein and nucleotide. To determine any structural differences in the solution phase between the metal ion derivatives of AMPPNP which may affect their ΔC_p , nuclear magnetic resonance (NMR) and circular dichroism (CD) measurements were performed on solutions of the N-Hsp90 and compared to the NMR results determined previously for Mg^{2+} -AMPPNP binding to N-Hsp90.

3.3.3 Two Dimensional ^1H - ^{15}N Heteronuclear Single Quantum Coherence (HSQC) Experiment to Analyze the Effect of Structural Change in Presence of Different Metals

To determine any structural differences in the solution phase between the divalent metal ion derivatives of AMPPNP after binding to N-Hsp90, nuclear magnetic resonance (NMR) spectroscopy was used. A ^1H - ^{15}N HSQC spectrum can effectively probe protein conformational changes in N-Hsp90-AMPPNP induced by substitution of Ca^{2+} , Mn^{2+} and Cd^{2+} in place of Mg^{2+} . The peaks in the ^1H - ^{15}N HSQC NMR spectrum represent main-chain and side-chain amide groups and provide a residue-specific fingerprint of the overall protein conformation. ^1H - ^{15}N HSQC in principle gives the backbone amide resonance values for all the residues in protein with the exception of prolines. Prolines are not observed in the ^1H - ^{15}N HSQC experiment due to the lack of amide proton. As well as the amide backbone, some side-chain NH groups such as those in arginine, asparagine, glutamine and tryptophan are also observed in the spectrum (Figure 3.3.9). Asparagine and glutamine side-chains produce a strong doublet and one weaker doublet per residue

The ^1H - ^{15}N HSQC spectrum of the N-Hsp90 (Residues 1-207) obtained at 800 MHz. and assigned by Salek et al. (108) is shown in Figure 3.3.9. In the ^1H - ^{15}N HSQC spectrum asparagine and glutamine side-chains are at the top right hand part of the spectrum. There are also crosspeaks from arginine $\text{N}_\epsilon\text{H}_\epsilon$ side-chain observed, which appears at an aliased nitrogen frequency in the 2D fourier transformed ^1H - ^{15}N HSQC spectrum and are usually located around 85 to 87 ppm.

Figures 3.3.5, 3.3.6, 3.3.7 and 3.3.8 describes ^1H - ^{15}N HSQC spectrum of Mg^{2+} -AMPPNP, Mn^{2+} -AMPPNP, Ca^{2+} -AMPPNP and Cd^{2+} -AMPPNP bound N-Hsp90 protein respectively. The glycine residues at the top of the spectrum in the apo protein show a different position in the Mg^{2+} -AMPPNP bound spectrum. Overall about 50 crosspeaks show different positions between the two spectra, suggesting a possible different conformation between the Mg^{2+} -AMPPNP and the apo protein. Residues Leu93, Gly94, Ala107, Ala110 and Gly111 are some examples and happen to be located at the ADP/ATP binding site. Other residues affected are Leu31, Arg32, Asn37, Ala38 and Leu42, which are all located in the second long helix that comprises the side of the ADP/ATP binding pocket and according to the crystallographic structure, are involved in nucleotide interaction.

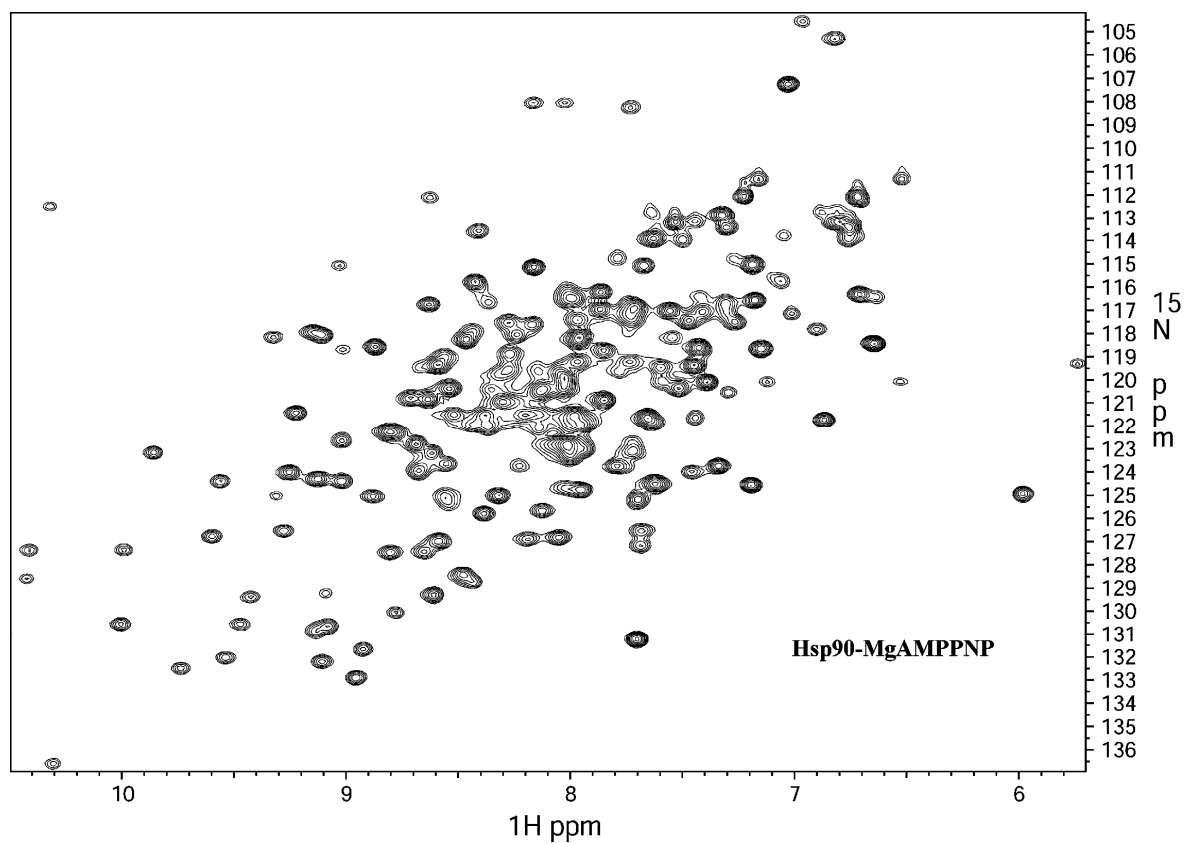


Figure 3.3.5 ^1H - ^{15}N HSQC spectrum of N-Hsp90-MgAMPPNP obtained at 600 MHz and 25 °C.

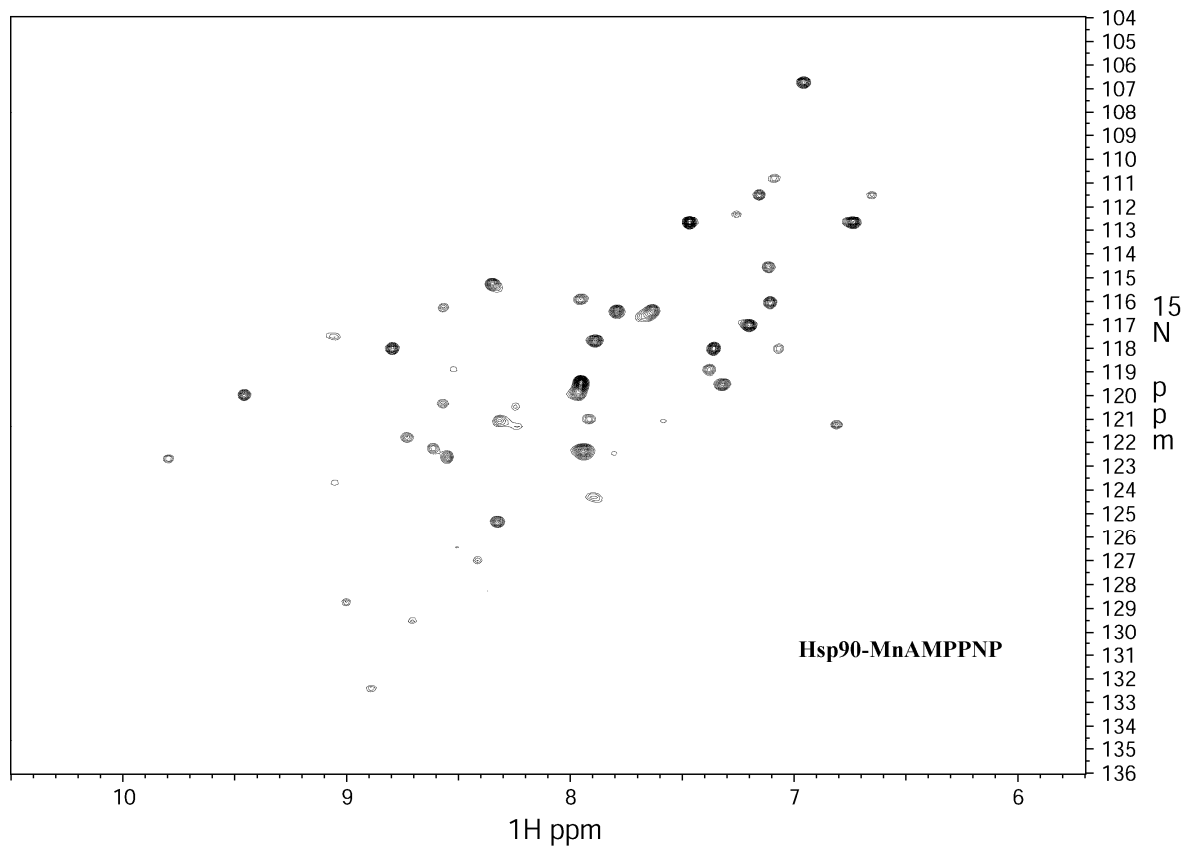


Figure 3.3.6 ^1H - ^{15}N HSQC spectrum of N-Hsp90-MnAMPPNP obtained at 600 MHz and 25 °C.

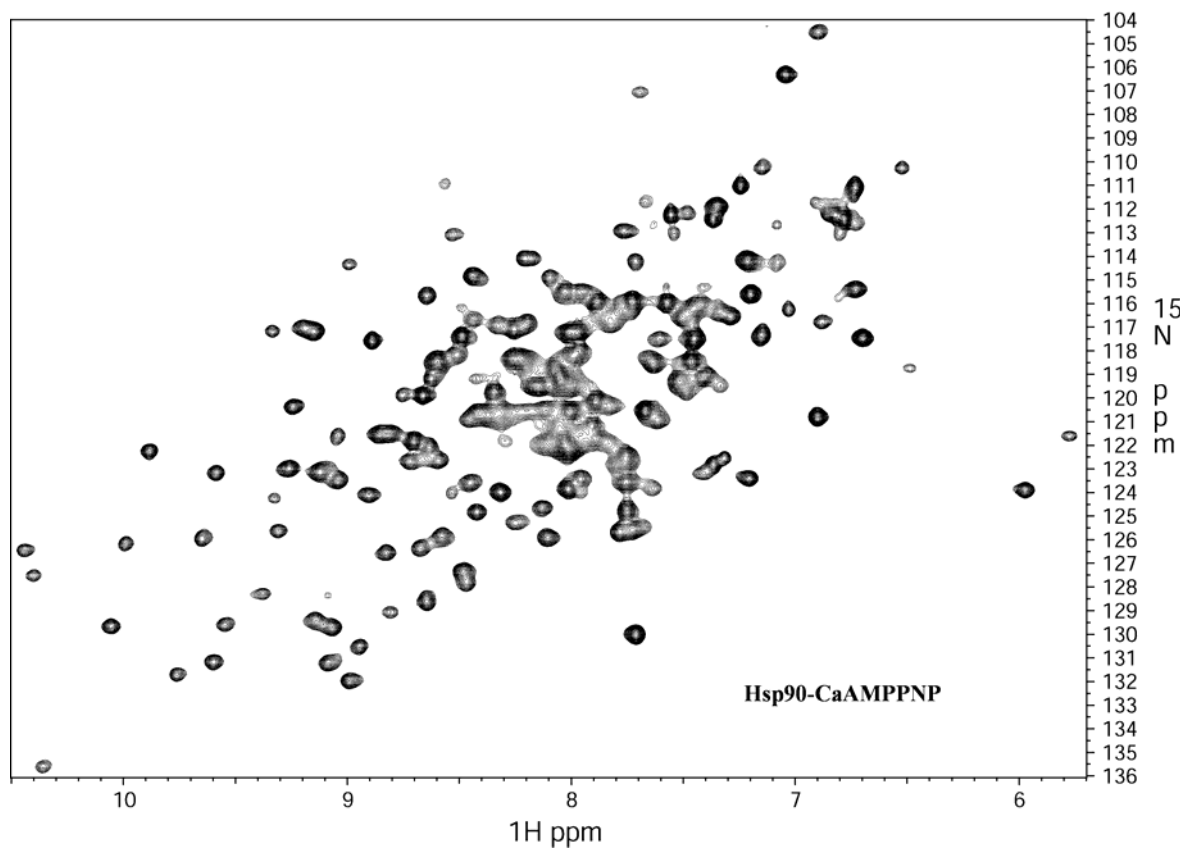


Figure 3.3.7 ^1H - ^{15}N HSQC spectrum of N-Hsp90-CaAMPPNP obtained at 600 MHz and 25 °C.

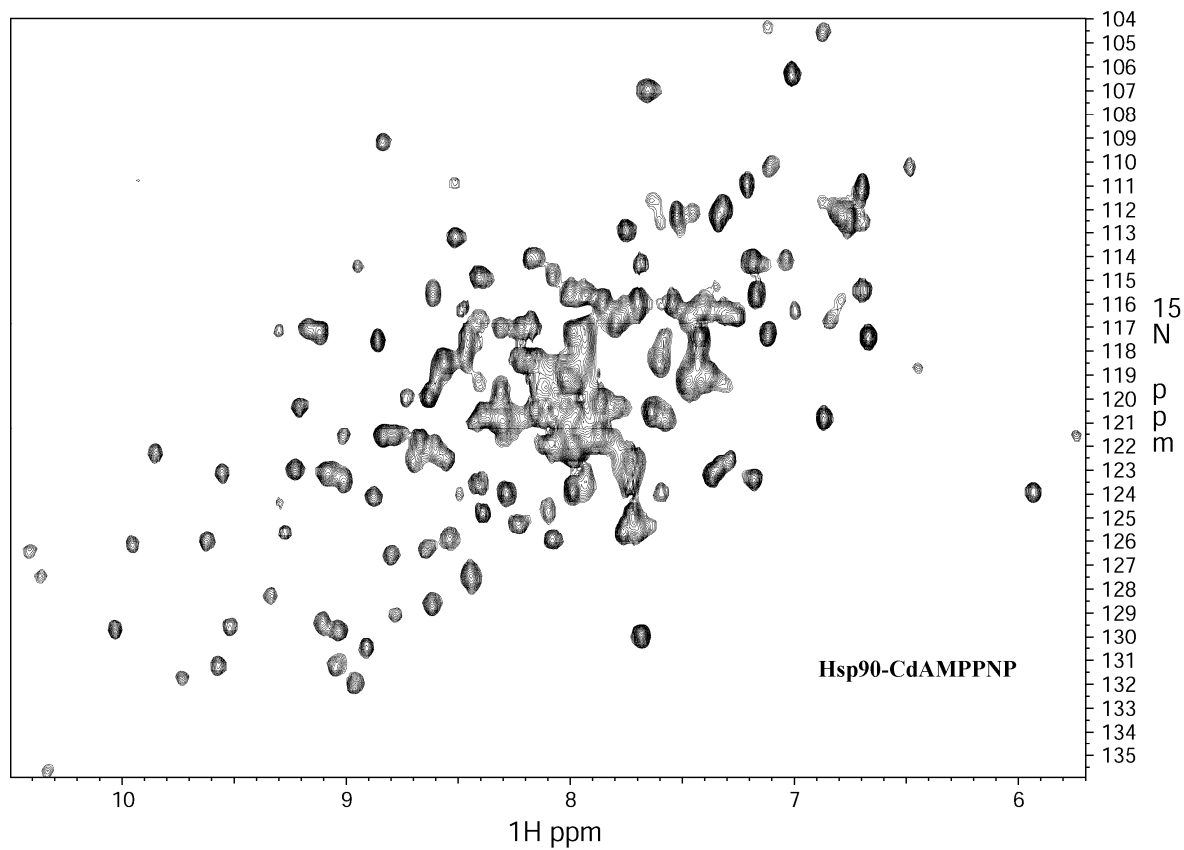


Figure 3.3.8 ^1H - ^{15}N HSQC spectrum of N-Hsp90-CdAMPPNP obtained at 600 MHz and 25 °C.

Comparison of the Mg^{2+} -AMPPNP bound spectra to that of apo N-Hsp90 suggests that it could be a good model for studying the possible conformational change in substitution of various metal divalent cations in the AMPPNP-N-Hsp90 binding interaction. However an accurate comparison will be difficult due to the paramagnetic nature of Mn^{2+} and the resultant broadening of peaks. Also, according to calorimetric measurements, Ca^{2+} -AMPPNP binds to N-Hsp90 with a weak affinity, which results from the presence of various conformations of apo- Ca^{2+} AMPPNP observed in the spectrum. These differences could also be due to the residues in the apo- and/or bound spectrum.

The broad distribution of chemical shift resonance in all the divalent metal cations-AMPPNP binding to N-Hsp90 spectra confirms a folded domain. Overall there are about 200 backbone and 34 side-chain resonances in the HSQC spectrum (108). In this spectrum there is considerable overlap at the centre, which can largely be attributed to connecting loops and α -helices in its structure. Most of the glycine residues appear at the top of the 1H - ^{15}N HSQC spectrum. These glycines are mainly in loops and turns and are not part of any secondary structure. C-terminal residues such as Lys207 can be seen as strong peaks at the bottom centre of the spectrum as shown in Figure 3.3.9.

Mg^{2+} -AMPPNP binding to N-Hsp90 substantially increased the NMR chemical shift dispersion, demonstrating that Mg^{2+} -AMPPNP bound N-Hsp90 adopts a stable tertiary structure. The 1H - ^{15}N HSQC spectrum of N-Hsp90-AMPPNP showed undetectable change upon substitution of Ca^{2+} , Mn^{2+} and Cd^{2+} in place of Mg^{2+} (Figure 3.3.5 to 3.3.8). Mg^{2+} caused a greater number of peaks to appear (200 peaks *versus* 207 residues) and the NMR intensities were in general much more uniform than those of N-Hsp90- Ca^{2+} -AMPPNP, N-Hsp90- Mn^{2+} -AMPPNP and N-Hsp90- Cd^{2+} -AMPPNP. Gly94 peak shifts towards the right upon binding of Mg^{2+} -AMPPNP to N-Hsp90, as compared to the apo protein. The same peak in Mn^{2+} -AMPPNP, Cd^{2+} -AMPPNP spectra appears in the apo spectrum due to weak binding/overlap of apo and Mn^{2+} -AMPPNP/ Cd^{2+} -AMPPNP spectra. For Ca^{2+} -AMPPNP binding to N-Hsp90, 4 equivalents of Ca^{2+} -AMPPNP per N-Hsp90 in 20 mM Tris buffer pH 8.00 at 25 °C was added; confirming weak binding affinity as indicated by the calorimetric data

Due to the paramagnetic nature of Mn^{2+} , NMR studies were also carried out with Cd^{2+} -AMPPNP. The paramagnetic nature of Mn^{2+} causes NMR resonances to broaden substantially rather than shift (198). Whilst Ca^{2+} -AMPPNP is weak binder and causes resonances to appear for the apo form as well as Ca^{2+} -AMPPNP bound form, resulting in vague resonance.

3. Results and Discussion

The data obtained from comparison of the four different ^1H - ^{15}N HSQC NMR spectra, indicates that the chemical shifts of the binding site residues are not significantly affected by the substitution of various divalent metal cations. Moreover, analysis of the binding thermodynamics shows that the divalent metal substitution influences N-Hsp90-AMPPNP interaction.

The initial characterization of the divalent metal ion-nucleotide binding properties of N-Hsp90 provided by our work raises the question that positive ΔC_p observed in N-Hsp90- Mg^{2+} -AMPPNP is not due to structural rearrangement or conformational change, and can mainly be attributed to water desolvation from the interface of the divalent metal cations upon binding to N-Hsp90.

Although detailed characterization of structural rearrangement after binding of the divalent metal ion-nucleotide binding to N-Hsp90 by crystallography or NMR is beyond the scope of this study, our preliminary NMR studies provided evidence concerning the nature of conformational change. However broadening of the spectrum in Mn^{2+} -AMPPNP binding and weak binding of Ca^{2+} -AMPPNP resulted in somewhat unconvincing results. As a result, a separate CD experiment was also carried out and is discussed in Section 3.3.4.

3.3.4 Circular Dichroism (CD) Spectroscopy of Divalent Metal-AMPPNP Binding to N-Hsp90

The interaction between protein and ligand leads to structural change and leads to characteristic secondary structural CD spectra. This secondary structure determination by CD is exploited to understand structural change after ligand binding.

Therefore to characterise the structure of N-Hsp90 and assess possible secondary structural changes resulting from substitution of various divalent cations, far UV-CD spectra were recorded on different samples. Irrespective of the divalent metal cation used, the same protein concentration and pH were used in all of the samples. The CD spectra of the N-Hsp90 (on its own, red) and AMPPNP bound N-Hsp90 with Mg^{2+} (blue), Mn^{2+} (pink), Cd^{2+} (green) and Ca^{2+} (yellow) are shown in Figure 3.3.10. The ultraviolet CD spectrum of protein can predict important characteristics of protein secondary structure and can readily be used to estimate the fraction of a molecule that is in the α -helix, β -sheet, β -turn or some other (random) conformation. The α -helical CD spectrum is characterised by two negative bands at 222 and 208 nm and a positive band at 192 nm, which are

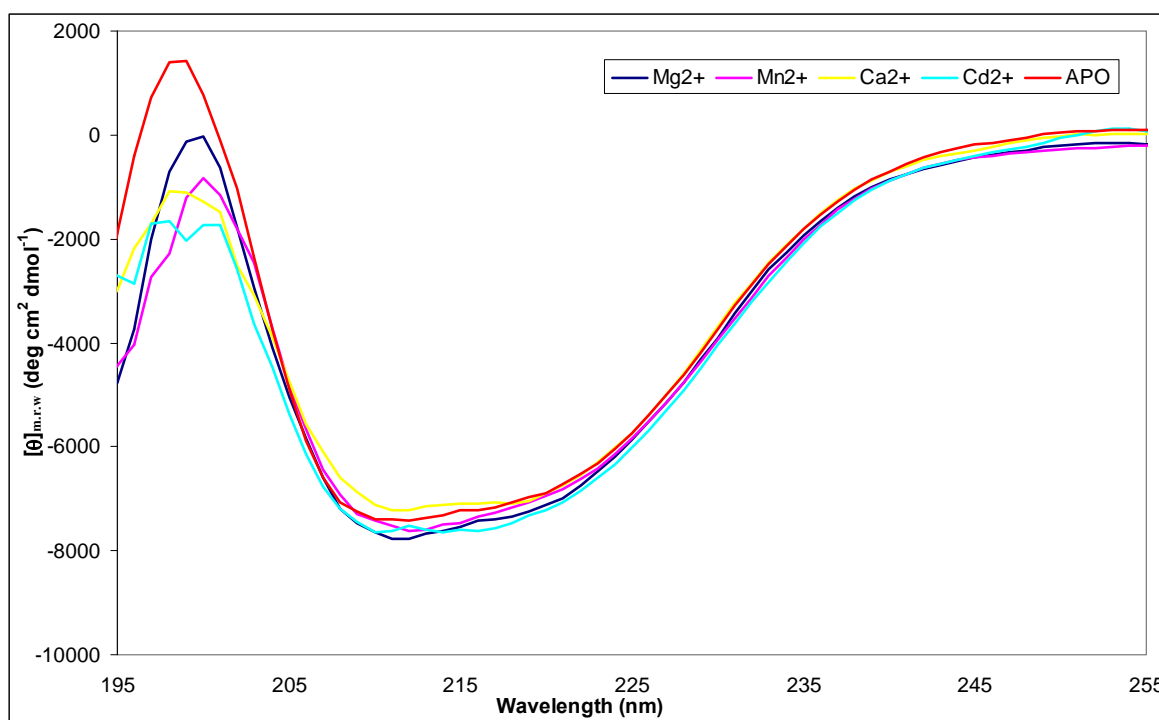


Figure 3.3.10 Circular dichroism spectroscopic analysis (mean residue ellipticity, $[\theta]_{m.r.w}$ vs. wavelength) of the substitution of various divalent metal cations like Mn^{2+} , Cd^{2+} , Ca^{2+} in place of Mg^{2+} for AMPPNP-binding to N-Hsp90. N-Hsp90 was subjected to CD analysis in combination with Mg^{2+} -AMPPNP (blue), Mn^{2+} -AMPPNP (pink), Ca^{2+} -AMPPNP (yellow), Cd^{2+} -AMPPNP (green) and unbound N-Hsp90 (red). N-Hsp90 was pre-incubated with AMPPNP in the presence/absence of various divalent metal cations. N-Hsp90 was dialyzed against 20 mM Tris-base (pH 8.00) and then CD spectra were recorded. Spectra shown are corrected by subtraction of Tris-base buffer CD spectrum.

normally used in CD analysis. The CD spectrum of the typical β -sheet has a negative band near 215 nm and a positive band near 198 nm. However, the β -sheet CD spectrum is difficult to characterise due to the variations in the geometry of β -structure in polypeptides and proteins.

Figure 3.3.10 shows the differences in the CD spectra of the four different divalent cations substituted in N-Hsp90-AMPPNP binding and are compared with the apo spectrum (Red). These spectra suggest that apo N-Hsp90 adopts a high degree of α -helical and β -sheet content, consistent with the presence of 9 α -helices and 8 anti-parallel β -sheets in the crystal structure. The CD spectrum slightly differs in the region of 195-200 nm between the apo and metal bound structures, with the apo form showing a higher α -helical content. However it must be noted that, this region is subject to interference from external factors, such as absorption of light by solvent and presence of divalent metals. In this far-UV region (below 200 nm) only very dilute, non-absorbing buffers and buffer constituents allow accurate measurements (199).

The CD spectrum however does not change much upon inter-substitution of various divalent metals like, Mg^{2+} , Mn^{2+} , Cd^{2+} and Ca^{2+} . Although Cd^{2+} CD spectrum shows a slight negative peak and could possibly be attributed to absorption of CD signal by Cd^{2+} on its own. These results combined with NMR results (described in Section 3.3.3) suggest that N-Hsp90- Mg^{2+} -AMPPNP adopts a well folded secondary structure and does not undergo global conformational change upon in-substitution of various divalent metal cations, however minor local conformational changes cannot be ruled out.

3.3.5 Is Tight Ordering of Water Around Mg^{2+} Responsible for Positive ΔC_p in N-Hsp90-ADP/ATP Interactions?

To better understand the role of water on positive ΔC_p in multivalent binding systems, such as N-Hsp90 and Mg^{2+} -ADP/ATP, we have studied the thermodynamics of binding of a simple multivalent system: the binding of EDTA to various divalent metal cations (Figure 3.3.11). The attractiveness of this system lies in the fact that the intermolecular cross-linking interactions are not observed in this EDTA-divalent metal cation interaction. As a result, this model can be used for understanding the role of water reorganisation and desolvation upon metal binding to protein and resultant changes in their binding thermodynamics.

EDTA is the chemical compound ethylenediaminetetraacetic acid, otherwise known as edentate or versene. It is a polyprotic acid containing four carboxylic acid groups (acidic hydrogens are red, Figure 3.3.11) and two amine groups with lone pair electrons (magenta dots, Figure 3.3.11). EDTA is a chelating agent, forming chelates with most monovalent, divalent, trivalent and tetravalent metal ions, such as silver (Ag^+), calcium (Ca^{2+}), copper (Cu^{2+}), iron (Fe^{3+}) or zirconium (Zr^{4+}). EDTA contains 4 carboxylic acid and 2 tertiary amine groups that can participate in acid-base reactions. Besides the four carboxylic group hydrogens, EDTA can add two more hydrogens onto the amine groups. It forms a chelate in 1:1 metal-to-EDTA complexes. The fully deprotonated form (all acidic hydrogens removed) of EDTA binds to the metal ion. The equilibrium or binding constants for most metals, especially the transition metals are very large.

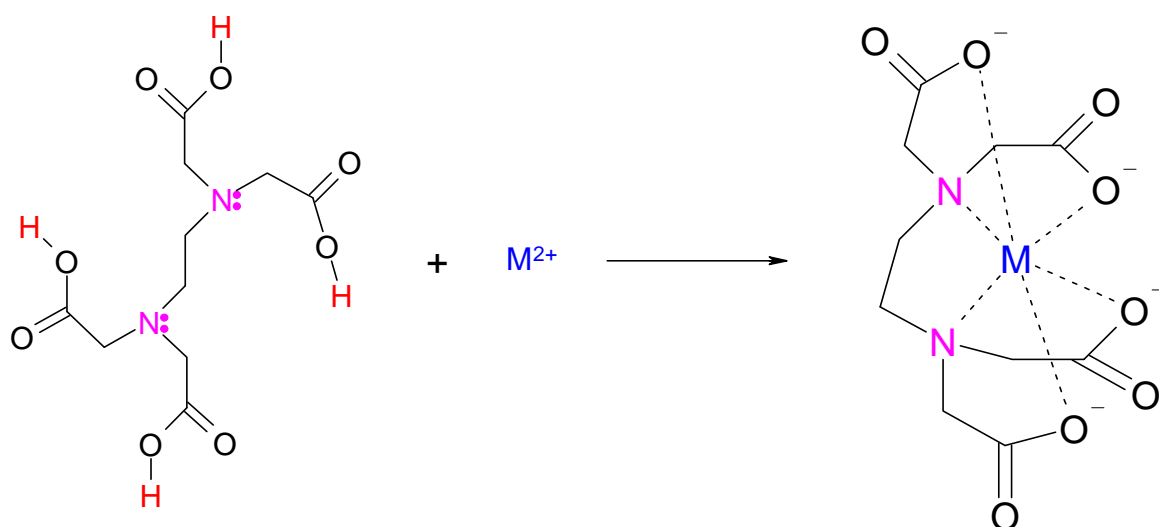


Figure 3.3.11 Chelate formation of EDTA upon binding to divalent metal cations chelate formation results in complete desolvation of waters from the surface of divalent metal cations.

Metal Ion (Compound Used)	Ionic radii (Å)	Preferred coordination
Mg (MgCl ₂)	0.72	6
Mn (MnCl ₂)	0.83	6
Ca (CaCl ₂)	0.99	6, 8

Table 3.3.8 Coordination number and Ionic radii of divalent metal cations.

For consistency with other titrations conducted, 20 mM Tris-base pH 8.00 buffer was used throughout this investigation. Tables 3.3.10, 3.3.11 and 3.3.12 show various thermodynamic parameters for Mg²⁺, Mn²⁺ and Ca²⁺ binding to EDTA in 20 mM Tris buffer at pH 8.00; corresponding ITC binding isotherms obtained at 20 °C are also shown in Figure 3.3.12 and comparative data presented in Table 3.3.9.

Calorimetric measurements show a binding stoichiometry of 0.77 to 1 for all divalent metal cations binding to EDTA, indicating a 1:1 binding. Comparing the energetics of Mg²⁺ and Ca²⁺ binding to EDTA in 20 mM Tris-buffer (Figure 3.3.13 and Table 3.3.9), it was observed that the $\Delta\Delta G$ of $-7.82 \text{ kJ}\cdot\text{mol}^{-1}$ includes a $\Delta\Delta H$ term of $-45.26 \text{ kJ}\cdot\text{mol}^{-1}$ and a $T\Delta\Delta S$ term of $37.44 \text{ kJ}\cdot\text{mol}^{-1}$. The corresponding $\Delta\Delta H$, $T\Delta\Delta S$ and

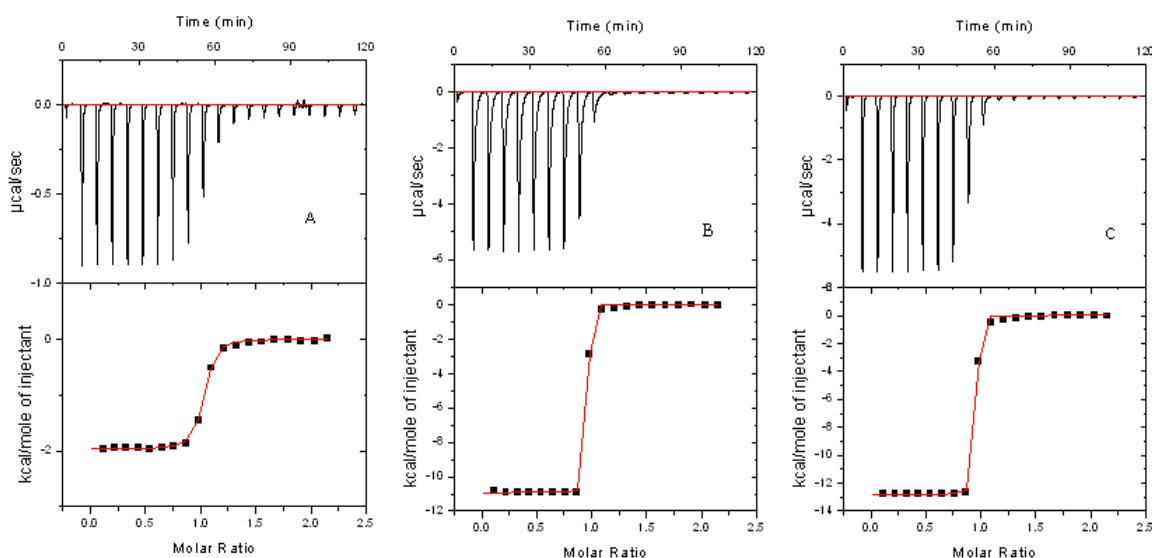


Figure 3.3.12 Isothermal titration calorimetric analysis of Mg²⁺-AMPPNP binding (A), Mn²⁺-AMPPNP binding (B) and Ca²⁺-AMPPNP binding to N-Hsp90 (C). Trace of the calorimetric titration of 20 x 15- μl aliquots of 1 mM MgCl₂ into 100 μM EDTA (A), 1 mM MnCl₂ into 100 μM EDTA (B) and 1 mM CaCl₂ into 100 μM EDTA (C) (top), and integrated binding isotherms (bottom).

Ligand binding EDTA	Ionic radii (Å)	ΔH_{obs} (kJ·mol ⁻¹)	$T\Delta S_{\text{obs}}$ (kJ·mol ⁻¹)	ΔG_{obs} (kJ·mol ⁻¹)	ΔC_p (kJ·mol ⁻¹ ·K ⁻¹)
Mg ²⁺	0.72	- 8.24 ± 0.04	29.17	- 37.41	0.20 ± 0.00
Mn ²⁺	0.83	- 53.29 ± 0.19	- 7.81	- 45.48	- 0.22 ± 0.15
Mn ²⁺ #	0.83	- 6.64 ± 0.04	9.04	- 15.68	- 0.01 ± 0.00
Ca ²⁺	0.99, 1.14	- 53.50 ± 0.22	- 8.27	- 45.23	0.19 ± 0.00

Table 3.3.9 Comparison of thermodynamical parameters for binding of various divalent metal cation binding to EDTA at 20 °C. Titration carried out in triple buffer pH 8.00. # Experiment conducted at pH 6.00.

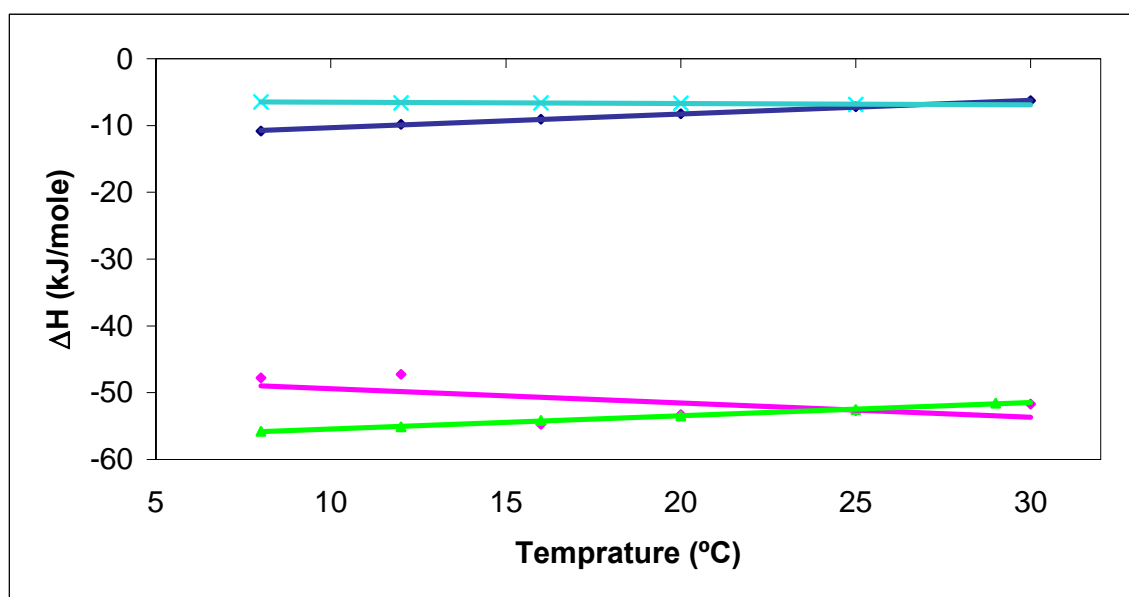


Figure 3.3.13 Temperature dependence of the ΔH on binding of Mg²⁺ (blue), Mn²⁺ (pink) and Ca²⁺ (yellow) to EDTA in 20 mM Tris buffer at pH 8.00, while aqua coloured line denotes Mn²⁺ binding to EDTA at pH 6.00 (Triple Buffer) . The data are summarized in Table 3.3.5.3, 3.3.5.4, 3.3.5.5 and 3.3.5.6.

$\Delta\Delta G$ for Mn²⁺ binding to EDTA at 20 °C were -45.05 kJ·mol⁻¹, 36.98 kJ·mol⁻¹ and -8.07 kJ·mol⁻¹ respectively.

Relative to Mg²⁺, the ΔH accompanies binding of Mn²⁺ and Ca²⁺ to EDTA is distinctly more favourable and thus the corresponding entropy change is rather less favourable. Also ΔH follows a somewhat indirect but clear trend, where Mg²⁺ with

3. Results and Discussion

Ligand	Temp (°C)	Stoichiometry (n)	$K_b \times 10^4$ (M ⁻¹)	$K_d^{(2)}$ (μM)	ΔH_{obs} (kJ·mol ⁻¹)	$T\Delta S_{\text{obs}}$ (kJ·mol ⁻¹)	ΔG_{obs} (kJ·mol ⁻¹)	ΔC_p (kJ·mol ⁻¹ ·K ⁻¹)
Magnesium-EDTA	8	1.00 ± 0.00	60.88 ± 3.91	164.25	- 10.83 ± 0.02	25.62	- 36.45	0.20 ± 0.00
	12	0.98 ± 0.00	58.86 ± 5.84	169.89	- 9.82 ± 0.04	27.07	- 36.89	
	16	0.97 ± 0.00	51.46 ± 3.80	194.32	- 9.07 ± 0.03	28.02	- 37.09	
	20	0.98 ± 0.00	47.49 ± 5.73	210.50	- 8.24 ± 0.04	29.17	- 37.41	
	25	0.99 ± 0.00	52.26 ± 6.97	191.35	- 7.20 ± 0.04	31.09	- 38.29	
	30	1.00 ± 0.00	47.82 ± 8.73	209.11	- 6.27 ± 0.05	32.43	- 38.70	

Table 3.3.10 Summary of the thermodynamic parameters for the binding interaction of 100 μM EDTA with 1 mM Magnesium in 20 mM Tris buffer as a function of temperature (pH 8.00).

Ligand	Temp (°C)	Stoichiometry (n)	$K_b \times 10^{-6}$ (M ⁻¹)	$K_d^{(2)}$ (nM)	ΔH_{obs} (kJ·mol ⁻¹)	$T\Delta S_{\text{obs}}$ (kJ·mol ⁻¹)	ΔG_{obs} (kJ·mol ⁻¹)	ΔC_p (kJ·mol ⁻¹ ·K ⁻¹)
Manganese-EDTA	8	0.94 ± 0.00	28.21 ± 6.72	35.44	- 47.77 ± 0.12	- 7.70	- 40.07	- 0.22 ± 0.15
	12	0.84 ± 0.00	51.36 ± 12.47	19.47	- 47.23 ± 0.13	- 5.18	- 42.59	
	16	0.88 ± 0.00	126.10 ± 77.80	7.93	- 54.75 ± 0.27	- 9.53	- 45.22	
	20	0.89 ± 0.00	129.70 ± 80.90	7.71	- 53.29 ± 0.19	- 7.81	- 45.48	
	25	0.89 ± 0.00	82.74 ± 48.39	12.08	- 52.66 ± 0.25	- 18.91	- 33.75	
	29	0.87 ± 0.00	67.49 ± 26.77	14.81	- 51.70 ± 0.32	- 6.45	- 45.25	

Table 3.3.11 Summary of the thermodynamic parameters for the binding interaction of 100 μM EDTA with 1 mM Manganese in 20 mM Tris buffer as a function of temperature (pH 8.00).

¹ Data was fitted to a one-set-of-sites model.

² Dissociation constant values (K_d) were calculated as the reciprocal of the observed equilibrium binding constant ($K_d = 1 / K_{\text{obs}}$).

3. Results and Discussion

Ligand	Temp (°C)	Stoichiometry (n)	$K_b \times 10^4$ (M ⁻¹)	$K_d^{(2)}$ (μM)	ΔH_{obs} (kJ·mol ⁻¹)	$T\Delta S_{\text{obs}}$ (kJ·mol ⁻¹)	ΔG_{obs} (kJ·mol ⁻¹)	ΔC_p (kJ·mol ⁻¹ ·K ⁻¹)
Calcium-EDTA	8	0.90 ± 0.00	80.77 ± 46.24	12.38	- 55.76 ± 0.24	- 13.23	- 42.53	
	12	0.87 ± 0.00	71.03 ± 13.84	14.07	- 55.13 ± 0.17	- 12.24	- 42.89	
	16	0.88 ± 0.00	131.10 ± 67.43	7.62	- 54.17 ± 0.20	- 9.28	- 44.89	0.19 ± 0.00
	20	0.89 ± 0.00	116.10 ± 75.62	8.61	- 53.50 ± 0.22	- 8.27	- 45.23	
	25	0.89 ± 0.00	87.27 ± 46.94	11.45	- 52.54 ± 0.22	- 7.24	- 45.30	
	29	0.87 ± 0.00	72.56 ± 32.53	13.78	- 51.58 ± 0.34	- 6.13	- 45.45	

Table 3.3.12 Summary of the thermodynamic parameters for the binding interaction of 100 μM EDTA with 1 mM Calcium in 20 mM Tris buffer as a function of temperature (pH 8.00).

Ligand	Temp (°C)	Stoichiometry (n)	$K_b \times 10^{-6}$ (M ⁻¹)	$K_d^{(2)}$ (nM)	ΔH_{obs} (kJ·mol ⁻¹)	$T\Delta S_{\text{obs}}$ (kJ·mol ⁻¹)	ΔG_{obs} (kJ·mol ⁻¹)	ΔC_p (kJ·mol ⁻¹ ·K ⁻¹)
Manganese-EDTA	8	0.81 ± 0.00	53.67 ± 93.04	18.63	- 6.48 ± 0.03	8.38	-14.87	
	12	0.80 ± 0.00	17.33 ± 9.39	57.70	- 6.60 ± 0.03	7.86	- 14.46	
	16	0.79 ± 0.00	23.09 ± 10.01	43.30	- 6.60 ± 0.02	8.15	- 14.76	- 0.01 ± 0.00
	20	0.77 ± 0.00	84.99 ± 89.16	11.79	- 6.64 ± 0.04	9.04	- 15.68	
	25	0.79 ± 0.00	80.50 ± 119.80	12.42	- 6.84 ± 0.03	9.14	- 15.98	

Table 3.3.13 Summary of the thermodynamic parameters for the binding interaction of 158 μM EDTA with 1.8 mM Manganese in 100 mM PIPES, 50 mM Tris base, 50 mM Ethanolamine (Triple Buffer) as a function of temperature (pH 6.00).

¹ Data was fitted to a one-set-of-sites model.

² Dissociation constant values (K_d) were calculated as the reciprocal of the observed equilibrium binding constant ($K_d = 1 / K_{\text{obs}}$).

3. Results and Discussion

the smallest ionic radii of 0.72 Å, binds to EDTA with $-8.24 \pm 0.04 \text{ kJ}\cdot\text{mol}^{-1}$. However as the ionic radius is increased from Mg^{2+} (0.72 Å) to Mn^{2+} (0.83 Å) and Ca^{2+} (0.99 Å), ΔH also increases to $-53.29 \pm 0.19 \text{ kJ}\cdot\text{mol}^{-1}$ and $-53.50 \pm 0.22 \text{ kJ}\cdot\text{mol}^{-1}$ respectively, a jump of around $-45 \text{ kJ}\cdot\text{mol}^{-1}$. This thermodynamic signature has two possible explanations. On the one hand, EDTA may experience a relatively more intense conformational change upon binding Mn^{2+} and Ca^{2+} , as compared to Mg^{2+} . If right, the more negative ΔH and less favourable $T\Delta S$ terms could reflect improved van der Waals contacts and decreased conformational entropy, respectively.

Alternatively, one of the Ca^{2+} and Mn^{2+} ions could retain a water molecule after binding to EDTA. In this circumstance, incomplete dehydration of the divalent metal cation would improve the overall enthalpy of binding, but preservation of the bound water molecule would reduce the entropic driving energy.

ΔC_p values for binding of Mg^{2+} , Mn^{2+} and Ca^{2+} to EDTA in 20 mM Tris buffer at pH 8.00 were also deduced by conducting calorimetric experiments over a temperature range of 8 to 30 °C and are given in Tables 3.3.10, 3.3.11 and 3.3.12 respectively. The ΔC_p for the binding of Mg^{2+} is about $0.20 \pm 0.00 \text{ kJ}\cdot\text{mol}^{-1}\cdot\text{K}^{-1}$ and is about $0.01 \text{ kJ}\cdot\text{mol}^{-1}\cdot\text{K}^{-1}$ higher than the ΔC_p of Ca^{2+} binding to EDTA. However, Mn^{2+} binds to EDTA with a ΔC_p of $-0.22 \pm 0.15 \text{ kJ}\cdot\text{mol}^{-1}\cdot\text{K}^{-1}$, which matches well with the negative ΔC_p observed for the binding of Mn^{2+} -AMPPNP to N-Hsp90. A difference of $0.42 \text{ kJ}\cdot\text{mol}^{-1}\cdot\text{K}^{-1}$ of $\Delta\Delta C_p$ is equivalent to about 42.0 to 46.00 Å of solvent accessible surface area as calculated from ΔS_{ASA} equations. Comparison of ΔC_p in Mg^{2+} , Mn^{2+} and Ca^{2+} to EDTA is illustrated in Figure 3.3.13.

Notably, ΔC_p values for binding of Mn^{2+} binding to EDTA showed a large error of $-0.15 \text{ kJ}\cdot\text{mol}^{-1}\cdot\text{K}^{-1}$ in the observed negative ΔC_p of $-0.22 \text{ kJ}\cdot\text{mol}^{-1}\cdot\text{K}^{-1}$. Additionally there was a large scatter in the ΔH values between 12 °C and 16 °C, showing instability of Mn^{2+} cation in these conditions. Therefore a repetition of the same experiment in triple buffer pH 6.00 was carried out, as experiments suggested a more stable Mn^{2+} cation at lesser pH.

At pH 6.00 the binding of Mn^{2+} to EDTA shows a marked decrease in the observed ΔH value, and decreases from $-52.66 \pm 0.25 \text{ kJ}\cdot\text{mol}^{-1}$ (20 mM Tris buffer) at pH 8.00 to $-6.84 \pm 0.03 \text{ kJ}\cdot\text{mol}^{-1}$ (pH 6.00) in 100 mM PIPES, 50 mM Tris base, 50 mM Ethanolamine (Triple Buffer), showing a difference of $45.82 \text{ kJ}\cdot\text{mol}^{-1}$. This large massive negative difference in ΔH can be attributed to relative stabilisation of Mn^{2+}

3. Results and Discussion

cation at lower acidic pH of 6.00 and protonation of EDTA. However experiments conducted showed a negative ΔC_p of $-0.1 \pm 0.00 \text{ kJ}\cdot\text{mol}^{-1}\cdot\text{K}^{-1}$, which confirms the results obtained at pH 8.00.

In this calorimetric study, we have assumed from the start that thermodynamic parameters describing complexation arise from favourable interaction between the metal ion and electronegative elements of the EDTA (O, N) and resulting desolvation. From this calorimetric data, we can reach three conclusions: the basis of affinity in EDTA-metal ion binding is enthalpic and not entropic; ΔH of binding increases with increasing van der Waals radii and decreasing charge density; ΔC_p values for binding are large (considering the size of complex), although a direct correlation between ΔC_p and solvation-related surface accessible area is unclear.

Overall this system (EDTA binding to various divalent metal cations) has proved an excellent model for understanding positive ΔC_p in N-Hsp90-Mg²⁺-ADP/ATP interactions, with binding of both Ca²⁺ and Mg²⁺ to EDTA showing positive ΔC_p . The consistency of the observed thermodynamic values demonstrates that solvation/desolvation related contributions to binding across the divalent metal cations are similar and can be successfully transferred to understand positive ΔC_p in protein-nucleotide (small molecule) interactions, especially N-Hsp90-Mg²⁺-ADP/ATP interaction.

3.3.6 Conclusion: Ca^{2+} and Mn^{2+} Substitution in Place of Mg^{2+} : Implications for the Binding Energetics and ΔCp of binding for ADP/AMPPNP to N-Hsp90

Peeraer et al. (200), have studied substitution of Ca^{2+} in place of Mg^{2+} in HPSP^{‡‡}-phosphoserine binding by X-ray crystallography. Interestingly, Mg^{2+} metal in this crystal structure displays almost perfect octahedral coordination geometry with six ligands, whereas Ca^{2+} coordination in the active site shows a distortion from octahedral plane. This distortion of the octahedral geometry happens due to the fact that the Ca^{2+} ion prefers seven ligands in its coordination sphere, instead of the six preferred by Mg^{2+} . As a result, one water molecule in Ca^{2+} ion coordination is forced out of the plane. Additionally, coordination of spherical metal ions is optimized by packing the maximum number of ligand atoms and the preferred coordination number is primarily a function of the size of the ion (201; 202); [the effective ionic radius of a Mg^{2+} ion (0.72 Å) is considerably smaller than that of a Ca^{2+} ion (1.06 Å) (202)]. In addition to the differences in geometry between Ca^{2+} and Mg^{2+} in the active site, the metal-ligand distances are also quite different. Comparison of the replacement of the Mg^{2+} by a Ca^{2+} ion shows that there is an increase in all metal-ligand distances, with average distances of 2.1 Å for Mg^{2+} and 2.4 Å for Ca^{2+} (200). All these factors resulting from the combination of dissimilar geometry and changed metal-ligand distances drastically affect the reaction mechanism of HPSP when the Mg^{2+} ion is substituted by a Ca^{2+} ion.

These differences in geometry observed between Ca^{2+} and Mg^{2+} in the active site of HPSP, can be used in investigating the effect of substitution of Mg^{2+} by Ca^{2+} on ΔCp of N-Hsp90-ADP/AMPPNP binding. In N-Hsp90-ADP/AMPPNP binding, Ca^{2+} will bind to ADP/AMPPNP first, which after binding will release up to two water molecules into the bulk solvent, from the first hydration shell of Ca^{2+} . Subsequently this Ca^{2+} -AMPPNP ligand complex will bind to N-Hsp90 in the same position and confirmation as Mg^{2+} -AMPPNP. As a result, Ca^{2+} will form a direct H-bond with O atoms (OD1) of the carboxamide side-chain of Asn37. This will result in further displacement of one more water molecule from the first shell of Ca^{2+} into bulk water. Nevertheless, Ca^{2+} with its larger ionic radii (1.06 Å) can form a H-bond with O atom (OD1) of Asp40, in fact Ca^{2+} can form a bidentate bond conformation with the O atom

‡‡ Human Phosphoserine phosphatase

3. Results and Discussion

(OD2) of Asp40 (Figure 3.3.14). This bidentate H-bond formation will displace more than two water molecules from the surface of Ca^{2+} . Furthermore Ca^{2+} on its own due to its larger ionic radii and doubled atomic volume ($\text{Ca}^{2+} = 29.9 \text{ cm}^3/\text{mol}$, $\text{Ca}^{2+} = 13.97 \text{ cm}^3/\text{mol}$) can destabilise more tightly bound water molecules from the binding cavity, releasing water molecules into bulk water solvent. It is also observed that the tendency of Ca^{2+} to bind water molecules, at least in the crystal structure, is less than for the Mg^{2+} ion (1.5 versus 2.2 water molecules on the average per metal ion site, respectively) (202). Thus all these factors will play an important role in increasing ΔC_p to $1.04 \text{ kJ}\cdot\text{mol}^{-1}\cdot\text{K}^{-1}$, as compared to $0.28 \text{ kJ}\cdot\text{mol}^{-1}\cdot\text{K}^{-1}$ observed in Mg^{2+} -AMPPNP binding to N-Hsp90.

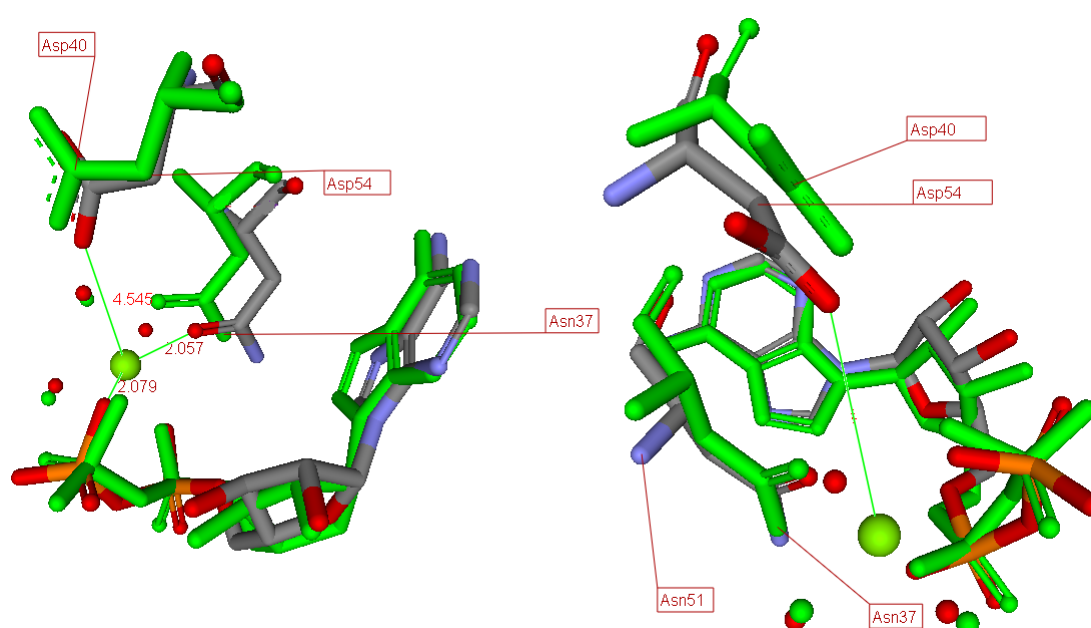


Figure 3.3.14 Two different poses of Mg^{2+} -ADP with bound water molecules and protein residues. Structure coloured according to element, indicates human N-Hsp90; whereas green coloured structure indicates yeast N-Hsp90. Please note that yeast N-Hsp90 structure lacks Mg^{2+} molecule in crystal structure. (Figure generated using DS ViewerPro 5.0 (56)).

Comparison of Mn^{2+} -AMPPNP and Mg^{2+} -AMPPNP binding shows some striking similarities between crystal structures containing Mg^{2+} and those containing Mn^{2+} . The similarities include that both Mg^{2+} and Mn^{2+} generally bind six ligands (as was found in about 75% of the total number of structures for each), and oxygen is the most likely ligand for both, although less so for Mn^{2+} (77% for Mg , 61% for Mn) (196). Consequently the tendency of Mn^{2+} to bind water molecules will be less than for Mg^{2+} ion and as a result Mn^{2+} binds more frequently to nitrogen atoms than the Mg^{2+} ion.

3. Results and Discussion

As AMPPNP lacks nitrogen atoms in the phosphate side-chain, it will probably result in weakly bound Mn^{2+} . As a result Mn^{2+} will keep more water molecules in its first hydration shell than a Mg^{2+} ion. Consequently after binding, this network of ordered water molecules may not be getting disordered or affected significantly upon binding to N-Hsp90, as Mn^{2+} will also find a relative absence of nitrogen groups in the binding site except Asn37. With Asn37, Mn^{2+} will be displacing one water molecule from a possible 4-6 water molecules coordinated by Mn^{2+} -AMPPNP. However for other water molecules, it will keep them, which will result in weakly trapping these water molecules in the binding site. This relative entrapment of water molecules results in the observation of a slight negative $\Delta\Delta C_p$ change of $-0.18 \pm 0.03 \text{ kJ}\cdot\text{mol}^{-1}\cdot\text{K}^{-1}$ as compared to Mg^{2+} -AMPPNP binding to N-Hsp90.

Additionally, the results obtained from the GRID simulation gives support to this hypothesis. The results obtained (discussed in detail in Section 3.3.1) show that the binding of Ca^{2+} is the most energetically favourable divalent metal cation in the N-Hsp90-ADP metal binding pocket with a potential binding energy of $-35.13 \text{ kcal}\cdot\text{mol}^{-1}$, which is followed closely by Mg^{2+} with $-32.85 \text{ kcal}\cdot\text{mol}^{-1}$. Mn^{2+} is at the bottom of all three cations and shows a favourable energy of $-29.73 \text{ kcal}\cdot\text{mol}^{-1}$. When interpreted in terms of water ordering around Ca^{2+} , Mg^{2+} and Mn^{2+} , this implies that Mn^{2+} is least likely to desolvate the water molecule after binding to N-Hsp90 as compared to Mg^{2+} or Ca^{2+} . In addition from the position predicted by GRID for Mn^{2+} ion, it can also be predicted that it will trap more water molecules in the cavity formed between N-Hsp90 and Mn^{2+} -ADP.

Likewise, if we compare titration of Ca^{2+} -AMPPNP, Mg^{2+} -AMPPNP and Mn^{2+} -AMPPNP to N-Hsp90 with Ca^{2+} , Mg^{2+} and Mn^{2+} binding to EDTA, a clear correlation in observed ΔC_p can be seen. As both Ca^{2+} and Mg^{2+} bind to EDTA with a positive ΔC_p of around $0.19 \pm 0.00 \text{ kJ}\cdot\text{mol}^{-1}\cdot\text{K}^{-1}$ and $0.20 \pm 0.00 \text{ kJ}\cdot\text{mol}^{-1}\cdot\text{K}^{-1}$ as compared to negative ΔC_p of $-0.22 \pm 0.15 \text{ kJ}\cdot\text{mol}^{-1}\cdot\text{K}^{-1}$ observed for Mn^{2+} binding to EDTA.

3.4 Conclusion

ΔC_p is one of the major thermodynamic parameter, used largely in quantifying protein unfolding and protein-ligand binding studies. With more than half a dozen definitions, ΔC_p is also one of the hardest thermodynamic quantities to understand in physico-chemical terms, but is richest in insight. ΔC_p is also responsible for the temperature dependence of ΔH and ΔS and determines which one will dominate at a particular temperature. Nonetheless, ΔC_p also remains the major thermodynamic parameter, where the most basic questions are still largely unanswered with sources coming from hydration (protein-solvent, and accompanying solvent-solvent interactions) identified particularly well as compared to the protein-ligand interaction.

To understand the role of ΔC_p in protein-ligand interactions in addition to solvation/desolvation parameters, we have used N-Hsp90-ADP/AMPPNP and N-Hsp90-geldanamycin as model systems in this study. Consequently, we have used a wide range of methods including calorimetry, simulation and structural analysis to understand the binding related ΔC_p . As we progressed through the project, it becomes clear that the general explanation of protein-ligand association is difficult and intricate to explain in N-Hsp90-Mg²⁺ADP/ATP interaction due to strict synergy of the resulting electrostatic and partial hydrophobic interactions, compared to a simple and straightforward case of hydrophobic interactions in geldanamycin binding with N-Hsp90.

Semi-empirical $\Delta SASA$ calculations suggested that surface area burial accounts for part of the observed positive ΔC_p , making this system unique. This was an important observation, considering that previous observations of positive ΔC_p (7; 8; 203) were unable to assign any particular reasons for their observation. Additionally, calorimetric titrations in different buffers and pH conditions displayed that a positive ΔC_p of $0.28 \pm 0.03 \text{ kJ}\cdot\text{mol}^{-1}\cdot\text{K}^{-1}$ observed for AMPPNP-Mg²⁺ binding to N-Hsp90 remains unaffected in different buffer and at pH 7.00 and above, although due to protonation it falls to a zero ΔC_p value at pH 6.00 and below. This pH effect is due to acidic groups that start to protonate at approximately pH 6.00. Also altering the solvent from H₂O to D₂O pointed towards strong experimental evidence that the reorganisation of solvent during binding contributes significantly to the observed ΔH , however keeping ΔC_p unaffected.

These observations forced us to look into the signs and magnitudes of the thermodynamic parameters of protein-ligand interaction processes in terms of our knowledge of the thermodynamical behaviour of intermolecular interactions (Table 3.3.1). This made us think about possible sources of discrepancy in ionic or charge-charge interactions, as all other interactions had assigned magnitudes. Also semi-empirical $\Delta SASA$ based methods account for all other factors except charge-charge interactions.

Understanding of the ΔC_p from EDTA-metal chelation allowed us to successfully investigate our thermodynamic results obtained for divalent metal cation-AMPPNP binding to N-Hsp90 in solution. This allowed us to speculate that the predominant origin of the large positive ΔC_p upon ADP/ATP binding to N-Hsp90 must be found in conspicuous water ordering that embeds the Mg^{2+} -ADP/ATP environment. The hydrogen bonding network of water molecules in this region is remarkably strong because of their small van der Waals radii. This network of ordered water molecules is disordered/affected significantly upon binding of Mg^{2+} -ADP/ATP to N-Hsp90. Unquestionably the crystal structure of N-Hsp90 bound to ADP (Figure 3.3.14) indicates that most of these strongly ordered water molecules are missing or transferred to bulk solvent from the first and second hydration shells of Mg^{2+} . Additionally Mg^{2+} in Mg^{2+} -ADP forms a direct H-bond with the carbonyl oxygen of Asn37 (Figure 3.3.14), displacing a tightly bound water molecule from first solvation shell of the Mg^{2+} -ADP upon binding to N-Hsp90. As a result of these observations, an understanding of the role played by metals in ΔC_p has started to emerge with the substitution of Mg^{2+} by Ca^{2+} and Mn^{2+} highlighting the key phenomenon of water ordering and disordering upon ligand binding to the protein.

So on the basis of available evidence, a model for the binding and resultant understating of observed ΔC_p in Mg^{2+} -ADP/AMPPNP binding to N-Hsp90 can be proposed:

1. Mg^{2+} -ADP/AMPPNP binds the solvent exposed N-Hsp90, resulting in both charged (ionic) polar and hydrophobic interactions.
2. At 25 °C, the energetics of Mg^{2+} -ADP/AMPPNP binding to the N-Hsp90 is enthalpically favourable and entropically opposed, which results in a relatively weak ΔG of binding.

3. Although the binding is likely to be linked to solution pH, this pH linkage is not expected to have an effect on the observed positive ΔC_p of binding at pH 7.00 and above.

4. The $\Delta SASA$, in addition to displacement of water molecules from the surface of the Mg^{2+} ion accompanying association of Mg^{2+} -ADP/AMPPNP to N-Hsp90, can mainly be regarded as the factor responsible for the observed positive ΔC_p of binding.

The observed energetics of Mg^{2+} -ADP/AMPPNP binding to N-Hsp90 deviates from the average thermodynamic behaviour for protein-ligand interactions and therefore care must be taken when assigning $\Delta SASA$ related parameters to the binding of proteins with the divalent metal cation-nucleotides and probably in other intrinsic metal binding studies. Additionally, the observed energetics of Mg^{2+} -ADP/AMPPNP binding could also be considered when developing empirical, surface area-based methods for estimating the energetics of protein-ligand, protein-protein and protein-nucleic acid interactions.

So in conclusion, it appears that water molecules desolvated from the surface of divalent metal cations in a polar/charged environments have distinctly large thermodynamic effects, which are not adequately represented in the current accessible surface area based models for calculation of ΔC_p . However in the absence of extensive structural data, such large effects could be easily misinterpreted as coupled folding and can lead to an inaccurate view of protein-ligand interaction mechanisms. With further work, the relative magnitude of hydration and charge-charge interactions of various divalent metal cations on modulating ΔC_p , established by this work can be developed into a universal descriptor for the thermodynamic analysis for future investigations, specially in $\Delta SASA$ based structure-based drug design and protein folding studies. Additionally the present study has tried, and was successful in, eliminating some of the difficulties that have arisen from the attempts to interpret ΔC_p solely in terms of hydrophobic contribution.

4. Chapter

Investigating Binding Affinity of a Series of CDK2 Inhibitors by ITC and Using Semi-Empirical Approaches to Design New Inhibitor Based on Calorimetric Data

4.1 Introduction

CDKs are implicated in cell division and their deregulated activity is thought to contribute to the initiation and progression of several diseases such as cancer. CDKs catalyze the transfer of a phosphate group from ATP to a specific substrate amino-acid residue (serine or threonine), and the majority of drug discovery research in this area has been aimed at developing small molecules that mimic ATP and bind competitively to its binding site(72; 204). As a result, a number of groups have been working on the identification and development of CDK inhibitors(205; 206). One such inhibitor, 2,4-bis anilino pyrimidine, a pyrimidine analogue, is also being developed as a potential CDK2/CDK4 inhibitor by Breault et al. (104). This molecule has shown moderate binding of 34 μM (IC_{50}) towards CDK2. While a similar compound, 4,6-bis anilino pyrimidine, in which the pyrimidine N3 is moved to the equivalent of the 5 position also demonstrates affinity towards CDK2 (Figure 4.1.1). However, it binds with a lower IC_{50} of $>100 \mu\text{M}$, which is 3-4 times lower than the binding affinity exhibited by 2,4-bis anilino pyrimidine.

In an effort to resolve the differences in biophysical properties that dictate these distinctly different binding properties, thermodynamic analysis characterizing the

CDK2 binding properties of these two similar bis anilino pyrimidine analogues was conducted. Additionally, we aim to investigate the influence of minor alteration in the position of the various substituent groups on the binding thermodynamics, particularly ΔH and $T\Delta S$. To achieve this goal we have used 2,4-bis anilino pyrimidine and 4,6-bis anilino pyrimidine as base inhibitors and analogues were designed by the addition of small chemical substituent groups such as halogens, amines, alcohols and nitrile groups.

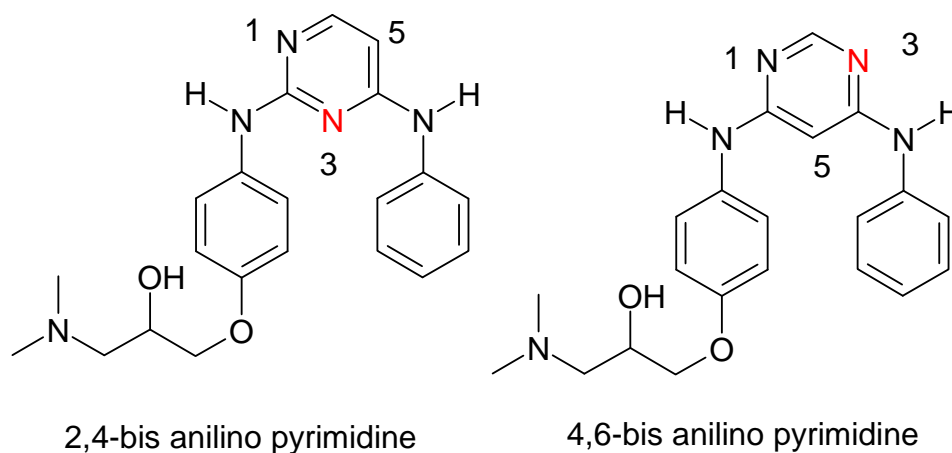


Figure 4.1.1 Chemical Structure of 2,4-bis anilino pyrimidine (left) and 4,6-bis anilino pyrimidine (right) with changed position of nitrogen in the pyrimidine ring denoted by red colour.

Additionally, in this chapter we have also tried to correlate various thermodynamic parameters (mainly ΔG) with computationally derived parameters such as van der Waals, electrostatic and solvent accessible surface area terms with success in determination of ΔG from LIE calculations. This study represents a small ligand based approach to better understanding of protein-ligand binding thermodynamics.

4.2 Thermodynamics of Binding of Bis anilino pyrimidine to CDK2

All of the 2,4-bis anilino pyrimidines and 4,6-bis anilino pyrimidines were synthesized and supplied by AstraZeneca, Alderely Park, Macclesfield, Cheshire. Both of these 2,4-bis anilino pyrimidine and 4,6-bis anilino pyrimidines have similar structures, barring the position of nitrogens in the middle of the pyrimidine ring (Figure 4.1.1). The first subset was comprised of 7 ligands (Table 4.2.1A) and was designed and synthesized by Breault et al. (104). Analogues in this set (2,4-bis anilino pyrimidine) were synthesized by reacting 2,4-dichloro pyrimidine with appropriately substituted aniline to introduce the B ring (Table 4.2.1A-Figure a).

The second set (Table 4.2.1B) consisted of 11 ligands and were designed and synthesized by Beattie et al. (207). This set of 11 compounds was synthesized by reacting 4,6-dichloro pyrimidine with 4-hydroxy aniline to give monochloro intermediate (Table 4.2.1B-Figure b). This monochloro intermediate was then treated with appropriate substituted aniline to introduce ring B. The phenol was then alkylated with epibromohydrin followed by ring opening resulting in the final compounds shown in Table 4.2.1A and 4.2.1B.

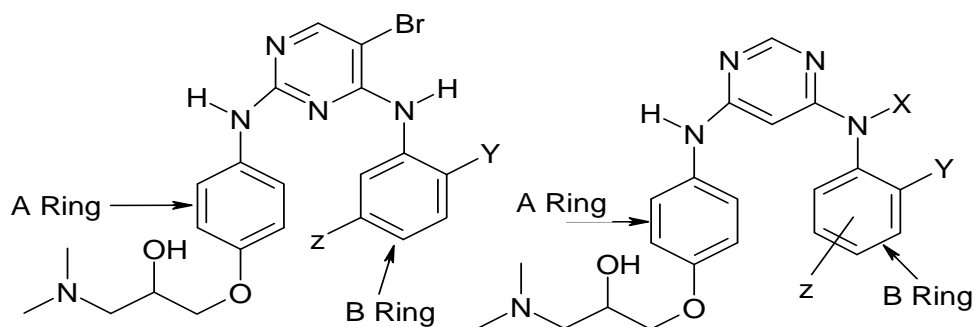


[Figure a] 2,4-Bis Anilino Pyrimidine

[Figure b] 4,6-Bis Anilino Pyrimidine

Ligand	AlogP ^{§§}	X	Y	Z
M387441	3.82	H	H	H
M395323	4.94	H	Cl	Cl
M407492	4.57	Br	H	H
M415913	4.97	H	F	CF ₃
M404457	4.48	H	Cl	H
M437249	4.02	H	F	H
M404797	3.59	H	OCH ₃	H

Table 4.2.1A Substituents used for substitution along with their appropriate positions on 2,4-bis anilino pyrimidine along with their positions [Figure a].

Ligand	AlogP ^{§§}	X	Y	Z
M389750	4.80	CH ₃ CN	Br	4-CH ₃
M365370	4.25	H	F	5-F
M410038	4.58	H	Br	H
M365538	4.78	H	F	4-CF ₃
M417061	3.73	H	NO ₂	H
M388031	4.99	H	Cl	4-CH ₃
M365677	3.82	H	OCH ₃	H
M386279	4.53	H	F	4-CH ₃
M365377	4.50	H	Cl	H
M386872	3.91	C ₂ H ₅ OH	F	4-F
M410581	3.57	H	OH	H

Table 4.2.2B Substituents used for substitution along with their appropriate positions on 4,6-bis anilino pyrimidine [Figure b].

^{§§} AlogP is an octanol/water partition coefficient.

4.2.1 Thermodynamics of Various 2,4-Bis Anilino Pyrimidine Ligands with CDK2

Thermodynamics for binding of 2,4-bis anilino pyrimidine to CDK2 were studied using ITC. However due to the low aqueous solubility of 2,4-bis anilino pyrimidine, dimethyl sulfoxide (DMSO) was used to dissolve the compound into concentrated stock solutions (~10 mg/ml). The DMSO-ligand solutions were then diluted 1:50 in 20 mM HEPES buffer (pH 7.40). The DMSO content in all of the experiments carried out was 2% (v/v).

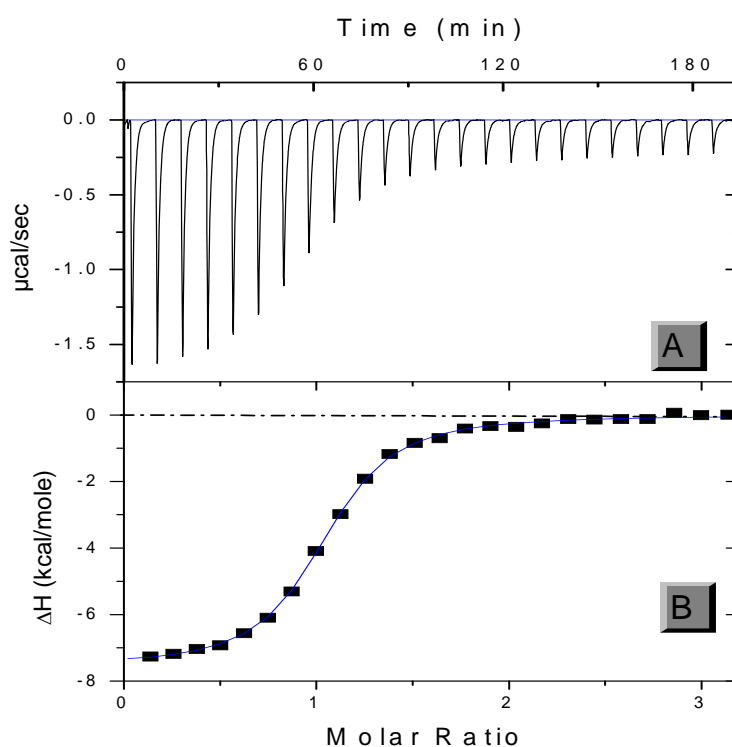


Figure 4.2.1 A: Raw data for titration of M407492 with a CDK2 at 25 °C in 20 mM. HEPES. pH 7.4. **B:** Binding isotherm derived from A, corrected for the heats of dilution; the line represents the least squares fit to the single site binding model.

Figure 4.2.1 shows the raw data of a typical binding experiment, the titration of M415913 with CDK2 in 20 mM HEPES buffer pH 7.4 at 25 °C. This titration shows binding as a strong exothermic event. The heat of dilution peaks (not shown in Figure 4.2.1) are very small, exothermic and equal in size. This indicates that, at this concentration, under the adopted buffer conditions, no aggregation occurs, which is significant considering the hydrophobic nature of the ligands. Figure 4.2.1 also shows

the corresponding binding isotherm. The stoichiometry in all titrations was close to 1. The resulting thermodynamic parameters are listed in Tables 4.2.2, 4.2.3 and 4.2.4.

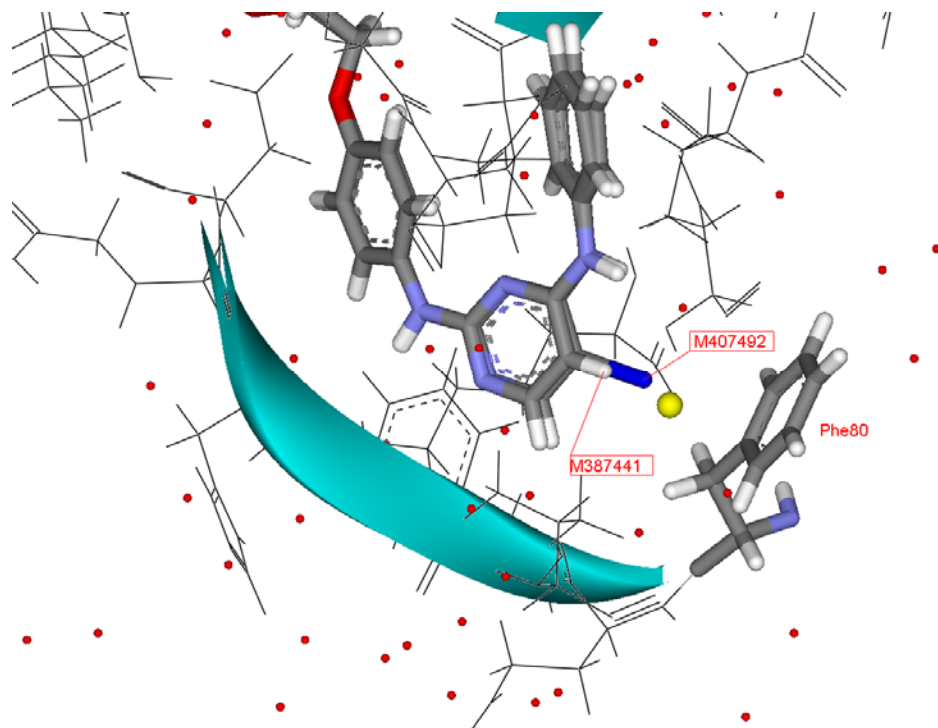


Figure 4.2.2 Superposition of the binding modes of M387441 and M407492, displaying interactions made by bromine with Phe80 of CDK2. The Bromine atom in M407492 displaces water molecule (yellow sphere) found in the complex formed by CDK2 and M387441. Also the B-ring in M407492 adopts an orientation similar to M387441. M407492 shows about ~23 times more affinity than M387441. Red -other water molecules, Blue -bromine atom. (Figure generated using DS ViewerPro 5.0 (56))

Amongst all the seven analogues, M407492 shows the highest affinity for CDK2, which is ~23 times higher than M387441 (K_d 39.49 μM). At 25 °C, the K_d is around 1.72 μM with ΔH being the main driving force behind the binding event, with a minimal unfavourable $T\Delta S$ contribution (Table 4.2.2). The high binding affinity for M407492 could partially be attributed to polarizability of 5-bromine substitution on the pyrimidine ring, which stacks with the aromatic ring of Phe80, allowing an improved attraction of the π -electron cloud towards bromine (Figure 4.2.2). This bromine atom displaces a water molecule, which was present in the binding site of M387441. Interestingly, this water molecule stacks up against the hydrophobic phenyl ring of Phe80. M407492 shares the same structural features as M387441, except a bromine atom on the X-position (Table 4.2.1a). Also the high affinity observed in M407492 validates the adopted substitution approach in achieving better binding affinities.

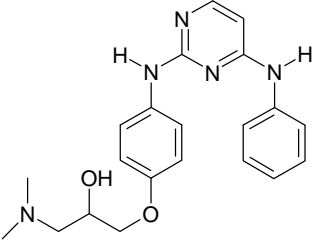
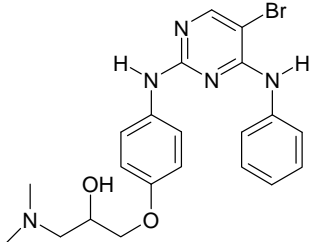
Name of Molecule	Stoichiometry	K_d (μM)	ΔH ($\text{kJ}\cdot\text{mol}^{-1}$)	$T\Delta S$ ($\text{kJ}\cdot\text{mol}^{-1}$)	ΔG ($\text{kJ}\cdot\text{mol}^{-1}$)
 M387441	1.01 ± 0.06	39.49	-35.90 ± 2.95	-10.74	-25.08
 M407492	0.99 ± 0.01	1.72	-36.03 ± 0.59	-3.14	-32.85

Table 4.2.3 Thermodynamic binding parameters for M387441 and M407492.

In general, all of the 2,4-bis anilino pyrimidine ligands interact with the monomeric CDK2, with central pyrimidine N1 acting as a hydrogen bond acceptor, while 6-aniline NH serves as a hydrogen bond donor.

As substitution had proved a successful way to improve binding thermodynamics in M407492, we decide to investigate substitution at the 2 position of the B-ring and used 3 compounds namely: M404457, M437249 and M404797 (Table 4.2.3). However (in contrast to M407492), M404457, M437249 and M404797 showed very small improvement in the binding affinity, as compared to M387441. M404457 differs from M437249 in having chlorine in place of fluorine in the 2-position. Both compounds show similar ΔG , however they show large differences in ΔH of around $17.89 \text{ kJ}\cdot\text{mol}^{-1}$ with opposing signs for $T\Delta S$. These substitutions would be expected to stack against Asn132, Ala144 and Asp144, which form a bigger hydrophilic pocket along with other amino acids such as Val18, Gly 11 and Ile10.

Experimentally the binding constant increases as more steric bulk is substituted at the ortho position of the B-ring $K_H < K_F < K_I < K_{OCH_3}$. One explanation might be that increasing the steric bulk of the substituents leads to progressive distortion of the binding pocket and its surroundings, which is also reflected in increasing ΔG of these

4. Results and Discussion

ligands. Interestingly this increasing ΔG is complemented with decreasing ΔH and increasingly favourable $T\Delta S$, showing a clear thermodynamic trend among this series. This result highlights the power of calorimetric data in discriminating thermodynamic parameters for a series of small molecules substituted with different substituents.

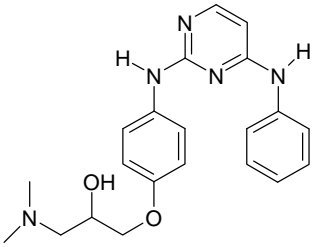
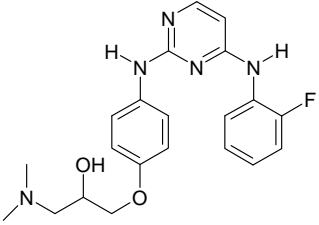
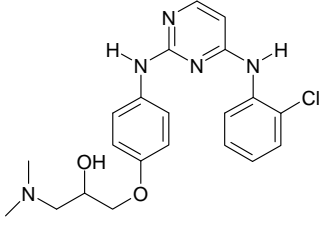
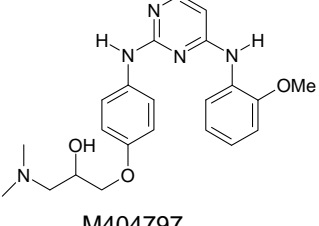
Name of Molecule	Stoichiometry	K_d (μM)	ΔH ($\text{kJ}\cdot\text{mol}^{-1}$)	$T\Delta S$ ($\text{kJ}\cdot\text{mol}^{-1}$)	ΔG ($\text{kJ}\cdot\text{mol}^{-1}$)
 M387441	1.01 ± 0.06	39.49	-35.90 ± 2.95	-10.74	-25.08
 M437249	1.01 ± 0.02	23.46	-42.76 ± 1.65	-16.34	-25.50
 M404457	1.05 ± 0.01	18.45	-24.87 ± 0.54	2.09	-26.96
 M404797	1.01 ± 0.06	22.47	-18.56 ± 1.98	7.90	-26.50

Table 4.2.4 Thermodynamic binding parameters for various Y-monosubstituted 2,4-bis anilino pyrimidine analogues.

We therefore decided to look at the binding thermodynamics of the disubstituted analogues as introducing or increasing bulk of the 4,5 position should lead to increased

4. Results and Discussion

activity, possibly because the bioactive ring B orientation becomes more favourable for binding CDK2.

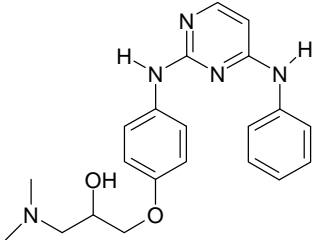
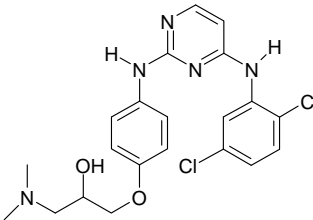
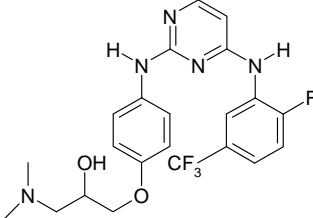
Name of Molecule	Stoichiometry	K_d (μM)	ΔH ($\text{kJ}\cdot\text{mol}^{-1}$)	$T\Delta S$ ($\text{kJ}\cdot\text{mol}^{-1}$)	ΔG ($\text{kJ}\cdot\text{mol}^{-1}$)
 M387441	1.01 ± 0.06	39.49	-35.90 ± 2.95	-10.74	-25.08
 M395323	1.12 ± 0.01	6.28	-32.94 ± 0.88	-3.26	-29.64
 M415913	1.08 ± 0.02	2.16	-24.95 ± 0.75	7.27	-32.27

Table 4.2.5 Thermodynamic binding parameters for various disubstituted 2,4-bis anilino pyrimidine analogues.

This subset contained two compounds; M395323 and M415913 (Table 4.2.4). $\Delta\Delta G$ relative to M387441 for the introduction of various substituents on the 2,5 position of the B ring was found to be more favourable, with substituted fluorine analogue M415913 (2-F, 5-CF₃) showing the best binding affinity, with ΔG of about $-32.27 \text{ kJ}\cdot\text{mol}^{-1}$. M415913 also binds to CDK2 with favourable ΔH and $T\Delta S$, while binding of M395323 incurs an entropic penalty of $-3.26 \text{ kJ}\cdot\text{mol}^{-1}$. Looking at the X-ray and docked conformations, these substitutions stack against a hydrophilic pocket lined by Asn132, Ala144, Asp144, Val18, Gly 11 and Ile10. This hydrophilic pocket can easily accommodate larger substituents; however the B-ring is very flexible and affords different conformations as compared to the monosubstituted analogue, suggesting

disubstitution as an approach to improve binding affinity in bis anilino pyrimidine compounds. Also note that M415913 binds with favourable ΔH and $T\Delta S$, which can only be calculated from calorimetric methods and not by other techniques like Surface Plasmon Resonance (SPR) and enzyme assays.

M395323 and M404457 share similar molecular structure except an extra chlorine substitution on the B ring of M395323, at the 5- position. Both of these ligands bind to monomeric CDK2 with similar binding affinity of 27 to 30 $\text{kJ}\cdot\text{mol}^{-1}$, but possess different values of ΔH (-32.94 and -24.85, respectively), showing a difference of about 8 $\text{kJ}\cdot\text{mol}^{-1}$ along with a $T\Delta S$ difference of about 5.15 $\text{kJ}\cdot\text{mol}^{-1}$. M415913 and M437249 also share similar molecular structure except for a trifluoromethyl substitution at the 5-position on the B ring of M415913. M415913 binds to CDK2 with a K_d of 2.16 μM , while M437249 binds to CDK2 with a K_d of 23.46 μM . This translates into a ΔG difference of 5.85 $\text{kJ}\cdot\text{mol}^{-1}$ in favour of M415913. M415913 also binds to CDK2 with favourable ΔH and $T\Delta S$, while binding of M437249 incurs a large entropic penalty of -16.34 $\text{kJ}\cdot\text{mol}^{-1}$.

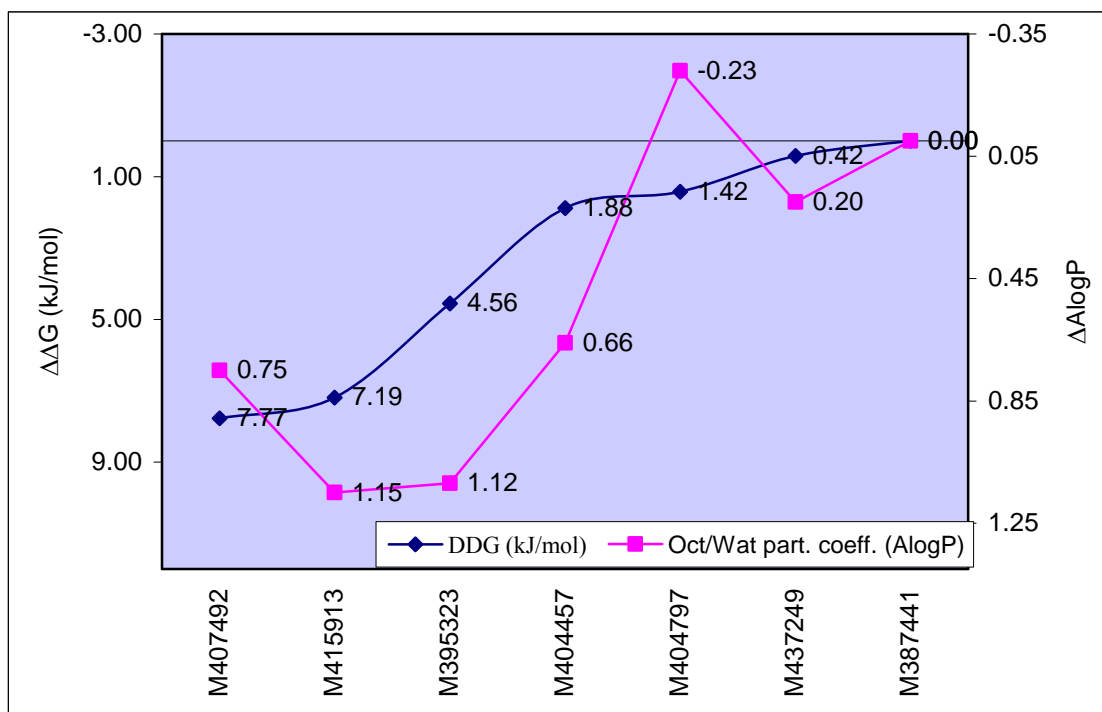


Figure 4.2.3 Comparison of relative experimental ΔG vs relative AlogP (with respect to M387441) of binding to CDK2 with various 2,4-bis anilino pyrimidines at 25 °C.

In Figure 4.2.3, the $\Delta\Delta G$ relative to M387441 (i.e., going from 2,4-bis anilino pyrimidine to their respective substituent groups is compared) at 25 °C is plotted with their respective AlogP values. The graph shows increasing hydrophobicity results in increasing ΔG of binding, excluding M404797 and M407492. However, the absolute magnitude of ΔG binding is not directly proportional to the corresponding estimates of the octanol/water partition coefficients (AlogP). Interestingly, such a direct correlation of hydrophobicity with ΔG of binding is also observed by Talhout et al. (208) in their study of hydrophobically modified benzamidinium chloride inhibitors, where they have shown increasing hydrophobicity results in increased ΔG binding to trypsin.

4.2.2 Thermodynamics of Various 4,6-Bis Anilino Pyrimidine Ligands with CDK2

Microcalorimetry was also used to characterise the binding of 4,6-bis anilino pyrimidine to CDK2. Similar to 2,4-bis anilino pyrimidines, the 4,6-bis anilino pyrimidines are also highly hydrophobic in nature and as a result DMSO was used to dissolve the compound into concentrated stock solutions (~10 mg/ml). The DMSO-ligand solutions were then diluted 1:50 to 1:20 in 20 mM HEPES buffer (pH 7.4). The DMSO content in the individual experiments was never higher than 5% (v/v), with the majority of experiments carried out at 2% (v/v). All titrations were well defined with clear binding isotherms and in most of the cases stoichiometry was close to 1 or 1.

The structure and thermodynamic binding parameters of 4,6-bis anilino pyrimidines are given in Tables 4.2.5, 4.2.6, 4.2.7 and 4.2.8. Out of all 4,6-bis anilino pyrimidine analogues, M410581 binds tightest to monomeric CDK2 with ΔG of $-27.00 \text{ kJ}\cdot\text{mol}^{-1}$. This ΔG consists of about 70% entropic contribution ($18.73 \text{ kJ}\cdot\text{mol}^{-1}$), with the rest $8.28 \pm 0.35 \text{ kJ}\cdot\text{mol}^{-1}$ coming from the enthalpic component. The very high entropic component points towards the displacement of water molecules by M410581 and suggests a novel binding mode.

M365677, M417061, M365677 and M410581 derive from the same backbone structure of 4,6-bis anilino pyrimidine but have different substituent groups. Varying the substituents from hydroxyl to methoxy groups at the ortho position of the B-ring, results in small variations in their thermodynamic modes of binding. Although substituents with longer chains result in better ΔH , however it results in unfavourable entropy resulting in lower ΔG . Interestingly, the results obtained within this limited subseries support the fact that a range of substituents are well tolerated with 2-OH and 2-NO₂ derivatives being the most potent. The crystal structure and docked conformations of the 4,6-bis anilino pyrimidines show that the B-ring in this series takes up a range of conformations/orientations within the series, compared to 2,4-bis anilino pyrimidines, making interpretation of the thermodynamic trends difficult. The 2-Cl and 2-F derivatives were chosen for further investigation because the accessibility of the polyfunctional anilines could allow us to determine thermodynamic parameters for a disubstituted B-ring, which we believe can result in enhancement of binding affinity (observed previously in 2,4-bis anilino pyrimidine analogues).

4. Results and Discussion

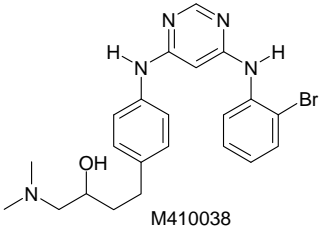
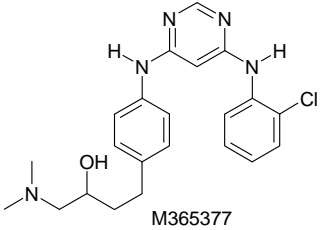
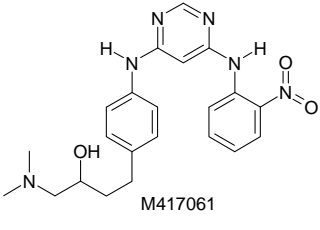
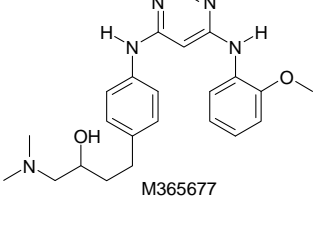
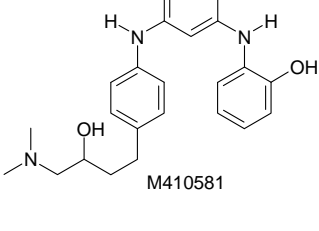
Name of Molecule	Stoichiometry	K_d (μM)	ΔH ($\text{kJ}\cdot\text{mol}^{-1}$)	$T\Delta S$ ($\text{kJ}\cdot\text{mol}^{-1}$)	ΔG ($\text{kJ}\cdot\text{mol}^{-1}$)
 M410038	0.95 ± 0.12	60.97	-35.45 ± 6.36	-11.33	-24.08
 M365377	1.03 ± 0.02	34.05	-24.29 ± 0.76	1.17	-25.46
 M417061	1.07 ± 0.06	29.06	-29.39 ± 2.60	-3.51	-25.87
 M365677	0.91 ± 0.03	42.24	-29.59 ± 1.71	-4.68	-24.91
 M410581	1.12 ± 0.03	18.02	-8.28 ± 0.35	18.73	-27.00

Table 4.2.6 Structure and thermodynamic parameters for various monosubstituted 4,6-bis anilino pyrimidine analogues.

Compound M365370, resulting from the substitution of fluorine at the 2 and 5 positions of the B-ring of M410038, showed further improvements in binding affinity. The active site costructure of M365370 bound to CDK2 is shown in Figure 4.2.4 as determined from X-ray crystallography to a resolution of 1.60 Å by Beattie et al.(207).

M365370 forms several specific and non-specific hydrogen bonds with CDK, including H-bonds between pyrimidine N1 to NH amide from Leucine 83 and between the 6-anilino NH and backbone oxygen atom. Also the dimethylamino propanediol tail forms several non specific H-bonds with the CDK2; this strong network of H-bonds should contribute significantly towards ΔH . However the binding enthalpy of about $-9.15 \pm 1.34 \text{ kJ}\cdot\text{mol}^{-1}$ is about 3 to 3.5 times smaller than the ΔH exhibited by M4100038, but there is an entropic gain of about $28.80 \text{ kJ}\cdot\text{mol}^{-1}$, which added together results in a ΔG increase of $2.55 \text{ kJ}\cdot\text{mol}^{-1}$.

M388031 and M386279 also share the same molecular backbone of 4,6-bis anilino pyrimidine; fluorine is substituted in place of chlorine in M386279. Both of these compounds show similar thermodynamics, with similar values of ΔH and $T\Delta S$. This thermodynamic comparison highlights the fact that similar compounds bind with a similar thermodynamic signature.

All other disubstituted compounds like M365538, M365370, M388031 and M386279 bind with smaller ΔH , but with much more favourable $T\Delta S$. However none of

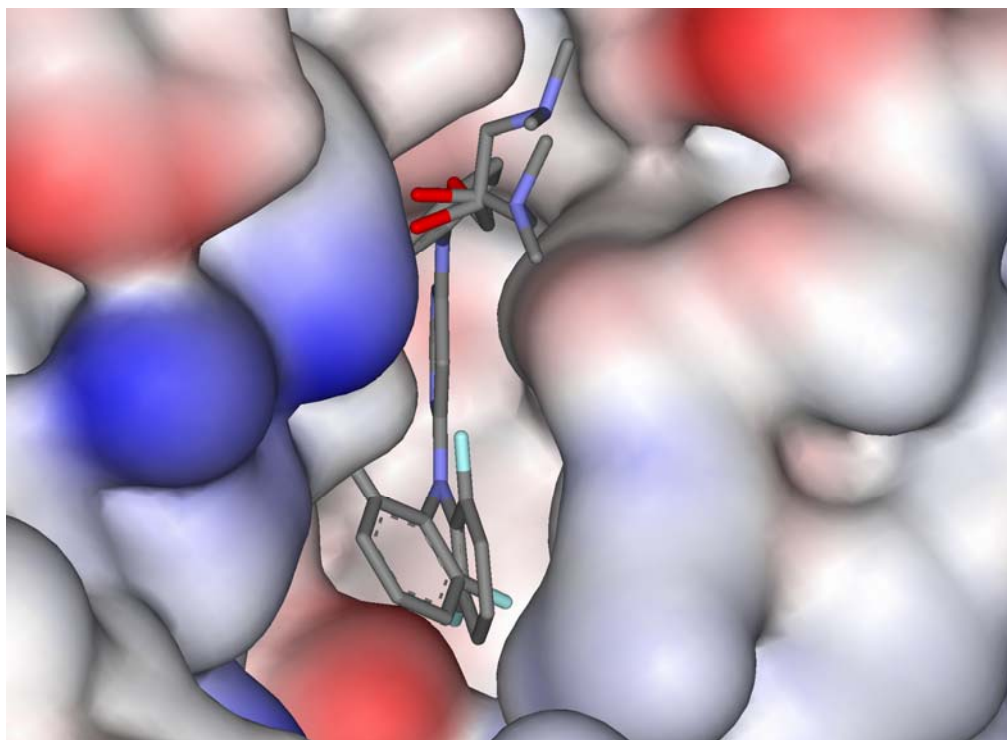


Figure 4.2.4 Costructure of M365370 bound to CDK2 showing the Connolly surface of the binding site colour coded according to electrostatic potential. Red indicates negatively charged surface area, and blue indicates positively charged surface area. M365370 indicates two similar binding modes with CDK2 with equal occupancies. Moreover these two orientations vary in the position of their dimethylamino propanediol flexible tail, as it does not form any direct H-bond with any of the protein residues. (Figure generated using DS ViewerPro 5.0 (56))

4. Results and Discussion

the disubstituted compounds tested bound significantly tighter, as measured by ITC than other monosubstituted analogues. This result contradicts the result obtained for the disubstituted 2,4-bis aniline pyrimidine analogues, which shows significant improvements in their binding affinity.

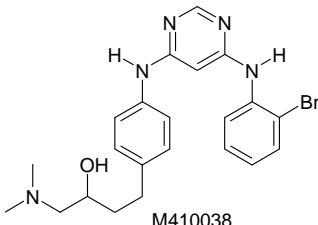
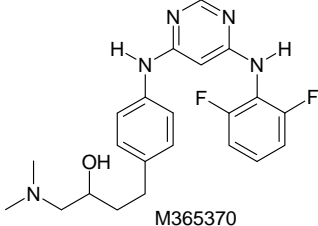
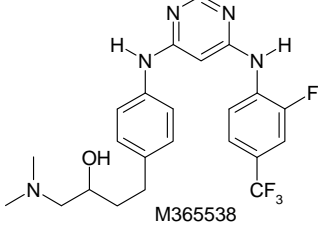
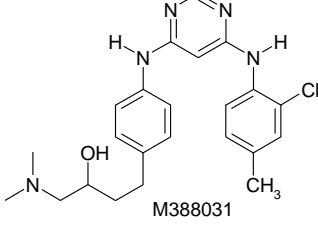
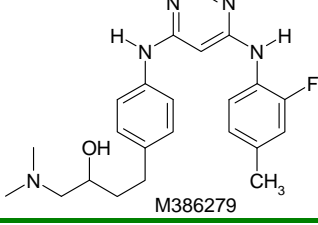
Name of Molecule	Stoichiometry	K_d (μM)	ΔH ($\text{kJ}\cdot\text{mol}^{-1}$)	$T\Delta S$ ($\text{kJ}\cdot\text{mol}^{-1}$)	ΔG ($\text{kJ}\cdot\text{mol}^{-1}$)
 M410038	0.95 ± 0.12	60.97	-35.45 ± 6.36	-11.33	-24.08
 M365370	1.14 ± 0.09	21.04	-9.15 ± 1.34	17.47	-26.63
 M365538	1.18 ± 0.05	19.33	-13.59 ± 1.14	-13.25	-26.84
 M388031	1.38 ± 0.14	41.40	-19.56 ± 3.44	5.39	-25.00
 M386279	1.08 ± 0.04	74.73	-24.24 ± 1.67	-0.71	-23.49

Table 4.2.7 Figure 4.2.6 Structure and thermodynamic parameters for disubstituted 4,6-bis anilino pyrimidines analogues.

The ΔG of binding for M410038 was $-24.08 \text{ kJ}\cdot\text{mol}^{-1}$ and was one of the lowest of the compounds listed, calculated from the equilibrium dissociation constant (K_d) of $60.97 \mu\text{M}$ determined by calorimetry. M410038 forms several H-bonds with CDK2,

4. Results and Discussion

which contribute significantly towards the binding enthalpy of $-35.45 \pm 6.36 \text{ kJ}\cdot\text{mol}^{-1}$. However, the small hydrophobic Phe80 subpocket was unoccupied by M410038.

Molecular modelling studies indicate that an appropriately positioned cyanomethyl group could be extended into the Phe80 binding pocket by tethering on to the nitrogen of the B-ring aniline. Compound M389750, shown in Table 4.2.7 was synthesized based on the modeling results (207). Extending the cyanomethyl group of M389750 into Phe80 modestly improved ligand affinity, as indicated by the thermodynamic parameters listed. The K_d was $30.00 \text{ }\mu\text{M}$, and the ΔH was $-43.81 \pm 1.48 \text{ kJ}\cdot\text{mol}^{-1}$. An improved ΔG of binding resulted from $\Delta\Delta H$ of $-8.36 \text{ kJ}\cdot\text{mol}^{-1}$ and unfavourable $T\Delta\Delta S$ of $-6.64 \text{ kJ}\cdot\text{mol}^{-1}$ compared to M410038.

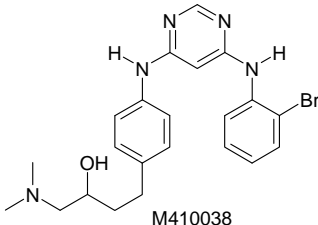
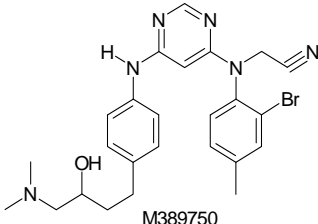
Name of Molecule	Stoichiometry	K_d (μM)	ΔH ($\text{kJ}\cdot\text{mol}^{-1}$)	$T\Delta S$ ($\text{kJ}\cdot\text{mol}^{-1}$)	ΔG ($\text{kJ}\cdot\text{mol}^{-1}$)
 M410038	0.95 ± 0.12	60.97	-35.45 ± 6.36	-11.33	-24.08
 M389750	1.03 ± 0.02	30.00	-43.81 ± 1.48	-17.97	-25.79

Table 4.2.8 Structure and thermodynamic parameters for M410038 and M389750.

The structure of M389750 bound to CDK2 has also been solved by Beattie et al. (207) revealing a binding mode consistent with the design hypothesis: the B-ring orientation was similar to that found for M365370 but with the cyanomethyl group displacing the bridging water molecule. The nitrile C lies within 1.3 \AA of the water. The nitrile triple bond is stacked against the π cloud of the Phe80 side-chain, with its polarity complimentary to the local electrostatic potential caused by the Lys33 side-chain (Figure 4.2.5). This improved intermolecular interaction can be observed as the improved ΔH of binding, which is about $-8.36 \text{ kJ}\cdot\text{mol}^{-1}$ and is more favourable than the ΔH observed for M410038.

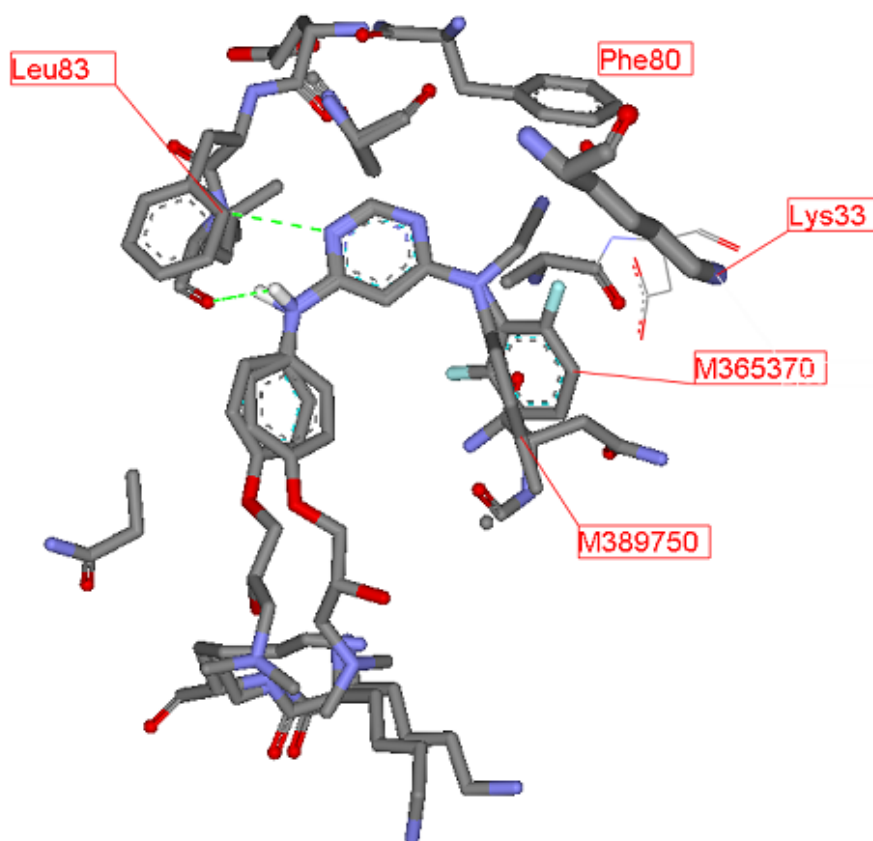


Figure 4.2.5 Figure 4.2.5 Overlay of binding modes of M389750 and M365370. The ring B in M389750 adopts an orientation similar to M365370. The nitrile C lies within 1.3 Å of the position occupied by the bridging water molecule in the complex between M365370 and CDK2. (Figure generated using DS ViewerPro 5.0 (56))

M386872, which results from the addition of an ethanolic side-chain to the 4-aniline nitrogen of M365370 is shown in Table 4.2.8. This substitution showed slight improvement in binding affinity, with both M365370 and M386872 binding CDK2 with similar ΔG values of $-26.63 \text{ kJ}\cdot\text{mol}^{-1}$ and $-25.25 \text{ kJ}\cdot\text{mol}^{-1}$. Also both these compounds bind with similar ΔH and $T\Delta S$ values indicating that both these compounds bind in similar fashion with the ethanolic side-chain playing no major role in binding thermodynamics. Further investigation of the X-ray structure of M365370 and the docked structure of M386872 reveals a similar conformation of the B-ring in the bound position to CDK2. This might explain some of the similarities in binding thermodynamics.

However, comparing the difference in ΔH for binding with M389750 binding with a much higher ΔH of $-43.81 \text{ kJ}\cdot\text{mol}^{-1}$ as compared to $-11.58 \text{ kJ}\cdot\text{mol}^{-1}$ for M386872,

4. Results and Discussion

a difference of $-32.23 \text{ kJ}\cdot\text{mol}^{-1}$. As in M386872, the alkyl alcoholic side-chain stacks against the π cloud of the Phe80 side-chain. However its polarity is not very complimentary to the local electrostatic potential of the surrounding. Also the bulky alkyl side-chain cannot be accommodated well by this binding mode, presumably causing an entropically favourable alternative orientation.

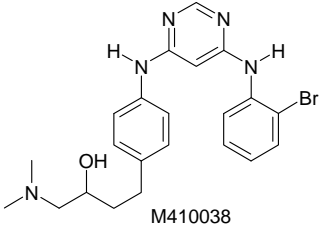
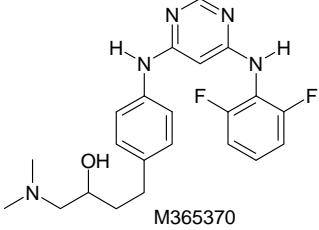
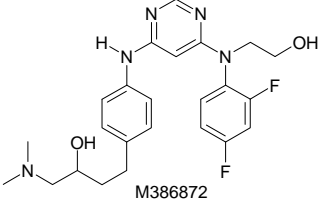
Name of Molecule	Stoichiometry	K_d (μM)	ΔH ($\text{kJ}\cdot\text{mol}^{-1}$)	$T\Delta S$ ($\text{kJ}\cdot\text{mol}^{-1}$)	ΔG ($\text{kJ}\cdot\text{mol}^{-1}$)
 M410038	0.95 ± 0.12	60.97	-35.45 ± 6.36	-11.33	-24.08
 M365370	1.14 ± 0.09	21.04	-9.15 ± 1.34	17.47	-26.63
 M386872	1.13 ± 0.04	37.13	-11.58 ± 0.80	13.67	-25.25

Table 4.2.9 Structure and thermodynamic parameters for M365370 and M386872.

The binding mode of the 4,6-bis anilino pyrimidine series is the same as found earlier in the 2,4-bis anilino pyrimidine series, where they both utilize a single pyrimidine nitrogen and the A-ring aniline NH to form hydrogen bonds to the protein backbone. However the tilt or conformation of the B-ring with respect to pyrimidine was found to vary substantially between different complex structures both within and between the two series. This might go some way to explaining why the thermodynamics of the two series is difficult to understand and do not appear to correlate.

Also the calorimetric results indicated that 2,4-substituted pyrimidines were generally more potent than the 4,6-substituted pyrimidines. For example, M415913, a 2,4-bis substituted analogue is about 18 times more potent (in terms of K_d) than M365538 a 4,6-bis substituted analogue having the same substituents.

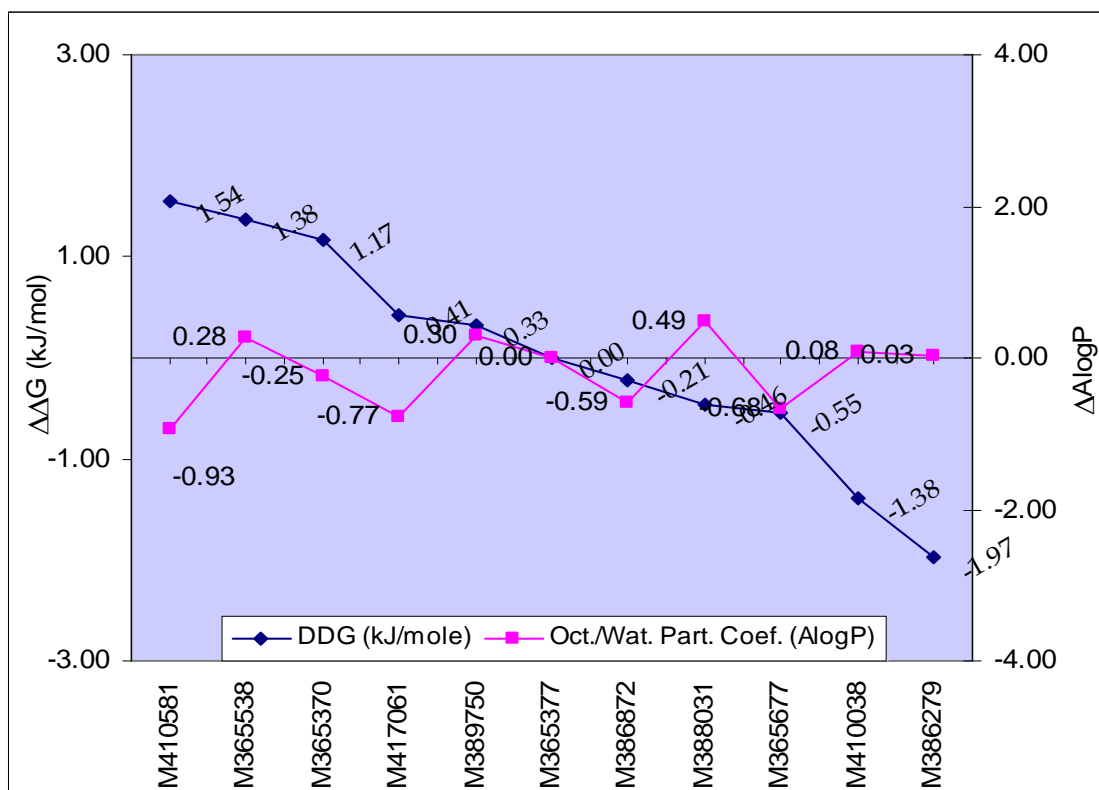


Figure 4.2.6 Comparison of relative experimental ΔG vs relative AlogP (with respect to M365377) of binding to CDK2 with various 4,6-bis anilino pyrimidines at 25 °C.

Experimental calorimetric results, especially ΔG of binding, are also compared with the octanol/water partition constant (AlogP) (Figure 4.2.6). The relative ΔG and AlogP were calculated by using M365377 as the base molecule, since it has only the basic skeleton of 4,6-bis anilino pyrimidine moiety. These results show no clear correlation between ΔG and AlogP, contradicting the results obtained for 2,4-bis anilino pyrimidine analogues. One reason for the lack of correlation would be the similar ΔG values observed for the 4,6-bis anilino pyrimidine analogues. However AlogP calculations are also prone to error, due to the unavailability of logP values for some of the complicated side-chains used in the present series.

4.3 ΔG Calculation by Linear Interaction Energy (LIE) Method

Various computational methods could be used for predicting protein-ligand binding affinity (82; 136; 209-211). In this study, we decided to use the Linear Interaction Energy (LIE) method, a linear response semi-empirical approach based on force field simulation developed by Aqvist and co-workers (79; 86; 212), to calculate the binding free energy of the CDK2-bis aniline pyrimidine inhibitor complexes. The LIE method employs experimental data on binding free energy values for a set of ligands (referred to as the training set) to estimate the binding affinities for a set of novel compounds. The method is based on the linear response approximation (LRA), which dictates that the binding free energy of a protein-ligand system is a function of polar and nonpolar energy components that scale linearly with the electrostatic and van der Waals interactions between a ligand and its environment. The free energy of binding for the complex is derived from considering only two states: (1) free ligand in the solvent and (2) ligand bound to the solvated protein. The conformational changes and entropic effects pertaining to unbound receptor are taken into account implicitly and only interactions between the ligand and either the protein or solvent are computed during molecular mechanics calculations. A detailed description of LIE is given in Section 1.7.

Due to the straightforward nature of using LIE calculations to obtain van der Waals, electrostatic and solvent accessible surface area terms, we decided to use these calculations in this study. LIE parameters are therefore used to investigate the correlation between calorimetrically obtained ΔG values of protein-ligand interactions for CDK2-2,4-bis anilino pyrimidine and CDK2-4,6-bis anilino pyrimidine with ΔG values calculated from LIE computations. Going further we also tried to investigate the effect of substitution of small functional groups on van der Waals (U_{vdw}), electrostatic (U_{elec}) or cavity (U_{cav}) energy by LIE calculations and their correlation with calorimetric ΔG .

Calculation of LIE values was carried out in stages and included protein preparation, docking of ligands and LIE calculations and is described below.

4.3.1 Preparation of X-ray Crystal Structure of CDK2 for Docking and Inhibitor Binding Modes

A total of 6 water molecules and 34 protein residues in an 8 Å radius of the CDK2-M395323 binding pocket were identified as the ligand binding site. These binding site residues are located in different subregions of the CDK2 structure. Explicit water molecules play a very critical role in structure-based drug design applications and have been described extensively by Pospisil et al. (213) and Ladbury et al. (214). 1H01 contains a water molecule (HOH107), in the binding pocket and is required for the binding of M395323. However this molecule is displaced in the M407492 bound structure. Therefore this water molecule was not kept in the final prepared structure of CDK2, which subsequently was used for docking.

Also the inhibitor-binding interfaces of CDK2 for both 2,4-bis anilino pyrimidine and 4,6-bis anilino pyrimidine analogues are very similar and calorimetric experiments predict similar thermodynamic parameters for ligand binding, only one factor is responsible for the thermodynamic difference: a structural difference in the binding modes of the two different inhibitor series.

4.3.2 Docking Bis anilino Pyrimidine Inhibitors with GOLD

As discussed in the Bissantz et al. study (215), GOLD docking is very effective at returning solutions (conformations or poses) close (in terms of the RMSD) to the X-ray conformation for this target. Our results show that each of the top eight poses returned for the reference structure (M407492) had very reasonable all-atom RMSD values of 1.15 to 1.96 Å (we regard RMSD values less than 2.50 Å to be of acceptable quality), compared to the X-ray structure and could have been much better, if the reference structure did not have a flexible tail, as this dimethylamino propanediol tail lacks rigidity and forms loose H-bonds with the protein residues. The overlay of the structure ensemble returned for M407492 is shown in Figure 4.3.1. The GOLD fitness scores obtained were between 28.55 to 37.86 with an average value of 31.77. However the best GOLD fitness score values do not coincide with the best RMSD values and this is observed in many other studies (216). This presents a fundamental problem for conventional scoring methods because, for the most part, the selection of the “best” pose for each molecule is based on ranking the docking solutions using the fast scoring

functions, and poorer conformations sometimes achieve quite high scores. For this reason we decided to use InterAction Fingerprints (IAF) (216) for obtaining best poses of docked conformations for further SGB-LIE study.

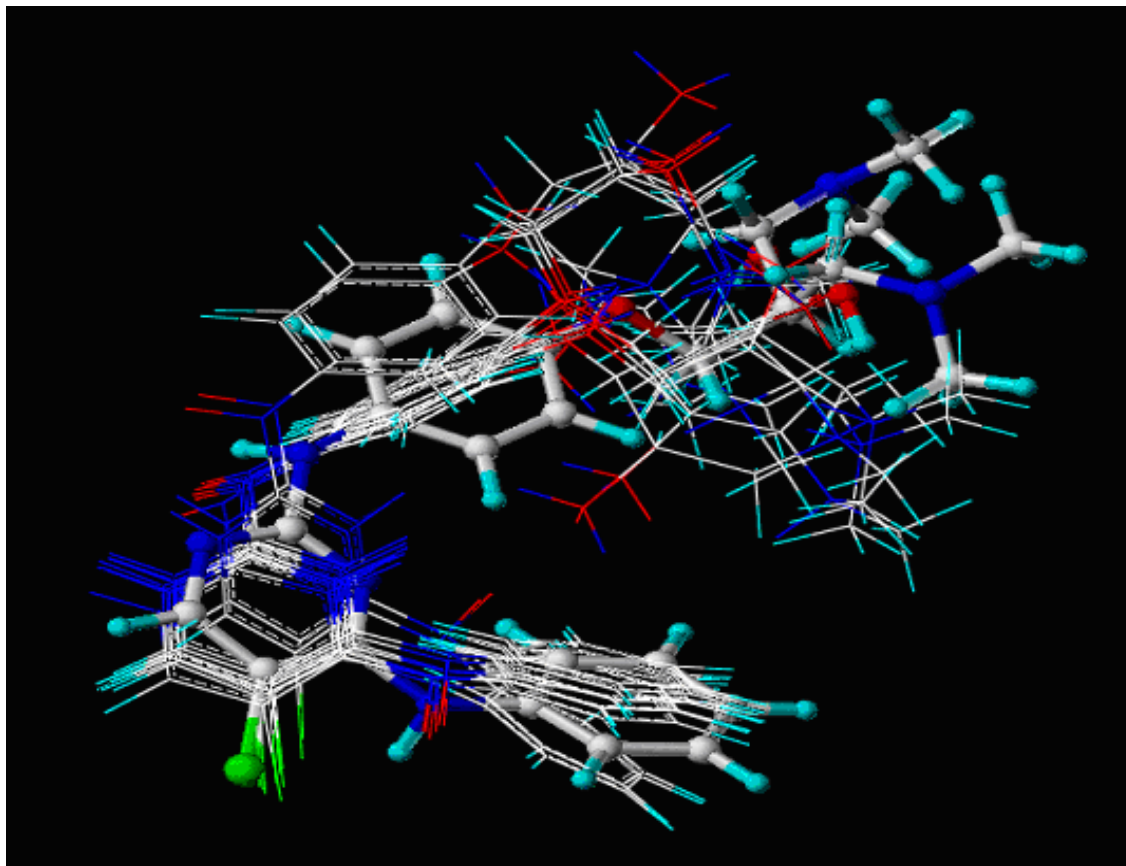


Figure 4.3.1 Figure of 8 best conformations matched with X-crystal structure of M407492. (Figure generated using DS ViewerPro 5.0 (56))

4.3.3 Structural Alignment with IAF

IAF was used to analyze the result and retrieve suitable poses for a typical GOLD docking study. A subtle advantage of the IAF methodology is that scoring is biased toward the observed crystallographic binding mode. This means each “pose” scored highly using the IAF similarity-based method should be preferred, even if its energy score is lower than its “ensemble siblings” from the results of a docking study. Each ensemble comprised of 10 docking poses of an individual small molecule inhibitor (bis-anilino pyrimidine). The poses adopted diverse binding modes, varied in their orientations relative to the target protein, and were complex to interpret visually.

We have used 1H00, 1H01, 1H07 and 1H08 (PDB id) as reference structures for generating IAF fingerprints. Once the best RMSD conformation for the reference structure(s) has been determined, the IAFs are generated for the pose.

4.3.4 LIE calculation

ΔG values obtained by ITC were used as a training set for the LIE Method. The training set for building a binding affinity model was comprised of two subsets of bis-anilino pyrimidine analogues (Table 4.2.1). The first subset comprised 7 ligands, while the second set consisted of 11 ligands.

Both subsets show a large diversity with respect to the K_d values for the binding of CDK2. With around 30 orders of magnitude difference between the K_d values and satisfactory diversity in the structures, the combined set of 18 ligands is ideal to be considered as a training set, as the set does not suffer from bias due to similarity of structures. Also the training set containing 18 analogues contains enough data points not to suffer from underparametrisation or overparametrisation by the SGB-LIE model.

This training set was docked into the CDK2 binding site (discussed in detail in Section 4.3.2). An appropriate visual inspection in tandem with a structural and potential energy analysis has been performed to properly evaluate the quality of each starting pose. The second criterion was based on the statistical validation of the LIE energy model. The SGB-LIE calculations were performed using the LIASION module integrated in the MAESTRO MM package. The simulations were performed for both the ligand free and ligand bound states.

The various interaction energy terms described in the methods were collected and presented in Table 4.3.1. From the results obtained, it is clear that the largest contribution for the binding energy comes from the van der Waals interactions, which is expected as bis-anilino pyrimidine analogues are lipophilic in nature and can also be noticed in the calculated AlogP values (Table 4.2.1). Due to their lipophilic nature they interact favourably with apolar amino acids present in the binding cavity. The cavity energy term in the bound state is smaller than the free state for all the compounds, as there is less energy penalty for creating a cavity in solvent when part of the ligand is buried into the hydrophobic binding site. The reaction field energy term in the free state lies in a narrow range for all compounds, but it varies widely in the bound state as the solvent accessible surface area varies with the ligand structure in the bound form. The

energy values in Table 4.3.1 were used to fit equation 1.7.1 using the Multiple Linear Regression (MLR) algorithm. The values obtained for the three fitting parameters, α , β and γ are 0.88, 0.04 and 0.22, respectively. The large value of van der Waals energy signifies the fact that it contributes significantly towards the ΔG of binding. The contribution of the cavity term to the overall free energy term is also significant and points towards the hydrophobic nature of the ligand.

$$\Delta G = 0.88 \pm 0.18 \langle U_{\text{vdw}} \rangle + 0.04 \pm 0.06 \langle U_{\text{elec}} \rangle + 0.22 \pm 0.68 \langle U_{\text{cav}} \rangle \quad 4.3.1$$

Overall, for this set of 16 inhibitors, a squared correlation coefficient $r^2 = 0.66$ was obtained, which provides one measure of the quality of fit. The average error was $1.74 \text{ kJ}\cdot\text{mol}^{-1}$ (Figure 4.10). Furthermore, the chi-square was 7.7 and p-value was 0.0039 and was less than 0.005, which is normally accepted as upper limit for measurements. However M407492 and M365538 were not taken into account during LIE calculations as the equation fitting gave rise to a greater error.

For the purposes of LIE, we are interested in models with an r^2 greater than 0.6, a standard deviation lower than 1 log unit, and a p-value less than 0.05. Also, for an LIA model to make intuitive sense the α , β and γ coefficients calculated when using the OPLS-2001 force-field should all be positive. From the data obtained, we have managed to achieve all these parameters.

Satisfied with the fitness of the binding affinity model developed using the training set, we decide to correlate various parameters in SGB-LIE calculations with the ΔH and $T\Delta S$. These two parameters (ΔH and $T\Delta S$) were obtained by calorimetric measurement and described in the previous section. The main aim of this study was to obtain a model to predict thermodynamics from SGB-LIE parameters. However the α , β , and γ obtained could also have been used in predicting affinities for the new analogues.

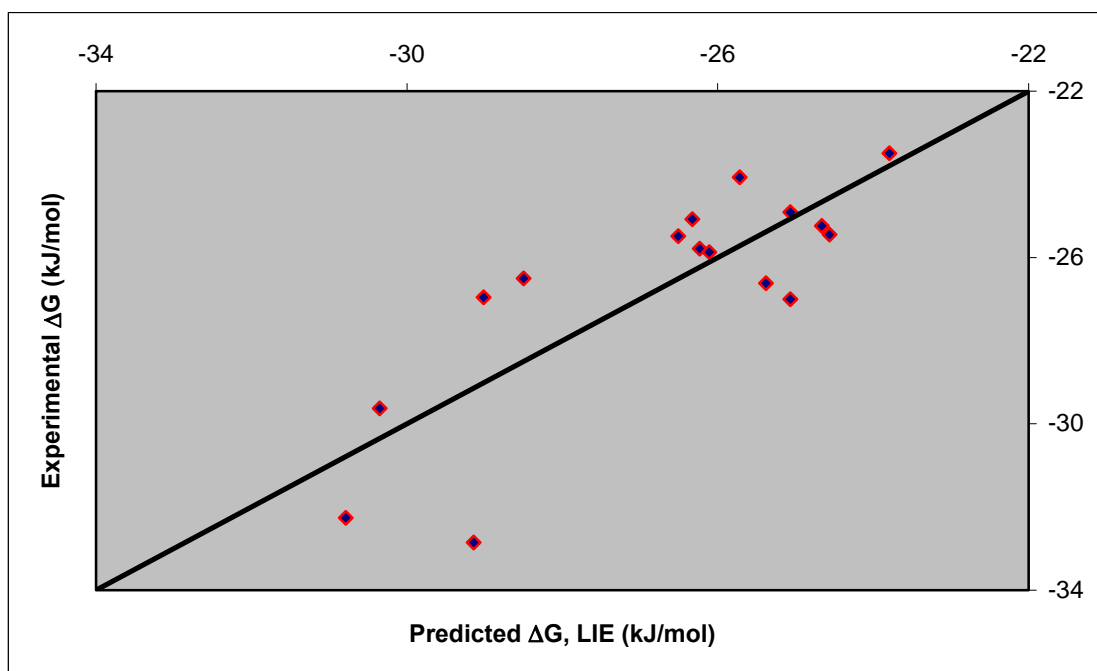


Figure 4.3.2 ΔG values estimated by the SGB-LIE method for 16-bis anillino pyrimidine analogues consisting the experimental ΔG vs. the SGB-LIE ΔG^{ab} . ^a The correlation coefficient (R^2) and rms between the two data sets are 0.66 and 1.74 $\text{kJ}\cdot\text{mol}^{-1}$, respectively. ^b M365538 and M388031 were excluded from SGB-LIE calculations.

4. Results and Discussion

Ligand	$U_{\text{vdw}}^{\text{f}*}$ (kcal·mol ⁻¹)	$U_{\text{ele}}^{\text{f}*}$ (kcal·mol ⁻¹)	$U_{\text{rxn}}^{\text{f}}$ (kcal·mol ⁻¹)	$U_{\text{cav}}^{\text{f}}$ (kcal·mol ⁻¹)	$U_{\text{vdw}}^{\text{b}}$ (kcal·mol ⁻¹)	$U_{\text{ele}}^{\text{b}}$ (kcal·mol ⁻¹)	$U_{\text{rxn}}^{\text{b}}$ (kcal·mol ⁻¹)	$U_{\text{cav}}^{\text{b}}$ (kcal·mol ⁻¹)
M387441	0.00	0.00	- 28.99	7.33	-43.23	-9.42	-21.13	4.80
M395323	0.00	0.00	-24.86	6.54	-48.03	-8.26	-17.06	5.50
M407492	0.00	0.00	- 27.82	7.50	-47.00	-5.87	-17.38	6.38
M415913	0.00	0.00	-28.96	7.32	-48.59	-3.64	-17.47	4.87
M404457	0.00	0.00	- 27.11	7.36	-46.54	-10.76	-18.32	6.08
M437249	0.00	0.00	- 28.01	6.40	-43.45	-13.77	-18.20	5.67
M404797	0.00	0.00	- 22.51	7.65	-45.92	-12.47	-21.38	6.26
M389750	0.00	0.00	- 22.29	7.84	-43.19	-12.94	-10.88	5.70
M365370	0.00	0.00	- 32.59	7.48	-42.49	-5.98	-9.29	5.40
M410038	0.00	0.00	- 28.41	7.44	-42.56	-13.19	-8.57	5.60
M365538	0.00	0.00	- 23.14	7.72	-31.76	-5.33	-8.55	4.70
M417061	0.00	0.00	- 34.02	7.53	-42.92	-15.01	-10.83	5.61
M388031	0.00	0.00	- 29.18	6.62	-38.26	-10.18	-7.81	5.82
M365677	0.00	0.00	- 27.99	7.68	-42.42	-8.51	12.04	7.03
M386279	0.00	0.00	- 30.06	5.58	-41.04	-4.39	-8.54	6.48
M365377	0.00	0.00	- 29.87	7.54	-41.90	-4.04	-7.49	6.35
M386872	0.00	0.00	- 32.29	7.65	-41.42	-6.85	-13.08	4.55
M410581	0.00	0.00	- 34.12	6.53	-40.71	-36.37	-22.65	5.71

Table 4.3.1 The data are collected from a 30 ps. Simulation after a 15 ps. equilibration. Each ligand shows the LIE component for bound-free state. * Absence of explicit interaction between the ligands and solvent in the free state results in a van der Waals and electrostatic energy equal to zero.

4. Results and Discussion

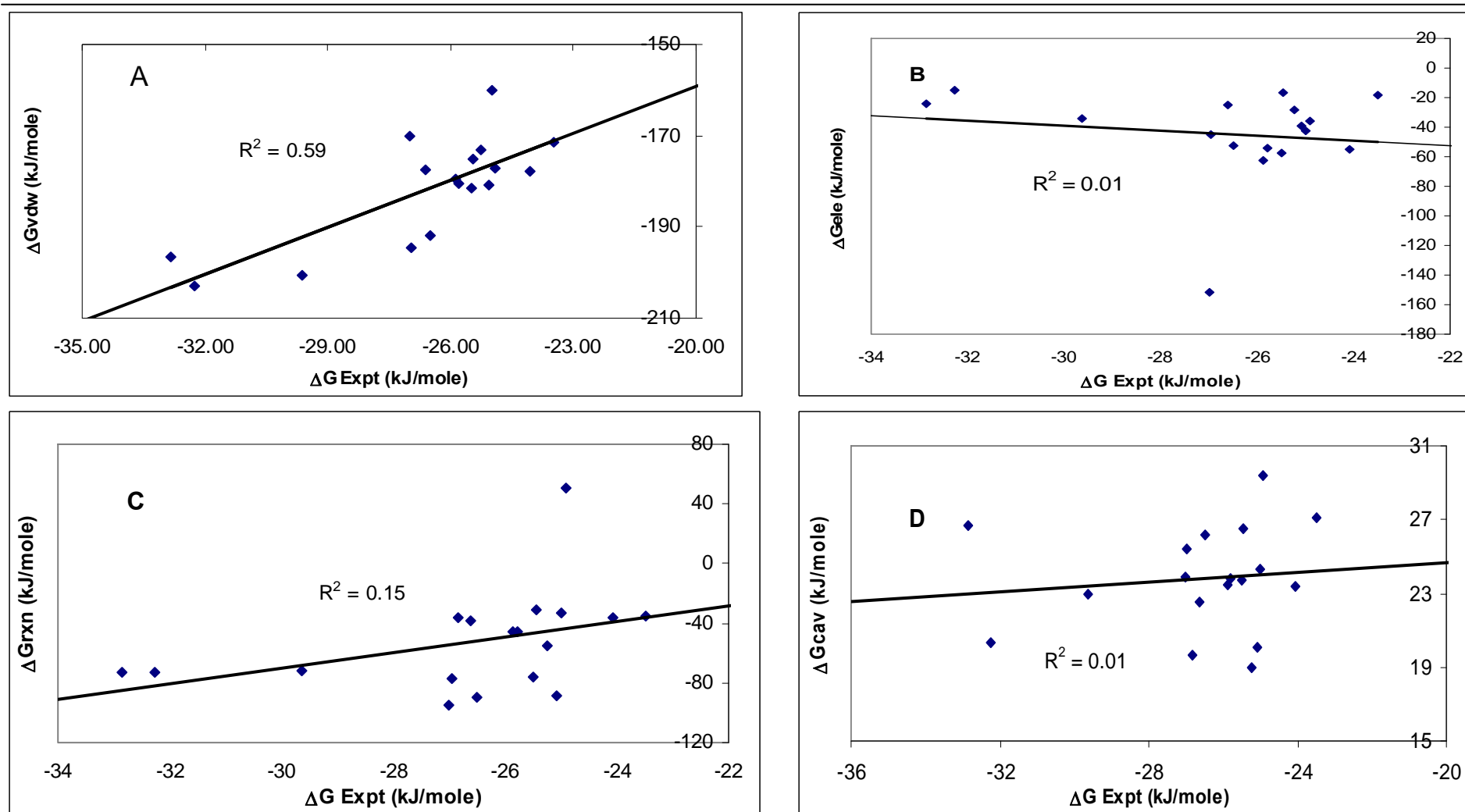


Figure 4.3.3 Plot of A: van der Waals, B: electrostatic, C: reaction field, and D: cavity energies vs. experimental binding affinity for binding of 2,4-bisanillinopyrimidine and 4,6-bis anilino pyrimidine to CDK2.

Ligand name	Experimental ΔG (kJ·mol ⁻¹)	Predicted, LIE ΔG (kJ·mol ⁻¹)	$\Delta\Delta G$ (kJ·mol ⁻¹)
M395323	-29.63	-30.35	0.72
M407492	-32.85	-29.14	-3.70
M415913	-32.26	-30.79	-1.47
M404457	-26.96	-29.01	2.05
M437249	-25.49	-26.51	1.02
M404797	-26.5	-28.50	2.00
M387441	-25.08	-26.32	1.24
M389750	-25.79	-26.23	0.44
M365370	-26.62	-25.38	-1.24
M410038	-24.07	-25.72	1.65
M417061	-25.87	-26.11	0.24
M365677	-24.91	-25.06	0.15
M386279	-23.49	-23.79	0.30
M365377	-25.45	-24.56	-0.89
M386872	-25.24	-24.66	-0.58
M365538	-26.83	-24.43	-2.40
M388031	-24.99	-24.70	-0.29
M410581	-27	-25.07	-1.93

Table 4.3.2 Table showing differences in ΔG calculated from calorimetry and ΔG calculated from LIE.

The predicted free energy values for the test set ligands are plotted against the calorimetrically obtained values in Figure 4.3.2. Apart from M365538, all other ΔG values match closely between the calorimetric and LIE free energy values for the rest of the ligands in the test set with RMS deviation of less than 0.5 kcal·mol⁻¹ (2.09 kJ·mol⁻¹). The poor ΔG predictions for M407492 and M365538 could be attributed partially to their novel binding modes and difference in substituents.

All of the computed van der Waals, electrostatic, reaction field and cavity energies are reported in Table 4.3.1, whereas Figure 4.3.3A, Figure 4.3.3B, Figure 4.3.3C and Figure 4.3.3D show the van der Waals, electrostatic, reaction field and cavity terms plotted against the ΔG for binding of 2,4-bis anilino pyrimidine and 4,6-bis anilino pyrimidine with CDK2. This correlation shows that the van der Waals term is most correlated with $r^2 = 0.59$ and has the greatest slope. The Coulombic and solvation terms are less well correlated, whereas the solvation term is really just a scatter of points with correlation coefficient r^2 of 0.01.

As expected the cavity energy for the free ligand increases as the solvent accessible surface area increases or as the substituents are added on to the ring. The comparison of the Coulomb and solvation terms, shows that they tend to oppose each other, as one would expect, and is consistent with earlier observations from the Liaison calculations. Placing one or more charges on the bis-anilino pyrimidine ring causes dramatic swings in the electrostatic energy and can be seen as a high electrostatic energy of about $-15.01 \text{ kcal}\cdot\text{mol}^{-1}$ in values calculated for M517061. However M410581 displays highest electrostatic energy of about $-36.37 \text{ kcal}\cdot\text{mol}^{-1}$ and is unusual for a small molecule possessing a hydroxyl group on the B-ring. However, Åqvist and Hansson (79) demonstrated that the presence of hydroxyl groups in solvent and solvated compounds interfered with the electrostatic linear response. This was mainly attributed to the short range character of dipolar fields and the existence of hydrogen bonding in and between the simulated states (solute and solvent in their studies). Generally speaking, the use of continuum-solvation leads to total electrostatic terms that are large relative to explicit solvent simulations and results in correspondingly smaller coefficients for β .

We also tried to correlate ΔH and $T\Delta S$ with van der Waals, electrostatic, reaction field and cavity energies. However, ΔH and $T\Delta S$ were correlated poorly with all these parameters with r^2 lower than 0.1. Also, in theory ΔH and $T\Delta S$ correlation with van der Waals, electrostatic, reaction field and cavity energies is difficult to obtain as most of the free energy perturbation algorithms are heavily biased towards the calculation of ΔG of binding.

Finally, one of the main advantages of the SGB-LIE method over other computational methods for calculating binding affinities is the fact that SGB-LIE includes a solvent model. Since binding of the ligand to the receptor as well as binding to the solvent is taken into account, the LIE handles the desolvation free energy reasonably well. Initially, the electrostatic part was calculated by an electrostatic linear response approximation (parameter β), whereas the van der Waals contribution (parameter α) was calculated by calibration against experimental binding data. Since the latter is dependent on experimental data, it may implicitly take into account other contributions, such as force field errors and systematic entropy terms.

4.4 Conclusion

Investigating molecular recognition requires through knowledge of the binding thermodynamics of the system, together with insight into the structure of the complex of interest. The present study provides unique insight into the effects of substituent modification and position on the biophysical properties associated with the interactions of related bis-anilino pyrimidines with CDK2.

This study shows that substituent position could be correlated with changes in thermodynamic properties, and through a series of systematic modifications of the bisanilino pyrimidine system, we have demonstrated that the placement and type of polyfunctional groups added to the aniline B-ring plays a pivotal role in dictating the thermodynamic mechanism by which these compounds interact with CDK2. The orientation of these groups may result in favourable contacts with neighboring amino acids and will ultimately influence the biological effectiveness.

In this study we have used a combination of calorimetric experiment and SGB-LIE calculations to investigate underlying thermodynamics for the series of bis-anilino pyrimidine inhibitors to CDK2 and involved developing a SGB-LIE computational model for prediction of binding affinities using calorimetric derived ΔG . We obtained an excellent linear correlation r^2 of 0.66, between experimental and calculated ΔG values for compounds that bind to CDK2 with K_d values ranging from 1.72 μM to 74.73 μM , a 44-fold difference. The excellent correlation for the compounds of the training set is remarkable. The LIE approach provided a very good method for prediction of absolute ligand binding affinities, as well as binding orientation of ligands.

The close estimation of ΔG for a wide range of compounds establishes the LIE methodology as an efficient tool for screening novel compounds with very similar structures. Compared to empirical methods, such as scoring functions, the LIE method is more accurate due to the semi-empirical approach adopted in which real experimental data are used to build the binding affinity model. Also the SGB-LIE method seems promising when compared to the FEP or TI methods in achieving comparable accuracy with much faster speed.

5. Chapter

Protein-Ligand Interactions: An Epilogue

Summary of Thesis and Conclusion

5.1 Summary of Thesis

This research work has mainly been devoted to the investigation of positive ΔC_p in protein-ligand interactions (especially N-Hsp90-Mg²⁺ADP/ATP interaction). The background necessary to understand protein-ligand interactions, together with the aims and background of the thesis, has been presented in Chapter 1, while experimental results have been discussed in the following chapters. In this concluding chapter, a broader view on the conclusions in the light of their importance for understanding protein-ligand interactions is presented, and will give some suggestions for future projects.

From the early 90s, there has been a strong interest in establishing and refining correlations between binding and structural features of the protein-ligand complex and observed changes in thermodynamic quantities. This correlation is not only important to in-depth understanding of the physical principles of molecular recognition, but is also needed for developing simplified algorithms to predict thermodynamics in

5. Conclusion and Further Work

structure-based and/or rational drug design strategies. To date several researchers had proposed parameterisation of binding parameters in terms of $\Delta SASA$ calculation. However discrepancies are widespread, as these correlations ignore water molecules and metal ions present at the binding interface.

Additionally, current views about protein-ligand interactions state that electrostatic forces drive the binding of charged species and burial of hydrophobic and polar surfaces controls the ΔC_p associated with the binding interaction. However from this research work, it can be noted that for the interaction of protein with a divalent cation plus nucleotide the electrostatic components in overall binding energetics is expected to be significant due to the ionic nature of the ligand. Whereas the calculated ΔC_p is expected to be small, due to the size of the surface area burial. As a result, we have carried out several experiments to investigate the sign and magnitude of ΔC_p in electrostatic interactions and shown that positive ΔC_p is linked to disordering of a tightly ordered water molecules from the Mg^{2+} ion in the N-Hsp90- Mg^{2+} ADP/ATP binding. As a result, a binding or folding event, where tightly ordered water molecules are released from a surface of a metal ion after binding to protein, can result in significant ΔC_p independent of the changes calculated from exposed hydrophobic surface and coupled conformational transitions. This observation was also confirmed by carrying out binding titrations of various divalent metal cations with EDTA.

Resultantly, this outcome has a wide reaching implication in the calculation of thermodynamics of binding from $\Delta SASA$ based methods and shows that the interaction involving electrostatic component should be treated differently. This can be considered as a major achievement of this work as previous studies conducted for investigating positive ΔC_p in protein-ligand interactions had failed to draw any significant conclusions about its origin.

Next in Chapter 4, the binding thermodynamics of the minor structural modifications on bis-anilino pyrimidine binding to CDK2 and their resultant correlation with van der Waals, electrostatic, reaction field and cavity energy were investigated.

Results show that the contribution of the basic phenyl ring of M387441, which binds in a hydrophobic pocket, is primarily enthalpy driven. However after substitution, the monosubstituted and disubstituted bis-anilino pyrimidine analogues showed varied thermodynamic signature, indicating that significant enthalpy-entropy compensation can be expected even upon introducing slight structural change. In other words, the ΔG of binding fluctuated much less with modifications of the inhibitors, than their constituting

enthalpic and entropic contributions. This observation makes designing new drugs more difficult, since a relatively large change in the structure of an inhibitor may not give the substantially enhanced binding affinity that was aimed for, but may instead result in a moderate change.

On the positive side, we were successful in predicting ΔG of binding by computational method like SGB-LIE. This method could be used as a precursor in a rational drug development strategy before introducing a new structural modification in investigating a ligand. Additionally this study shows that electrostatic, van der Waals and hydrophobic interactions based solely on the buried surface area were insufficient to fully understand the binding thermodynamics and highlights the danger of using empirical/semi empirical models blindly to correlate thermodynamics with binding energies obtained from simulation, even in the simplest case. However, if used wisely, this technique could be a boon in development of rational drug design strategies.

5.2 Further Work

1. This research work has established the fact that positive ΔC_p can be observed in protein-ligand interactions, which is contrary to the normally observed negative ΔC_p . Resultantly more experiments can be conducted with a protein-ligand system, where metal ligand is required for binding of protein-nucleotide interactions.
2. The data obtained in N-Hsp90-ADP/ATP titration could be used for developing a SASA correlation for prediction of ΔC_p in different buffers, solvents, salts and at different pH conditions. Additionally a correction factor could also be added to $\Delta SASA$ calculations, where divalent metals and bound waters play an important role in ligand binding.
3. Correlation of various thermodynamics with van der Waals, electrostatic, and solvent accessible terms showed promising results and needs extensive further investigation with a bigger dataset containing several series of ligands and biomolecules. This will give a clear idea about the correlation between these parameters and also will act as an ideal starting point for building up theoretical models for prediction of thermodynamics of closely related compounds.

6. References

1. Ladbury, J. E. (2001) Isothermal titration calorimetry: application to structure-based drug design, *Thermochimica Acta* 380, 209-215.
2. Gomez, J. and Freire, E. (1995) Thermodynamic mapping of the inhibitor site of the aspartic protease endothiasepsin, *J. Mol. Biol.* 252, 337-350.
3. Ohtaka, H., Muzammil, S., Schon, A., Velazquez-Campoy, A., Vega, S., and Freire, E. (2004) Thermodynamic rules for the design of high affinity HIV-1 protease inhibitors with adaptability to mutations and high selectivity towards unwanted targets, *Int. J. Biochem. Cell Biol.* 36, 1787-1799.

6. References

4. Velazquez-Campoy, A., Luque, I., Todd, M. J., Milutinovich, M., Kiso, Y., and Freire, E. (2000) Thermodynamic dissection of the binding energetics of KNI-272, a potent HIV-1 protease inhibitor, *Protein Sci.* *9*, 1801-1809.
5. Henriques, D. A., Ladbury, J. E., and Jackson, R. M. (2000) Comparison of binding energies of SrcSH2-phosphotyrosyl peptides with structure-based prediction using surface area based empirical parameterization, *Protein Sci.* *9*, 1975-1985.
6. Karplus, M. and Janin, J. (1999) Comment on: 'The entropy cost of protein association', *Protein Engineering Design and Selection* *12*, 185-186.
7. Niedzwiecka, A., Stepinski, J., Darzynkiewicz, E., Sonenberg, N., and Stolarski, R. (2002) Positive heat capacity change upon specific binding of translation initiation factor eIF4E to mRNA 5' cap, *Biochemistry* *41*, 12140-12148.
8. Robblee, J. P., Cao, W., Henn, A., Hannemann, D. E., and De La Cruz, E. M. (2005) Thermodynamics of nucleotide binding to actomyosin V and VI: a positive heat capacity change accompanies strong ADP binding, *Biochemistry* *44*, 10238-10249.
9. Hermans, J. and Wang, L. (1997) Inclusion of Loss of Translational and Rotational Freedom in Theoretical Estimates of Free Energies of Binding. Application to a Complex of Benzene and Mutant T4 Lysozyme, *Journal of the American Chemical Society* *119*, 2707-2714.
10. Lumry, R. and Rajender, S. (1970) Enthalpy-entropy compensation phenomena in water solutions of proteins and small molecules-A ubiquitous property of water, *Biopolymers* *9*, 1125-1127.
11. Tanford, C. (1978) The hydrophobic effect and the organization of living matter, *Science* *200*, 1012-1018.
12. Sharp, K. A. and Madan, B. (1997) Hydrophobic effect, water structure, and heat capacity changes, *J. Phys. Chem. B* *101*, 4343-4348.
13. Chaplin, M. (2005) Water structure and science, <http://www.lsbu.ac.uk/water/vibrat.html>.
14. Dill, K. A. and Bromberg, S. (2002) Water as a solvent, in *Molecular Driving Forces: Statistical Thermodynamics in Chemistry & Biology* (Dill, K. A. and Bromberg, S., Eds.) pp 577-591, Garland Science, New York.
15. Cohen, C. (2005) The hydrophobic effect, http://www.bio.brandeis.edu/classes/biochem104/hydrophobic_effect.pdf.

16. Bouvier, D. (1999) Hydrophobic effect and van der Waals interactions, http://www.arpe.snv.jussieu.fr/td_2_eng/hydhyd.html.
17. Perrin, C. L. and Nielson, J. B. (1997) "Strong" hydrogen bonds in chemistry and biology, *Annu. Rev. Phys. Chem.* 48, 511-544.
18. Baker, E. N. and Hubbard, R. E. (1984) Hydrogen bonding in globular proteins, *Prog. Biophys. Mol Biol* 44, 97-179.
19. Fleming, P. J. and Rose, G. D. (2005) Do all backbone polar groups in proteins form hydrogen bonds?, *Protein Sci.* 14, 1911-1917.
20. McDonald, I. K. and Thornton, J. M. (1994) Satisfying hydrogen bonding potential in proteins, *J Mol Biol* 238, 777-793.
21. Matthew, J. B., Weber, P. C., Salemme, F. R., and Richards, F. M. (1983) Electrostatic orientation during electron transfer between flavodoxin and cytochrome c, *Nature* 301, 169-171.
22. Sharp, K. A. and Honig, B. (1990) Electrostatic interactions in macromolecules-theory and applications, *Annual Review of Biophysics and Biophysical Chemistry* 19, 301-332.
23. (2009) Lennard-Jones potential, http://en.wikipedia.org/wiki/Lennard-Jones_potential.
24. Knapp, M., Bellamacina, C., Murray, J. M., and Bussiere, D. E. (2006) Targeting cancer: the challenges and successes of structure-based drug design against the human purinome, *Curr. Top. Med. Chem* 6, 1129-1159.
25. Boehr, D. D., Farley, A. R., Wright, G. D., and Cox, J. R. (2002) Analysis of the π - π stacking interactions between the aminoglycoside antibiotic kinase APH(3')-IIIa and its nucleotide ligands, *Chemistry & Biology* 9, 1209-1217.
26. Arunan, E. and Gutowsky, H. S. (1993) The rotational spectrum, structure and dynamics of a benzene dimer, *Journal of Chemical Physics* 98, 4294-4296.
27. Gallivan, J. P. and Dougherty, D. A. (1999) Cation- π interactions in structural biology, *Proc. Natl. Acad. Sci. U. S A* 96, 9459-9464.
28. Zhong, W., Gallivan, J. P., Zhang, Y., Li, L., Lester, H. A., and Dougherty, D. A. (1998) From ab initio quantum mechanics to molecular neurobiology: A cation- π binding site in the nicotinic receptor, *PNAS* 95, 12088-12093.
29. Tame, J., O'Brien, R., and Ladbury, J. E. (1998) Isothermal titration calorimetry of biomolecules, in *Biocalorimetry: Applications of Calorimetry in the*

6. References

- Biological Sciences* (Ladbury, J. E. and Chowdhry, B. Z., Eds.) pp 27-38, John Wiley & Sons Ltd., West Sussex.
30. Murphy, K. P. and Freire, E. (1992) Thermodynamics of structural stability and cooperative folding behavior in proteins, *Adv. Protein Chem.* *43*, 313-361.
 31. Spolar, R. S. and Record, M. T., Jr. (1994) Coupling of local folding to site-specific binding of proteins to DNA, *Science* *263*, 777-784.
 32. Makhatadze, G. I. and Privalov, P. L. (1995) Energetics of protein structure, *Adv. Protein Chem.* *47*, 307-425.
 33. Myers, J. K., Pace, C. N., and Scholtz, J. M. (1995) Denaturant m values and heat capacity changes: relation to changes in accessible surface areas of protein unfolding, *Protein Sci.* *4*, 2138-2148.
 34. Edsall, J. T. (1935) Apparent molal heat capacities of amino acids and other organic compounds, *J. Am. Chem. Soc.* *8*, 1506-1507.
 35. Kauzman, W. (1959) Some factors in the interpretation of protein denaturation, *Adv. Protein Chem.* *14*, 1-63.
 36. Ooi, T., Oobatake, M., Nemethy, G., and Scheraga, H. A. (1987) Accessible surface areas as a measure of the thermodynamic parameters of hydration of peptides, *Proc. Natl. Acad. Sci. U. S. A* *84*, 3086-3090.
 37. Spolar, R. S., Ha, J. H., and Record, M. T., Jr. (1989) Hydrophobic effect in protein folding and other noncovalent processes involving proteins, *Proc. Natl. Acad. Sci. U. S. A* *86*, 8382-8385.
 38. Makhatadze, G. I. and Privalov, P. L. (1990) Heat capacity of proteins. I. Partial molar heat capacity of individual amino acid residues in aqueous solution: hydration effect, *J Mol Biol* *213*, 375-384.
 39. Loladze, V. V., Ermolenko, D. N., and Makhatadze, G. I. (2001) Heat capacity changes upon burial of polar and nonpolar groups in proteins, *Protein Sci.* *10*, 1343-1352.
 40. Guinto, E. R. and Di, C. E. (1996) Large heat capacity change in a protein-monovalent cation interaction, *Biochemistry* *35*, 8800-8804.
 41. Morton, C. J. and Ladbury, J. E. (1996) Water-mediated protein-DNA interactions: the relationship of thermodynamics to structural detail, *Protein Sci.* *5*, 2115-2118.

42. Sturtevant, J. M. (1977) Heat capacity and entropy changes in processes involving proteins, *Proc. Natl. Acad. Sci. U. S A* 74, 2236-2240.
43. Frank, H. S. and Evans, M. W. (1945) Free volume and entropy in condensed systems III. Entropy in binary liquid mixtures; Partial molal entropy in dilute solutions; Structure and thermodynamics in aqueous electrolytes, *The Journal of Chemical Physics* 13, 507-532.
44. Gill, S. J. and Wadso, I. (1976) An equation of state describing hydrophobic interactions, *Proc. Natl. Acad. Sci. U. S A* 73, 2955-2958.
45. Ritossa, F. (1962) New puffing pattern induced by temperature shock and Dnp in drosophila, *Experientia* 18, 571-&.
46. Hartl, F. U. and Hayer-Hartl, M. (2002) Molecular chaperones in the cytosol: from nascent chain to folded protein, *Science* 295, 1852-1858.
47. Morimoto, R. I., Kline, M. P., Bimston, D. N., and Cotto, J. J. (1997) The heat shock response: regulation and function of heat-shock proteins and molecular chaperones, *Essays Biochem.* 32, 17-29.
48. Whitesell, L. and Lindquist, S. L. (2005) HSP90 and the chaperoning of cancer, *Nat. Rev. Cancer* 5, 761-772.
49. Pratt, W. B. and Toft, D. O. (1997) Steroid receptor interactions with heat shock protein and immunophilin chaperones, *Endocr. Rev.* 18, 306-360.
50. Young, J. C., Moarefi, I., and Hartl, F. U. (2001) Hsp90: a specialized but essential protein-folding tool, *J. Cell Biol.* 154, 267-273.
51. Goetz, M. P., Toft, D. O., Ames, M. M., and Erlichman, C. (2003) The Hsp90 chaperone complex as a novel target for cancer therapy, *Ann Oncol* 14, 1169-1176.
52. Panaretou, B., Prodromou, C., Roe, S. M., O'Brien, R., Ladbury, J. E., Piper, P. W., and Pearl, L. H. (1998) ATP binding and hydrolysis are essential to the function of the Hsp90 molecular chaperone in vivo, *EMBO J.* 17, 4829-4836.
53. Pearl, L. H. and Prodromou, C. (2006) Structure and mechanism of the HSP90 molecular chaperone machinery, *Annual Review of Biochemistry* 75, 271-294.
54. Prodromou, C., Roe, S. M., O'Brien, R., Ladbury, J. E., Piper, P. W., and Pearl, L. H. (1997) Identification and structural characterization of the ATP/ADP-binding site in the Hsp90 molecular chaperone, *Cell* 90, 65-75.

6. References

55. Stebbins, C. E., Russo, A. A., Schneider, C., Rosen, N., Hartl, F. U., and Pavletich, N. P. (1997) Crystal structure of an Hsp90-geldanamycin complex: Targeting of a protein chaperone by an antitumor agent, *Cell* 89, 239-250.
56. (2002) Discovery Studio ViewerPro 5, Accelrys Software Inc, San Diego, CA.
57. Wallace, A. C., Laskowski, R. A., and Thornton, J. M. (1995) Ligplot - A program to generate schematic diagrams of protein ligand interactions, *Protein Engineering* 8, 127-134.
58. Morgan, D. O. (1997) Cyclin-dependent kinases: engines, clocks, and microprocessors, *Annu. Rev. Cell Dev. Biol.* 13, 261-291.
59. Kamb, A. (1995) Cell-cycle regulators and cancer, *Trends Genet.* 11, 136-140.
60. Shapiro, G. I. and Harper, J. W. (1999) Anticancer drug targets: cell cycle and checkpoint control, *J. Clin. Invest* 104, 1645-1653.
61. Senderowicz, A. M. and Sausville, E. A. (2000) Preclinical and clinical development of cyclin-dependent kinase modulators, *J. Natl. Cancer Inst.* 92, 376-387.
62. Malumbres, M. and Barbacid, M. (2005) Mammalian cyclin-dependent kinases, *Trends in Biochemical Sciences* 30, 630-641.
63. Hwang, H. C. and Clurman, B. E. (2005) Cyclin E in normal and neoplastic cell cycles, *Oncogene* 24, 2776-2786.
64. Krek, W., Xu, G., and Livingston, D. M. (1995) Cyclin A-kinase regulation of E2F-1 DNA binding function underlies suppression of an S phase checkpoint, *Cell* 83, 1149-1158.
65. Chen, Y. N., Sharma, S. K., Ramsey, T. M., Jiang, L., Martin, M. S., Baker, K., Adams, P. D., Bair, K. W., and Kaelin, W. G., Jr. (1999) Selective killing of transformed cells by cyclin/cyclin-dependent kinase 2 antagonists, *Proc. Natl. Acad. Sci. U. S A* 96, 4325-4329.
66. Sherr, C. J. and Roberts, J. M. (1999) CDK inhibitors: positive and negative regulators of G1-phase progression, *Genes Dev.* 13, 1501-1512.
67. De Bondt, H. L., Rosenblatt, J., Jancarik, J., Jones, H. D., Morgan, D. O., and Kim, S. H. (1993) Crystal structure of cyclin-dependent kinase 2, *Nature* 363, 595-602.
68. Knighton, D. R., Zheng, J. H., Ten Eyck, L. F., Ashford, V. A., Xuong, N. H., Taylor, S. S., and Sowadski, J. M. (1991) Crystal structure of the catalytic

- subunit of cyclic adenosine monophosphate-dependent protein kinase, *Science* 253, 407-414.
69. Johnson, L. N., Noble, M. E., and Owen, D. J. (1996) Active and inactive protein kinases: structural basis for regulation, *Cell* 85, 149-158.
70. Johnson, L. N., Lowe, E. D., Noble, M. E. M., and Owen, D. J. (1998) The structural basis for substrate recognition and control by protein kinases, *Febs Letters* 430, 1-11.
71. Davies, T. G., Pratt, D. J., Endicott, J. A., Johnson, L. N., and Noble, M. E. (2002) Structure-based design of cyclin-dependent kinase inhibitors, *Pharmacol. Ther.* 93, 125-133.
72. Davies, T. G., Tunnah, P., Meijer, L., Marko, D., Eisenbrand, G., Endicott, J. A., and Noble, M. E. (2001) Inhibitor binding to active and inactive CDK2: the crystal structure of CDK2-cyclin A/indirubin-5-sulphonate, *Structure* 9, 389-397.
73. Legraverend, M., Tunnah, P., Noble, M., Ducrot, P., Ludwig, O., Grierson, D. S., Leost, M., Meijer, L., and Endicott, J. (2000) Cyclin-dependent kinase inhibition by new C-2 alkynylated purine derivatives and molecular structure of a CDK2-inhibitor complex, *J. Med. Chem.* 43, 1282-1292.
74. Noble, M. E. and Endicott, J. A. (1999) Chemical inhibitors of cyclin-dependent kinases: insights into design from X-ray crystallographic studies, *Pharmacol. Ther.* 82, 269-278.
75. Schulze-Gahmen, U., Brandsen, J., Jones, H. D., Morgan, D. O., Meijer, L., Vesely, J., and Kim, S. H. (1995) Multiple modes of ligand recognition: crystal structures of cyclin-dependent protein kinase 2 in complex with ATP and two inhibitors, olomoucine and isopentenyladenine, *Proteins* 22, 378-391.
76. Pierce, M. M., Raman, C. S., and Nall, B. T. (1999) Isothermal titration calorimetry of protein-protein interactions, *Methods* 19, 213-221.
77. Ladbury, J. E. and Chowdhry, B. Z. (1996) Sensing the heat: the application of isothermal titration calorimetry to thermodynamic studies of biomolecular interactions, *Chem. Biol.* 3, 791-801.
78. Wiseman, T., Williston, S., Brandts, J. F., and Lin, L. N. (1989) Rapid measurement of binding constants and heats of binding using a new titration calorimeter, *Anal. Biochem.* 179, 131-137.
79. Aqvist, J. and Hansson, T. (1996) On the validity of electrostatic linear response in polar solvents, *Journal of Physical Chemistry* 100, 9512-9521.

80. Cochran, S., Li, C. P., and Bytheway, I. (2005) An experimental and molecular-modelling study of the binding of linked sulfated tetracyclitols to FGF-1 and FGF-2, *Chembiochem.* 6, 1882-1890.
81. Rizzo, R. C., Tirado-Rives, J., and Jorgensen, W. L. (2001) Estimation of binding affinities for HEPT and nevirapine analogues with HIV-1 reverse transcriptase via Monte Carlo simulations, *J. Med. Chem.* 44, 145-154.
82. Singh, P., Mhaka, A. M., Christensen, S. B., Gray, J. J., Denmeade, S. R., and Isaacs, J. T. (2005) Applying linear interaction energy method for rational design of noncompetitive allosteric inhibitors of the sarco- and endoplasmic reticulum calcium-ATPase, *J. Med. Chem.* 48, 3005-3014.
83. Zoete, V., Michielin, O., and Karplus, M. (2003) Protein-ligand binding free energy estimation using molecular mechanics and continuum electrostatics. Application to HIV-1 protease inhibitors, *J. Comput. Aided Mol. Des* 17, 861-880.
84. Zhou, R., Friesner, R. A., Ghosh, A., Rizzo, R. C., Jorgensen, W. L., and Levy, R. M. (2001) New linear interaction method for binding affinity calculations using a continuum solvent model, *J. Phys. Chem. B* 105, 10388-10397.
85. Carlson, H. A. and Jorgensen, W. L. (1995) An extended linear response method for determining free energies of hydration, *The Journal of Physical Chemistry* 99, 10667-10673.
86. Marelius, J., Ljungberg, K. B., and Aqvist, J. (2001) Sensitivity of an empirical affinity scoring function to changes in receptor-ligand complex conformations, *Eur. J. Pharm. Sci.* 14, 87-95.
87. Goodford, P. J. (1984) Drug design by the method of receptor fit, *J. Med. Chem.* 27, 558-564.
88. Goodford, P. J. (1985) A computational procedure for determining energetically favorable binding sites on biologically important macromolecules, *J. Med. Chem.* 28, 849-857.
89. Brown, N. R., Noble, M. E., Endicott, J. A., and Johnson, L. N. (1999) The structural basis for specificity of substrate and recruitment peptides for cyclin-dependent kinases, *Nat. Cell Biol.* 1, 438-443.
90. Delaglio, F., Grzesiek, S., Vuister, G. W., Zhu, G., Pfeifer, J., and Bax, A. (1995) NMRPipe: a multidimensional spectral processing system based on UNIX pipes, *Journal Of Biomolecular NMR* 6, 277-293.

91. Kraulis, P. J. (1989) ANSIG: a program for the assignment of protein H2D NMR spectra by interactive computer graphics, *Journal of Magnetic Resonance* 84, 627-633.
92. Provencher, S. W. and Glockner, J. (1981) Estimation of globular protein secondary structure from circular-dichroism, *Biochemistry* 20, 33-37.
93. Pedretti, A., Villa, L., and Vistoli, G. (2002) VEGA: a versatile program to convert, handle and visualize molecular structure on Windows-based PCs, *Journal of Molecular Graphics and Modelling* 21, 47-49.
94. Pedretti, A., Villa, L., and Vistoli, G. (2004) VEGA-An open platform to develop chemo-bio-informatics applications, using plug-in architecture and script programming, *Journal of Computer-Aided Molecular Design* 18, 167-173.
95. Lindahl, E., Hess, B., and van der Spoel, D. (2001) GROMACS 3.0: a package for molecular simulation and trajectory analysis, *J. Mol. Model.* 7, 306-317.
96. Van Der, S. D., Lindahl, E., Hess, B., Groenhof, G., Mark, A. E., and Berendsen, H. J. (2005) GROMACS: fast, flexible, and free, *J. Comput. Chem.* 26, 1701-1718.
97. van Aalten, D. M., Bywater, R., Findlay, J. B., Hendlich, M., Hooft, R. W., and Vriend, G. (1996) PRODRG, a program for generating molecular topologies and unique molecular descriptors from coordinates of small molecules, *J. Comput. Aided Mol. Des* 10, 255-262.
98. Berendsen, H. J., Postma, J. P., van Gunsteren, W. F., and Hermans, J. (1981) Interaction models for water in relation to protein hydration, in *Intermolecular Forces* (Pullman, B., Ed.) pp 331-342, D. Reidel Publishing Co., Dordrecht.
99. Humphrey, W., Dalke, A., and Schulten, K. (1996) VMD: Visual molecular dynamics, *Journal of Molecular Graphics* 14, 33-&.
100. van Buuren, A. R. and Berendsen, H. J. (1993) Molecular dynamics simulation of the stability of a 22-residue alpha-helix in water and 30% trifluoroethanol, *Biopolymers* 33, 1159-1166.
101. Turner, P. (2003) XMGRACE, <http://plasma-gate.weizmann.ac.il/Grace/>.
102. Makarov, V. A., Andrews, B. K., Smith, P. E., and Pettitt, B. M. (2000) Residence times of water molecules in the hydration sites of myoglobin, *Biophys. J.* 79, 2966-2974.
103. David van der Spoel (2004) GROMACS exercises, <http://www.csc.fi/chem/courses/gmx2004/exercises/#mozTocId530967>.

104. Breault, G. A., Ellston, R. P., Green, S., James, S. R., Jewsbury, P. J., Midgley, C. J., Pauptit, R. A., Minshull, C. A., Tucker, J. A., and Pease, J. E. (2003) Cyclin-dependent kinase 4 inhibitors as a treatment for cancer. Part 2: identification and optimisation of substituted 2,4-bis anilino pyrimidines, *Bioorg. Med. Chem. Lett.* *13*, 2961-2966.
105. Verdonk, M. L., Cole, J. C., Hartshorn, M. J., Murray, C. W., and Taylor, R. D. (2003) Improved protein-ligand docking using GOLD, *Proteins-Structure Function and Genetics* *52*, 609-623.
106. Liaison, version 3.0, Schrödinger, LLC, New York, NY, 2004.
107. Jorgensen, W. L., Maxwell, D. S., and Tirado-Rives, J. (1996) Development and testing of the OPLS all-atom force field on conformational energetics and properties of organic liquids, *Journal of the American Chemical Society* *118*, 11225-11236.
108. Salek, R. M., Williams, M. A., Prodromou, C., Pearl, L. H., and Ladbury, J. E. (2002) Backbone resonance assignments of the 25kD N-terminal ATPase domain from the Hsp90 chaperone, *J Biomol. NMR* *23*, 327-328.
109. Dullweber, F., Stubbs, M. T., Musil, D., Sturzebecher, J., and Klebe, G. (2001) Factorising ligand affinity: a combined thermodynamic and crystallographic study of trypsin and thrombin inhibition, *J. Mol. Biol.* *313*, 593-614.
110. Grunau, A., Paine, M. J., Ladbury, J. E., and Gutierrez, A. (2006) Global effects of the energetics of coenzyme binding: NADPH controls the protein interaction properties of human cytochrome P450 reductase, *Biochemistry* *45*, 1421-1434.
111. Ladbury, J. E., Wynn, R., Thomson, J. A., and Sturtevant, J. M. (1995) Substitution of charged residues into the hydrophobic core of Escherichia coli thioredoxin results in a change in heat capacity of the native protein, *Biochemistry* *34*, 2148-2152.
112. Perozzo, R., Jelesarov, I., Bosshard, H. R., Folkers, G., and Scapozza, L. (2000) Compulsory order of substrate binding to herpes simplex virus type 1 thymidine kinase. A calorimetric study, *J. Biol. Chem.* *275*, 16139-16145.
113. Dunitz, J. D. (1995) Win some, lose some: enthalpy-entropy compensation in weak intermolecular interactions, *Chem. Biol.* *2*, 709-712.
114. Lachenmann, M. J., Ladbury, J. E., Qian, X., Huang, K., Singh, R., and Weiss, M. A. (2004) Solvation and the hidden thermodynamics of a zinc finger probed by nonstandard repair of a protein crevice, *Protein Sci.* *13*, 3115-3126.
115. Lumry, R. (2003) Uses of enthalpy-entropy compensation in protein research, *Biophysical Chemistry* *105*, 545-557.

116. Chiosis, G., Timaul, M. N., Lucas, B., Munster, P. N., Zheng, F. F., Sepp-Lorenzino, L., and Rosen, N. (2001) A small molecule designed to bind to the adenine nucleotide pocket of Hsp90 causes Her2 degradation and the growth arrest and differentiation of breast cancer cells, *Chemistry & Biology* 8, 289-299.
117. Maiti, R., Van Domselaar, G. H., Zhang, H., and Wishart, D. S. (2004) SuperPose: a simple server for sophisticated structural superposition, *Nucleic Acids Res.* 32, W590-W594.
118. Bohm, M., Sturzebecher, J., and Klebe, G. (1999) Three-dimensional quantitative structure-activity relationship analyses using comparative molecular field analysis and comparative molecular similarity indices analysis to elucidate selectivity differences of inhibitors binding to trypsin, thrombin, and factor Xa, *J. Med. Chem.* 42, 458-477.
119. Renatus, M., Bode, W., Huber, R., Sturzebecher, J., and Stubbs, M. T. (1998) Structural and functional analyses of benzamidine-based inhibitors in complex with trypsin: Implications for the inhibition of factor Xa, tPA, and urokinase, *J. Med. Chem.* 41, 5445-5456.
120. Cooper, A. (2005) Heat capacity effects in protein folding and ligand binding: a re-evaluation of the role of water in biomolecular thermodynamics, *Biophys. Chem.* 115, 89-97.
121. Freire, E. (1993) Structural thermodynamics: Prediction of protein stability and protein binding affinities, *Archives of Biochemistry and Biophysics* 303, 181-184.
122. Yamada, K. (1999) Thermodynamic analyses of calcium binding to troponin C, calmodulin and parvalbumins by using microcalorimetry, *Molecular and Cellular Biochemistry* 190, 39-45.
123. Cooper, A., Johnson, C. M., Lakey, J. H., and Nollmann, M. (2001) Heat does not come in different colours: entropy-enthalpy compensation, free energy windows, quantum confinement, pressure perturbation calorimetry, solvation and the multiple causes of heat capacity effects in biomolecular interactions, *Biophys. Chem.* 93, 215-230.
124. Ladbury, J. E. and Williams, M. A. (2004) The extended interface: measuring non-local effects in biomolecular interactions, *Curr. Opin. Struct. Biol.* 14, 562-569.
125. Holdgate, G. A., Tunnicliffe, A., Ward, W. H., Weston, S. A., Rosenbrock, G., Barth, P. T., Taylor, I. W., Pauptit, R. A., and Timms, D. (1997) The entropic penalty of ordered water accounts for weaker binding of the antibiotic novobiocin to a resistant mutant of DNA gyrase: a thermodynamic and crystallographic study, *Biochemistry* 36, 9663-9673.

6. References

126. Bergqvist, S., Williams, M. A., O'Brien, R., and Ladbury, J. E. (2004) Heat capacity effects of water molecules and ions at a protein-DNA interface, *Journal of Molecular Biology* 336, 829-842.
127. Hennessey, J. P. and Johnson, W. C. (1981) Information-content in the circular-dichroism of proteins, *Biochemistry* 20, 1085-1094.
128. Manavalan, P. and Johnson, W. C. (1983) Sensitivity of circular-dichroism to protein tertiary structure class, *Nature* 305, 831-832.
129. Fukada, H. and Takahashi, K. (1998) Enthalpy and heat capacity changes for the proton dissociation of various buffer components in 0.1 M potassium chloride, *Proteins* 33, 159-166.
130. Good, N. E., Winget, G. D., Winter, W., Connolly, T. N., Izawa, S., and Singh, R. M. (1966) Hydrogen ion buffers for biological research, *Biochemistry* 5, 467-477.
131. Jelesarov, I. and Bosshard, H. R. (1994) Thermodynamics of ferredoxin binding to ferredoxin:NADP⁺ reductase and the role of water at the complex interface, *Biochemistry* 33, 13321-13328.
132. Baker, B. M. and Murphy, K. P. (1996) Evaluation of linked protonation effects in protein binding reactions using isothermal titration calorimetry, *Biophysical Journal* 71, 2049-2055.
133. Cooper, A. (1999) Thermodynamic analysis of biomolecular interactions, *Curr. Opin. Chem. Biol.* 3, 557-563.
134. Banerjee, S. K., Vandenhoff, G. E., and Rupley, J. A. (1974) Dependence on pH of the free energy and enthalpy of interaction of monosaccharides and disaccharides with lysozyme, *J. Biol. Chem.* 249, 1439-1444.
135. Nguyen, B., Stanek, J., and Wilson, W. D. (2006) Binding-linked protonation of a DNA minor-groove agent, *Biophysical Journal* 90, 1319-1328.
136. Oda, M., Furukawa, K., Ogata, K., Sarai, A., and Nakamura, H. (1998) Thermodynamics of specific and non-specific DNA binding by the c-Myb DNA-binding domain, *J. Mol. Biol.* 276, 571-590.
137. Bolen, D. W., Flogel, M., and Biltonen, R. (1971) Calorimetric studies of protein-Inhibitor Interaction .1. Binding of 3'-cytidine monophosphate to ribonuclease-A at pH 5.5, *Biochemistry* 10, 4136-4140.
138. Cameron, A. E. and Wichers, E. (1962) Report of international commission on atomic weights, *Journal of the American Chemical Society* 84, 4175-4197.

139. Megaw, H. D. (1934) Cell dimensions of ordinary and heavy ice, *Nature* *134*, 900-901.
140. Nemethy, G. and Scheraga, H. A. (1964) Structure of water and hydrophobic bonding in proteins. IV. The thermodynamic properties of liquid deuterium oxide, *The Journal of Chemical Physics* *41*, 680-689.
141. Connelly, P. R., Thomson, J. A., Fitzgibbon, M. J., and Bruzzese, F. J. (1993) Probing hydration contributions to the thermodynamics of ligand binding by proteins. Enthalpy and heat capacity changes of tacrolimus and rapamycin binding to FK506 binding protein in D₂O and H₂O, *Biochemistry* *32*, 5583-5590.
142. Chervenak, M. C. and Toone, E. J. (1994) A direct measure of the contribution of solvation to the thermodynamics of binding, *Biophysical Journal* *66*, A359.
143. Chervenak, M. C. and Toone, E. J. (1994) A direct measure of the contribution of solvent reorganization to the enthalpy of ligand-binding, *Journal of the American Chemical Society* *116*, 10533-10539.
144. Tuominen, V. U., Myles, D. A. A., Dauvergne, M. T., Lahti, R., Heikinheimo, P., and Goldman, A. (2004) Production and preliminary analysis of perdeuterated yeast inorganic pyrophosphatase crystals suitable for neutron diffraction, *Acta Crystallographica Section D-Biological Crystallography* *60*, 606-609.
145. Artero, J. B., Hartlein, M., McSweeney, S., and Timmins, P. (2005) A comparison of refined X-ray structures of hydrogenated and perdeuterated rat gamma ε-crystallin in H₂O and D₂O, *Acta Crystallogr. D Biol. Crystallogr.* *61*, 1541-1549.
146. Connelly, P. R. and Thomson, J. A. (1992) Heat capacity changes and hydrophobic interactions in the binding of FK506 and rapamycin to the FK506 binding protein, *Proc. Natl. Acad. Sci. U. S. A* *89*, 4781-4785.
147. Habash, J., Raftery, J., Nuttall, R., Price, H. J., Wilkinson, C., Kalb, A. J., and Helliwell, J. R. (2000) Direct determination of the positions of the deuterium atoms of the bound water in -concanavalin A by neutron Laue crystallography, *Acta Crystallogr. D Biol. Crystallogr.* *56 (Pt 5)*, 541-550.
148. Finer-Moore, J. S., Kossiakoff, A. A., Hurley, J. H., Earnest, T., and Stroud, R. M. (1992) Solvent structure in crystals of trypsin determined by X-ray and neutron diffraction, *Proteins* *12*, 203-222.
149. Coates, L., Erskine, P. T., Wood, S. P., Myles, D. A., and Cooper, J. B. (2001) A neutron Laue diffraction study of endothiapepsin: implications for the aspartic proteinase mechanism, *Biochemistry* *40*, 13149-13157.

6. References

150. Wlodawer, A., Borkakoti, N., Moss, D. S., and Howlin, B. (1986) Comparison of 2 Independently Refined Models of Ribonuclease-A, *Acta Crystallographica Section B-Structural Science* 42, 379-387.
151. Wlodawer, A., Savage, H., and Dodson, G. (1989) Structure of Insulin - Results of Joint Neutron and X-Ray Refinement, *Acta Crystallographica Section B-Structural Science* 45, 99-107.
152. Meilleur, F., Contzen, J., Myles, D. A. A., and Jung, C. (2004) Structural stability and dynamics of hydrogenated and perdeuterated cytochrome P450cam (CYP101), *Biochemistry* 43, 8744-8753.
153. Arnett, E. M. and McKelvey, D. R. (1969) *Solute-Solvent Interactions* Marcel Dekker, New York.
154. Kresheck, G. C., Schneider, H., and Scheraga, H. A. (1965) The effect of D₂O on the thermal stability of proteins. Thermodynamic parameters for the transfer of model compounds from H₂O to D₂O, *J. Phys. Chem.* 69, 3132-3144.
155. Ben Naim, A., Ting, K. L., and Jernigan, R. L. (1990) Solvent effect on binding thermodynamics of biopolymers, *Biopolymers* 29, 901-919.
156. Ben Naim, A. (1990) Solvent effects on protein association and protein folding, *Biopolymers* 29, 567-596.
157. Makhatadze, G. I., Clore, G. M., and Gronenborn, A. M. (1995) Solvent isotope effect and protein stability, *Nat. Struct. Biol.* 2, 852-855.
158. Benjamin, L. and Benson, G. C. (1962) A deuterium isotope effect on the excess enthalpy of methanol-water solutions, *J. Phys. Chem.* 67, 858-861.
159. Cioni, P. and Strambini, G. B. (2002) Effect of heavy water on protein flexibility, *Biophys. J.* 82, 3246-3253.
160. Eisenhaber, F., Lijnzaad, P., Argos, P., Sander, P., and Scharf, M. (1995) The double cubic lattice method: Efficient approaches to numerical integration of surface area and volume and to dot surface contouring of molecular assemblies, *Journal of Computational Chemistry* 16, 273-284.
161. Prodromou, C., Roe, S. M., Piper, P. W., and Pearl, L. H. (1997) A molecular clamp in the crystal structure of the N-terminal domain of the yeast Hsp90 chaperone, *Nat. Struct. Biol.* 4, 477-482.
162. Privalov, P. L. and Makhatadze, G. I. (1992) Contribution of hydration and non-covalent interactions to the heat capacity effect on protein unfolding, *J. Mol. Biol.* 224, 715-723.

163. Robertson, A. D. and Murphy, K. P. (1997) Protein structure and the energetics of protein stability, *Chem. Rev.* *97*, 1251-1268.
164. Yang, A. S., Sharp, K. A., and Honig, B. (1992) Analysis of the heat capacity dependence of protein folding, *J. Mol. Biol.* *227*, 889-900.
165. Helms, V. and Wade, R. C. (1995) Thermodynamics of water mediating protein-ligand interactions in cytochrome P450cam: a molecular dynamics study, *Biophys. J* *69*, 810-824.
166. Wade, R. C., Mazor, M. H., McCammon, J. A., and Quijoch, F. A. (1991) A molecular dynamics study of thermodynamic and structural aspects of the hydration of cavities in proteins, *Biopolymers* *31*, 919-931.
167. Damjanovic, A., Garcia-Moreno, B., Lattman, E. E., and Garcia, A. E. (2005) Molecular dynamics study of water penetration in staphylococcal nuclease, *Proteins* *60*, 433-449.
168. Denisov, V. P. and Halle, B. (1996) Protein hydration dynamics in aqueous solution, *Faraday Discuss.* 227-244.
169. Berndt, K. D., Beunink, J., Schroder, W., and Wuthrich, K. (1993) Designed replacement of an internal hydration water molecule in BPTI: structural and functional implications of a glycine-to-serine mutation, *Biochemistry* *32*, 4564-4570.
170. Williams, M. A., Goodfellow, J. M., and Thornton, J. M. (1994) Buried waters and internal cavities in monomeric proteins, *Protein Sci.* *3*, 1224-1235.
171. Bizzarri, A. R. and Cannistraro, S. (2002) Molecular dynamics of water at the protein-solvent interface, *J. Phys. Chem. B* *106*, 6617-6633.
172. Levitt, M. and Park, B. H. (1993) Water: now you see it, now you don't, *Structure* *1*, 223-226.
173. Qian, Y. Q., Billeter, M., Otting, G., Muller, M., Gehring, W. J., and Wuthrich, K. (1989) The structure of the antennapedia homeodomain determined by NMR spectroscopy in solution: comparison with prokaryotic repressors, *Cell* *59*, 573-580.
174. Barratt, E., Bingham, R. J., Warner, D. J., Laughton, C. A., Phillips, S. E., and Homans, S. W. (2005) Van der Waals interactions dominate ligand-protein association in a protein binding site occluded from solvent water, *J. Am. Chem Soc.* *127*, 11827-11834.

175. Hess, B. (2002) Convergence of sampling in protein simulations, *Physical Review e* 65, 03191001-03191010.
176. Frauenfelder, H., Sligar, S. G., and Wolynes, P. G. (1991) The energy landscapes and motions of proteins, *Science* 254, 1598-1603.
177. Chen, C., Beck, B. W., Krause, K., and Pettitt, B. M. (2006) Solvent participation in *Serratia marcescens* endonuclease complexes, *Proteins* 62, 982-995.
178. Ross, P. D. and Subramanian, S. (1981) Thermodynamics of protein association reactions: forces contributing to stability, *Biochemistry* 20, 3096-3102.
179. Matulis, D. and Bloomfield, V. A. (2001) Thermodynamics of the hydrophobic effect. II. Calorimetric measurement of enthalpy, entropy, and heat capacity of aggregation of alkylamines and long aliphatic chains, *Biophys. Chem.* 93, 53-65.
180. Dill, K. A., Truskett, T. M., Vlachy, V., and Hribar-Lee, B. (2005) Modeling water, the hydrophobic effect, and ion solvation, *Annu. Rev. Biophys. Biomol. Struct.* 34, 173-199.
181. Raschke, T. M. and Levitt, M. (2005) Nonpolar solutes enhance water structure within hydration shells while reducing interactions between them, *Proc. Natl. Acad. Sci. U. S A* 102, 6777-6782.
182. Bakk, A., Hoyer, J. S., and Hansen, A. (2002) Apolar and polar solvation thermodynamics related to the protein unfolding process, *Biophys. J.* 82, 713-719.
183. Gill, S. J., Nichols, N. F., and Wadso, I. (1976) Calorimetric determination of enthalpies of solution of slightly soluble liquids II. Enthalpy of solution of some hydrocarbons in water and their use in establishing the temperature dependence of their solubilities, *The Journal of Chemical Thermodynamics* 8, 445-452.
184. Gill, S. J., Downing, M., and Sheats, G. F. (1967) The enthalpy of self-association of purine derivatives in water, *Biochemistry* 6, 272-276.
185. Pimentel, G. C. and McClellan, A. L. (1971) Hydrogen bonding, *Annual Review of Physical Chemistry* 22, 347-385.
186. Ross, P. D. and Shapiro, J. T. (1974) Heat of interaction of DNA with polylysine, spermine, and Mg^{2+} , *Biopolymers* 13, 415-416.
187. Shiao, D. D. and Sturtevant, J. M. (1976) Heats of binding protons to globular proteins, *Biopolymers* 15, 1201-1211.

6. References

188. Misra, V. K., Hecht, J. L., Yang, A. S., and Honig, B. (1998) Electrostatic contributions to the binding free energy of the lambdacl repressor to DNA, *Biophys. J.* 75, 2262-2273.
189. Gregory, D. S., Martin, A. C., Cheetham, J. C., and Rees, A. R. (1993) The prediction and characterization of metal binding sites in proteins, *Protein Eng* 6, 29-35.
190. Schymkowitz, J. W., Rousseau, F., Martins, I. C., Ferkinghoff-Borg, J., Stricher, F., and Serrano, L. (2005) Prediction of water and metal binding sites and their affinities by using the Fold-X force field, *Proc. Natl. Acad Sci U. S. A* 102, 10147-10152.
191. Sodhi, J. S., Bryson, K., McGuffin, L. J., Ward, J. J., Wernisch, L., and Jones, D. T. (2004) Predicting metal-binding site residues in low-resolution structural models, *J. Mol. Biol.* 342, 307-320.
192. Rajasekaran, M. B., Nilapwar, S. M., Andrews, S. C., and Watson, K. A. (2009) EfeO-cupredoxins: major new members of the cupredoxin superfamily with roles in bacterial iron transport, *BioMetals*.
193. Kalidas, Y. and Chandra, N. (2008) PocketDepth: a new depth based algorithm for identification of ligand binding sites in proteins, *J. Struct. Biol.* 161, 31-42.
194. Nayal, M. and Di, C. E. (1994) Predicting Ca²⁺-binding sites in proteins, *Proc. Natl. Acad. Sci. U. S. A* 91, 817-821.
195. Obermann, W. M., Sondermann, H., Russo, A. A., Pavletich, N. P., and Hartl, F. U. (1998) In vivo function of Hsp90 is dependent on ATP binding and ATP hydrolysis, *J. Cell Biol.* 143, 901-910.
196. Bock, C. W., Katz, A. K., Markham, G. D., and Glusker, J. P. (1999) Manganese as a replacement for magnesium and zinc: Functional comparison of the divalent ions, *Journal of the American Chemical Society* 121, 7360-7372.
197. Christianson, D. W. (1997) Structural chemistry and biology of manganese metalloenzymes, *Prog. Biophys. Mol. Biol.* 67, 217-252.
198. Bertini, I. and Luchinat, C. (1996) NMR of paramagnetic substances, *Coord. Chem. Rev.* 150, 1-296.
199. (2009) Circular dichroism spectroscopy. <http://www.ruppweb.org/cd/cdtutorial.htm#Examples>
200. Peeraer, Y., Rabijns, A., Collet, J. F., Van Schaftingen, E., and De Ranter, C. (2004) How calcium inhibits the magnesium-dependent enzyme human phosphoserine phosphatase, *European Journal of Biochemistry* 271, 3421-3427.

201. Gilli, R., Lafitte, D., Lopez, C., Kilhoffer, M., Makarov, A., Briand, C., and Haiech, J. (1998) Thermodynamic analysis of calcium and magnesium binding to calmodulin, *Biochemistry* 37, 5450-5456.
202. Katz, A. K., Glusker, J. P., Beebe, S. A., and Bock, C. W. (1996) Calcium ion coordination: A comparison with that of beryllium, magnesium, and zinc, *Journal of the American Chemical Society* 118, 5752-5763.
203. Banerjee, M., Poddar, A., Mitra, G., Surolia, A., Owa, T., and Bhattacharyya, B. (2005) Sulfonamide drugs binding to the colchicine site of tubulin: thermodynamic analysis of the drug-tubulin interactions by isothermal titration calorimetry, *J. Med. Chem.* 48, 547-555.
204. Hall, M. and Peters, G. (1996) Genetic alterations of cyclins, cyclin-dependent kinases, and Cdk inhibitors in human cancer, *Adv. Cancer Res.* 68, 67-108.
205. Lawrie, A. M., Noble, M. E., Tunnah, P., Brown, N. R., Johnson, L. N., and Endicott, J. A. (1997) Protein kinase inhibition by staurosporine revealed in details of the molecular interaction with CDK2, *Nat. Struct. Biol.* 4, 796-801.
206. Wang, S., Wood, G., Meades, C., Griffiths, G., Midgley, C., McNae, I., McInnes, C., Anderson, S., Jackson, W., Mezna, M., Yuill, R., Walkinshaw, M., and Fischer, P. M. (2004) Synthesis and biological activity of 2-anilino-4-(1H-pyrrol-3-yl) pyrimidine CDK inhibitors, *Bioorg. Med. Chem. Lett.* 14, 4237-4240.
207. Beattie, J. F., Breault, G. A., Ellston, R. P., Green, S., Jewsbury, P. J., Midgley, C. J., Naven, R. T., Minshull, C. A., Pauptit, R. A., Tucker, J. A., and Pease, J. E. (2003) Cyclin-dependent kinase 4 inhibitors as a treatment for cancer. Part 1: identification and optimisation of substituted 4,6-bis anilino pyrimidines, *Bioorg. Med. Chem. Lett.* 13, 2955-2960.
208. Talhout, R., Villa, A., Mark, A. E., and Engberts, J. B. F. N. (2003) Understanding binding affinity: A combined isothermal titration calorimetry/molecular dynamics study of the binding of a series of hydrophobically modified benzamidinium chloride inhibitors to trypsin, *Journal of the American Chemical Society* 125, 10570-10579.
209. Pan, X., Tan, N., Zeng, G., Han, H., and Huang, H. (2006) 3D-QSAR and docking studies of aldehyde inhibitors of human cathepsin K, *Bioorg. Med. Chem.* 14, 2771-2778.
210. Chong, L. T., Duan, Y., Wang, L., Massova, I., and Kollman, P. A. (1999) Molecular dynamics and free-energy calculations applied to affinity maturation in antibody 48G7, *Proc. Natl. Acad. Sci. USA* 96, 14330.

211. Eriksson, M. A. L., Pitera, J., and Kollman, P. A. (1999) Prediction of the binding free energies of new TIBO-like HIV-1 reverse transcriptase inhibitors using a combination of PROFEC, PB/SA, CMC/MD, and free energy calculations, *J. Med. Chem.* 42, 868.
212. Marelius, J., Hansson, T., and Aqvist, J. (1998) Calculation of ligand binding free energies from molecular dynamics simulations, *International Journal of Quantum Chemistry* 69, 77-88.
213. Pospisil, P., Kuoni, T., Scapozza, L., and Folkers, G. (2002) Methodology and problems of protein-ligand docking: case study of dihydroorotate dehydrogenase, thymidine kinase, and phosphodiesterase 4, *J. Recept. Signal. Transduct. Res.* 22, 141-154.
214. Ladbury, J. E. (1996) Just add water! The effect of water on the specificity of protein-ligand binding sites and its potential application to drug design, *Chemistry & Biology* 3, 973-980.
215. Bissantz, C., Folkers, G., and Rognan, D. (2000) Protein-based virtual screening of chemical databases. 1. Evaluation of different docking/scoring combinations, *J. Med. Chem* 43, 4759-4767.
216. Mpamhanga, C. P., Chen, B. N., Mclay, I. M., and Willett, P. (2006) Knowledge-based interaction fingerprint scoring: A simple method for improving the effectiveness of fast scoring functions, *Journal of Chemical Information and Modeling* 46, 686-698.